

Towards a Search for Heavy Neutral Leptons Decaying into Neutral Pions in the Short-Baseline Near Detector



Vu Chi Lan Nguyen

Supervisors: Prof. Vitaly Kudryavtsev
Prof. Neil Spooner

Department of Physics & Astronomy
University of Sheffield

This dissertation is submitted for the degree of
Doctor of Philosophy

August 2024

Abstract

Heavy Neutral Lepton (HNL) is proposed to be the right-handed heavy partner to the left-handed Standard Model (SM) neutrino, motivated by neutrino mass mechanisms. HNLs are hypothesised to be produced from kaon decays in the Booster Neutrino Beam (BNB) and subsequently decay in the Short-Baseline Near Detector (SBND), leaving observable signals for detection. The presented thesis focuses on the HNL channel $N \rightarrow \nu\pi^0$ in the mass range of 140–260 MeV, where the neutral pion decays into di-photon showers inside the detector. SBND is a 112 ton liquid argon time projection chamber, which offers an exceptional resolution in calorimetry, spatial and timing. The capability of SBND to search for HNLs is assessed in this thesis, of which the analysis exploits the boosted topology and late arrival features of HNL signals. Two selections of HNLs are presented, with one having more aggressive background rejection than the other. Both have a background rejection $\mathcal{O}(10^{-4})$ while maintaining a signal efficiency of $\sim 30\%$. Moreover, an assessment of sensitivity under the assumption of an improved timing reconstruction is also given. The treatment of statistical and systematic uncertainties is outlined, followed by a limits setting procedure to set upper limits on the coupling $|U_{\mu 4}|^2$ of Majorana HNLs at the 90% confidence level. Three result scenarios are presented, demonstrating the current and potential physics capabilities of SBND.

Declaration

This thesis represents the original work of the author except for where specific references are made to the work of others. The presented work has not been submitted in whole or in part for consideration for any other degree or qualification in this, or any other university. Due to the collaborative nature of particle experiments, the thesis relies upon the work of collaborators from the Short-Baseline Near Detector (SBND) and other experiments.

The overviews of Heavy Neutral Leptons (HNLs) and physics of liquid argon time projection chambers, given in Chapters 2 and 3 respectively, contain work to which the author did not contribute. References assign credit for the work and figures presented.

The overview of SBND given in Chapter 4 relies on work performed by the entire SBND collaboration [1, 2]. Figures not made by the author are labelled with references to the source. In the scope of detector installation, the author helped with the cabling of the Photon Detection System (PDS) boxes and their installation to the detector alongside B. Carlson and B. Bogart. The author also installed the PDS readout electronics, under the guidance of M. Stancari and W. Badgett.

Also in Chapter 4, the flux prediction employs the Booster Neutrino Beam simulation developed in MiniBooNE [3]. The flux simulation was performed by Z. Pavlovic and the flux reader was developed by M. Del Tutto. The author assisted with validating the fluxes at SBND after updating to the kaon reweighting scheme from SciBooNE [4] .

In the simulation framework of SBND described in Chapter 5, the author contributed to the development of the MeVPrtl generator for simulating beyond standard model particles. This generator was a joint effort of SBND and ICARUS collaborators, led by G. Putnam. The author developed and validated the physics of HNL simulation with R. Alvarez-Garrote and L. Pelegrina-Gutierrez. The implementation of the generator into SBND was performed together with R. Alvarez-Garrote. Moreover, the author identified and helped implement a fix in the GENIE generator to enable the timing simulation

of neutrino interactions, which necessitated the HNL analysis using Monte Carlo (MC) samples.

In Chapter 6, the charge reconstruction toolkits, Wirecell [5] and Pandora [6], were developed before the author’s involvement. The author updated the track-shower separation algorithm within Pandora, with the help of E. Tyley and D. Brailsford. The PDS and CRT reconstruction and analysis tools were contributed by SBND collaborators with credits provided in the references. Most importantly, the author would like to thank F. Nicolas-Arnaldos, R. Alvarez-Garrote, D. Garcia-Gamez and J. I. Crespo-Anadon, who pioneered the timing reconstruction using the SBND PDS, which the HNL analysis relies on.

The study of the DAQ timing performance in Chapter 7, relies on work performed by SBND collaborators. The hardware and software of the White Rabbit timing system as well as the CRT Sharps was setup before the author’s involvement. The author contributed in the calibration and installation of the SPEC-TDC module and the cabling of timing signals under the guidance of M. Stancari, G. A. Lukhanin and W. Badgett. The timing characterisation of FEB modules was performed with the help of M. Stancari and H. Lay. The timing characterisation of CAEN digitisers received inputs from M. Stancari.

In Chapter 8, the presented work in the scope of charge calibration was performed under the guidance of M. Mooney and many discussions with G. Putnam and J. Mueller. A summary of results from the ICARUS collaboration is included, with references assigned credit in the work and figures presented.

The selection of HNLs in Chapter 9 contains many elements shared across SBND collaborators. MC samples used in the selection were a collaborative work with H. Lay and R. Alvarez-Garrote. The selection software was built with help from H. Lay. Moreover, the cosmic rejection tool CRUMBS was developed by H. Lay, the flash matching tool OpT0 was developed by L. Tung and the particle identification tool Razzled was developed by H. Lay with groundwork done by E. Tyley. Finally, the selection sparked many useful discussions with R. Alvarez-Garrote, L. Pelegrina-Gutierrez and J. I. Crespo-Anadon.

The uncertainty reweighting in Chapter 10 was performed using the framework shared across the SBND and ICARUS collaboration, developed before the author’s involvement. The author would like to thank H. Lay, J. Mueller, and J. Kim for their help in understanding uncertainty treatments. The procedure to set upper limits was performed using the pyhf package [7], with references assign credit for the employed statistical methods [8–10]. Finally, the author would like to thank A. M. Szelc, whose idea was to search for HNLs by exploiting their lateness, that started this entire thesis.

Vu Chi Lan Nguyen
August 2024

Acknowledgements

First and foremost, I would like to thank my mom and dad for supporting me emotionally and financially through my PhD. I appreciate their trust in me to follow my passion in a foreign country away from home. Without them, I would not be where I am today.

I would like to thank my supervisors Neil for accepting me into the physics program at Sheffield and Vitaly for taking the lead in the supervisor role. I am grateful for the autonomy and freedom to explore my physics interests. I understand that my PhD journey was a wild card with unfamiliar research topics and multiple last minute trips to Fermilab. Yet, they remained as accommodating and guiding as ever to keep me on the right track.

October 2020, at the peak of Covid, was certainly an odd time to move to a new city. Somehow, the Sheffield group made it feel like home. Anthony and Ala, thank you for teaching me about actual hardware. Ed, thank you for teaching me every possible thing that a first year PhD student should know. Rhiannon and Anna, despite your later arrival, your support and positivity only add to my experience at Sheffield.

Ali, you were my very first friend in Sheffield and another fellow sharing the same PhD boat as me. As promised, I truly appreciate our Wednesday KFC after lab teaching, late night fried chicken orders and many more chicken-related memories that keep me afloat through difficult times.

Working at SBND has only been an amazing experience that reassures my decision to pursue physics. I owe thanks to so many people across various working groups for their support towards the completion of this thesis, and many more thanks to everyone in SBND for giving into my ideas during my term as SBND young representative. Most importantly, I would like to give a special thanks to Michelle for her guidance not only at Fermilab but also on my journey at SBND.

the-real-sbnd, your friendships cannot go unmentioned. Especially, Henry, this thesis would not exist without your help on every front. Jiaoyang, thank you for joining the production team with me. Rodrigo, thank you for cross checking every step of my analysis.

Fran, thank you for answering all my dumb PDS-related questions. Lynn, thank you for all the plants and cat photos. Bear, thank you for gaining me access to Zuko and Roo. Mun, thank you for my very first Chicago tour. Thank you all for the jokes and rants as we were doing our best to navigate through our PhD journeys.

Finally, Lane, words cannot describe your unconditional support through this entire experience. Thank you for everything!

Table of contents

List of figures	xvii
List of tables	xxiii
Nomenclature	xxv
1 Introduction	1
2 Heavy Neutral Leptons	3
2.1 Motivation of Heavy Neutral Leptons	3
2.2 Production of Heavy Neutral Leptons	6
2.3 Decay Channels of Heavy Neutral Leptons	8
2.4 Previous Searches For Heavy Neutral Leptons	11
2.4.1 Peak Searches	12
2.4.2 Decay Searches	14
2.5 Concluding Remarks	16
3 Physics of Liquid Argon Time Projection Chambers	17
3.1 Overview of LArTPCs	18
3.2 Particle Interactions in Liquid Argon	20
3.2.1 Production of Ionisation Electrons	20
3.2.2 Production of Scintillation Photons	23
3.2.3 Recombination	24

3.3	Particle Propagation in Liquid Argon	26
3.3.1	Electron Drift	26
3.3.2	Photon Propagation	28
3.4	Detection of Electrons and Photons	30
3.4.1	Wire Planes	30
3.4.2	Photomultiplier Tubes and X-ARAPUCAs	31
3.5	Concluding Remarks	32
4	The Short-Baseline Near Detector and Booster Neutrino Beam	33
4.1	The Short-Baseline Near Detector Physics Program	34
4.2	The Short-Baseline Near Detector	36
4.2.1	Time Projection Chamber	37
4.2.2	Photon Detection System	38
4.2.3	Cosmic Ray Tagger	40
4.2.4	Readout Electronics	41
4.2.5	Hardware Trigger	42
4.2.6	Data Acquisition	43
4.2.7	Event Building	44
4.3	The Booster Neutrino Beam	46
4.4	Concluding Remarks	49
5	Simulation Framework Of SBND	51
5.1	Overview of The Simulation Framework	51
5.2	HNL Generator: MeVPrtl	52
5.3	SM Generators	57
5.3.1	Neutrino Generator: GENIE	57
5.3.2	Cosmic Generator: CORSIKA	59
5.4	Particle Propagation and Detector Response Simulation	60
5.4.1	Particle Propagation Simulation	60

Table of contents

5.4.2	Wire Response Simulation	61
5.4.3	Photon Detection System Response Simulation	61
5.4.4	Cosmic Ray Tagger Response Simulation	62
5.5	Concluding Remarks	62
6	Reconstruction Framework Of SBND	65
6.1	Overview of The Reconstruction Framework	65
6.2	Time Projection Chamber Reconstruction	66
6.2.1	Signal Processing	67
6.2.2	Hit Finding	69
6.2.3	Pandora Pattern Recognition	69
6.2.4	Track-Shower Separation Boosted Decision Tree	71
6.3	Photon Detection System and Cosmic Ray Tagger Reconstruction	74
6.3.1	Photon Detection System Reconstruction	75
6.3.2	Cosmic Ray Tagger Reconstruction	77
6.4	High Level Analysis Tools	77
6.4.1	Subsystem Matching	78
6.4.2	Cosmic Rejection	79
6.4.3	Particle Identification	80
6.5	Concluding Remarks	80
7	Timing Performance of the Data Acquisition System	81
7.1	Timing Reference System of the Data Acquisition	81
7.1.1	Time and Frequency Transfer To Subsystems	82
7.1.2	Precise Timestamping	83
7.2	Timing Performance of Front End Board Modules	85
7.2.1	Evaluation of Internal Clock Resolution	85
7.2.2	Alternative Timing Reconstruction	88
7.3	Timing Performance of CAENV1730 Digitisers	90

7.3.1	Internal Clock and Timestamp Structure	91
7.3.2	Evaluation of Clock Synchronisation	92
7.3.3	Clock Jittering Correction	95
7.4	Concluding Remarks	99
8	Calibration of Time Projection Chambers	101
8.1	Electron Lifetime Measurement	101
8.1.1	Electron Lifetime Extraction Procedure	102
8.1.2	Bias Study From Diffusion and Space Charge Effects	104
8.2	Delta Ray Fluctuations on Recombination Simulation	107
8.2.1	Simulation of Delta Rays and Recombination	108
8.2.2	Impacts of Delta Ray Fluctuations On Recombination Magnitude . .	109
8.2.3	Impacts of Delta Ray Fluctuations On Recombination Smearing . .	113
8.2.4	Recombination Studies From The ICARUS Experiment	116
8.3	Concluding Remarks	117
9	Selection of Heavy Neutral Leptons	119
9.1	Selection Introduction	120
9.1.1	Signal and Background Definition	120
9.1.2	Description of MC Samples	122
9.1.3	Selection Efficiency Definition	123
9.1.4	The Beam Bucket Distribution	124
9.2	Cosmic Background Removal	125
9.2.1	Pandora Unambiguous Cosmic Removal	125
9.2.2	Beam Spill Cut	126
9.2.3	CRUMBS Cut	126
9.3	Neutrino Background Removal	127
9.3.1	Fiducial Volume Cut	127
9.3.2	Number of Hits Cut	129

Table of contents

9.3.3	SM Neutrino Track Removal	129
9.4	HNL Shower Selection	133
9.4.1	Electron Shower Removal	133
9.4.2	Track Score Cut	134
9.4.3	Calorimetry Cut	135
9.4.4	Theta Angle Cut	137
9.4.5	Invariant Mass Cut	138
9.5	Selection Result	139
9.6	Study of Timing Resolution Improvement	141
9.7	Concluding Remarks	145
10	Sensitivity Predictions for Heavy Neutral Leptons at SBND	147
10.1	Uncertainty Assessment	148
10.1.1	The Reweighting Method	148
10.1.2	Error Propagation Formulation	150
10.1.3	Signal Uncertainty Sources	150
10.1.4	Background Uncertainty Sources	152
10.2	Limits Setting Procedure	156
10.2.1	Hypothesis Definition	156
10.2.2	Likelihood-based Test Statistic	158
10.2.3	The CL _s Method	159
10.2.4	Computing Test Statistic Distributions	161
10.2.5	Setting The Upper Limits	162
10.3	Results	164
10.3.1	Comparison Across Different Beam Bucket Distributions	164
10.3.2	Comparison With Other Experiments	168
10.4	Concluding Remarks	169
11	Conclusions	171

Table of contents

References	175
Appendix A Hardware Triggering At SBND	183
Appendix B Data Streaming At SBND	185
Appendix C Timing Distribution At SBND	187
Appendix D Lenient Beam Bucket Distribution	189
Appendix E Stringent Beam Bucket Distribution	191
Appendix F Smeared Truth Beam Bucket Distribution	193

List of figures

2.1	Neutrino and Heavy Neutral Lepton Production Feynman Diagrams	7
2.2	Kinematic Factor of Heavy Neutral Leptons	8
2.3	Branching Ratio of Heavy Neutral Leptons	10
2.4	Heavy Neutral Lepton and Neutral Pion Decay Feynman Diagrams	11
2.5	Experimental Upper Limits on The Mixing $ U_{\mu 4} ^2$ of Heavy Neutral Leptons	15
3.1	Liquid Argon Time Projection Chamber Diagram	19
3.2	Muon Energy Loss in a Copper Medium	21
3.3	Mean Free Path of Photons in Liquid Argon	22
3.4	Event Display of a Neutrino Interaction	23
3.5	Energy Deposition in Liquid Argon Diagram	24
3.6	Recombination Factor in Liquid Argon	25
3.7	Charge and Light Yield as a Function of Electric Field	26
3.8	Impacts of Space Charge Effects on Tracks	28
3.9	Group Velocity and Rayleigh Scattering Length of Photons in Liquid Argon .	30
3.10	Induced Currents on an Induction and a Collection Wire Plane	31
4.1	Short-Baseline Neutrino Program	35
4.2	Short-Baseline Near Detector 3D Model	36
4.3	Anode Plane Assemblies Schematic	37
4.4	Time Projection Chamber Photographs	38
4.5	Photon Detection System 3D Model	39

4.6	Cosmic Ray Tagger Diagrams	40
4.7	Data Acquisition Flow Chart	44
4.8	Chronological Structure of a Physics Event Diagram	45
4.9	BNB Beam Bucket Measured by SBND CRTs in 2017-2018	46
4.10	Particle Production in the BNB Diagram	47
4.11	Simulated Fluxes of Secondary Mesons From the BNB	48
4.12	Simulated Neutrino Fluxes at the Front Face of SBND	49
5.1	Simulation Framework of SBND	52
5.2	MeVPrtl Generator Workflow	53
5.3	Simulated Energy Spectra of HNLs Decaying Inside SBND	54
5.4	Kinematics Distributions of Neutral Pions From HNLs	55
5.5	Time of Flight of Particles From the BNB to SBND Diagram	56
5.6	Arrival Time of SM Neutrinos and HNLs at the Front Face of SBND	56
5.7	Modulus of the Arrival Time Distibutions of SM Neutrinos and HNLs	57
5.8	Volume Boundary of the GENIE Generator	59
6.1	Reconstruction Framework of SBND	66
6.2	Signal Processing Steps	68
6.3	Event Displays of a Neutrino Interaction Before and After Signal Processing	68
6.4	Hit Finding Diagram	69
6.5	Cone-Like Variable Diagrams	72
6.6	New Variable Distributions of Track-Shower Separation BDT	73
6.7	Score Distributions of Updated Track-Shower Separation BDT	74
6.8	Waveform Deconvolution and Hit Finding on PMT Waveforms	75
6.9	Reconstructed Light Yield at SBND	77
7.1	White Rabbit Timing System Flow Chart	82
7.2	SPEC-TDC Module Photograph and Signal Inputs	84
7.3	CRT Sharps Photograph	86

List of figures

7.4 Variation of T0 Timestamps of T0 Clock Reset Events Against Event Number	87
7.5 Variation of T0 Timestamps of T1 Clock Reset Events Against Event Number	87
7.6 Variation of T0 Timestamps of T1 Clock Reset Events Against T0 Timestamp	88
7.7 Reconstructed Beam Spill Using CRT Sharps	89
7.8 Reconstructed Beam Bucket Using CRT Sharps	90
7.9 Waveform Digitised By CAEN Timing Structure	92
7.10 Clock Synchronisation Schemes	92
7.11 Variation of CAEN Timestamps Using the Daisy Chain Clock Scheme	94
7.12 Variation of CAEN Timestamps Using the Fan Out Clock Scheme	94
7.13 Clock Jitterin Cases	96
7.14 Clock Jitterin Cases	97
7.15 Clock Jittering Correction Steps	98
8.1 Cathode Stitch Diagram	103
8.2 dQ/dx Profile Fitted With a Laundau-Gaussian	104
8.3 Most Probable Value dQ/dx Against Drift Time	104
8.4 Electron Lifetime Measurement Biases	106
8.5 Event Display of a Cosmic Muon and Delta Rays	107
8.6 Charge to Energy Loss Conversion of a 1 GeV Proton	111
8.7 Impacts of Delta Ray Fluctuations on Protons	111
8.8 Charge to Energy Loss Conversion of a 1 GeV Muon	112
8.9 Impacts of Delta Ray Fluctuations on Muons	112
8.10 Energy-Residual Range Scale of Protons at Different Delta Ray Thresholds .	114
8.11 Energy-Residual Range Scale of Muons at Different Delta Ray Thresholds .	115
8.12 Recombination Factor Against Delta Ray Threshold	116
9.1 Event Display of Di-Photon Showers From Heavy Neutral Leptons	121
9.2 Event Display of a Neutral Current Interaction Containing a Neutral Pion .	121

9.3 Event Display of a Charged Current Interaction Containing a Muon and a Proton	122
9.4 Beam Spill Cut	126
9.5 CRUMBS Cut	127
9.6 Fiducial Volume Cut	128
9.7 Number of Hits Cut	129
9.8 Muon Cuts	130
9.9 Proton and Pion Cuts	132
9.10 Electron Cut	133
9.11 Track Score Cut	135
9.12 Calorimetry Cut	136
9.13 Theta Angle Cut	137
9.14 Neutral Pion Invariant Mass Cut	138
9.15 Beam Bucket Distributions After Selection	140
9.16 Summar of Selection Efficiency.	140
9.17 Smearing Contributors To The Beam Bucket Diagram	141
9.18 Beam Bucket Distributions Using True and Reconstructed Variables	143
9.19 Beam Bucket Distributions of SM Neutrinos Assuming an Improved Timing Resolution	145
9.20 Beam Bucket Distributions of SM Neutrinos and HNLs Assuming an Improved Timing Resolution	145
 10.1 Uncertainties of Heavy Neutral Leptons	153
10.2 Total Uncertainty of Heavy Neutral Leptons	153
10.3 Uncertainties of SM Neutrinos and Cosmic Backgrounds	157
10.4 Total Uncertainty of SM Neutrinos and Cosmic Backgrounds	157
10.5 Distribution of Test Statistics Acquired From Toy Throwing	161
10.6 Distribution of Test Statistics Acquired From Asymptotic Approximation	162
10.7 Beam Bucket Distributions Used in the Limits Setting	165

List of figures

10.8 Expected Upper Limits On The Coupling $ U_{\mu 4} ^2$ for Majorana HNLs	166
10.9 Comparison Between Limits Setting Using The Entire Distribution and Only Edge Bins	167
10.10 Upper Limits Comparison Between The Lenient, Stringent and Smeared Truth Distribution	168
10.11 Comparison Between SBND Expected Upper Limits and Existing Results . .	170
A.1 Hardware Triggering Flow Chart	184
B.1 Grafana Online Monitoring Web Page	186
B.2 Minargon Online Monitoring Web Page	186
C.1 Clock Signal Distribution	187
C.2 PPS Signal Distribution	188
D.1 Lenient Beam Bucket Distributions in the Mass Range 140 - 200 MeV	189
D.2 Lenient Beam Bucket Distributions in the Mass Range 220 - 260 MeV	190
E.1 Stringent Beam Bucket Distributions in the Mass Range 140 - 200 MeV . . .	191
E.2 Stringent Beam Bucket Distributions in the Mass Range 220 - 260 MeV . . .	192
F.1 Smeared Truth Beam Bucket Distributions in the Mass Range 140 - 200 MeV	194
F.2 Smeared Truth Beam Bucket Distributions in the Mass Range 220 - 260 MeV	195

List of tables

9.1 Table summarising the lenient and stringent selection.	142
10.1 Table summarising modifiers used to constrain uncertainties.	164
10.2 Table summarising expected upper limits results.	169

Nomenclature

AC Alternating Circuit

APA Anode Plane Assemblies

ArgoNeuT Argon Neutrino Teststand

AV Active Volume

BDT Boosted Decision Tree

BNB Booster Neutrino Beam

BSM Beyond Standard Model

C.L. Confidence Level

CC Charged Current

CE Cold Electronics

CERN European Organisation for Nuclear Research

CPA Cathode Plane Assembly

CPT Charge Parity Time symmetries

CRT Cosmic Ray Tagger

CRUMBS Cosmic Rejection Using a Multi-system Boosted decision tree Score

CV Central Value

DAQ Data AcQuisition

DCA Distance of Closest Approach

DUNE Deep Underground Neutrino Experiment

ETRIG Event TRIGger

FD Fine Delay

FEB Front End Board

FMC Field programmable gate arrays Mezzanine Card

FTRIG Flash TRIGger

FV Fiducial Volume

HNL Heavy Neutral Lepton

ICARUS Imaging Cosmic And Rare Underground Signals

KDAR Kaon Decay At Rest

KE Kinetic Energy

KEK High Energy Accelerator Research Organization (Kō Enerugī Kasokuki Kenkyū Kikō)

LArTPC Liquid Argon Time Projection Chamber

LSND Liquid Scintillator Neutrino Detector

MC Monte Carlo

MCS Multiple Coulomb Scattering

MicroBooNE Micro Booster Neutrino Experiment

MiniBooNe Mini Booster Neutrino Experiment

MIP Minimum Ionising Particle

MTC/A Master Trigger Card Analog

NC Neutral Current

NTB Nevis Trigger Board

Nomenclature

NTP Network Time Protocol

NuMI Neutrinos at the Main Injector beam

NuTeV Neutrino at the Tevatron

PDF Probability Density Function

PDS Photon Detection System

PE PhotoElectron

PID Particle IDentification

PIENU Pion → Electron + Neutrino

PMNS Pontecorvo-Maki-Nakagawa-Sakata

PMT PhotonMultipler Tube

POT Protons On Target

PPS Pulse Per Second

PTB Penn Trigger Board

QE Quantum Efficiency

RWM Resistor Wall Monitor

s.d. standard deviation

SBN Short-Baseline Neutrino

SBND Short-Baseline Near Detector

SCE Space Charge Effect

SER Single Electron Response

SIN Swiss Institute for Nuclear Research

SiPM Silicon PhotoMultiplier

SM Standard Model

SPEC Simple PCIe FMC Carrier

- SVEC** Simple VME FMC Carrier
- T2K** Tokai to Kamioka
- TAI** Coordinated Universal Time
- TDC** Time to Digital Converter
- TPB** TertraPhenyl Butadiene
- TPC** Time Projection Chamber
- UTC** International Atomic Time
- VUV** Vacuum Ultraviolet
- WIB** Warm Interface Board
- WR** White Rabbit

Chapter 1

Introduction

Neutrino oscillation implies that neutrinos have mass, which cannot be currently explained by the Standard Model (SM) due to an absence of a right-handed partner to the left-handed neutrinos. Chapter 2 begins with the motivation of a right-handed heavy neutrino state, referred to as *Heavy Neutral Lepton* (HNL), allowing for the construction of neutrino mass. An overview of a minimal HNL model is given, covering the production and decay of HNLs. The focus is on kinematically allowed channels that can be produced from the Booster Neutrino Beam (BNB) and subsequently decay in the Short-Baseline Near Detector (SBND).

In the following, a description of the Liquid Argon Time Projection Chamber (LArTPC) is provided in Chapter 3, which is the main detection technology of SBND. The operating principles of an LArTPC are presented, identifying key physical processes of the two main detection signals, ionisation electrons and scintillation photons, that underpin the performance of an LArTPC.

Chapter 4 then provides an overview of the SBND and the BNB. The chapter begins with the physics program of SBND, followed by the detector design, describing each subsystem that comprises the detector. The BNB is discussed next, detailing the beam design and presenting the secondary meson fluxes and neutrino fluxes arriving at SBND.

The simulation framework at SBND is outlined in Chapter 5, to produce Monte Carlo (MC) samples representing data. A description of different generators to simulate SM neutrinos, cosmic muons and HNLs is first provided. The HNL generator is covered in detail to illustrate the physics behind the late arrival of HNLs compared to SM neutrinos, which the work presented in later chapters relies upon. Finally, the simulation of the particle propagation and the detector response is summarised.

Moreover, the reconstruction framework is provided in Chapter 6, covering the reconstruction for each detection subsystem: (1) TPC, (2) Photon Detection System (PDS) and (3) Cosmic Ray Tagger (CRT). Specifically in the TPC reconstruction workflow, an update to an algorithm separating track-like and shower-like reconstructed objects is detailed. An overview of some high-level analysis tools, combining complementary signals from all subsystems, is given next.

Chapter 7 outlines the timing performance of the Data AcQuisition (DAQ) at SBND. The chapter begins with a description of the White Rabbit timing system set up to maintain timing synchronisation across different DAQ subsystems. The timing precision of the readout electronics of the CRT and PDS are then accessed, which are the two detection subsystems with timing resolution $\mathcal{O}(1\text{ ns})$.

Two studies within the scope of charge calibration are discussed in Chapter 8. The first study is on the measurement of electron lifetime, performed on MC samples of anode-to-cathode crossing cosmic muon tracks that fully traverse the detector volume. The second study is to assess the impacts of delta ray fluctuations on recombination, also performed on MC samples with varying delta ray thresholds.

Selection procedures developed to select HNL signals and reject backgrounds from SM neutrinos and cosmic muons are presented in Chapter 9. Firstly, a signal and background definition is provided, followed by a description of MC samples used to perform the selection. Cuts for rejecting tracks from cosmic muons and SM interactions are detailed, followed by cuts optimised to identify HNL showers. The selection results are summarised next. Finally, a study to assess the sensitivity of SBND to HNLs assuming an improvement in timing reconstruction is presented.

Finally, the capabilities of SBND to search for HNLs are assessed in Chapter 10. The sources and treatments of uncertainties in the analysis are discussed. The procedure used to set upper limits at the 90% confidence level is detailed next. The results are then presented, covering three scenarios that can be achieved at SBND. A discussion of the results is finally given, including suggestions for future developments.

Chapter 2

Heavy Neutral Leptons

Neutrino oscillation is the key evidence suggesting that neutrinos have mass, a phenomenon that cannot currently be explained by the Standard Model (SM). This motivates an additional right-handed neutrino state that allows for the construction of the Dirac and/or Majorana mass term of neutrinos. If the new state is very heavy, it can potentially provide a new mass generation mechanism to explain the lightness of neutrinos. The heaviness of this new state compared to neutrinos gains it the name *Heavy Neutral Lepton* (HNL). HNLs are proposed to interact with SM gauge bosons, allowing them to be produced and decay via SM gauge interactions. This leads to the focus of this work on the search for HNLs in the mass range $\mathcal{O}(100 \text{ MeV})$ that are produced from the Booster Neutrino Beam and then decay into SM observables inside the Short-Baseline Near Detector (SBND) at Fermilab.

This provides an overview on the theory of HNLs and a summary of search results for their existence. In Section 2.1, the motivation of HNLs as a minimal extension to the SM is presented. Section 2.2 provides the explanation for the production mechanism of HNLs from meson decays. Following this, Section 2.3 covers the details of HNL decays into SM observables. Section 2.4 then summarises the existing upper limits on the coupling and mass phase space of HNLs through two different experimental methods: peak searches and decay searches. Finally, Section 2.5 provides some concluding remarks.

2.1 Motivation of Heavy Neutral Leptons

The phenomenon of three-flavour neutrino oscillation is well-established. Active neutrinos are produced and detected as their flavour states ν_μ , ν_e and ν_τ . Neutrino oscillation

describes the neutrino flavour states changing from one flavour to another as the neutrinos propagate across a distance. Neutrino oscillation directly implies the existence of non-zero mass for at least two out of the three neutrino states. Whilst the Standard Model (SM) of particle physics has proved extremely successful, unfortunately, it currently provides no mechanism for the mass generation of neutrinos. The absence of a right-handed chiral partner to the left-handed chiral neutrino means that no Dirac mass term can be built via the Yukawa coupling of the Higgs to the opposite chirality fields.

This motivates the introduction of a right-handed neutrino such that the neutrino mass can be constructed using the same recipe as all other SM particles. The Dirac mass term in the neutrino Lagrangian after spontaneous symmetry breaking is as follows [11]:

$$\mathcal{L}_D = -m_D (\bar{\nu}_L \nu_R + \bar{\nu}_R \nu_L), \quad (2.1)$$

where $m_D = Yv/\sqrt{2}$ is the Dirac mass, Y is the Yukawa coupling, v is the Higgs vacuum expectation value, and the subscript R and L denotes the right and left chiral state of the ν neutrino and $\bar{\nu}$ anti-neutrino field. While the Dirac mass term requires the existence of both left and right-handed chiral states, the Majorana mass term was proposed by Ettore Majorana in 1937 requiring only one chiral state [12]. Under the condition that a particle is its own antiparticle, the charge conjugation operator C can be applied to ν_R such that $\nu_R^C = C\bar{\nu}_R^T$, where the resulting ν_R^C has the correct properties to be used in place of ν_L in Eq. 2.1 [13]. The construction of the Majorana state violates the charge conservation and is forbidden for any other SM particles except for neutrinos due to their neutral charges. In this case, the Majorana mass term in the neutrino Lagrangian is as follows [13]:

$$\mathcal{L}_M = -\frac{1}{2} M (\bar{\nu}_R^C \nu_R + \bar{\nu}_R \nu_R^C), \quad (2.2)$$

where M is the Majorana mass. The factor of a half is introduced to account for double counting since the term $\bar{\nu}_R$ and ν_R^C are not independent.

A right-handed neutral state provides a hypothetical neutrino mass mechanism not only via the Dirac or the Majorana mass term but also by combining both mass terms. A generalised Lagrangian in this case is as follows [11]:

$$\mathcal{L}_{DM} = -\frac{1}{2} \left[m_D \bar{\nu}_L \nu_R + m_D \bar{\nu}_R^C \nu_L^C + M \bar{\nu}_R^C \nu_R \right] + h.c. \quad (2.3)$$

The Lagrangian presented here allows for the seesaw mechanism to construct the physical masses of active neutrinos assuming the Majorana mass term is much larger than the

2.1 Motivation of Heavy Neutral Leptons

Dirac mass term, $M \gg m_D$ [11, 14]. Under the assumption of only two neutrino states for simplicity, the seesaw mechanism would give the mass of a left-handed neutrino state $m_\nu \approx \frac{m_D^2}{M}$ and a right-handed neutrino state $m_N \approx M$, such that the heaviness of m_N suppresses the physical mass of the left-handed neutrino m_ν . Thus, a right-handed heavy neutrino state is a very attractive addition to the SM as an answer to the neutrino mass mechanism, explaining the extreme lightness of active neutrinos.

The neutral nature of right-handed neutrinos requires all SM charges to be zero implying that they do not interact directly via the strong, electromagnetic, or weak forces. These weaker-than-weak right-handed particles are often referred to as *sterile neutrinos*. The only direct coupling to the new sterile state is the neutrino-Higgs interaction. This leads to mixing-mediated interactions with SM gauge bosons, allowing them to be produced and decay via SM gauge interactions with a rate suppressed by the coupling [15]. The mass range of sterile neutrinos can span over many orders of magnitudes, and the number of flavour or mass states is unconstrained.

In the mass range $\mathcal{O}(1 \text{ eV})$, they are known as *light* sterile neutrinos and are proposed to participate in oscillation with the active neutrinos. Over a short baseline distance, the addition of a single light sterile neutrino to neutrino oscillation might enhance or reduce the number of observed neutrino interactions for a given channel. Particularly, this model can explain the outstanding anomaly observed by the LSND and MiniBooNE experiments, where an excess of ν_e and $\bar{\nu}_e$ interactions was measured at low energy [16–18].

In the mass range $> \mathcal{O}(10 \text{ eV})$, sterile neutrinos are now considered *heavy* since they are significantly more massive compared to active neutrinos. This gains them the name *Heavy Neutral Leptons* (HNLs). HNLs do not participate in oscillation with active neutrinos due to coherence loss [15]. As a consequence of being heavier than active neutrinos, the wave packet of HNLs moves much slower compared to that of active neutrinos and immediately undergoes propagation decoherence. Instead, HNLs are proposed to travel over some distance before decaying into SM observables.

Different theoretical models of HNLs have been developed, and a comprehensive review can be found in Ref. [18]. In the search for HNLs presented here, the existence of HNLs will be explored in a minimal way by assuming an addition of a single HNL to the SM. From a generic phenomenological approach, an HNL can be added to the SM by extending the Pontecorvo-Maki-Nakagawa-Sakata (PMNS) matrix. The PMNS matrix, describing the coupling of the SM neutrino flavour eigenstate ν_α ($\alpha = e, \mu, \tau$), and the

mass eigenstate ν_i ($i = 1, 2, 3$), is as follows:

$$U_{PMNS} = \begin{pmatrix} U_{e1} & U_{e2} & U_{e3} \\ U_{\mu 1} & U_{\mu 2} & U_{\mu 3} \\ U_{\tau 1} & U_{\tau 2} & U_{\tau 3} \end{pmatrix}. \quad (2.4)$$

The flavour eigenstate ν_α undergoes weak interaction, whilst the mass eigenstate ν_i describes the neutrino propagation in space and time. For the addition of a single right-handed neutrino with mass m_N , the PMNS matrix can be extended to describe the mass mixing between SM neutrinos and the new flavour eigenstate N as follows:

$$U_{PMNS}^{Extended} = \begin{pmatrix} U_{e1} & U_{e2} & U_{e3} & U_{e4} \\ U_{\mu 1} & U_{\mu 2} & U_{\mu 3} & U_{\mu 4} \\ U_{\tau 1} & U_{\tau 2} & U_{\tau 3} & U_{\tau 4} \\ U_{N1} & U_{N2} & U_{N3} & U_{N4} \end{pmatrix}, \quad (2.5)$$

where the index 4 is reserved for the new mass eigenstate. Then, the flavour eigenstate ν_α of SM neutrinos can be written as the linear combination of the mass eigenstate ν_i and the HNL flavour eigenstate N as follows:

$$\nu_\alpha = \sum_i U_{\alpha i} \nu_i + U_{\alpha 4} N, \quad (2.6)$$

where the coupling $U_{\alpha i}$ ($\alpha = e, \mu, \tau$ and $i = 1, 2, 3$) are elements of the SM PMNS matrix, and the coupling $U_{\alpha 4}$ are the extension. For simplicity, this work only considers an HNL coupling to only one flavour at a time, such that at most only one of the three couplings U_{e4} , $U_{\mu 4}$ and $U_{\tau 4}$ is non-zero.

2.2 Production of Heavy Neutral Leptons

In any SM neutrino production processes, HNLs can be produced in place of neutrinos with a rate suppressed by the coupling $|U_{\alpha 4}|^2$, if kinematically allowed. Fig. 2.1a illustrates the two-body decay of a charged kaon K^+ producing a muon neutrino ν_μ and Fig. 2.1b illustrates the substitution of the ν_μ with an HNL N having $L = +1$ mediated by the coupling $|U_{\alpha 4}|^2$. This implies that HNLs can be probed from the Booster Neutrino Beam (BNB), which is an abundant source of mesons and will be further detailed in Section 4.3. Since the BNB is primarily made up of positively charged mesons, the following section will focus on the parent mesons K^+ and π^+ .

2.2 Production of Heavy Neutral Leptons



Fig. 2.1 Feynman diagrams of (a) $K^+ \rightarrow \mu^+ \nu_\mu$ and (b) $K^+ \rightarrow \mu^+ N$.

In general, the branching ratio $Br(m^+ \rightarrow l_\alpha^+ N)$ of a two-body decay of a charged meson m^+ into a lepton l_α^+ ($\alpha = e, \mu, \tau$) and an HNL N can be expressed in terms of the analogous branching ratio into an SM neutrino as follows [19]:

$$Br(m^+ \rightarrow l_\alpha^+ N) = Br(m^+ \rightarrow l_\alpha^+ \nu_\alpha) \left(\frac{|U_{\alpha 4}|^2}{1 - |U_{\alpha 4}|^2} \right) \rho_N \left(\frac{m_{l_\alpha}^2}{m_{m^+}^2}, \frac{m_N^2}{m_{m^+}^2} \right), \quad (2.7)$$

where $Br(m^+ \rightarrow l_\alpha^+ \nu_\alpha)$ is the branching ratio of the charged lepton m^+ decaying into a lepton l_α^+ and an SM neutrino ν_α , m_{m^+} is the mass of the charged meson, m_{l_α} is the mass of the daughter lepton and m_N is the mass of the daughter HNL. The kinematic factor ρ_N accounts for the available phase space of the daughter HNL in the decay and has the complete expansion as follows [19]:

$$\rho_N(x, y) = \frac{(x + y - (x - y)^2) \sqrt{1 + x^2 + y^2 - 2(x + y + xy)}}{x(1-x)^2}, \quad (2.8)$$

where $x = m_{l_\alpha}^2 / m_{m^+}^2$ and $y = m_N^2 / m_{m^+}^2$.

The kinematic factor ρ_N in Eq. 2.8 is plotted in Fig. 2.2, for $l_\alpha = \mu^+$, e^+ and $m^+ = \pi^+$, K^+ in the range $0 \leq m_N \leq 500$. Four HNL production channels that are probable at the BNB are shown: (1) $K^+ \rightarrow Ne^+$ in the dashed red line, (2) $K^+ \rightarrow N\mu^+$ in the solid pink line, (3) $\pi^+ \rightarrow Ne^+$ in the dashed dark blue line and (4) $\pi^+ \rightarrow N\mu^+$ in the solid light blue line. Production channels associated with the τ -flavour mixing are not shown since they are kinematically forbidden for the BNB energies. The kinematic factor for each illustrated channel is constrained by the available mass after the two-body decay of the parent meson. The upper limit of the HNL mass is therefore $m_N = m_{m^+} - m_{l_\alpha}$ ($\alpha = e, \mu$), as shown by the vertical grey lines. Here it can be seen that the HNL production from π^+ decays limits the HNL mass to < 140 MeV while the HNL production from K^+ decays allows for the HNL mass up to 495 MeV. Thus, the search for HNLs presented here focuses on the HNL production channel from K^+ to probe mass as high as 495 MeV.

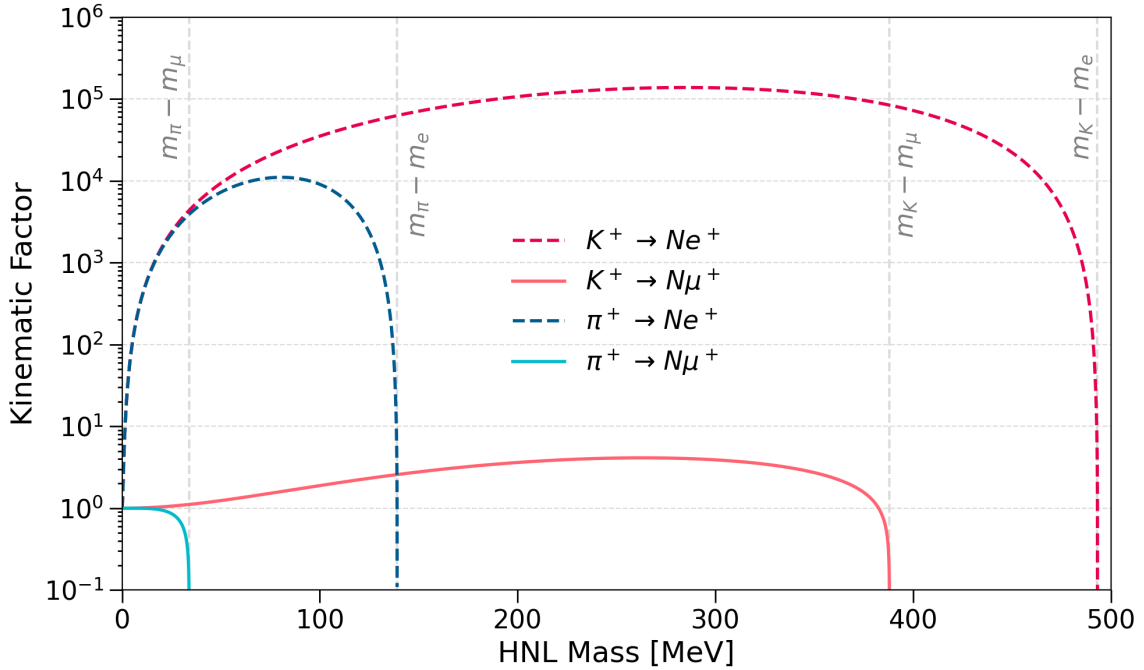


Fig. 2.2 Kinematic factor of the HNL production from meson decays.

Furthermore, the magnitude of the kinematic factor of the HNL production shown in Fig. 2.2 is larger than 1, indicating an enhancement to the production rate. This is because of the helicity suppression observed in mesons decaying into an SM neutrino having an opposite effect for mesons decaying into an HNL [19]. Instead, it is helicity *enhancement* due to HNLs being massive. For the HNL production channel that this work focuses on, a significant enhancement is evident for the production rate of $K^+ \rightarrow e^+ N$ as it is increased by a factor of 10^5 . On the other hand, the kinematic factor of $K^+ \rightarrow \mu^+ N$ only peaks at 4, implying a negligible enhancement in the production rate.

2.3 Decay Channels of Heavy Neutral Leptons

For HNLs to be detected, they are hypothesised to be able to decay into SM observables [19]. The proposed lifetime of HNLs should be sufficient so that an HNL produced from the BNB will survive long enough to reach the detector and then decay in flight. At the mass range < 495 MeV, the kinematically-allowed decay channels of an HNL are as follows [15]:

2.3 Decay Channels of Heavy Neutral Leptons

$$\begin{aligned} N \rightarrow e^- \pi^+, \quad N \rightarrow \mu^- \pi^+, \quad N \rightarrow \nu \pi^0, \quad N \rightarrow \nu \gamma, \\ N \rightarrow \nu e^- e^+, \quad N \rightarrow \nu \mu^- \mu^+, \quad N \rightarrow \nu \mu^- e^+, \quad N \rightarrow \nu \nu \nu. \end{aligned} \tag{2.9}$$

These decay channels conserve the lepton number under the assumption that HNLs are Dirac particles with $L = +1$. If HNLs are Majorana particles, such that the lepton number conservation is violated, then the charge conjugates for these decays that would be forbidden in the Dirac case are allowed.

Fig. 2.3 depicts the branching ratios of the decay channels shown in Eq. 2.9, as a function of the HNL mass. Solid lines are branching ratios via the μ -flavour mixing and dashed lines are branching ratios via the e -flavour mixing. The branching ratios were plotted referencing decay widths from Ref. [15, 20, 21]. Decay widths of HNLs have been derived independently across various literature sources and an overview of the discrepancies is summarised in Ref. [21]. The sources used here have been found to be in good agreement with each other.

For $m_N < 135$ MeV, the dominant branching ratio occurs in the channel $N \rightarrow \nu \nu \nu$ as shown by the light green lines. However, this channel is almost unobservable since the detection of SM neutrinos relies on the already-small cross section of neutrino scattering with the detector material. The other two channels in this mass range are $N \rightarrow \nu e^- e^+$ and $N \rightarrow \nu \gamma$, as shown by the light pink and grey lines. The channel $N \rightarrow \nu \gamma$ is highly suppressed compared to the channel $N \rightarrow \nu e^- e^+$, and thus, the final state of an $e^- e^+$ pair provides the best sensitivity within this mass range.

For $m_N > \sim 140$ MeV, an HNL has sufficient mass to decay into either a neutral pion ($m_{\pi^0} = 135$ MeV) or a charged pion ($m_{\pi^\pm} = 140$ MeV). For the e -flavour mixing, the channel $N \rightarrow e^- \pi^+$ dominates over the channel $N \rightarrow \nu \pi^0$ across the mass range from 135 to 495 MeV, as shown by the dashed dark blue and dashed pink line respectively. In the case of the μ -flavour mixing, the leading channel within the mass range of $135 < m_N < 245$ MeV is $N \rightarrow \nu \pi^0$ as shown by the solid pink line. Beyond $m_N > 245$ MeV, equivalent to the mass of a muon and a charged pion, the dominant decay channel begins to shift to the channel $N \rightarrow \mu^- \pi^+$ as shown by the solid light blue line. Finally, both channels $N \rightarrow \nu \mu^- e^+$ and $N \rightarrow \nu \mu^- \mu^+$ are not competitive compared to any other channels at the same mass value.

Based on the assessment above it was decided in this work to focus on searching for HNLs through the decay channel $N \rightarrow \nu \pi^0$, which will be covered in Chapter 9 and 10. This is the leading channel of the μ -flavour mixing within the mass range of $135 < m_N < 245$ MeV. Sensitivity in the same mass range of the e -flavour mixing has been extensively

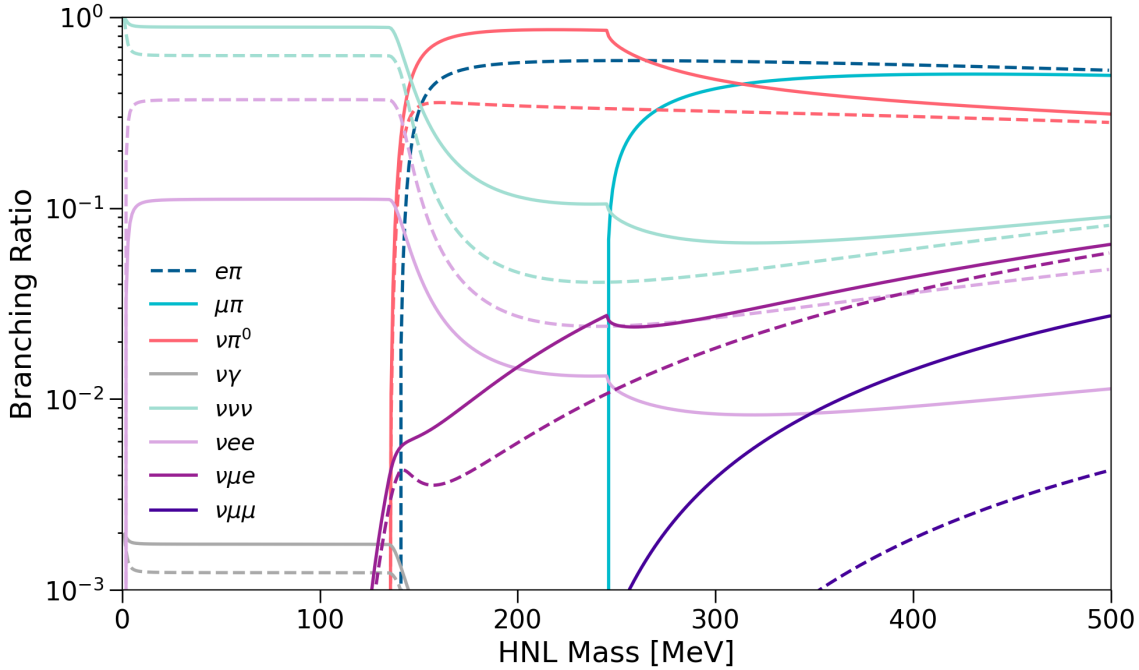


Fig. 2.3 Branching ratio of probable decay channels of an HNL produced from the BNB.

explored by many experiments as summarised by Ref. [18]. The decay width for the $N \rightarrow \nu\pi^0$ channel as taken from Ref. [21] is as follows

$$\Gamma(N \rightarrow \nu\pi^0) = \frac{G_F^2 m_N^3}{32\pi} f_\pi^2 |U_{\mu 4}|^2 \left(1 - \left(\frac{m_{\pi^0}}{m_N}\right)^2\right)^2 \quad (2.10)$$

where G_F is the Fermi constant, f_π is the pion decay constant and m_{π^0} is the mass of a neutral pion. It is noted that the equivalent equations from Ref. [15, 20] contain an additional factor of 2 in the denominator. Eq. 2.10 was chosen from Ref. [21] since the source is more recently dated.

Fig. 2.4a shows the diagram of the HNL decaying into the final state $\nu\pi^0$. The SM neutrino is expected to leave no detectable signatures due to the very small scattering cross section. Meanwhile, the neutral pion is a particle made up of the superposition of the quark pair $u\bar{u}$ and $d\bar{d}$. The annihilation of the quark and antiquark makes it a very short-lived particle with a mean lifetime of $8.52 \pm 0.18 \times 10^{-17}$ s [22]. The neutral pion has been measured to decay into two photons $98.823 \pm 0.034\%$ of the time. Fig. 2.4b shows the Feynman diagram for this decay. The photon pair results in a clear signature inside a Liquid Argon Time Projection Chamber (LArTPC): two electromagnetic showers without

2.4 Previous Searches For Heavy Neutral Leptons

any associated hadronic activities at the decay vertex. This signal topology will face very challenging background separation from some SM neutrino channels also containing a π^0 in the final state. As described in more detail in Chapters 9, differences in the final state kinematics from the HNL signal to the SM neutrino background enable an effective separation.

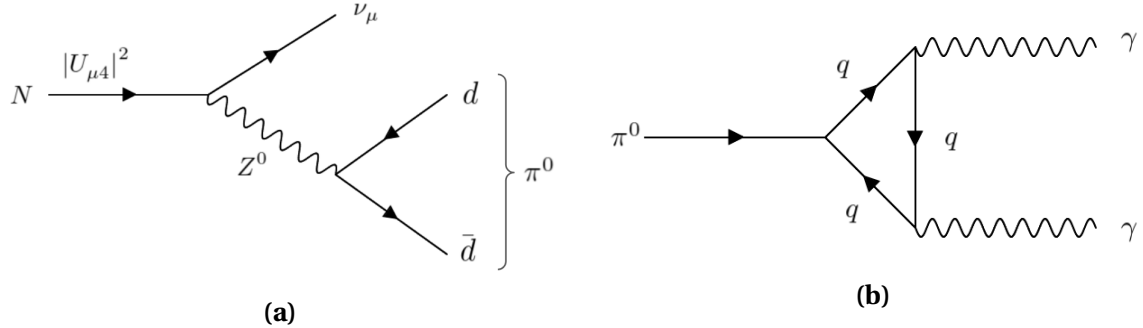


Fig. 2.4 Feynman diagrams of (a) $N \rightarrow \nu\pi^0$ and (b) $\pi^0 \rightarrow \gamma\gamma$.

As previously discussed in Section 2.2, HNLs can be either Dirac or Majorana particles in nature. The difference between Dirac and Majorana HNLs is not only the lepton number conservation but also the polarisation of the decay products. For the neutral current final state $\nu\pi^0$, Majorana HNLs decay isotropically, whereas in the case of Dirac HNLs, the angular distribution of the daughter particles is no longer isotropic. The helicity of the daughter neutrino determines the direction of the daughter neutral pion and the angular distributions of the two charge conjugate final states, $\nu\pi^0$ and $\bar{\nu}\pi^0$, add up to an isotropic distribution [23]. As the neutrino is undetectable, the observed angular distribution of the neutral pion is expected to be insufficient to determine the Dirac or Majorana nature of HNLs. For simplicity in this search for HNLs via the channel $\nu\pi^0$, it is therefore assumed that HNLs are Majorana particles.

2.4 Previous Searches For Heavy Neutral Leptons

Searches for HNLs have been conducted by various experiments over the decades across a wide range of masses. Oscillation experiments and precise β -decay experiments have probed HNLs in the mass range between eV and keV, neutrino beam dump experiments have targeted the MeV-scale HNLs and collider experiments have primarily explored HNLs with masses in the GeV-scale and above. To date, no evidence of HNL existence has been found, and thus, experiments have set upper limits on the coupling $|U_{\alpha 4}|^2$ ($\alpha = e, \mu, \tau$).

Commonly, the contour on the experiment sensitivity is expressed in terms of the coupling $|U_{\alpha 4}|^2$ as a function of the HNL mass.

Here, current experimental limits on HNLs around $\mathcal{O}(100 \text{ MeV})$ are presented, focusing specifically on the mass range of $0 < m_N < 265 \text{ MeV}$, which is relevant to the final states $\nu\pi^0$. In this mass range, two key experimental methods are used, so-called peak searches and decay searches. Peak searches probe only the production rate of HNLs, whereas decay searches probe both production and decay rates. Fig. 2.5 summarises the presented upper limits at 90% confidence level (C.L.) from both experimental methods, with details on individual limits to be discussed in Section 2.4.1 and 2.4.2.

2.4.1 Peak Searches

Peak search experiments measure the energy spectrum resulting from the meson decay that would produce an HNL. Typically, the two-body leptonic decay of a meson is modelled as $m \rightarrow l + \text{Missing}$, where m is the parent meson, a pion or a kaon, and l is the daughter particle, a pion or a lepton [24]. The *missing* decay products are attributed to either HNLs or SM neutrinos. HNLs are expected to exit the detector before decaying, whereas SM neutrinos escape the detector before interacting, serving as the primary background for this search. Since the momenta of m and l can be measured, the missing invariant mass can therefore be derived as $m_{\text{missing}}^2 = (P_m - P_l)^2$, where P_m and P_l are the 4-momenta of the parent and daughter particle. Given the near-zero mass of SM neutrinos, the mass of the daughter HNL can be treated as $m_N = m_{\text{missing}}$. Consequently, an excess over the background at m_{missing} potentially indicates the existence of HNLs.

To infer the upper limits on the coupling parameter, the flavour α ($\alpha = \mu, e$) of the daughter lepton determines the flavour of the coupling $|U_{\alpha 4}|^2$, and the amplitude of the decay spectrum at m_{miss} determines the upper limits. Limits placed by the peak searches are insensitive to the Dirac or Majorana nature of HNLs as this does not impact the kinematics of the meson decay. For the coupling $|U_{\mu 4}|^2$, the most competitive limits have been established by the following experiments on the pion and kaon decay spectrum, and are plotted in Fig. 2.5 as dashed lines.

Pion Decay Spectrum Peak Searches

- SIN (Swiss Institute for Nuclear Research) performed a peak search using stopping positive pions decay via the channel $\pi^+ \rightarrow \mu^+ + \text{Missing}$, with a scintillator in 1981

2.4 Previous Searches For Heavy Neutral Leptons

and a germanium detector in 1987. The pion enabled probing HNLs within the low mass range $\mathcal{O}(10 \text{ MeV})$. Upper limits of $|U_{\mu 4}|^2$ were placed at the level of 10^{-4} in the mass range 1-20 MeV [25–27].

- The **PIENU** collaboration at TRIUMF also searched for HNLs using stopping pions. The most recent result in 2019 set the most stringent limits on $|U_{\mu 4}|^2$ at the level of 10^{-5} in the mass range of 15-34 MeV, extending beyond the result reported by SIN [28].

Kaon Decay Spectrum Peak Searches

- The **KEK** collaboration conducted an experiment known as E89, which aimed to search for HNLs using the muon range spectrum resulting from stopping kaon decays during 1981-1982. Following this, experiment E104 in 1983 was carried out with an improved momentum resolution and background suppression. The kaons were produced using a 0.5 GeV proton beam, and 3×10^6 muons from kaon decays were analysed using a magnetic spectrograph. The E89 experiment result set limits on $|U_{\mu 4}|^2$ between 10^{-4} - 10^{-6} within the mass range of 70-300 MeV. Additionally, the combined results from the E89 and E104 experiments extended the sensitivity towards the lower mass range between 45-300 MeV, although these findings were unpublished at the time of writing and therefore plotted as the dotted line in Fig. 2.5 [29–31].
- The **E949** collaboration at Brookhaven National Laboratory performed a kaon decay experiment using 21.5 GeV protons in 2002. The analysis on the decays of 2×10^{21} stopping kaons set limits on $|U_{\mu 4}|^2$ at the level of 10^{-7} - 10^{-9} within the mass range of 175-300 MeV [32].
- The **NA62** collaboration, a kaon decay experiment at the CERN super proton synchrotron, analysed 10^8 stopping kaons from 400 GeV protons extracted from the synchrotron. The first results from a data set in 2015 set upper limits on $|U_{\mu 4}|^2$ at the level of 10^{-7} - 10^{-6} for the HNL mass between 250-373 MeV. Updated results using a larger dataset collected in 2016-2018 significantly improved the limits by an order of magnitude to 10^{-8} - 10^{-7} , and extended the mass range to 200-384 MeV [33, 34].

2.4.2 Decay Searches

Decay searches look for decay products from HNLs. HNLs are hypothesised to be produced outside of the detector and then decay in flight into SM observables inside the detector. Different combinations of HNL production and decay channels yield different observed event rates of the decay products. The flavour of the HNL production and decay channel both determine the flavour of the coupling $|U_{\alpha 4}|^2$ and the observed event rate determines the upper limit on the coupling.

Historically, decay searches have been performed in beam-dump experiments, which were designed explicitly to suppress SM background thereby enabling the search for rare decay processes. Recently, modern neutrino oscillation experiments have emerged as competitive beam-dump experiments alongside their neutrino physics programme. This is due to the resolution enhancement in their detection technologies that enable excellent SM background rejection, of which the Short-Baseline Near Detector is a prime example to be further detailed in this work. For the coupling $|U_{\mu 4}|^2$ within the mass range of 0-265 MeV, the most competitive limits have been set by the following experiments using neutrino beams, and are plotted in Fig. 2.5 as solid lines.

- The CERN **PS191** experiment in 1984 utilised an exposure of 19.2 GeV protons on a beryllium target, generating 10^{19} protons on target (POT). The detector was positioned at 128 m from the target at an off-axis angle of 2.3° to the beam. The detector volume was filled with helium, which was a sparse medium to reduce background rates arising from SM neutrino interactions. The large volume of 216 m³ provided a high rate of HNL signals. Limits on $|U_{\mu 4}|^2$ within the mass range of 120-350 MeV were placed at the level of 10^{-5} - 10^{-9} [35, 36]. A re-evaluation in 2022 found the limits to be lower than the original published results [37].
- The **NuTeV** collaboration at Fermilab conducted HNL searches in 1996 using a high energy neutrino beam produced by protons accelerated from the Tevatron ring. The dataset comprised an exposure of 3×10^{18} POT with an energy of 800 GeV. HNLs were produced from the D mesons resulting from proton collisions with the target. This enabled an exploration of the HNL mass up to 2000 MeV, surpassing any other beam-dump experiments described here. The experiment established limits on $|U_{\mu 4}|^2$ at the level of 10^{-6} - 10^{-7} within the mass range of 225-2000 MeV [38].
- The **T2K** collaboration searched for HNLs using their near detector ND280 located off-axis to the beam target at an angle of 2.04° . Only events occurring in the three

2.4 Previous Searches For Heavy Neutral Leptons

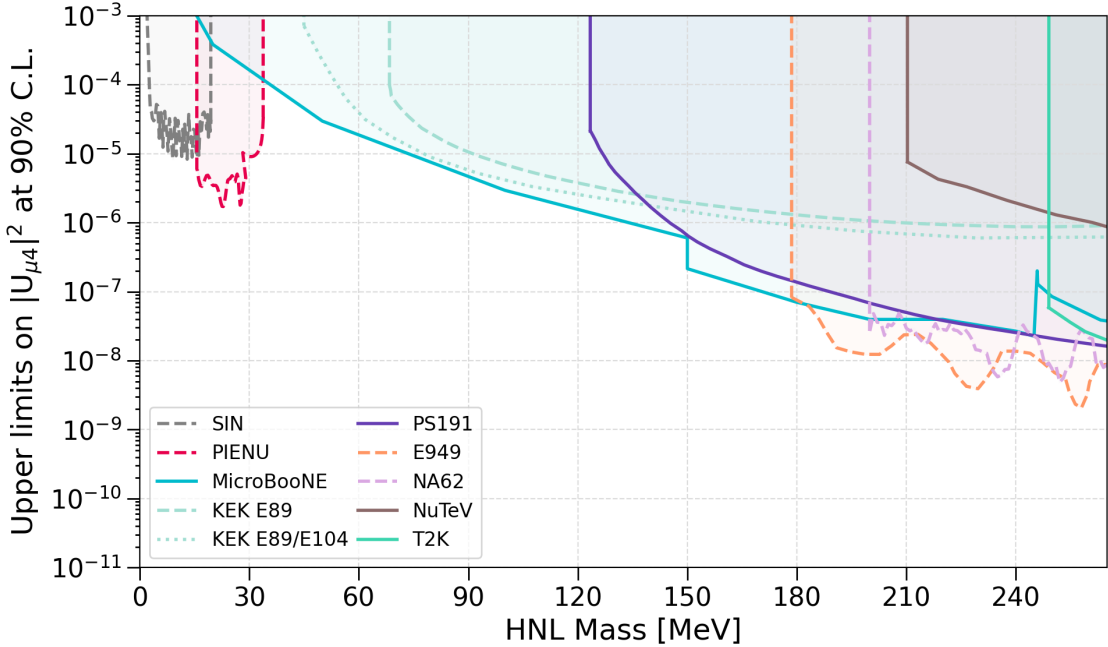


Fig. 2.5 Upper limits on the coupling $|U_{\mu 4}|^2$ at the 90% confidence level for Majorana HNLs in the mass range of $0 < m_N < 265$ MeV.

gaseous TPC volumes were selected to minimise background from SM neutrinos. A kinematic selection was performed on a dataset of 2×10^{21} POT and no signals were observed. The result constrained the coupling $|U_{\mu 4}|^2$ at the level of 10^{-8} - 10^{-9} in the mass range of 250-380 MeV. The limit plotted in Fig. 2.5 is a single-channel limit of $K^\pm \rightarrow N\mu^\pm$ and $N \rightarrow \mu^\pm\pi^\pm$. A more stringent limit on $|U_{\mu 4}|^2$ was also presented assuming the coupling $|U_{e 4}|^2$ and $|U_{\tau 4}|^2$ are non-zero. This allows for a marginalised limit on $|U_{\mu 4}|^2$ derived from other mixing results, which is not directly comparable here [39].

- The **MicroBooNE** collaboration conducted a series of searches for HNLs using their LArTPC, with the first result in 2020 and subsequent results in 2022 and 2023. The initial analysis was performed using an exposure of 2×10^{20} POT obtained from the on-axis BNB. A special delayed trigger was implemented to identify HNLs arriving at the detector later than SM neutrinos. Limits on $|U_{\mu 4}|^2$ were set at 10^{-7} for HNL masses spanning between 260-385 MeV. The latter two searches focused on HNLs arising from kaon decays in the NuMI beam absorber, which arrived at the detector at an angle to SM neutrinos from the BNB. The dataset included two runs with an exposure of 2×10^{20} and 5.01×10^{20} POT. The combined results incorporated multiple

HNL decay channels, probing a wide mass spectrum between 10-385 MeV. Notably, these recent results set the most stringent limits to date on $|U_{\mu 4}|^2$ at 10^{-4} - 10^{-7} within the mass range of 34-175 MeV, extending the findings from 2019 [40-42].

2.5 Concluding Remarks

HNLs are beyond the SM particles that can provide a natural explanation not just for the mass generation of active neutrinos but also for their extreme lightness. SBND, located only 110 m from the BNB, is capable of detecting HNLs resulting from meson decays in the beam, which then decay in flight inside the detector. Fig. 2.5 provides a summary of existing limits on the coupling $|U_{\mu 4}|^2$ of HNLs in the mass range of 0-265 MeV, showing that this phase space has been well-explored by various experiments very recently. For SBND to be competitive in this region, a high background rejection rate without comprising signal efficiency must be achieved when performing the kinematic selection. This can be obtained by exploiting the kinematic observables of HNL decay products for background rejection, including their delay compared to SM neutrinos as well as their boosted kinematics due to HNLs being massive. Toward this goal, novel detection technology and reconstruction techniques of SBND have demonstrated an excellent timing, spatial and calorimetry resolution. The following Chapter 3 and 4 will provide an overall description of the LArTPC technology, followed by details of the detection technology at SBND.

Chapter 3

Physics of Liquid Argon Time Projection Chambers

The Liquid Argon Time Projection Chamber (LArTPC) stands as a high precision detector in neutrino physics. In contrast to liquid scintillator neutrino experiments, LArTPCs collect both light and charge thereby providing a superior granularity for imaging neutrino interactions. The detector concept was first proposed in 1977 by Rubbia [43], bringing together the time projection chamber technology developed by Nygren [44, 45] and the liquid argon ionisation chamber developed by Willis and Radeka [46]. LArTPC provides excellent spatial, calorimetry and timing resolution while enabling a high neutrino interaction rate. Thus, this novel technology remains the primary choice for many neutrino experiments at Fermilab.

The following chapter will delve into the operating principles of a LArTPC, which is the detection technology employed by the Short-Baseline Near Detector to be discussed in the forthcoming Chapter 4. Section 3.1 provides an overview of the design of a LArTPC and the choice of liquid argon. In Section 3.2, a comprehensive discussion is presented on particle interactions with the liquid argon and the production of ionisation electrons and scintillation photons, which are the observables of a LArTPC. Following that, Section 3.3 outlines the propagation of the resultant electrons and photons through the liquid argon medium. Section 3.4 provides an insight into the detection mechanism of the ionisation electrons and scintillation photons using wire planes and novel optical detection technologies respectively. Finally, Section 3.5 concludes the chapter with some remarks.

3.1 Overview of LArTPCs

The Liquid Argon Time Projection Chamber (LArTPC) is the technology of choice for Fermilab's neutrino program, due to its ability to facilitate a high rate of neutrino interactions while maintaining an exceptional spatial, energy, and timing resolution. Moreover, the abundance and low cost of argon are ideal for scaling detectors to a large target mass, reaching up to tens of kilotons of liquid argon. Notably, the Short-Baseline Neutrino (SBN) programme [1] comprises three LArTPC experiments each of size in the hundreds of tons, located along the Booster Neutrino Beam (BNB): the Short-Baseline Near Detector (SBND) [2], MicroBooNE [47], and ICARUS [48]. This novel technology will also be utilised at the upcoming long baseline Deep Underground Neutrino Experiment (DUNE), of which two of the four far modules are LArTPCs, each with a volume of 17 kilotons [49].

Fig. 3.1 shows a diagram illustrating a general LArTPC. The TPC comprises a volume of LAr with a uniform electric field provided by a surrounding field cage, which is not shown in the diagram. To the right of the TPC is a cathode grounded at a high negative voltage and to the left is the anode plane assembly, and thus the resulting electric field direction is from left to right. The anode plane assembly is made up of three wire planes oriented at different angles, of which the diagram here shows three planes at the angle of 0° and $\pm 60^\circ$ to the vertical. Behind the wire planes is the Photon Detection System (PDS) comprising 9 PhotoMultiplier Tubes (PMTs).

The centre of the LArTPC in Fig. 3.1 also depicts an example interaction of an incoming neutrino scattering off an argon nucleus, shown as the dashed line since the neutral track of the neutrino is unobservable by the detector. Charged particles resulting from the neutrino interaction ionise and excite argon atoms as they traverse through the detector medium, producing ionisation electrons and scintillation photons in the process as shown by the solid lines. Ionisation electrons drift towards the anode in the opposite direction of the electric field. Upon arrival at the anode, ionisation electrons induce signals on the two inner wire planes and are collected on the outermost wire plane. The combination of signals from the three planes results in a high granularity three-dimensional image of the charged particle path. Moreover, since the wire planes are transparent to scintillation photons, the photons drift past the wire planes and are detected by the PDS. Scintillation photons provide additional information about the deposited energy and precise timing information of the neutrino interaction.

3.1 Overview of LArTPCs

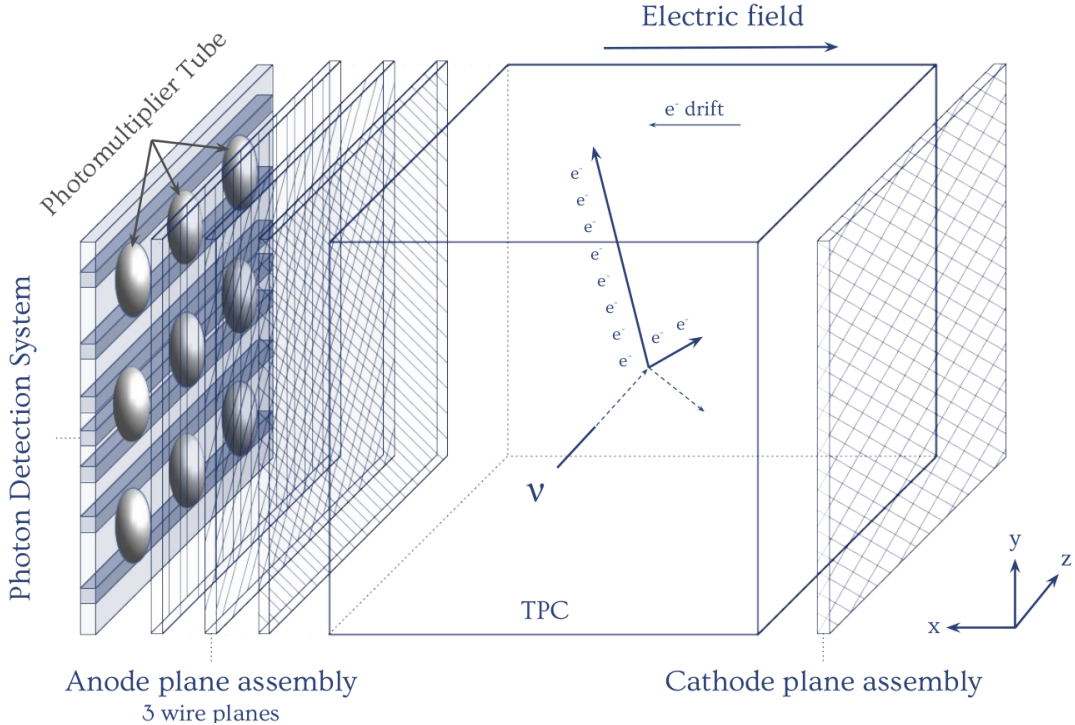


Fig. 3.1 Diagram illustrating the operating principles of a LArTPC [50].

Liquid argon makes an excellent medium for TPCs in neutrino experiments. Given that liquid argon has a reasonably high density of $1.39 \text{ g}\cdot\text{cm}^{-3}$ and an atomic mass of 40, it enables a high rate of neutrino interactions since the probability of neutrino interactions increases with the number of nucleons in the detector volume. Furthermore, given that argon is a noble element, most of the energy deposited by particles traversing through the medium is used for ionising and exciting atoms, producing ionisation electrons and scintillation photons in the processes. This maximises the efficiency of energy transfer into observable signals as well as enables a low energy threshold for detection in the order of $\mathcal{O}(10)$ MeV. In addition to argon being an abundant and cheap material for scaling the detector target mass, recent technology advancements in purifying liquid argon have resulted in a stable and pure liquid argon condition for LArTPC operation. This ensures that observable signals from electrons and photons can traverse the drift distance towards detection without being captured by contaminants [51]. Consequently, liquid argon continues to stand out as an advantageous target material for neutrino experiments.

3.2 Particle Interactions in Liquid Argon

Particle interactions in liquid argon and the production of ionisation electrons and scintillation photons as observable signals are discussed in the following section. Section 3.2.1 provides a description of the energy loss of charged particles traversing liquid argon and producing ionisation electrons. Following that, Section 3.2.2 details the production mechanism of scintillation photons via excitation and recombination. Finally, Section 3.2.3 goes into more detail of the physics of recombination that determines the yield of ionisation electrons and scintillation photons.

3.2.1 Production of Ionisation Electrons

Charged particles traversing a medium, such as liquid argon, undergo energy loss via ionisation, producing electrons. The typical energy loss profile is illustrated in Fig. 3.2, specifically for a muon traversing in a copper medium; however, the underlying principle applies to liquid argon. The plot depicts the stopping power, which is the energy loss per unit length divided by the density of the target medium, against the momentum of the traversing particle [52]. Heavy particles such as muons, pions, and protons, experience energy loss in liquid argon described by the Bethe-Bloch formalism [52]. For lighter and highly relativistic particles, such as > 100 MeV electrons in liquid argon, the primary mechanism for energy loss is through radiative effects.

Muons, pions and protons interact electromagnetically with argon atoms as they propagate through liquid argon primarily via ionisation, freeing electrons along their trajectories. These straight-line trajectories are referred to as *tracks*. The trajectories can also be deflected by many small angle scattering, a phenomenon known as Multiple Coulomb Scattering due to charged particles Coulomb scattering from nuclei [52]. Within the momentum range of 1-100 MeV, the energy deposited per unit length via ionisation dE/dx remains generally constant, often referred to as the Minimum Ionising Particle (MIP). In this MIP region, the distribution of dE/dx is described by a Landau-Gaussian convolution [52]. When the particle comes to a stop, the deposited energy increases, forming the Bragg peak. The energy loss profile described here is dependent on the mass of the traversing particle, making it a valuable tool for Particle IDentification (PID) [53]. This method is the most effective for protons separation from muons and pions as protons are significantly heavier.

3.2 Particle Interactions in Liquid Argon

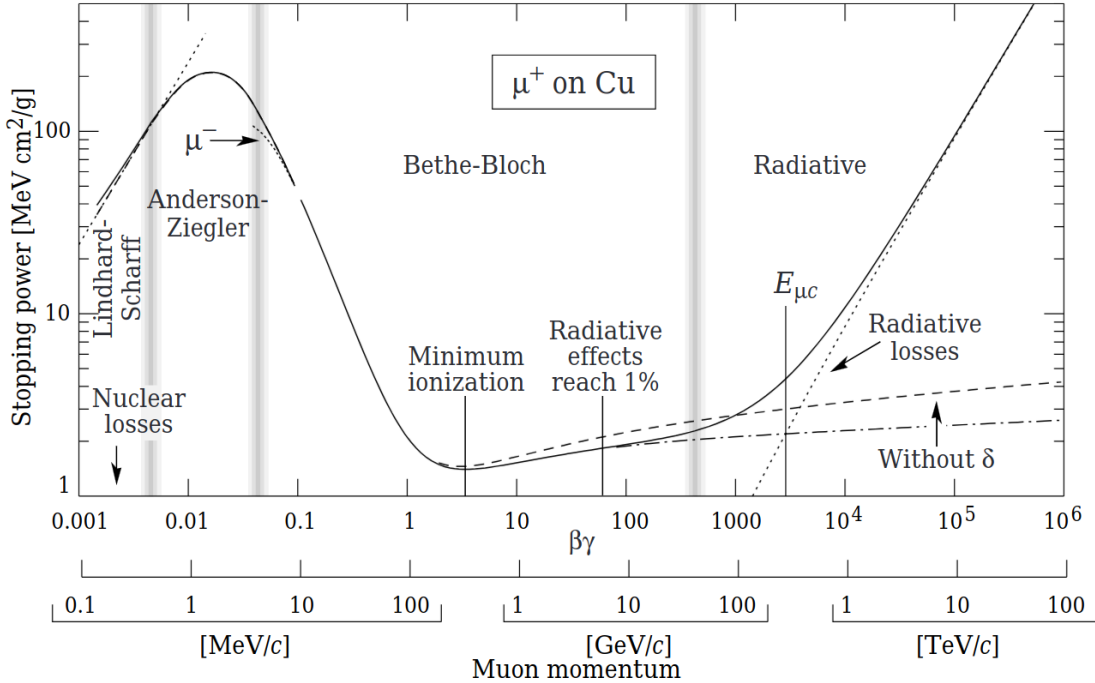


Fig. 3.2 Energy loss in matter for a muon traversing a copper medium [52].

Electrons with energy above the critical energy, which is the point losses due to ionisation are equal to losses from radiation, deposit energy via radiative effects. The critical energy for electrons in liquid argon is 39 MeV [54]. This process typically results in cones of electromagnetic activities, commonly referred to as *showers*. In the energy range relevant in a LArTPC, typically between 100-1000 MeV, showers deposit energy over a distance of ~ 1 m, and the shower length is logarithmic in energy. For electrons resulting from a muon decay with an energy of ~ 50 MeV, they neither resemble an ionisation track nor an electromagnetic shower. Instead, they result in a short linear segment of ionisation followed by a few clumps of deposited charge in the energy range of 1-10 MeV. This unique energy deposition of electrons is referred to as a *Michel electrons* and is often used by LArTPC experiments for energy calibration and identifying muons [55].

Photons deposit energy via Compton scattering and e^+e^- pair production, also producing electromagnetic showers similar to energetic electrons. Fig. 3.3 shows the mean free path of photons in liquid argon as a function of the photon energy for the two modes, Compton scattering by the solid blue line and pair production by the solid red line. At the low energy range < 50 MeV, the main interaction mode is via Compton scattering while at the high energy range > 50 MeV, pair production becomes the dominant effect. The mean free path for a photon for pair production is defined as 9/7 of the radiation length of

an electron and it is plotted as the solid cyan line at 18.1 cm. In the photon energy range of 100-1000 MeV relevant for LArTPCs, it can be seen that photons typically travel 20-30 cm without causing ionisation. This creates a gap between the interaction vertex and the start of the shower, known as the *conversion gap*. Both the energy loss profiles and the conversion gaps can be utilised to distinguish between electrons and photons.

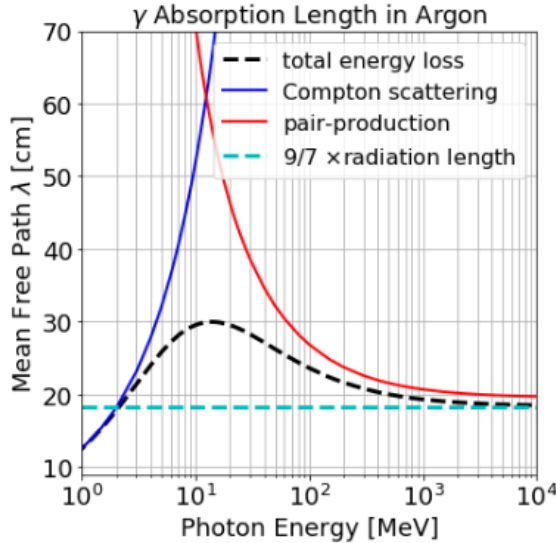


Fig. 3.3 Mean free path of photons traversing in liquid argon as a function of their energies [54].

Fig. 3.4 shows an event display of a simulated charged current ν_μ interaction containing a muon, a proton and a neutral pion in the final state. The colour scale corresponds to the magnitude of the energy deposition, where the colour green is lower in ionisation and the colour red is higher in ionisation. The muon results in a long minimum ionising track whilst the proton results in a short energetic stub, demonstrating the distinct difference between the energy loss profile of a muon and a proton. Moreover, as the muon comes to a stop, the colour scale changes from green to red, which indicates the increase in energy forming the Bragg peak. At the end of the muon track, it decays into a Michel electron that resembles a short linear segment low in energies. On the other hand, the neutral pion decays into two photons, which both undergo pair production producing electromagnetic showers. The photon showers are detached from the interaction vertex where both muon and proton tracks begin. This is the conversion gap feature unique to a photon shower.

3.2 Particle Interactions in Liquid Argon

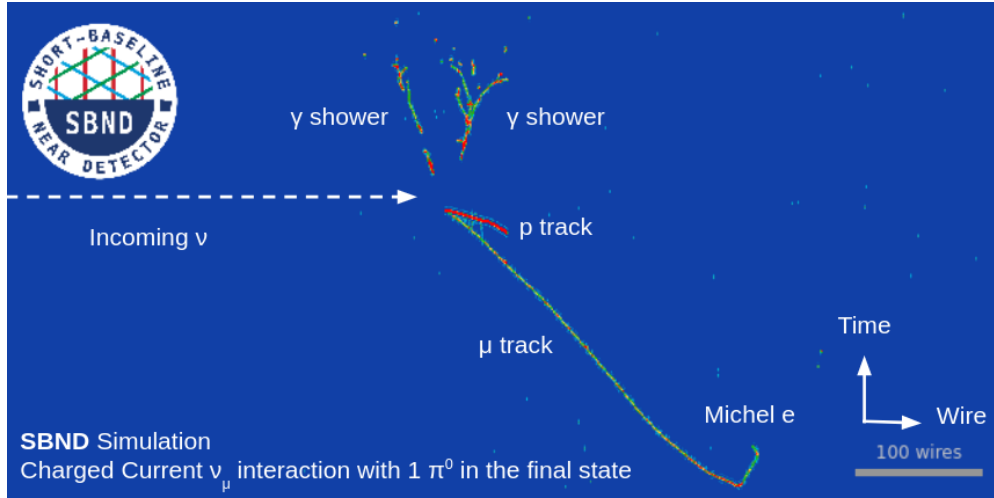


Fig. 3.4 Event display showing a simulated charged current ν_μ interaction containing a muon, a proton and a neutral pion in the final state.

3.2.2 Production of Scintillation Photons

Charged particles traversing liquid argon also produce scintillation photons, through two different processes that result in an argon excimer Ar_2^* as shown in Fig. 3.5. The first process is known as recombination, denoted by the arrows labelled *ionize* and *recombine*. Ionisation in liquid argon produces a free electron and an argon ion Ar^+ . The electron can either escape and drift towards the anode for detection, or recombine with an argon compound ion Ar_2^+ , forming an argon excimer. The second process is known as a self-trapped exciton, denoted by the arrow labelled *excite*. This begins when the charged particle does not have sufficient energy for ionisation, instead it excites the argon atom upon collision. The excited argon atom Ar^* self-traps with another argon atom Ar , forming an argon excimer. The resulting argon excimer from both processes is short-lived and undergoes radiative decay into two ground-state argon atoms. This produces scintillation photons with a wavelength of 128 nm in the Vacuum Ultraviolet (VUV) range [56].

The timing constant of the radiative decay depends on the excitation state of the argon excimer. This can be either a singlet state where the excited electron has the same spin as in the ground state or the triplet state where the excited electron has the same spin as another unpaired electron. The singlet state has a shorter mean lifetime with a decay constant $\tau_1 \approx 6 - 7$ ns, while the triplet state has a longer mean lifetime with a decay constant $\tau_3 \approx 1.5 - 1.6$ μ s [57]. These are referred to as the prompt and or late components, respectively. The time-dependent probability of light emission in pure liquid argon is

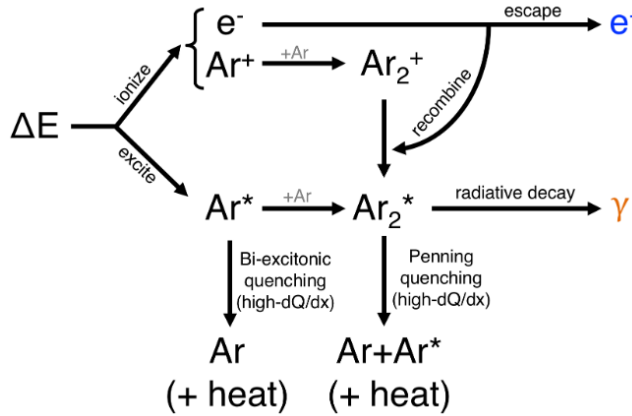


Fig. 3.5 Production of ionisation electrons and scintillation photons from energy deposition processes in liquid argon [56].

modelled as:

$$I(t) = \frac{A_1}{\tau_1} \exp\left(-\frac{t}{\tau_1}\right) + \frac{A_3}{\tau_3} \exp\left(-\frac{t}{\tau_3}\right), \quad (3.1)$$

where A_1 and A_3 are the decay amplitudes of the singlet and triplet state.

Liquid argon serves as an excellent medium for producing scintillation photons, such that the light yield is as high as $\sim 40,000$ photons per MeV of deposited energy in the absence of an electric field [58]. In a typical electric field at 500 V/cm, as configured in SBND, the light yield decreases to $\sim 20,000$ photons per MeV of deposited energy due to free electrons being drifted before recombination can occur [59]. Furthermore, high ionisation density may lead to non-radiative quenching effects [56]. Contaminants in liquid argon, such as oxygen and nitrogen, can absorb energy from argon excitons and excimers, without emitting any photons.

3.2.3 Recombination

The electron-ion recombination, as depicted by the arrow labelled *recombine* in Fig. 3.5, is a key physics process affecting the yield of ionisation electrons and scintillation photons. Recombination occurs almost immediately within 1-2 ns following the ionisation process. The recombination factor R is defined as the survival probability of electrons that do not recombine. Fig. 3.6 shows a comparison of various R models with a non-linear dependence on the energy density dE/dx for liquid argon at an electric field of 500 V/cm [60]. The Birks model, shown by the solid blue line, has been disfavoured due to spurious values at high charge density. The Box model, shown by the solid red line, is based on

3.2 Particle Interactions in Liquid Argon

the columnar theory around the charge deposition and can resolve the issue suffered by the Birks model. It has been recently modified for better agreement with the Birks model at low charge density which accounts for the presence of an electric field and local ionisation density. The modified Box model, as shown by the dotted red line, also contains experimentally derived parameters measured by the ArgoNeuT experiment [60].

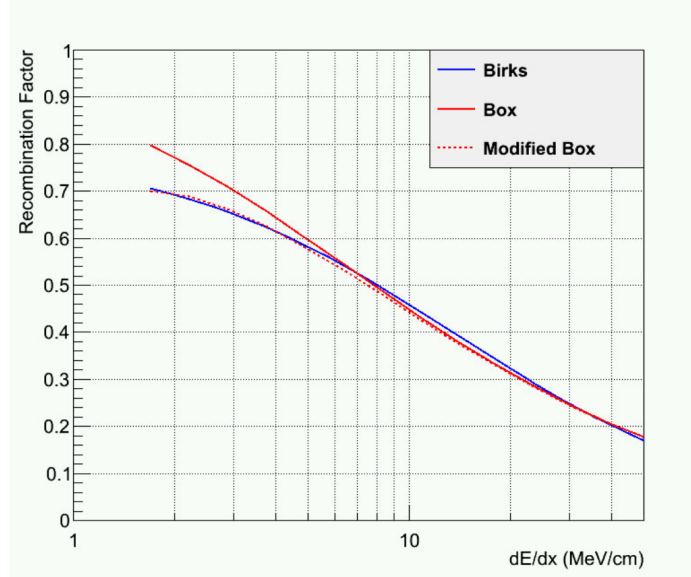


Fig. 3.6 Recombination factor in liquid argon as a function of the deposited energy density for an electric field of 500 V/cm [60].

The dependence of recombination on the electric field leads to an anti-correlation between the charge and light yield Q and L respectively, such that [60]:

$$Q = N_i R, \quad (3.2)$$

$$L = N_{ex} + N_i(1 - R), \quad (3.3)$$

where N_i is the number of electron-ion pairs and N_{ex} is the number of argon excitons. Fig. 3.7 illustrates the anti-correlation as a function of the electric field strength for various noble elements, of which argon is shown as dashed lines. A stronger electric field results in a higher number of ionisation electrons being separated from the argon ions and drifting towards the anode for detection before recombination can occur, thus increasing the charge yield. Conversely, scintillation photons are produced in the recombination process. In the presence of an electric field, recombination decreases, leading to a reduction in light yield. Furthermore, the recombination factor can be influenced at a local scale due to ionisation density resulting from interacting particles. The SBND detector operates with

an electric field of 500 V/cm, a region where the energy deposition to ionisation electrons and scintillation electrons are approximately equal as can be seen in Fig. 3.7. The impact of recombination on the observed physics will be further discussed in Chapter 8, Section 8.2.

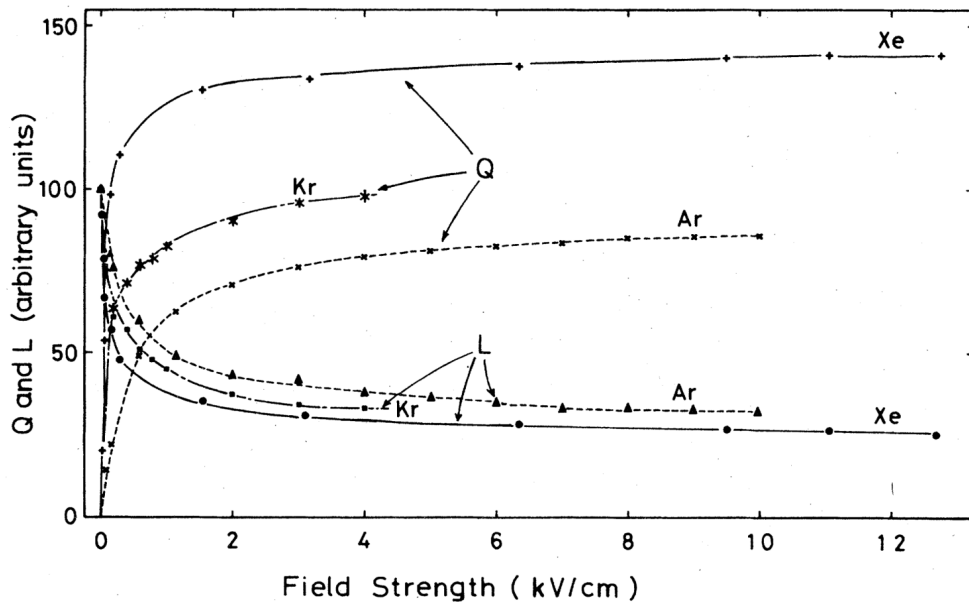


Fig. 3.7 Anti-correlation of charge yield Q and light yield L as a function of the electric field strength [61].

3.3 Particle Propagation in Liquid Argon

The following section provides a description of the transportation of ionisation electrons and scintillation photons through the liquid argon medium. Section 3.3.1 covers the details of different physics processes that electrons experience as they drift towards the anode, including diffusion, attenuation and the space charge effect. On the other hand, a discussion on the propagation of photons is presented in Section 3.3.2, detailing the process of Rayleigh scattering, absorption and wavelength shifting.

3.3.1 Electron Drift

Ionisation electrons that do not recombine drift towards the anode under the effect of an electric field. In a typical LArTPC with an electric field of 500 V/cm and a temperature of 88.4 K, the drift velocity of electrons is approximately $0.156 \text{ cm}/\mu\text{s}$ [62]. As the electrons

3.3 Particle Propagation in Liquid Argon

drift, they undergo diffusion, causing perturbations in their trajectories due to various effects. For example, it can be due to inelastic collisions with argon atoms. Diffusion causes the shape of a cloud of electrons produced in a point-like energy deposition to grow in volume while drifting. The effects increase with the drift distance, smearing both spatial and temporal resolutions.

Diffusion is parameterised in both the longitudinal and the transverse direction, which are parallel and perpendicular to the drift direction respectively. Longitudinal diffusion affects the temporal resolution, as individual electrons arrive at the wire either earlier or later relative to the electron cloud moving at the average drift velocity. The temporal smearing due to the longitudinal diffusion can be approximated as [63]:

$$\sigma_L \approx \sqrt{\frac{2D_L}{v_d^2} t}, \quad (3.4)$$

where D_L (cm²/s) is the longitudinal diffusion, v_d (cm/s) is the drift velocity and t (s) is the drift time. On the other hand, transverse diffusion broadens the cross section of the electron cloud arriving at the original wire, causing electrons to migrate to neighbouring wires. The spatial smearing due to the transverse diffusion can be approximated as [64]:

$$\sigma_T \approx \sqrt{2 \cdot D_T \cdot t}, \quad (3.5)$$

where D_T (cm²/s) is the transverse diffusion and t (s) is the drift time. Collectively, both longitudinal and transverse diffusion smear the distribution of deposited energy seen by each wire, thereby impacting the measured energy loss profile of a particle [64]. At the conditions expected for the SBND detector, the diffusion coefficients have been measured to be $D_L = 4.0$ cm²/s at the MicroBooNE detector [63] and $D_T = 8.8$ cm²/s [65].

In addition to diffusion, drifting electrons can also undergo attenuation. In this process, electrons are captured by electronegative impurities present in the liquid argon, most commonly oxygen and water [65]. This results in a reduction of electrons arriving at the wires, proportional to the drift distance. The number of charges collected on a wire Q_{wire} is typically modelled as an exponential suppression:

$$Q_{Wire}(t) = Q_{Dep} \cdot \exp\left(\frac{-t}{\tau}\right), \quad (3.6)$$

where Q_{Dep} is the original number of deposited charges, t (ms) is the drift time and τ (ms) is the electron lifetime characterising the level of charge attenuation. A high electron lifetime, resulting from a low level of contamination, is a critical operational factor for

achieving high efficiency in energy reconstruction. Recently reported from ProtoDUNE, which utilised the same membrane cryostat technology as SBND, the experiment measured a lifetime of ~ 10 ms, equivalent to an oxygen purity of 3.4 ppt [65]. This lifetime is significantly larger than the drift time of SBND, which is projected to be 1.25 ms, making the effect of attenuation almost negligible.

A final important issue in electron transport is the so-called Space Charge Effect (SCE). Argon ions, produced as part of the ionisation process, drift towards the cathode at a slower velocity than electrons. Typically, they have a drift velocity more than five orders of magnitude lower than that of electrons. [66]. Since SBND is a surface detector without an overburden, high exposure to cosmic rays leads to a high rate of ionisation. The resulting accumulation of slow-moving argon ions distorts the uniformity of the electric field, affecting both its intensity and direction. Fig. 3.8 illustrates the deformation of tracks drifting in the distorted electric field due to SCE. Track trajectories are impacted two-fold: bending away towards the detector edges as shown by the middle plot and bowing towards the cathode as shown by the right plot [67]. Moreover, distortions of the electric field also affect recombination previously discussed in Section 3.2.3, since the recombination factor is dependent on the electric field strength. Local fluctuations of recombination can subsequently impact the local charge yield resulting from an energy deposition.

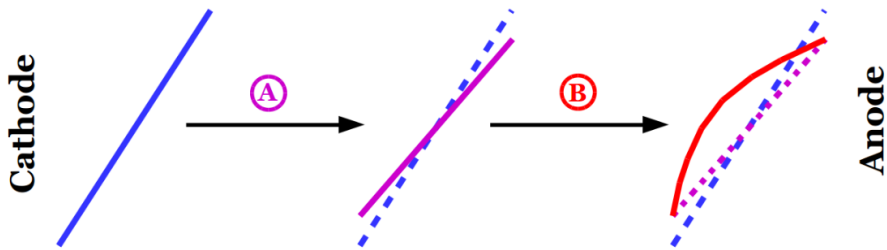


Fig. 3.8 Diagram showing the impacts of SCE on tracks: bending away towards the detector edges (middle) and bowing towards the cathode (right) [67].

3.3.2 Photon Propagation

Scintillation photons can propagate over long distances in liquid argon since the medium is transparent to its own light. As scintillation photons travel, they undergo Rayleigh scattering as the first-order effect, involving the photons elastically scattering off atoms, altering their trajectories. Reflections and refractions at the boundaries of the detector

3.3 Particle Propagation in Liquid Argon

material are second-order effects. While these effects do not change the number of photons, they modify the paths of propagation and lengthen the travel time [68]. The impact of these effects on the probability of photons reaching the Photon Detection System (PDS) depends on the locations where the photons are created and their paths taken to arrive at the PDS. This consequently leads to a non-trivial distribution of photon arrival time at the PDS, and the travel time can range from a few to several tens of nanoseconds. Particularly, this effect is the most impactful on the prompt component of scintillation photons. The Rayleigh scattering length λ_{RS} for VUV photons in liquid argon has been reported to be around 50 cm [69] up to 110 cm [70], which is comparable to the size of SBND.

In addition to Rayleigh scattering, scintillation photons can also undergo absorption, which arises due to contaminants in liquid argon. Contaminants like nitrogen [71] and methane [72] have a high absorption cross section for VUV photons. Other contaminants, like oxygen and water, have also been observed in commercial argon and can also attenuate the number of photons [73]. The absorption of scintillation photons is modelled as an exponential suppression similar to Eq. 3.6 modelling the electron attenuation. The number of photons surviving absorption N_γ is as follows:

$$N_\gamma(d) = N_0 \cdot \exp\left(\frac{-d}{\lambda_A}\right), \quad (3.7)$$

where N_0 is the original number of scintillation photons, d is the propagation distance and λ_A the absorption length. Moreover, the absorption rate is dependent on the Rayleigh scattering length. Photons with a shorter λ_{RS} undergo longer and more indirect paths, increasing their probability of absorption before reaching the PDS [74].

Finally, an enhancement method for lighting collection efficiency in LArTPC is wavelength shifting scintillation photons. Specifically at SBND, TetraPhenyl Butadiene (TPB) is employed to shift the wavelength of VUV photon from 128 nm to 430 nm, which falls within the visible light range. This is to better match the detection spectrum of optical detectors installed at SBND [68], of which a description of the SBND PDS will be detailed in Chapter 4. Additionally, it provides extra handles for light reconstruction, of which the improvement will be discussed in Chapter 6.

The propagation characteristics of photons differ between the VUV and visible range. Fig. 3.9 shows the group velocity on the left and the Rayleigh scattering length on the right as a function of the photon wavelength in liquid argon. The vertical dashed blue and red lines at 128 and 430 nm respectively are the wavelengths of scintillation photons in liquid argon and of photons re-emitted by TPB wavelength shifting. Here, it can be seen that

the group velocity of VUV photons is slower than that of visible photons. Moreover, the Rayleigh scattering length of VUV photons is two orders of magnitude smaller compared to visible photons. This results in VUV photons being more susceptible to Rayleigh scattering and having a higher probability of absorption [74].

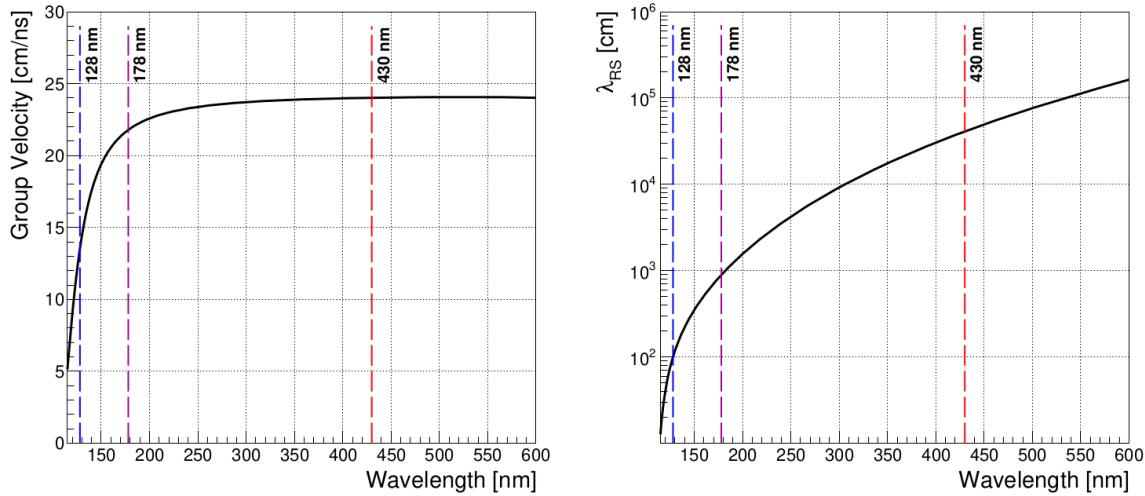


Fig. 3.9 Group velocity (left) and the Rayleigh scattering length (right) as a function of the photon wavelength in liquid argon [74].

3.4 Detection of Electrons and Photons

Upon arrival at the anode for detection, ionisation electrons and scintillation photons are read out by different detection technologies. Ionisation electron signals are recorded by the wire planes, which will be detailed in the following Section 3.4.1. Following that, Section 3.4.2 provides a description of two different types of optical detectors for detecting scintillation photons.

3.4.1 Wire Planes

Once arrive at the anode, ionisation electrons induce signals on the wire planes, which are made up of three planes separated by a few mm as previously depicted in Fig. 3.1. A bias voltage is applied to each wire plane to create a drift field across the three planes. This allows for electron transparency for the two innermost planes, also referred to as induction planes, where drifting electrons induce bipolar signals on the wires. The electrons are then collected on the outermost plane, producing a unipolar signal, hence, this plane is referred

3.4 Detection of Electrons and Photons

to as the collection plane. Fig. 3.10 shows an example of induced currents on a wire as a function of time. Here, it can be seen a bipolar signal on an induction plane in red and a unipolar signal on a collection plane in blue. The three planes are oriented at an angle of 60° with respect to each other, of which the diagram in Fig. 3.1 shows three planes at the angle of 0° and $\pm 60^\circ$ to the vertical. While three-dimensional spatial reconstruction of a signal requires a minimum of at least two wire planes, many modern LArTPC experiments use all three planes to improve the spatial resolution [2, 47–49, 53, 65].

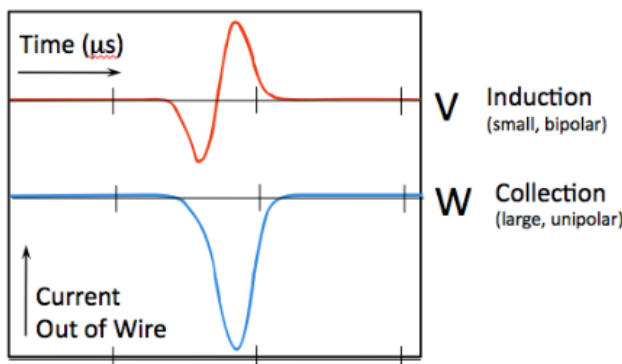


Fig. 3.10 Current signals on the induction and collection wire plane induced by a point-like charge deposition [53].

The signals induced or collected on the wire planes are then shaped, amplified, and digitized before acquisition. Then, the measured signals are deconvolved for noise removal and the amount of charge collected is correlated with the energy deposited in the detector. Finally, the reconstruction of spatial and energy information is performed, which allows for high level analysis like particle identification. The reconstruction of charge signals at SBND will be further discussed in Chapter 6, Section 6.2.

3.4.2 Photomultiplier Tubes and X-ARAPUCAs

Scintillation photons are detected by the PDS located behind the wire planes, as depicted in Fig. 3.1. For SBND, which will be detailed in the forthcoming Chapter 4, the primary detection technology in the PDS is Photomultiplier Tubes (PMTs), which have a Quantum Efficiency (QE) of up to 30% [75]. However, PMTs are typically large and require sufficient volume inside the detector for installation. Current and future LArTPC experiments are increasingly adopting Silicon PhotoMultipliers (SiPMs) due to their advantageous smaller size, lower power consumption, excellent signal-to-noise ratio, and a high QE of up to

40% [76]. The X-ARAPUCA device is a novel light collection technology utilising SiPMs, currently developed by Unicamp and being tested inside the SBND detector. Further description of X-ARAPUCA can be found in Ref. [77].

Both PMTs and X-ARAPUCAs are coated with wavelength shifting materials. The re-emitted light direction is isotropic, causing coated optical detectors to suffer a 50% reduction in efficiency due to photons being emitted away from the detection surface. PMTs are coated specifically with TPB, which can also impact the detection time as the emission of visible photons is not instantaneous. Multiple time components of re-emitted photons from TPB have been observed, with the majority of photons re-emitted within nanoseconds and a subset re-emitted as long as a few microseconds [78].

Photon signals measured by PMTs are digitized and acquired using a very high sampling frequency readout at the rate of 500 MHz [2]. This high sampling frequency gives the scintillation light signal much better timing resolution compared to the charge signal. As a result, it provides the most precise interaction timing information available in the detector. This is particularly important across different areas of the SBND detector. The PMT signals will be utilised for triggering which will be detailed in the forthcoming Chapter 4. In addition, the signals enable the timing resolution of the light reconstruction to reach the order of $\mathcal{O}(1)$ ns, which will be covered in Chapter 6. Then, the timing performance of the data acquisition to enable a stable and high frequency sampling of PMT signals will be further discussed in Chapter 7. All of these pave the way for the search for HNLs which is a key subject of this thesis, which will exploit the timing kinematic difference between HNL signals and SM neutrino backgrounds and will be covered in more detail in Chapter 9 and 10.

3.5 Concluding Remarks

Since originally proposed in 1977, the LArTPC concept has proven its potential for use in precision neutrino experiments. The understanding of particle interactions and their propagation within the detector, along with the detector's response to these particles, has significantly improved over time. Technological advancements in detection and readout now enable the scaling of LArTPCs from volumes of only several tons to even tens of kilotonnes, making them suitable for high multiplicity environments. This allows for the next generation of LArTPCs like the DUNE experiment to advance the field of neutrino physics. As described in the following Chapter 4, the SBND experiment and physics programme at Fermilab is a key part of this future.

Chapter 4

The Short-Baseline Near Detector and Booster Neutrino Beam

The Short-Baseline Near Detector (SBND) is the near detector of the Short-Baseline Neutrino (SBN) program at Fermilab. The program is motivated by anomalous results observed across various detectors involving accelerator, nuclear reactor, and solar neutrino experiments. For instance, the low energy excess in the ν_e and $\bar{\nu}_e$ interaction measurement observed by both LSND and MiniBooNE experiments is an outstanding anomaly for the past decade [16, 17]. In addition to being part of the SBN program, SBND also has its own extensive physics program focusing on high precision ν -Ar cross section measurements and physics beyond the Standard Model. This will not only benefit future long baseline neutrino experiments such as the Deep Underground Neutrino Experiment but also significantly advance the field of neutrino physics as a whole. At the time of writing, SBND has entered its commissioning phase, in preparation for calibration and physics data taking.

This chapter contains an overview of the SBND detector and the Booster Neutrino Beam (BNB), which are the detector and beam source used in the search for heavy neutral leptons in this thesis. The chapter begins with a discussion on the physics program of the SBND experiment in Section 4.1. Section 4.2 provides a detailed description of the detection technology of SBND, covering the time projection chamber, photon detection system, and cosmic ray tagger system. This section also elaborates on the hardware triggering system and the data acquisition system employed at SBND. Finally, an overview of the BNB is presented in Section 4.3, detailing the particle production process of the beam and the flux prediction at SBND. Finally, Sec 4.4 provides some concluding remarks.

4.1 The Short-Baseline Near Detector Physics Program

The Short-Baseline Near Detector (SBND) is part of the Short-Baseline Neutrino (SBN) Program located at Fermilab [1]. The program consists of three LArTPC detectors: SBND, MicroBooNE, and Imaging Cosmic Rare Underground Signals (ICARUS), positioned at distances of 110 m, 470 m, and 600 m, respectively, on-axis to the target of the Booster Neutrino Beam (BNB) as shown in Fig. 4.1. The near-far detector setup was designed to search for the potential existence of sterile neutrinos in the mass range of $\mathcal{O}(1 \text{ eV})$ that was briefly mentioned in Chapter 2, driven by a series of anomalies observed by previous short baseline experiments.

Amongst these earlier experiments was the Liquid Scintillator Neutrino Detector (LSND) experiment which utilised a stopped pion source to probe $\bar{\nu}_e$ via inverse beta decay and reported an excess of signal to the background at low energies with a 3.8σ level [16]. The MiniBooNE experiment was a neutrino accelerator experiment designed to measure the entire phase space covered by the LSND result [17]. This detector observed an excess of ν_e ($\bar{\nu}_e$) in ν_μ ($\bar{\nu}_\mu$) beam mode showing a discrepancy from the SM with a significance level of 4.5σ (2.8σ), reaching 6.0σ when combined with the LSND data. Additionally, a revisit to results from the nuclear reactor experiments indicated a deficit of $\bar{\nu}_e$ fluxes to the theoretical expectation at a 3σ level [79, 80]. Furthermore, gallium solar neutrino experiments observed an overall deficit in ν_e fluxes at a 3σ level during calibrations using radioactive neutrino sources [81, 82]. These main anomalous results collectively suggest the mass mixing of SM neutrinos with an addition eV-scale sterile neutrino at a short baseline to energy ratio of $L/E \approx 1 \text{ m/MeV}$. This can enhance or reduce the number of observed neutrino interactions for a given channel [1]. The goal of the SBN program is to pioneer the search for eV-scale sterile neutrino oscillations, covering the parameter phase space previously allowed by past experiments but at a significance level of $\geq 5\sigma$.

Additionally, measurements of ν -Ar interactions play a crucial role in the physics program of SBND, serving as a critical element in understanding neutrino oscillations [83]. Being the nearest to the beam target, SBND is presented with a unique opportunity to observe the largest unoscillated neutrino fluxes among the three detectors. Over the 3-year operational span, SBND aims to record a staggering 10 million neutrino events, originating from 1×10^{21} POT interactions [1]. This will establish SBND as the world leader in statistics for ν -Ar cross section measurements. More than 6 million ν_μ Charged Current (CC) events will be collected, reducing the statistical uncertainty to well below the percent level. Moreover, SBND is expected to record 45,000 ν_e CC events, hence providing the most

4.1 The Short-Baseline Near Detector Physics Program

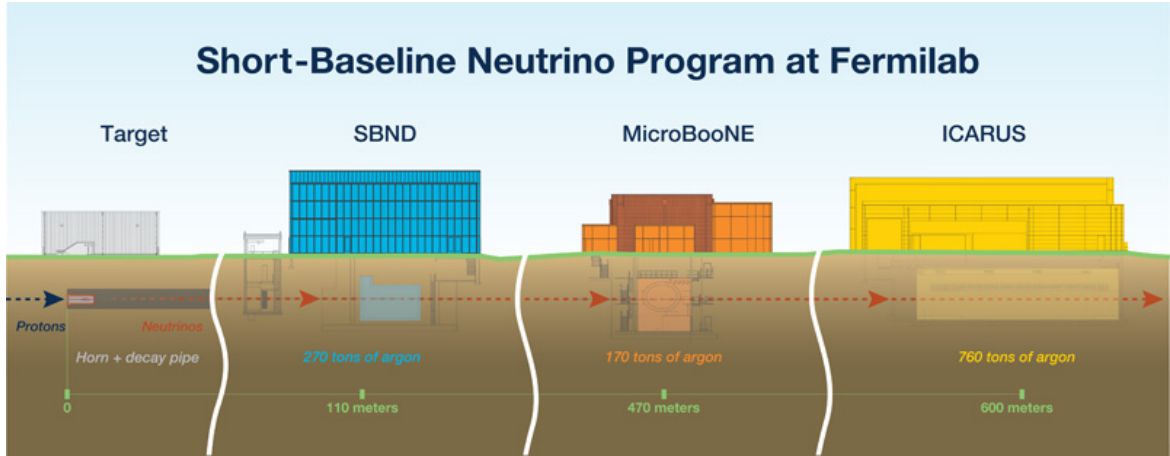


Fig. 4.1 Graphic showing the three LArTPC detectors made up the Short-Baseline Neutrino program: SBND, MicroBooNE and ICARUS [1].

extensive statistics for both inclusive and exclusive measurements of this channel to date. These measurements will be extremely beneficial for advancing the objectives of the SBN physics program, as well as contributing to the physics goals of the Deep Underground Neutrino Experiment (DUNE), which employs argon as its detector medium.

Finally, a key aspect of the physics program at SBND is the exploration of new scenarios leading to Beyond Standard Model (BSM) physics. Proximity to a high intensity beam and the resulting large statistics enable searches for very weakly coupled interactions coming from the BNB [1]. A key example is Heavy Neutral Leptons (HNLs), the primary focus of this thesis. These can be produced from meson decays in the BNB and subsequently decay in flight into SM observables for detection, as previously detailed in Chapter 2. Another compelling BSM candidate is light dark matter, which can be produced from neutral meson decay or proton bremsstrahlung [84]. As postulated by thermal relic models, these light dark matter particles could reach sub-GeV-scale masses. The particles may scatter and decay, resulting in electromagnetic showers without any hadronic activities inside SBND. Moreover, the dynamic mass mechanism of neutrinos opens avenues for new physics in the dark sector. The dark neutrino model proposes that right-handed neutrinos can scatter with nuclei to produce dark gauge bosons, subsequently decaying into di-lepton pairs [85]. In the case where the leptons are electrons, this could potentially explain the low energy excess anomalies observed by LSND and MiniBooNE [86]. These represent just a few examples of the diverse array of BSM scenarios that can be explored at the SBND detector. Other unmentioned possibilities such as new interactions, extra dimensions, and violations of Lorentz and charge parity time symmetries, among others, contribute to the rich physics program of SBND [1].

4.2 The Short-Baseline Near Detector

The SBND detector is a LArTPC with an active volume of 112 tons and dimensions of 400 cm (x-drift) \times 400 cm (y-height) \times 500 cm (z-length) [87]. As depicted in Fig. 4.2, the detector consists of two separate TPCs, each with a drift length of 200 cm, sharing a common Cathode Plane Assembly (CPA) positioned at the centre. On the east and west side of the detector are the Anode Plane Assemblies (APAs) made up of three wire planes, and located behind the wires is the Photon Detection System (PDS). The TPCs are surrounded by a field cage that provides a uniform electric field. The entire detector is placed inside a membrane cryostat, surrounded by 7 walls of Cosmic Ray Tagger (CRT) modules to provide a 4π solid angle coverage for cosmic ray rejection. The following sections provide an overview of each of the main subsystems of SBND.

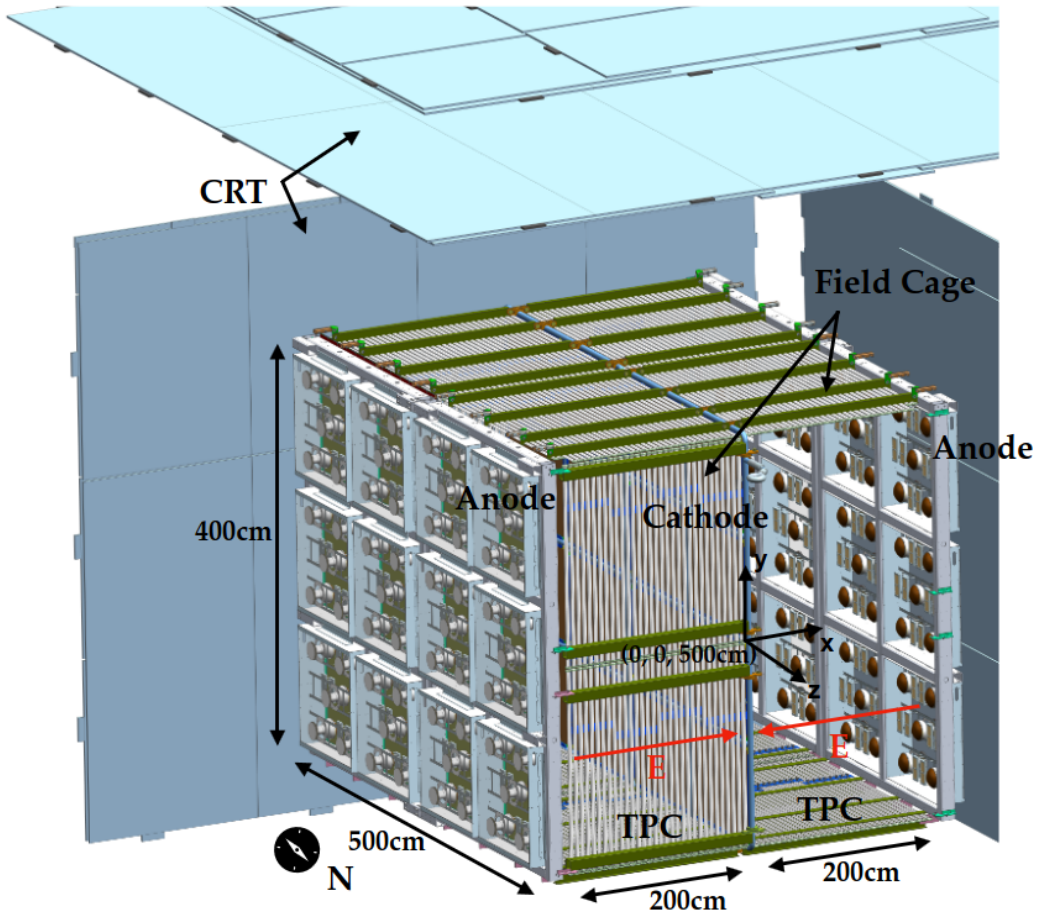


Fig. 4.2 3D model of the SBND detector, showing the LArTPC surrounded by 4 out of the 7 CRT walls [68].

4.2.1 Time Projection Chamber

Fig. 4.3 shows a complete APAs, of which each is located on the east and west sides of SBND. The plane is made up of two coupled APAs, where each APA measures $4\text{ m} \times 2.5\text{ m}$ and comprises a steel frame supporting three wire planes: two induction planes, denoted as U and V, oriented at angles of $\pm 60^\circ$ to the vertical collection plane denoted as Y. These wire planes U, V and Y are colour-coded as green, blue, and red, respectively. Each wire plane is constructed with $150\text{ }\mu\text{m}$ diameter copper-beryllium wires, with a wire pitch and plane spacing of 3 mm. The wires are tensioned to 7 N to prevent slackening when cooled down to liquid argon temperature at 88.4 K [88]. To maintain charge transparency for the induction planes and collection efficiency for the collection plane, a biased voltage of -200 V, 0 V, and 500 V is applied to planes U, V, and Y, respectively. In total, each TPC consists of 5,632 wires: 1,664 wires in the collection plane and 1,986 wires in each induction plane.

Two APAs are coupled together utilising jumper cables to bridge the 15 mm gap between the induction planes to form a single electronic channel. Attached to the top, left and right side of APAs are the cold electronics readout boards. They pre-amplify and digitise wire signals while submerged in liquid argon at a low temperature to minimise noise. Fig. 4.4a shows a photograph of a fully assembled APAs at SBND, where the PDS located behind the wires can also be seen.

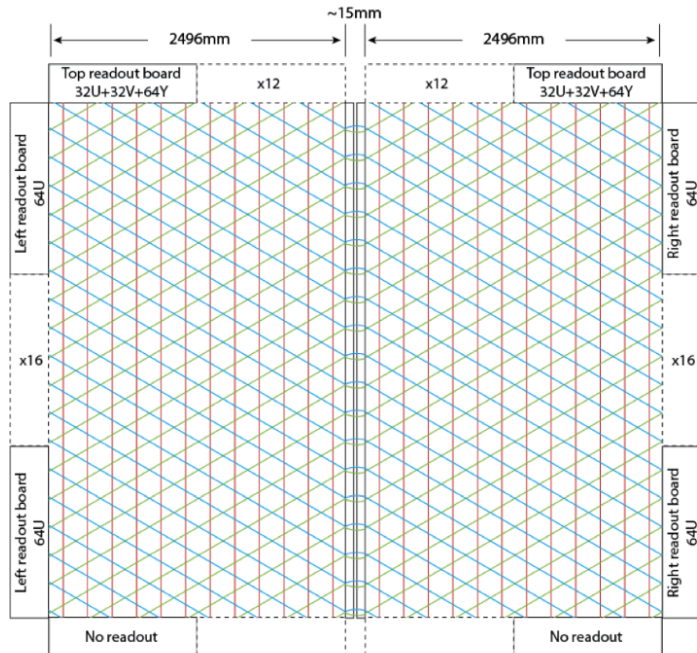


Fig. 4.3 Schematic showing two coupled APAs to form a complete APAs [87].

Fig. 4.4b shows a photograph of the fully assembled CPA. The plane consists of two steel frames, each containing 8 windows, adding to a total of 16 windows. Each window, measuring 60 cm × 50 cm, houses a fibreglass plate laminated on both sides with non-conductive reflective foils > 99% specular reflection in the visible range and coated with TetraPhenyl Butadiene (TPB). Furthermore, the plate is covered by a wire mesh, providing a high voltage at -100 kV supplied by a feedthrough donut from outside the cryostat.

The field cage consists of a sequence of electrodes arranged perpendicular to the drift direction. It can be seen in both Fig. 4.4a and 4.4b as the series of metal bars surrounding the TPC. These electrodes incrementally step up the voltage from -100 kV applied at the CPA to the ground voltage in increments of 3 kV. This gradual voltage increase is implemented to maintain a uniform electric field of 500 V/cm across the drift volume.



(a) View of the APA

(b) View of the CPA

Fig. 4.4 Photographs showing the fully assembled TPC of the SBND detector.

4.2.2 Photon Detection System

The PDS design of SBND is the most sophisticated system ever installed in a LArTPC, by incorporating both active and passive optical components [68]. The active detector integrates two different technologies: (1) a system of 120 Photomultiplier Tubes (PMTs) and (2) a system of 192 X-ARAPUCA devices. The PMTs are cryogenic 8"-diameter Hamamatsu R5912-MOD models [89], which are the primary light detection system. Meanwhile, the X-ARAPUCAs serve as a research and development platform for future experiments, incorporating multiple variations in their components for performance comparison. A summary of the X-ARAPUCA specifications can be found in Ref. [68]. The TPB-coated

4.2 The Short-Baseline Near Detector

reflective foils installed at the CPA are the passive component to improve the uniformity of light yield.

Fig. 4.5 shows a 3D model for each component of the SBND PDS. For the purpose of installation, the optical detectors are arranged into modular PDS boxes, of which a single PDS box is shown on the left of Fig. 4.5. Each box houses 5 PMTs, 4 coated and 1 uncoated PMT, along with 8 X-ARAPUCA devices, 4 coated and 4 uncoated. These PDS boxes are installed in a configuration of 4×3 behind each APAs as illustrated on the right of Fig. 4.5. This results in a total of 12 boxes per TPC volume. The TPB-coated reflective foils at the central cathode can also be seen on the right of Fig. 4.5.

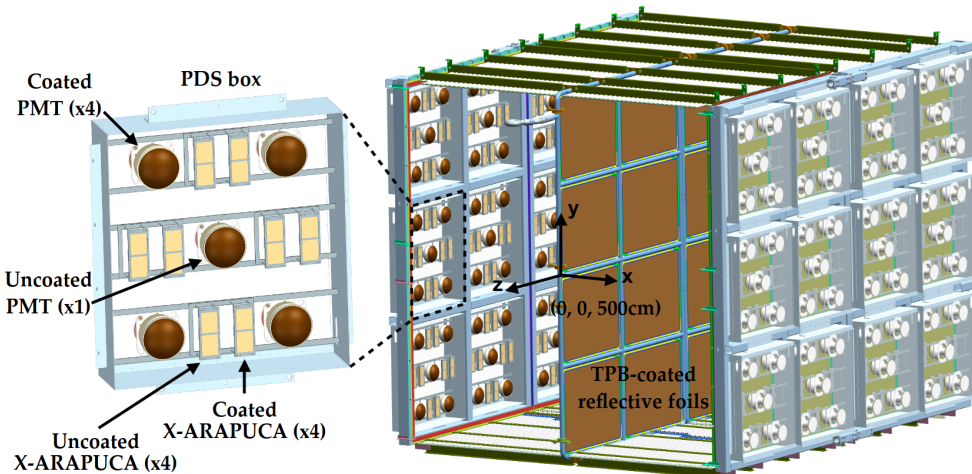


Fig. 4.5 3D model of a PDS box (left) and the PDS box arrangement on the east and west side of the TPC (right) [68].

Out of the two optical detectors, PMT signals are the primary light signals and are used to provide trigger conditions. The 120 PMTs are partitioned into two optically-isolated TPC volumes, each with 60 PMTs. Within each TPC, 48 PMTs are TPB-coated, and thus are sensitive to both direct VUV and reflected visible light, while the remaining 12 non-coated PMTs detect only reflected light. This ratio of coated to uncoated PMTs (4:1) is chosen to optimize light collection efficiency while maintaining the capability to distinguish between the two light components [68].

Having TPB is utilised at two locations: (1) evaporated onto reflective foils at the cathode, and (2) coated on the optical windows of the PMTs, leads to a difference in the spatial and arrival time distributions for direct VUV and reflected visible photons. Direct VUV photons arriving at coated PMTs are wavelength-shifted into the detectable wavelength range of PMTs. Reflected visible photons, resulting from VUV photons being wavelength shifted and reflected at the cathode, have to travel a longer distance before

being detected by uncoated PMTs. The spatial distribution of reflected visible photons is more diffused and spread across a larger number of optical detectors compared to direct VUV photons [74]. Such difference can be exploited to perform the timing reconstruction using only PMT signals, which will be further discussed in Section 6.3.1.

4.2.3 Cosmic Ray Tagger

Since SBND is a surface detector, it utilises a Cosmic Ray Tagger (CRT) system to effectively reject background from cosmic muons. Fig. 4.6 shows the operating principles of CRT strips and their orientation. As shown in the middle diagram, each CRT strip consists of a plastic scintillator strip with a width of 10.8 cm, connected to a pair of SiPMs via wavelength shifting optical fibres. The right diagram shows a coincident hit from perpendicular strips that allows for a 2D reconstruction of the hit location, and the number of photons collected for each strip improves the precision of the location tagging. 16 scintillator strips in parallel form a CRT module. Multiple CRT modules are arranged orthogonally to form a CRT wall, typically in the size of 7.5 m in height and 9 m in width.

The left diagram shows an example orientation of 2 CRT modules on top of each other, where CRT strips of each module are perpendicular to each other. The cryostat of SBND is entirely encased by 7 CRT walls, with 1 on each side and 2 positioned on top of the detector. Fig. 4.2 shows 4 out of the 7 CRT walls, particularly the south, west and top walls are visible. Additionally, the top 2 walls function as a telescopic array, facilitating the tagging of vertical downward going cosmic muons. This configuration enables a comprehensive strategy for cosmic background rejection utilising both geometrical and high precision timing information, which will be more detailed in Section 6.4.2.

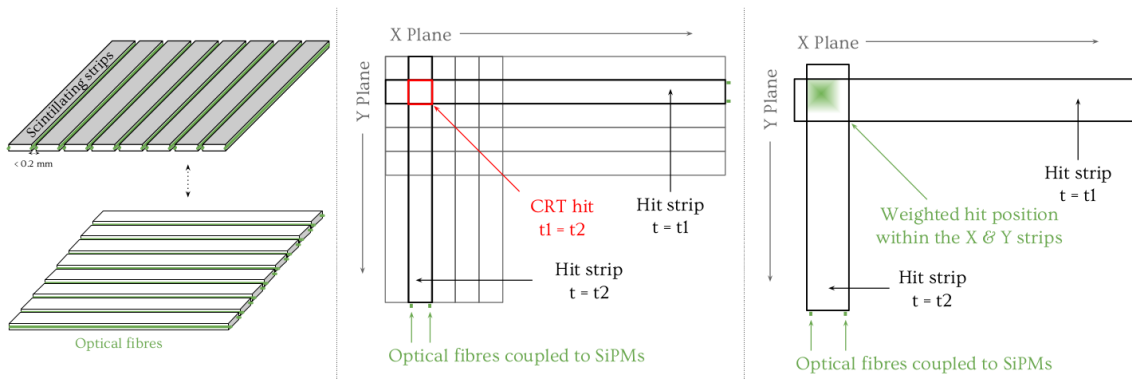


Fig. 4.6 Diagrams showing the operating principles of CRT strips (middle, right) and their perpendicular orientation (left) [50].

4.2.4 Readout Electronics

The readout electronics of each detection subsystem, TPC, PDS and CRT, are detailed as following. Firstly, TPC readouts comprise four components: (1) Cold Electronics (CE), (2) Warm Interface Boards (WIBs), (3) TPC crates and (4) Nevis Trigger Board (NTB). As shown in Fig. 4.3, the wires are connected to CE readout boards on the APAs. Located inside the cryostat, the CE components are submerged in liquid argon to reduce thermal noise as well as cable lengths [90]. They are responsible for amplifying and digitizing waveform signals at a sampling frequency of 2 MHz. Signals from the CE are sent outside of the cryostat to the WIBs via copper cold cables. The WIBs serve as a bridge between the CE and other TPC readouts through fibre optic links. This isolation architecture completely separates wire grounding from the building, thereby enabling a superior signal-to-noise ratio.

Following the WIBs, the data is transmitted to 11 TPC crates for reading out, buffering, and processing the wire signals. Data from TPC readout crates are directed by the NTB into two parallel independent streams of data. The main stream to record neutrino beam events relies on an external trigger, which reads out data with lossless compression. An additional continuous stream requires no external triggers and outputs data with lossy compression.

Regarding the electronics readouts of the PDS, CAEN digitizers are employed. 120 PMTs are readout by 8 CAEN V1730SB digitizers [91], which are capable of recording waveforms for 16 channels independently with a sampling frequency of 500 MHz. Meanwhile, the 192 X-ARAPUCAs are digitised by another model called V1740 [92], that can readout 64 channels at a lower sampling frequency of 62.5 MHz. Both of these models feature deep buffers to store longer waveforms and handle higher data rates. Additionally, the V1730SB model offers better waveform baseline stability against temperature fluctuations. Multiple CAEN digitizers can be synchronised such that they collectively behave as a single digitizer, which is critical to maintaining the timing resolution of the electronics at $\mathcal{O}(1\text{ ns})$. The characterisation of synchronisation across multiple V1730SB digitizers is detailed in Section 7.3.

Finally, the 7 CRT walls are read out by 144 Front End Board (FEB) modules [93]. Each FEB module is a multifunctional board capable of reading out 32 channels, with one channel per SiPM. The module can provide a bias voltage, which is adjustable for individual SiPMs, as well as signal amplification and shaping. Once the signal is shaped, the FEB can apply signal discrimination and self-triggering, such as coincidence for each pair of SiPMs in a CRT strip or coincidence across multiple FEBs for orthogonal CRT strips. Once the

signal passes the trigger, it is digitised and timestamped with respect to an input reference clock. The data is then stored in a buffer and read out via an Ethernet connection. The characterisation of the timing resolution of FEB modules is detailed in Section 7.2

4.2.5 Hardware Trigger

Triggering plays a vital role in the SBND detector to select only interesting physics events, given the detector is exposed to a high rate of backgrounds from cosmic muons. The main hardware trigger component in SBND is the Penn Trigger Board (PTB). It applies a programmable trigger logic based on external inputs and issues a trigger to the Data AcQuisition (DAQ) subsystem if the conditions are met. Details of the hardware trigger at SBND can be found in Appendix A, while a short summary is provided here.

In order to form a trigger, the PTB requires signals from the three subsystems: (1) beam system, (2) PMTs, and (3) CRTs. The beam system informs the PTB on the status on the BNB beam, and whether the beam has arrived at the detector hall. Signals from PMTs provides information regarding the intensity and locality of the energy deposited inside the detector, and whether it is consistent with a neutrino event. Signals from CRTs provides geometrical information of the energy deposited outside of the detector in the CRT walls, and whether it is consistent with a cosmic muon. The readout electronics of PMTs and CRTs are equipped with timing resolution $\mathcal{O}(1\text{ ns})$ and their output signals can quickly inform the PTB to form a trigger. Additionally, incorporating CRT signals marks SBND as the first instance of a LArTPC to employ CRTs as part of its triggering scheme [94].

Different combinations of signal inputs described here can form different *flavours* of triggers. The primary beam trigger requires PMT signals to coincide with the beam spill window. Conversely, for background estimation purposes, an anti-coincidence to the beam signal logic can be applied to select cosmic muons occurring outside of the beam spill window. The calibration trigger utilises coincidence across different CRT walls to select specific track topologies formed by cosmic muons. For example, anode-to-cathode-crossing cosmic tracks can be selected by requiring the east and west CRT walls to be coincident. These sets of tracks are useful for electron lifetime measurements, which will be explored in Section 8.1.

The importance about the hardware triggering at SBND is that a single triggered physics event constitutes of two types of triggers: (1) a single Event TRIGger (ETRIG) issued to the TPC readouts and (2) multiple Flash TRIGgers (FTRIGs) issued to the PDS

4.2 The Short-Baseline Near Detector

readouts. The ETRIG is used by the DAQ subsystem to acquire a long snapshot of the TPC waveform $\mathcal{O}(1 \text{ ms})$ while multiple FTRIGs are used to capture many short snapshots of optical detector waveforms $\mathcal{O}(10 \mu\text{s})$. The data is then assembled to build a physics event, of which the DAQ process will be explained in Section 4.2.6 and 4.2.7 next.

4.2.6 Data Acquisition

Upon receiving a hardware trigger, the DAQ subsystem begins to transport data from subsystem readouts to event builder machines. The SBND DAQ can assemble data from each subsystem into a physics event during real time data flow, known as the event building process. It must also be able to handle a high event rate due to the close proximity of SBND to the beam target. Additionally, the DAQ can apply software metrics to filter events for various data streams and data monitoring purposes.

Fig. 4.7 shows the data flow of the DAQ at SBND. The data flow begins with raw signals from detection subsystems, shown as the coloured dotted arrows. The signals are acquired by readout electronics, shown as colour boxes in the first column labelled *Readout Electronics*, that was covered earlier in Section 4.2.4. The boxes are colour-coded as red, blue and orange for the TPC, PDS and CRT readout respectively. Within this first column, 2 additional readout electronics are also included. The Penn Trigger Board, shown by the green box, is for the hardware triggering subsystem. The White Rabbit SPEC-TDC, shown by the purple box, is part of the White Rabbit timing subsystem and will be discussed in detail in Chapter 7.

Each of the readout electronics components is accompanied by a corresponding *board-reader*, shown by the second column labelled *Servers Hosting Boardreaders*. Boardreaders are software tools serving as a communication bridge between readout electronics and computer servers. The electronics send raw signals to the computer servers, shown as the grey dotted arrows. The software boardreaders send configurations to the electronics, shown as the grey dashed-dotted arrows.

The event building process occurs in the third column labelled *Event Builder Machines*. The raw signals are packaged into a data format known as *fragments* by boardreaders. The fragments are sent to event builders, as shown by the coloured solid arrows. The event builders assemble fragments from different readout electronics into physics events. The event building process will be discussed next in Section 4.2.7.

Finally, the fourth column labelled *Data Stream* illustrates the last stage of the data flow. Software metrics can be applied by event builders to separate physics events into

different streams of data, as shown by the grey dashed arrows. This assists with data management since different flavours of triggered events can be organised into different locations. An additional data stream for online monitoring is shown by the bottom right grey box. Details of the data streaming process is provided in Appendix B.

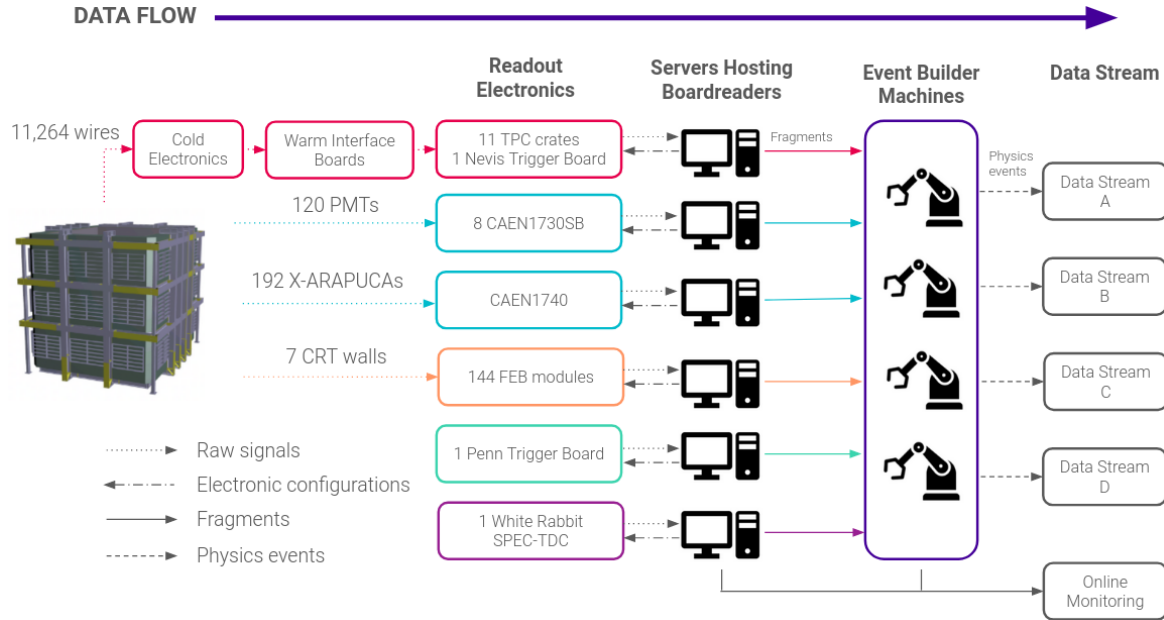


Fig. 4.7 Flow chart showing the data flow of data acquisition.

4.2.7 Event Building

One key process in the DAQ is event building. This is achieved by using the artdaq Toolkit, developed by the Real-Time Systems Engineering Department of Fermilab's Scientific Computing Division [95]. Within this framework, each discrete hardware readout component has a corresponding software module known as a *boardreader*. These boardreaders facilitate communication between the readout electronics and the event builder machines. They can send configurations directly to the hardware in one direction and retrieve data from the hardware in the opposite direction. Data acquired from the readouts is packaged by boardreaders into a digitised format called a *fragment*. In the scope of this work interested in the timing aspect of the DAQ that will be elaborated in Chapter 7, the critical information of a fragment is its timestamp corresponding to when the readout electronics receive a trigger.

Event builders assemble fragments from different readouts into a physics event based on their timestamps. Fig. 4.8 illustrates the chronological structure of a physics event

4.2 The Short-Baseline Near Detector

at SBND, containing only TPC, PMT and CRT fragments for simplicity. The time axis is shown as the purple arrow, where at the centre $t = 0$ ms corresponds to when the beam spill begins. The TPC fragment, as shown in red, is coincident with the beam spill to capture the neutrino event in the TPC. The readout length of a TPC fragment is 1.7 ms, covering the entire TPC drift length of 1.3 ms and including a padding of 0.2 ms before and after the drift. Aligning the TPC fragment with the beam spill is achieved through the ETRIG trigger issued to the TPC readouts such that it coincides with when the beam spill begins.

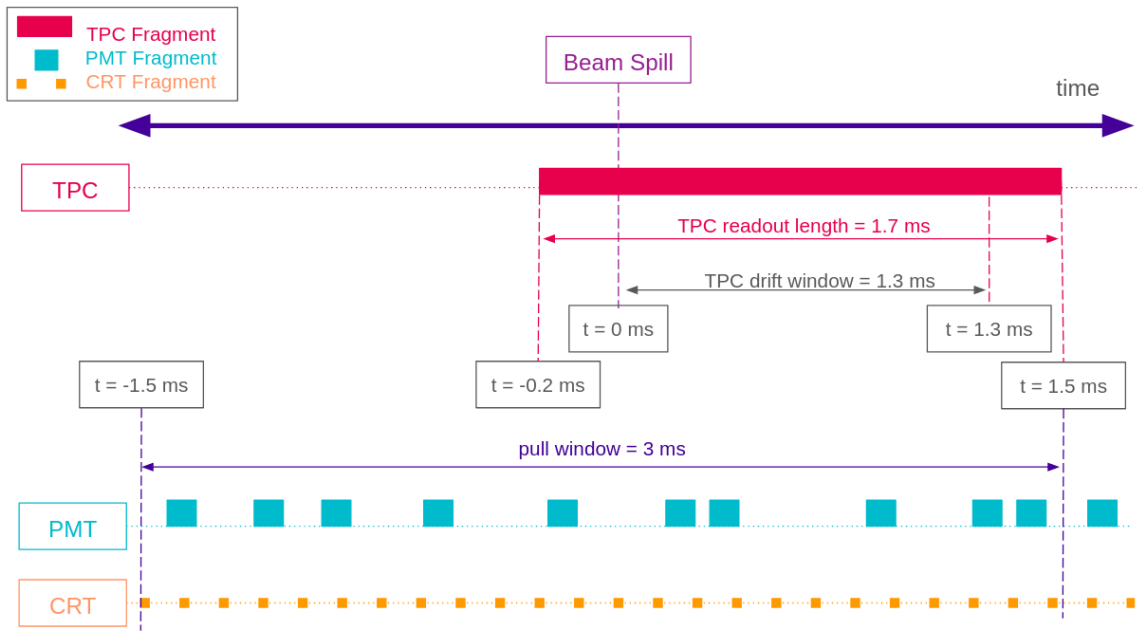


Fig. 4.8 Diagram depicting the chronological structure of a physics event.

Moreover, PMT and CRT fragments are shown in blue and orange respectively in Fig. 4.8. The fragment readout lengths from the PMT and CRT readouts are much shorter compared to TPC fragments, $\mathcal{O}(10 \mu\text{s})$ and $\mathcal{O}(10 \text{ ns})$ respectively. For a single physics event, in contrast to only a single ETRIG issued to the TPC readouts, multiple FTRIGs are issued to the PMT readouts throughout the beam spill to produce multiple fragments of PMTs. Similarly, CRT readouts are self-triggered independently and produce multiple fragments on the flight. PMT and CRT fragments that have timestamps within 1.5 ms before and after the beginning of the beam spill are packaged together with the TPC fragment to form a physics event.

Here in Fig. 4.8, a time symmetry can be seen in the chronological structure of a physics event at SBND. This is due to the different physics characteristics of photon

signals, detected by the CRTs and PMTs, and electron signals, detected by the TPC wires. Specifically, a photon produced in a CRT scintillator strip takes approximately 5 ns to travel from the far end of the strip until reaching a SiPM. Similarly, a photon produced in the TPC takes a maximum of 15 ns to propagate from a scintillation location to a PMT. In contrast, an ionisation electron produced takes 1.3 ms to fully drift from the cathode to the anode. This shows that photon signals propagate approximately six orders of magnitude faster than electron signals and consequently, need to be digitised and read out earlier.

4.3 The Booster Neutrino Beam

The SBND detector directly measures the neutrino flux coming from the BNB. Comprehensive technical details of the BNB can be found in Ref. [96]. The BNB operates by extracting protons with a kinetic energy of 8 GeV from the Booster synchrotron in spills made up of 7 to 11 pulses in a row at a frequency of 15 Hz, averaging to a rate of ~ 5 Hz. Each spill delivers 5×10^{12} protons within a beam spill window lasting 1.6 μ s. The structure of a beam spill structure consists of 81 neutrino buckets, with a Gaussian width of 1.308 ns and a spacing of 19 ns [97]. Fig. 4.9 depicts the beam bucket structure as measured by the CRTs of SBND, which was set up as a beam telescope to collect data from the BNB in 2017–2018 [94]. Neutrino buckets can be seen distinctively in the distribution, indicating that the BNB structure can be resolved with sufficient timing resolution. The timing resolution of the CRT readouts is $\mathcal{O}(1)$ ns, which will be demonstrated later in Section 7.2.

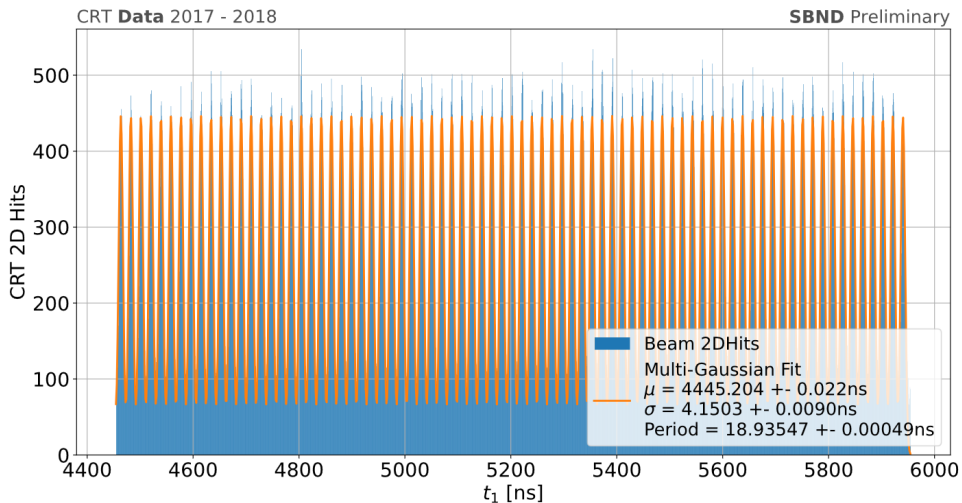


Fig. 4.9 Plot showing the BNB beam bucket measured by the CRTs of SBND during 2017–2018 [94].

4.3 The Booster Neutrino Beam

The particle production process in the BNB is illustrated in Fig. 4.10. Initially, protons are injected into the Booster synchrotron and accelerated from 400 MeV to 8 GeV kinetic energy, as shown by the red arrows. Their intensity is measured by two steroids, while their positioning and timing are monitored by beam position monitors and Resistive Wall Monitors (RWM) [98]. Upon exiting the Booster, the proton beam traverses focusing and defocusing quadrupole and dipole magnets before being focused onto the target of the BNB.

The protons collide on the target to produce secondary mesons, as shown by the blue arrows. The target consists of a beryllium cylinder measuring 71.1 cm in length and 0.51 cm in radius. The choice of beryllium was motivated by its replaceable ability in the event of radioactivity issues, as well as its ability to facilitate sufficient energy loss via an air cooling system. The target is placed inside a pulsed horn system, which acts as a 170 kA electromagnet to focus the secondary mesons. The polarity of the horn can be adjusted to focus positive (negative) mesons for operation in neutrino (antineutrino) mode. Downstream of the horn assembly, a concrete collimator absorbs particles that do not contribute to the neutrino flux, thereby reducing radiation elsewhere in the beamline.

The focused mesons then propagate through an air-filled cylindrical decay region spanning 45 m, depicted as the orange box. It is then terminated by a steel and concrete absorber located 50 m from the upstream face of the target, depicted as the purple box. Secondary mesons decay into tertiary neutrinos within the decay region, while long-lived muons are absorbed by the absorber. Subsequently, tertiary neutrinos traverse through a dirt region before reaching the SBND detector, as shown by the pink arrows.

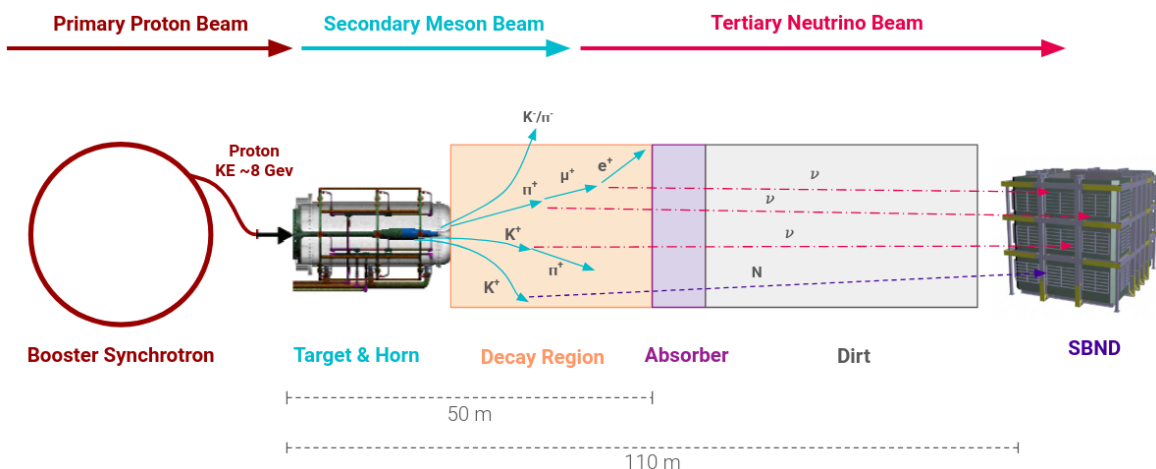


Fig. 4.10 Diagram showing the particle production in the BNB.

The production of HNLs from kaon decays alongside neutrinos is also shown as the purple arrow.

The beam is simulated using GEANT4 with different tunings for the composition of the secondary mesons and hadrons produced from $p + Be$ interactions [96]. The π^\pm production is tuned to the HARP data set using Sanford-Wang parametrisation. The K^+ production is extrapolated to the global K^+ production data using Feynman scaling-based parametrisation, and further constrained by SciBooNE's direct measurements of K^+ production from the BNB [4]. Other secondary hadrons and mesons such as p , n and K^- are modelled using the MARS hadronic interactions, however, their overall contribution to the neutrino flux is small. Interaction cross sections of $p/n + Be$ and $\pi^\pm + Be$ are also incorporated in flux predictions [99].

Fig. 4.11 depicts the primary contributors to the secondary meson fluxes at the BNB, namely pions and kaons. A small fraction of muons resulting from pion decays also contribute to the fluxes. These fluxes are shown for the BNB operating in neutrino mode, mainly composed of positively charged mesons. As discussed in Section 2.2, the flux

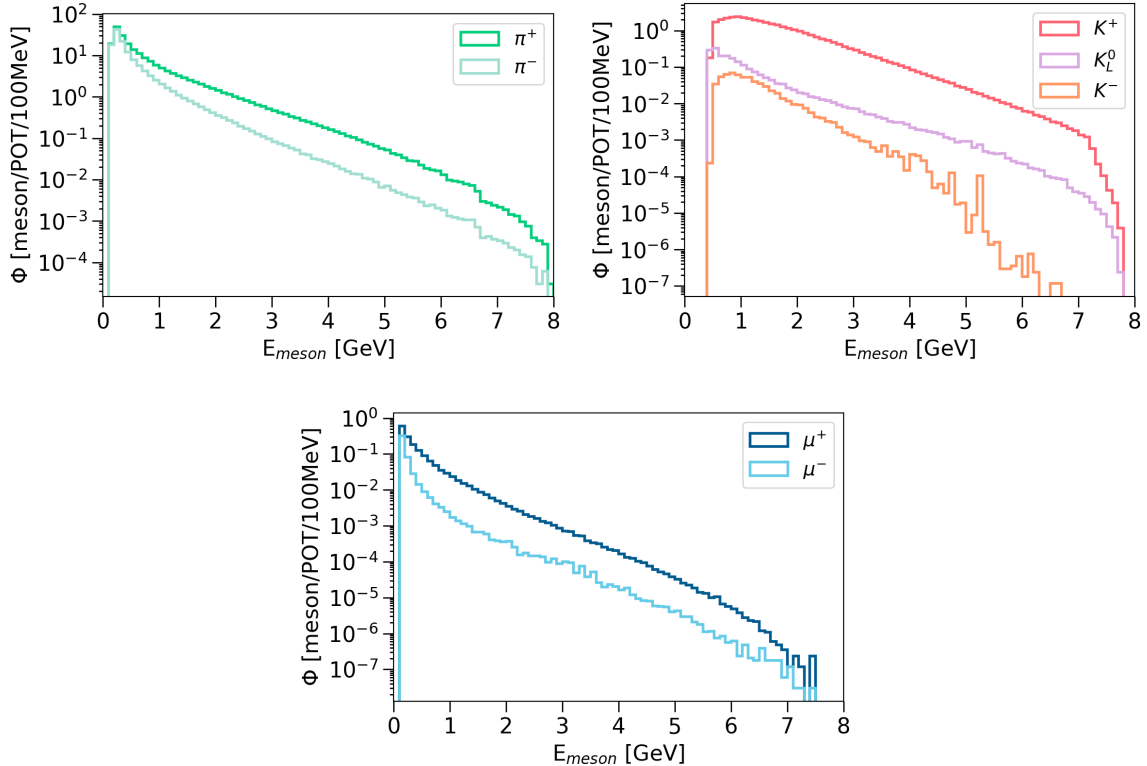


Fig. 4.11 Simulated fluxes for the secondary mesons produced in the BNB.

4.4 Concluding Remarks

of HNL comes from K^+ decays, which has energy peaking at $0.5 \sim 1$ GeV. Ref [96] has highlighted significant uncertainties in the K^+ production cross sections within this energy range. However, results from the SciBooNE experiment have demonstrated the validity of extrapolating higher energy K^+ data to the 1 GeV region using Feynman scaling [4].

The simulation of the neutrino flux at the front face of SBND is depicted in Fig. 4.12, shown for different flavours of neutrinos. The flux is predominantly composed of ν_μ ($\sim 90\%$), followed by $\bar{\nu}_\mu$ ($\sim 9\%$), while the combination of ν_e and $\bar{\nu}_e$ contributes less than 1%. Pion production is the dominant mechanism for both ν_μ and $\bar{\nu}_\mu$, followed by kaon and muon production. In the case of ν_e , muons produced from pion decay are the primary source at low energies, while kaon production becomes the dominant mode at higher energies. Finally, $\bar{\nu}_e$ mainly originates from K_L^0 production.

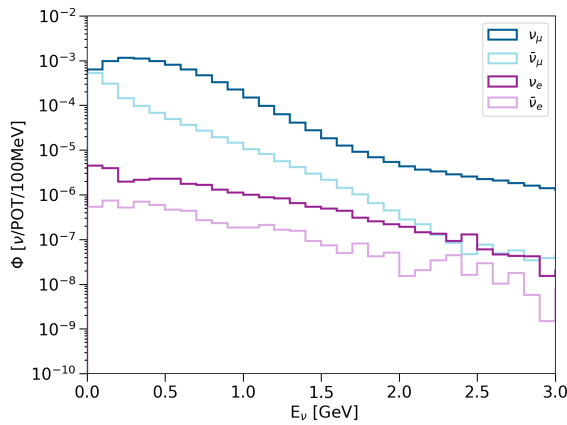


Fig. 4.12 Simulated neutrino fluxes at the front face of SBND.

4.4 Concluding Remarks

The SBND experiment, together with other experiments in the SBN program, aims to conclusively address the low energy excess observed across experiments such as LSND, MiniBooNE, and other nuclear reactor and solar neutrino experiments. SBND will play a crucial role in constraining systematic uncertainties by measuring large statistics of the unoscillated neutrino flux from the BNB. Additionally, SBND has a rich physics program covering neutrino cross section measurements and searches for BSM physics. Of particular relevance to this thesis, SBND aims to establish competitive limits on the mixing of HNLs within the probable mass range from the BNB.

The hardware of SBND comprises three key detection subsystems: the TPC, the PDS, and the CRT system, alongside the hardware triggering subsystem. Each of these subsystems has dedicated readout electronics, which are managed by a complex DAQ system. The SBND detector measures the flux coming from the BNB, which has a distinctive bucket structure which can be resolved with a sufficient timing resolution $\mathcal{O}(1 \text{ ns})$. This feature can be exploited in the search for HNLs at SBND since the mass of HNLs results in late arrival at the detector compared to the neutrino buckets. The following Chapter 5 will delve into SBND’s simulation framework that enables the exploration of the detector physics capabilities in the BSM regime.

Chapter 5

Simulation Framework Of SBND

Many modern particle physics experiments heavily rely on simulations to study the physics capabilities of the detector, to develop physics analysis tools as well as to relate experimental data to an underlying theoretical model they attempt to probe. The most common technique in simulation is Monte Carlo (MC), by random sampling from probability density functions (PDFs). PDFs can be modelled from theories, driven from experimental data or a combination of both. The search for Heavy Neutral Leptons (HNLs) at SBND presented in this thesis employs simulated MC samples mimicking data. This enables an exploration of the detector physics capabilities in the regime of physics beyond the Standard Model.

The following chapter provides a detailed description of the simulation framework of SBND to output simulated products that ideally represent real data. The chapter begins with an overview of the framework in Section 5.1. Following that, Section 5.2 includes details of the generator employed to generate HNLs, of which the development was contributed by the author. The summary of the generators of SM neutrinos and cosmic muons is given in Section 5.3. Section 5.4 covers the simulation of energy deposition as particles propagate through the detector and the detector response to the deposited energy. Finally, the chapter is concluded in Section 5.5 with some remarks.

5.1 Overview of The Simulation Framework

Similar to many other LArTPCs, the software framework for simulation, reconstruction and analysis of SBND is provided by the LArSoft framework [100]. The framework was built for neutrino experiments sharing the same common feature of having LArTPCs, while

still allowing for detector-specific customisation. This enables easy sharing of software tools across many collaborations including ArgoNeuT, MicroBooNE, ICARUS, SBND and DUNE. For example, the generator used to simulate HNLs, to be discussed in the next section, has been developed and shared across the SBND and ICARUS collaboration.

The simulation workflow of SBND under the LArSoft framework is depicted in Fig. 5.1. The process begins with a generator to produce primary particles that enter the detector, as shown by the purple box. The primary particles can be final states of neutrino interactions, cosmic muons or BSM particles depending on the type of generator. The propagation of the primary particle inside and outside the detector, and the resulting energy deposition is simulated using the Geant4 toolkit [101], as shown by the green boxes. For interactions inside the detector, the charge and light yield are calculated from the energy deposition. Ionisation electrons are propagated through the detector to the wire planes using the Wirecell toolkit [5], as shown by the red boxes. Scintillation photons are propagated to the photodetectors using a combination of a semi-analytical model and an optical library [68], as shown by the blue boxes. For interactions outside of the detector, only the energy depositions within CRT strips are converted into light yield, as shown by the orange box. The detector response is then simulated for each detector subsystem. By the end of this stage, the outputs from each detection subsystem ideally represent real data.

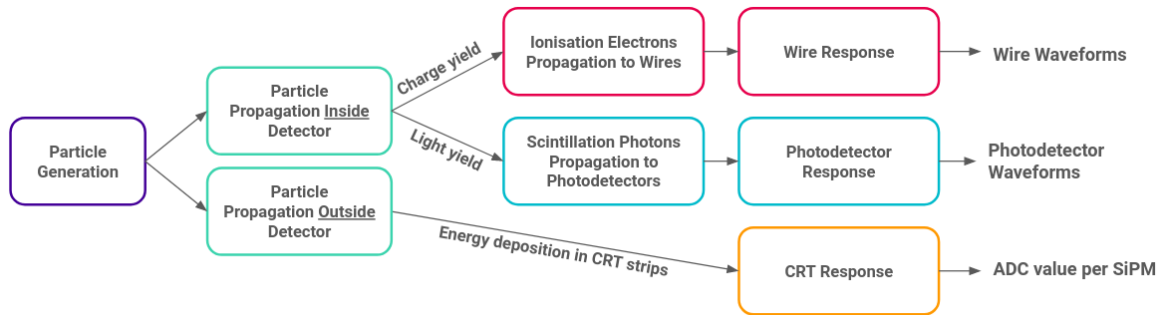


Fig. 5.1 Overview of the simulation framework of the SBND detector.

5.2 HNL Generator: MeVPrtl

BSM particles are generated using a generator called MeVPrtl, which was developed as a joint effort by collaborators from both ICARUS and SBND experiments. There are several BSM models implemented in the MeVPrtl generator, including HNLs, Higgs portal

5.2 HNL Generator: MeVPrtl

scalars [102] and heavy QCD axions [103]. It is a modular generator, allowing for easy adaptations for different beam sources and detectors, as well as a direct interface with the existing LArSoft framework. The workflow of the MeVPrtl is broken down into 4 stages, as illustrated in Fig. 5.2. The generator begins with taking an input of meson fluxes, representing the particles produced from a beam source. It then simulates the meson decaying to a BSM particle. The BSM particle is propagated to the detector and decays back into SM observables.

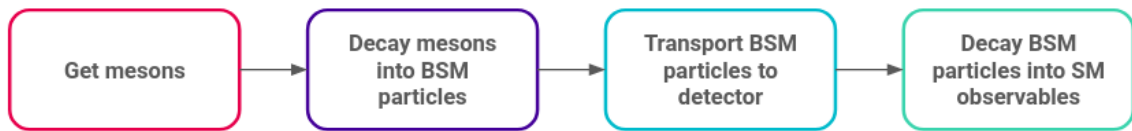


Fig. 5.2 Overview of the workflow of the MeVPrtl generator.

For generating HNLs coming from the BNB, the generator begins with sampling the K^+ fluxes of the BNB (See Fig. 4.11, Section 4.3). Instead of decaying into SM neutrinos, the kaons decay into HNLs, with the branching ratio defined by Eq. 2.7 (See Section 2.2). The daughter HNL and lepton are simulated using the two-body decay at rest in the centre of mass frame of the parent kaon and then boosted to the parent's lab frame by Lorentz boost. Due to HNLs having relatively high mass, the Lorentz boost results in HNLs having less transverse momentum than the SM neutrinos, travelling preferably to the parent kaon direction. The Lorentz boost can also flip the directions of HNLs that are emitted backwards, mostly originating from low energy kaons [104].

HNLs are then propagated to the detector by the ray tracing method, which forces HNLs to hit the SBND detector by picking a direction that impinges the particles at the detector's front face. The acceptance angle of HNLs to hit the detector is very collimated at $<\sim 5^\circ$, implying that only very forward-going HNLs are most likely to intersect the detector.

The total energy spectra of HNLs arriving at the SBND detector are depicted in Fig. 5.3 for the mass range between 140 and 260 MeV. The spectra plotted here, and all subsequent kinematics plots in this section, are labelled *true*, indicating they are at the truth level and not yet passed through detector simulation and reconstruction. The spectra are normalised to the same coupling $|U_{\mu 4}|^2 = 1 \times 10^{-7}$ and an exposure of 1×10^{21} POT projected for 3 years of data taking. At the same coupling, the expected HNL rate decreases with lower mass since the branching ratio of $N \rightarrow \nu\pi^0$ decreases with lower mass (See Fig. 2.3 Section 2.3). Additionally, given that the K^+ total energy spectra peak at 0.5 GeV and decrease at higher energy (See Fig. 4.11, Section 4.3), the HNL spectra also concentrate at

< 0.5 GeV, and substantially decrease at higher energy. A peak near zero can also be seen in all energy spectra across the mass range, corresponding to HNLs resulting from Kaon Decay At Rest (KDAR). Finally, the kinetic energy of HNLs is expected to decrease with higher mass. This is due to HNLs coming from a kaon decay and therefore, the lighter the HNL mass, the more kinetic energy is available.

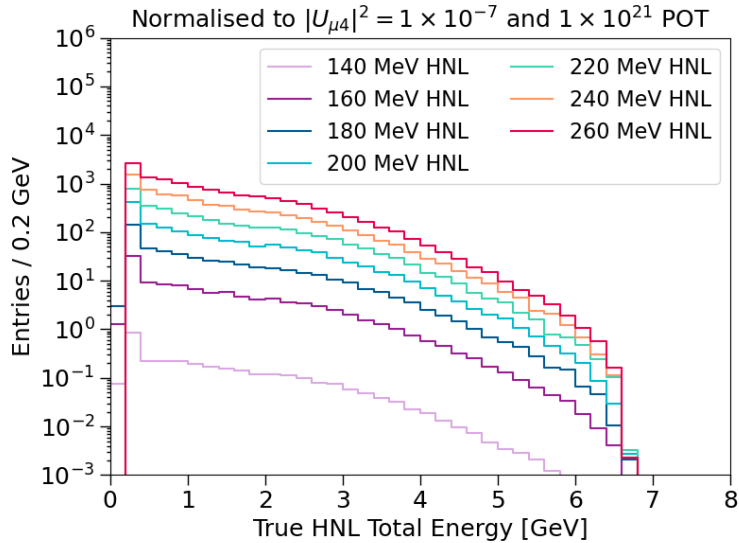


Fig. 5.3 Simulated energy spectra of HNLs decaying inside SBND.

Upon their arrival at the detector, HNLs decay back into the SM observables. For the $\nu\pi^0$ final state, the width of the decay is defined by Eq. 2.10 (See Section 2.3). The kinematics of the decay products are simulated for HNLs isotropically decaying in the rest frame and then boosted to the lab frame by Lorentz boost.

Fig 5.4 shows the true momenta and angle to the beam distributions of the π^0 . The plots are area-normalised for comparison across the HNL mass from 140 to 260 MeV. The peak in the momenta distribution at low GeV and the peak in the angular distribution at high angle are from the π^0 resulting from low energetic HNLs from KDAR. Moreover, the momenta distribution of the π^0 decreases with increasing HNL masses. This is due to the decreased boosting of HNLs at higher masses being less energetic. As a result, the angle to the beam of the π^0 also widens with heavier HNLs. However, at the heaviest HNL mass of 260 MeV considered in the search, the π^0 is still very collimated since its angular distribution concentrates in the region $< 20^\circ$. Therefore, the di-photon showers from the HNL-originated π^0 are expected to be more forward-going than those originating from SM neutrinos.

5.2 HNL Generator: MeVPrtl

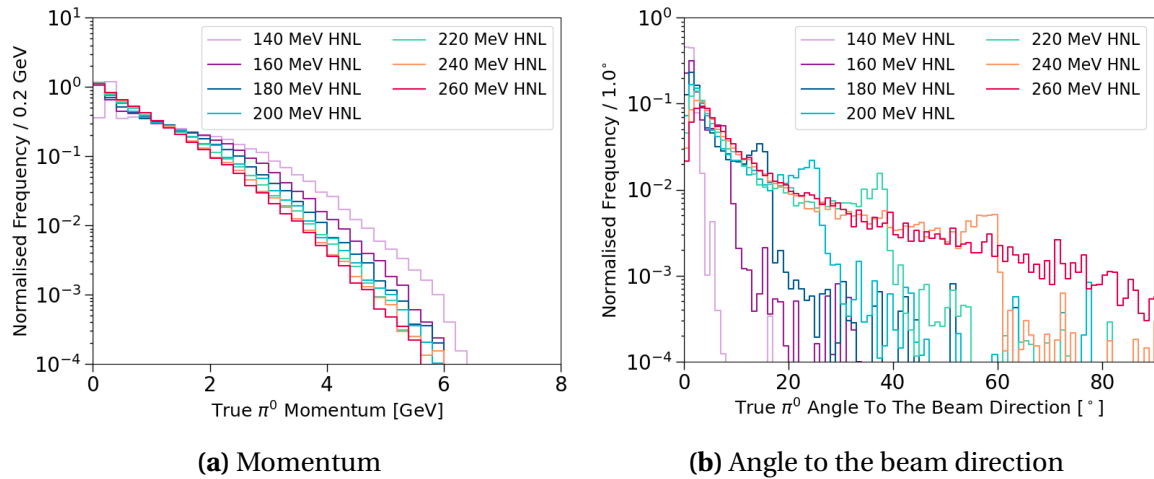


Fig. 5.4 Kinematics distributions of π^0 from HNLs decaying inside SBND.

The timing delay between HNLs compared to SM neutrinos due to HNLs being more massive can be exploited in the search for HNLs at SBND. The components that make up the time of flight for an HNL or a SM neutrino produced from the BNB and propagating to the SBND detector are illustrated in Fig. 5.5. The first component is the spill time of the protons from the Booster synchrotron, t_{spill} , as shown by the red arrow. The structure of t_{spill} is the beam bucket structure made up of 81 Gaussian buckets with a width of 1.308 ns and a spacing of 19 ns, which is the same for both HNLs and SM neutrinos. Details of the beam structure is given in Section 4.3.

The second component is the time of the secondary mesons, t_{meson} , as shown by the blue arrow. This is the period from when the mesons are produced until they decay into HNLs or SM neutrinos. This time accounts for the duration that the mesons travel down the decay pipe, and might interact, re-scatter or decay into other mesons. In the case of HNLs, t_{meson} is primarily the time of flight of the charged kaon K^+ before decaying into an HNL. On the other hand, SM neutrinos come from a variety of parent mesons t_{meson} . In both cases, t_{meson} introduces some smearing to the nanosecond-bucket structure of t_{spill} .

The last component is the time of flight of the SM neutrino or the HNL from the creation point to the interaction point inside the SBND detector. In the case of SM neutrinos, since they are nearly massless, their velocity can be approximated as the speed of light. Then, the time of flight of the SM neutrino is:

$$t_v = \frac{d_v}{c}, \quad (5.1)$$

where d_ν is the distance of a neutrino from the creation point to the interaction point inside the detector. Meanwhile, HNLs are massive and therefore, travel at a velocity $v_N < c$. The time of flight of the HNL is:

$$t_N = \frac{d_N}{v_N}, \quad (5.2)$$

where d_N is the distance of a HNL from the creation point to the decay point inside the detector. Additionally, since the energy of the HNL decreases with its mass, the heavier it is, the slower its velocity. Thus, heavier HNLs arrive even later compared to lighter HNLs.

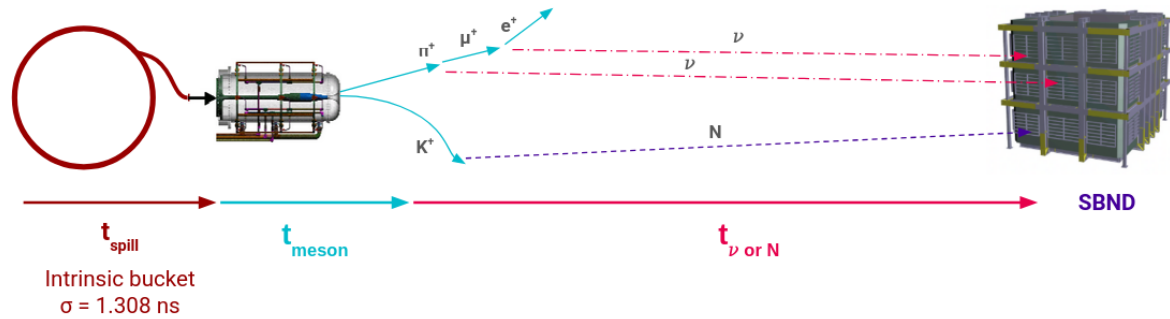


Fig. 5.5 Diagram depicting the time of flight of a particle from its production in the BNB to its detection in the SBND detector.

The advantage of the MeVPrtl generator is the consistency of simulating the time of flight of HNLs to the GENIE generator for simulating SM neutrinos. Fig. 5.6 shows the true simulated arrival time of SM neutrinos, in the dashed grey line, and 260 MeV HNLs, in the solid red line, at the front face of the SBND detector, recovering the beam spill structure of the BNB. The plot is area-normalised to enable the comparison between the two particles. Since SM neutrinos travel nearly at the speed of light, less smearing is introduced and the timing distribution shows sharp Gaussian peaks. On the other hand, HNLs travel slower

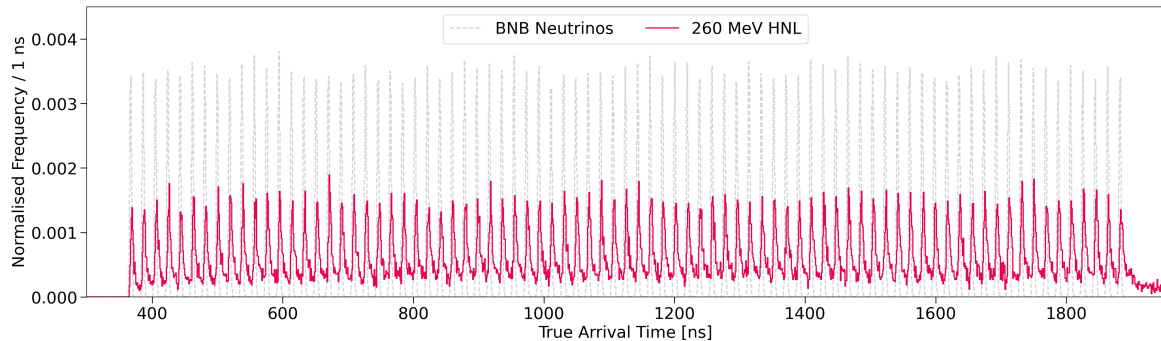


Fig. 5.6 Arrival time distribution at the front face of the SBND detector for SM neutrinos and HNLs.

5.3 SM Generators

and add additional smearing and delay tails to the Gaussian peaks. For clarity, shown in Fig. 5.7, is the result of 81 Gaussian peaks overlaid into 1 peak by taking the modulus of 19 ns. The timing distribution of the HNLs shows a clear difference from that of SM neutrinos, where delay tails on either side of the Gaussian peak can be seen. Between the mass of 140 to 260 MeV, the delay tails however do not increase significantly with mass.

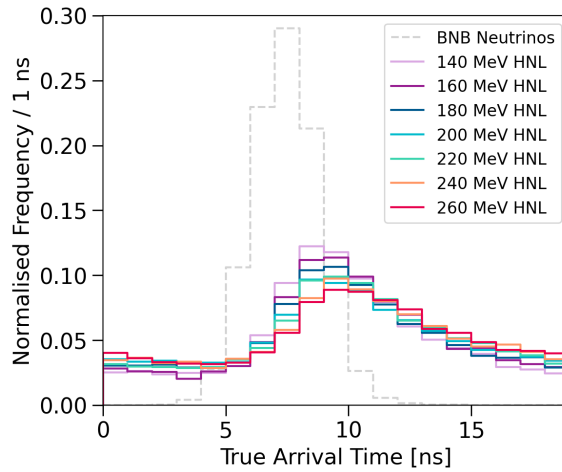


Fig. 5.7 Arrival time distribution for SM neutrinos and HNLs after applying a modulus of 19 ns .

5.3 SM Generators

For generating backgrounds from SM neutrinos and cosmic muons, the two generators are GENIE [105] and CORSIKA [106] respectively. Each generator will be discussed in Section 5.3.1 and Section 5.3.2.

5.3.1 Neutrino Generator: GENIE

SM neutrino interactions are generated by the GENIE generator [105], which provides a selection of theoretical and empirical models for different physical processes. These models can be combined into a *tune*, which is a set of optimised parameters used in the simulation for a better agreement between model and data. The GENIE tunes are made using an extensive dataset of electron, neutrino and hadron scattering experiments. The SBND collaboration is planning to use a tune that was specifically developed to serve as

a baseline model for the SBN and DUNE oscillation analysis. Details for the basis of the tune can be found in Table 1 in Ref. [107], with ongoing developments of tuning choices documented in Ref. [108].

In general, GENIE first selects a nuclear model that describes the momenta and potential energy of the nucleon to model nuclear effects. Then, the neutrino flux and the integrated cross section model are used to compute the probability that a neutrino interaction occurs. The differential cross section is then used to determine the type of neutrino interaction and the kinematic range. The neutrino interaction types include quasi-elastic, resonant, coherent, deep inelastic and ν -e elastic scatterings. In addition, neutrino interacting with an argon nucleus can produce hadrons within the nucleus. The hadrons propagate through the nucleus, interacting via different modes such as charge exchange, elastic scattering, absorption and pion production. Consequently, the hadron-nucleus interaction modifies the final state particles and their kinematics. Thus, the hadron transport interaction model is crucially important for predicting the final observables of neutrino interactions.

In addition to the tune, GENIE also provides a re-weighting scheme to evaluate the systematic uncertainties for a model chosen in the tune. Due to the scarcity of neutrino interaction data, particularly for $\nu - Ar$ interactions, the uncertainties in cross section modelling tend to be very large. The neutrino interaction re-weighting scheme and the resulting systematics uncertainties will be discussed in detail in Section 10.1.4.

At SBND, GENIE simulates neutrino interactions occurring both inside and outside of the detector volume, with a boundary defined in Fig. 5.8. All interactions occurring inside the detector volume are strictly kept, as shown by the dark blue box. Outside of the detector, a buffer volume is defined as 5 m surrounding the detector volume, as shown by the light blue box. An additional Rockbox volume is defined by extending the buffer volume backwards in the beam direction (z -axis) up to 15 m in front of the buffer volume, as shown by the orange box. Both these volumes are referred to together as the *Rockbox* volume in this thesis. Neutrino interactions within this volume are kept because their products can potentially deposit energy in the detector. These interactions are referred to as *dirt* neutrinos and constitute a significant background to the HNL search. The background rejection of dirt neutrinos will be covered in Chapter 9.

5.3 SM Generators

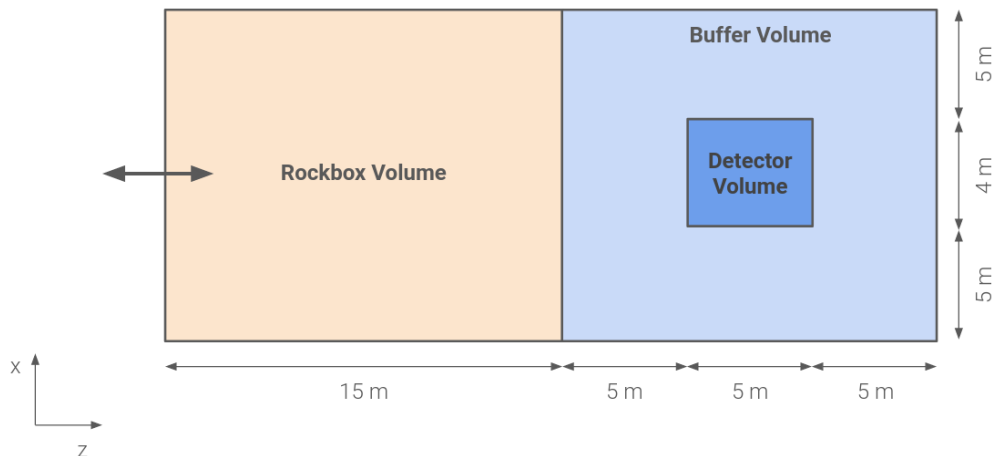


Fig. 5.8 Volume boundary defined by the GENIE generator to simulate neutrino interactions occurring inside and outside of the detector volume.

5.3.2 Cosmic Generator: CORSIKA

Cosmic interactions are simulated using the CORSIKA generator [106]. The generation begins with producing high energy primary particles incident in the Earth's atmosphere, of which only primary protons are kept. The primaries are then propagated through the atmosphere, interacting with the air to produce secondary hadrons that decay into long-lived particles reaching the Earth's surface. Within the SBND simulation geometry, this surface is specified to be just above the roof of the detector building. The surviving particles are then propagated to the SBND detector.

From a triggering perspective, there are two types of cosmic muons as follows

- **In-time** cosmic muons cross the detector at the same time as SM neutrinos being present inside the detector, such that the muons are *inside* the beam spill window. The cosmic muons produce enough light to induce a beam trigger.
- **Out-of-time** cosmic muons occur regardless of the trigger conditions. The muons cross the detector *outside* the beam spill window but within the readout window.

However, at the time of writing, triggering simulation is currently a work in progress at SBND and there not being simulated in the workflow. Only the timing requirement is simulated to keep only cosmic muons occurring within the readout window. The simulation currently does not accurately reflect the cosmic rate once factoring triggering conditions and therefore, comparison to data is necessary.

Being a surface-level detector, it is vitally important to understand the cosmic background at SBND due to the exposure to a high cosmic rate. Once SBND is operational, a particularly useful measurement is the rate of cosmic muons that cause a beam trigger, however, in the absence of the beam. This is equivalent to measuring the rate of cosmic muons that produce sufficient energy inside the detector to mimic SM neutrino interactions. This measurement allows for validation against the CORSIKA generator. Moreover, it also provides an expected cosmic rate given a triggering condition, which can be subsequently added to the simulation framework to better constrain the cosmic background.

5.4 Particle Propagation and Detector Response Simulation

After the generation stage of the simulation workflow, simulated particles are propagated through the detector and deposit energy, producing ionisation electrons and scintillation photons. The detector response to the ionisation electrons and scintillation photons is subsequently simulated, mimicking data. Section 5.4.1 first covers the simulation of particle propagation and energy deposition. Following that, Section 5.4.2, 5.4.3 and 5.4.4 provides a description of the simulation of the TPC, PDS and CRT response.

5.4.1 Particle Propagation Simulation

Once a particle is simulated inside the detector, it is propagated through the detector using the Geant4 toolkit [101]. Geant4 propagates the particle by each step dx , where the step length is randomised and capped at 0.3 mm (one order of magnitude less than the wire pitch). At each step, physics processes are simulated, such as energy deposition, interaction, decay and so on. The step propagation also accounts for the electric field distortion caused by the space charge effect due to high exposure to cosmic muons.

The main physics process for energy deposition in the detector is ionisation by charged particles. Similarly to the theory detailed in Section 3.2, the Geant4 toolkit simulates the ionisation process following the Bethe-Bloch formalism tuned to data [109]. The number of ionisation electrons and scintillation photons from the deposited energy is computed using the ModBox recombination model with ArgoNeuT parameters [60], and the charge-light anti-correlation from Eq. 3.2 and 3.3. Further discussion about the simulation of recombination, and the impacts of delta ray fluctuations on recombination will be detailed in Section 8.2. The result from the Geant4 toolkit is a complete set of charge and

light yields along the primary particle trajectories through the detector and the daughter particles produced from the primary.

5.4.2 Wire Response Simulation

Ionisation electrons are simulated to drift towards the wire planes using the WireCell toolkit [5]. The simulation transports the electrons and introduces smearing due to detector effects for transporting electrons through liquid argon under an electric field, which is previously discussed in Section 3.3.1. This includes charge attenuation due to impurities, longitudinal and transverse diffusion and finally, space charge effect.

Once drifting electrons arrive at the wire planes, a convolution of the field response and the electronic response is performed. The field response describes the current induced on wires due to ionisation electrons drifting past the induction planes. The electronic response describes the amplification and shaping of each wire's induced current by pre-amplifiers. The response functions are in two dimensions, time versus wire. This is to account for the long range charge induction effect on wire signal shapes. A digitisation step is then applied to produce an ADC-level, time-domain waveform for each wire channel. The waveform is then smeared by the ADC resolution, voltage range and baseline specification of the wire readouts. Finally, inherent electronic noise is added to the waveform to better match to observed data. MC waveforms at this stage should represent real data waveforms recorded by the wire readouts.

5.4.3 Photon Detection System Response Simulation

Scintillation photons are simulated to propagate to optical detectors, accounting for transport effects previously detailed in Section 3.3.2 such as Rayleigh scattering and boundary effects. In-depth details of the light simulation can be found in Ref. [68]. The simulation uses a combination of a semi-analytical model described in Ref. [110], and an optical library model available in LArSoft. The choice of which model to use depends on the location of the photon production. The semi-analytical model is used for those produced inside the active volume of the SBND detector, whilst the optical library model is used for those that originate outside of this volume.

The semi-analytical model calculates on-the-flight the geometrical aperture for each optical detector to a scintillation point, given that the emission of scintillation photons is isotropic. The model also extends to both direct visible photons and also reflected

VUV photons. Corrections for photon transport effects are applied to the number of photons detected by an optical detector. However, the semi-analytical method is limited by the geometrical information and does not include scintillation outside of the detector volume, for example, cosmic muons crossing behind an optical detector can produce non-negligible photons. Since PMTs are the primary subsystem for triggering, it is vital to consider this second-order contribution of photons for triggering studies. The optical library stores information on the fraction of incident photons for each optical detector for a given scintillation location, which can be looked up for any detector-location pairs during simulation.

For each type of optical detector, PMTs and X-ARAPUCAs, a respective photon detection efficiency is applied to the number of detected photons. Signal amplification and digitization are simulated, converting photons into an output signal known as a single electron response. Then, signal shaping such as overshoot and undershoot due to the AC circuit of the optical detectors are applied. Finally, random fluctuation in the signal integral and non-linearity response at high light intensities are applied to better mimic data. The final output is MC optical waveforms for each type of optical detector, mimicking data.

5.4.4 Cosmic Ray Tagger Response Simulation

The energy deposition outside of the cryostat from the Geant4 simulation stage in Section 5.4.1 is considered if it is within CRT strips. It is converted into photons within a strip and propagated down optical fibres towards the SiPMs for detection. The collection efficiency per SiPM is accounted for by dividing the light yield between the fibres on either side of the strip, based on the lateral position of the energy deposition within the strip. Propagation effects and signal attenuation are also simulated. Finally, the electronic response is simulated for the CRT readout, by assessing if a pair of SiPMs within a strip goes above a threshold within a pre-defined coincidence window. To better mimic the readout electronics of CRTs that process 32 SiPMs at a time, MC outputs of CRTs are in a group of 32 ADC values, where each value corresponds to a SiPM.

5.5 Concluding Remarks

This simulation framework of SBND is an end-to-end process, starting from the particle production, to its energy deposition and subsequently, the detector response to the energy

5.5 Concluding Remarks

deposition. The MC output of the simulation mimics data, providing the foundation to perform studies to understand and improve the detector performance and physics capabilities as well as compare against theoretical models. For example, the upcoming Chapter 6 will provide a description of the reconstruction framework at SBND, of which many algorithms have been developed using MC samples. Furthermore, the calibration studies presented in Chapter 8 were carried out using MC samples of protons and muons to better understand particle-dependent energy deposition. Finally, the search for HNLs presented in the two final Chapters 9 and 10 was also performed using MC samples to explore the capability of SBND in the BSM regime.

Chapter 6

Reconstruction Framework Of SBND

The process of extracting physics quantities from the raw data recorded from an experiment is known as reconstruction. At SBND, the physics characteristics of a particle can be reconstructed using multiple detection subsystems. For instance, a contained particle inside the TPC might deposit energy resulting in only waveforms recorded by the TPC wire planes and the PDS, meanwhile, an exiting particle might deposit additional energy in the CRT walls surrounding the TPC. For a given particle, the TPC reconstruction can extract various quantities describing its topology, calorimetry and kinematics using charge information. The PDS reconstruction can provide additional high resolution timing and calorimetry using light information. The CRT reconstruction can indicate if the particle is fully contained inside the detector. As a result, the reconstruction variables from all three detection subsystems are complementary to each other.

This chapter provides a summary of the reconstruction framework at SBND. Firstly, Sec. 6.1 gives an overview of the reconstruction workflow for each detection subsystem. The following Sec. 6.2 includes the details of the TPC reconstruction workflow from start to end. The reconstruction of the PDS and CRT subsystem are summarised in Sec. 6.3. Descriptions of some high level analysis tools using the reconstruction variables collectively from each detection subsystem are included in Sec. 6.4. Finally, the chapter is concluded in Sec. 6.5 with some remarks.

6.1 Overview of The Reconstruction Framework

Each detection subsystem in SBND requires a dedicated reconstruction workflow. An overview is illustrated in Fig. 6.1. The TPC reconstruction workflow is shown by the red

boxes. This process begins with raw wire waveforms going through the signal processing performed by the Wirecell tool kit [5]. This is followed by a hit finding algorithm to identify hits on the waveform. Output hits are then used by the Pandora package [6] to produce a 3D-reconstructed interaction, denoted as a *slice*. The PDS reconstruction workflow also follows a similar process to the TPC, as shown by the blue boxes. A waveform deconvolution is first performed on raw PDS waveforms to filter noise. Then, a hit finding algorithm identifies optical hits on the waveform and reconstruction is performed on the hits. The equivalent output to the TPC-reconstructed interaction from the PDS reconstruction is referred to as a *flash*. Finally, the reconstruction for the CRTs is much simpler compared to the other two subsystems, consisting of only a hit finding and a reconstruction algorithm, as shown by the orange boxes. The reconstruction variables from each detection subsystem are produced independently and can be matched together if they originate from the same interaction. The variables can also be combined and input into different high level analysis tools to extract more complex properties of the underlying interaction.

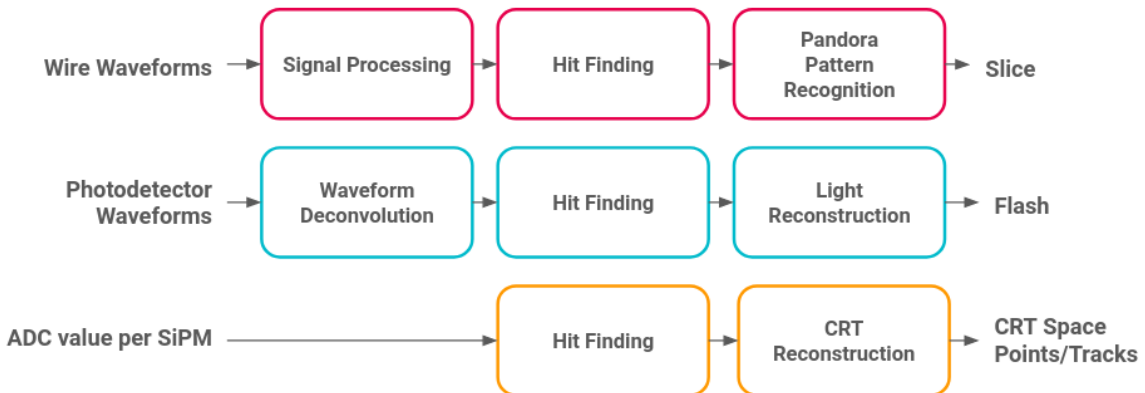


Fig. 6.1 Overview of the reconstruction workflow of the SBND detector.

6.2 Time Projection Chamber Reconstruction

This section covers the TPC reconstruction workflow, starting with Sec. 6.2.1 on the signal processing. Sec. 6.2.2 and 6.2.3 then detail the hit finding and Pandora reconstruction. Finally, Sec. 6.2.4 delves into the track and shower separation algorithm of Pandora.

6.2.1 Signal Processing

Signal processing is the first crucial step of TPC reconstruction, which is to deconvolve digitised raw waveforms and account for detector effects such as noise, electronics response and field response. At SBND, signal processing is implemented using the WireCell tool kit [5]. The tool has been used by other LArTPC experiments such as MicroBooNE [5] and ProtoDUNE [111].

Fig. 6.2 shows an illustration of the signal processing steps. In grey is the *true* ionisation charge deposited on a wire, simulated without any detector effects applied. In red is the raw waveform resulting from the deposited charge, convolved with noise, electronics and field response. The first step is noise filtering to remove the excess and correlated noise from raw waveforms. Then, the measured charge is deconvolved from the electronics and field response to recover the original charge deposited on the wire, as shown in orange. The deconvolution is 2D, where response functions consider the time response of a single wire as well as of neighbouring wires. This step is particularly important for the induction planes to convert bipolar into unipolar signals, such that the integral of the waveform can be used for charge estimation.

High frequency filters are applied to attenuate noise that is artificially amplified, using Gaussian and/or Weiner filters depending on whether the signal is unipolar or bipolar. The example here is a bipolar waveform and therefore, has both Gaussian and Weiner filters applied, shown in yellow and green respectively. Then, low frequency filters are utilised for peak finding and local baseline removal, as shown in blue. Finally, the deconvolved waveform per wire after baseline removal is shown in purple, which closely resembles the true charge as shown in grey. This demonstrates the excellent performance of the signal processing chain to de-tangle detector effects from raw waveforms and recover the original deposited charge.

Fig. 6.3 depicts event displays of a simulated neutrino event as seen by wires on the u plane. The left figure depicts distributions of true charge deposition on wires (shown in grey in Fig. 6.2). The middle and right figures illustrate the charge distributions using raw waveforms before signal processing (shown in red in Fig. 6.2) and deconvolved waveforms after signal processing (shown in purple in Fig. 6.2). The right figure shows clearly two tracks and two showers, that closely resemble the true charge deposition shown in the left figure, demonstrating the performance of signal processing. It is noted that the signal processing chain in SBND is currently a work in progress, as labelled so in Fig. 6.2 and 6.3. At the time of writing, work on the optimisation of the chain specifically for SBND electronics has begun.

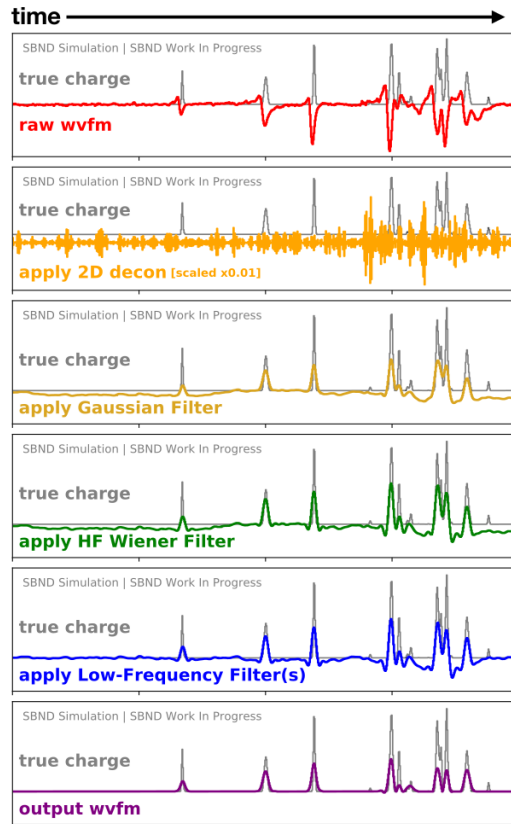


Fig. 6.2 Steps of signal processing applied to a bipolar raw waveform [112].

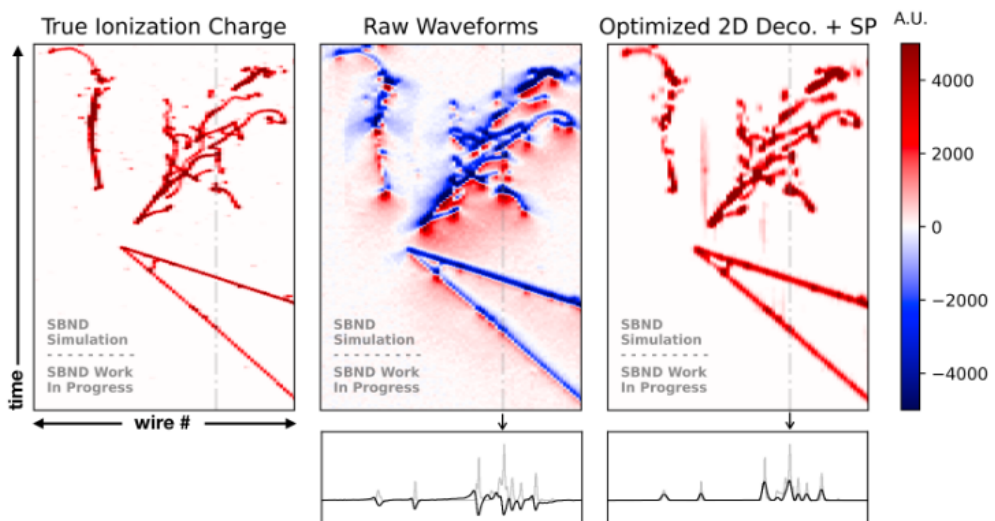


Fig. 6.3 Event displays of a simulated neutrino event using true ionisation charges (left), raw waveforms (middle) and deconvolved waveforms (right) [112].

6.2.2 Hit Finding

After signal processing, hit finding is performed on deconvolved waveforms to search for Gaussian-shaped pulses above a threshold. This is done using the `GausHitFinder` module [113] by fitting a series of Gaussians to the waveform. The number of pulses is determined by the number of maxima found when differentiating the waveform, where each pulse represents a hit. Fig. 6.4 demonstrates the hit finding process for a deconvolved waveform, showing four hits have been identified and fitted with a Gaussian. Once the hits are fitted, information describing the hit is extracted and used by downstream reconstruction. The peak time represents the time at which the charge arrives at the wire, used for determining the drift position and matching hit coincidence across wire planes. The height and the width of the Gaussian are used to calculate the integral of the pulse, representing the deposited charge on the wire, subsequently used in downstream analysis for calorimetry computation.

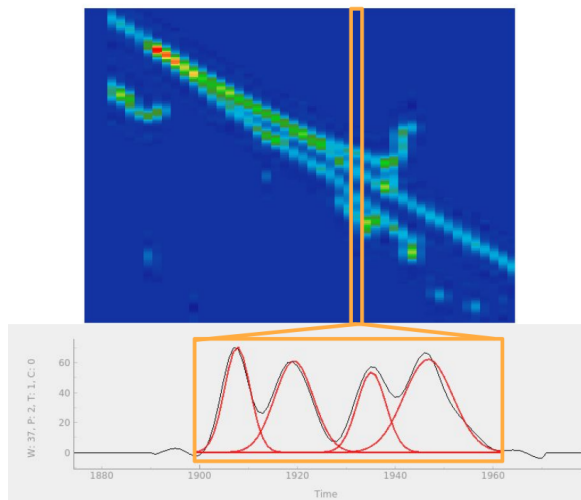


Fig. 6.4 Diagram illustrating the hit finding algorithm on a single wire [114].

6.2.3 Pandora Pattern Recognition

The output hits from the hit finding process are then used to perform 3D reconstruction, which is performed with the Pandora pattern recognition package [6]. The package was first developed for the International Linear Collider and later extended to other LArTPC experiments. It is made up of over 100 individual algorithms, each performing a specific task along the reconstruction chain. The output from Pandora represents an interaction,

containing a hierarchy of particles starting with a neutrino parent at the interaction vertex. This reconstructed object is referred to as a *slice*.

The reconstruction begins with a workflow to reconstruct cosmic-like objects that leave long tracks inside the detector. This workflow performs a 2D clustering on each wire plane independently, followed by 3D reconstruction under the assumption that all clusters are track-like. Then, a cosmic rejection is performed to identify if a cluster is cosmic-like or neutrino-like. The cosmic removal at this stage is deliberately cautious such that only very unambiguous cosmic muons in nature are removed.

The remaining clusters are then input into a second workflow dedicated towards neutrino reconstruction. This workflow begins with a slicing algorithm that divides clusters into *slices*, where each slice encapsulates hits coming from a single origin, representing an interaction. Then, 2D clustering is re-performed on each wire plane independently, however, with a new assumption that clusters can be both track-like and shower-like. A vertexing algorithm then identifies the interaction vertex of the slice and its associated clusters. A series of pattern matching algorithms grows the interaction out of the neutrino vertex and performs 3D reconstruction by matching 2D clusters across different planes. The output 3D reconstructed object associated with a vertex ideally represents a *particle* produced from an interaction.

At this stage, a *track score* is assigned to a particle if it has a track-like or a shower-like topology, which is determined by a dedicated Boosted Decision Tree (BDT). The development work on the track-shower separation BDT and its importance not only in the reconstruction workflow but also in the analysis workflow will be covered in Sec. 6.2.4 next. Both track and shower reconstruction tools are then performed on the particle. Finally, a hierarchy algorithm is performed to classify the hierarchy of particles in a slice, starting with a neutrino parent vertex, and other particles are children, grandchildren, etc. of the parent.

The last stage of reconstruction is calorimetry computation for the output slices and their associated particles. Both track and shower calorimetry computations first convert ADC units to charges, or the number of electrons, by multiplying by a charge calibration constant. The track calorimetry then computes the energy from the charge using the ModBox recombination formalism, factoring in the electric field distortion (See Eq. 8.4, Sec. 8.2.1). Meanwhile, the shower calorimetry reconstruction converts the measured charge to energy by multiplying it by a shower calibration constant, factoring in an averaged recombination factor. Once the SBND detector is operational, the calibration constants will be measured via dedicated calibration runs. The charge calibration constant

is expected to be computed from a sample of the anode-to-cathode crossing muons while the shower calibration constant can be acquired from using a standard candle of the neutral pion invariant mass [54].

6.2.4 Track-Shower Separation Boosted Decision Tree

As previously discussed, reconstructed particles from Pandora are assigned a track score determined by BDT, which is a binary classification machine learning tool. The track score spans between 0 and 1 such that if a particle has a very high track score close to 1, then the particle is track-like. Otherwise, if the track score is very close to 0, then the particle is shower-like.

The track-shower BDT has become more important in the reconstruction as well as the analysis workflow due to a new reconstruction paradigm introduced by Pandora. The traditional reconstruction approach was to perform only either track or shower reconstruction on a particle based on its track score. The new paradigm performs both track and shower reconstruction on a particle regardless of the track score. All reconstructed particles now have two sets of reconstruction variables for track-like and shower-like. The users have the freedom to decide which variables to use depending on their signal topology, and thus not pre-determined by Pandora. The track score can inform which appropriate reconstruction variables should be used for the analysis.

The track-shower separation BDT was trained on a series of reconstruction variables and was updated to include new variables in the training. The original BDT includes variables describing the geometrical topology of the particle such as its length, distance and direction with respect to the parent vertex, as well as calorimetry variables describing the charge distribution of the particle. More details of the input variables and the training of the BDT can be found in Ref. [114]. The update extended beyond the original work to include a brand new set of variables describing how cone-like the charge distribution of a particle as well as a new variable describing the particle hierarchy.

The cone variables were first developed by M. Haigh for particle identification [115] and were imported into Pandora for reconstruction purposes. There are three variables: (1) halo-total ratio, (2) concentration and (3) conicalness as depicted in Fig. 6.5. The diagrams depict the hit distribution of a particle, where each circle represents a hit associated with a charge value and the star represents the vertex of the hit cluster. The illustration is in 2D for simplicity, however the variables are computed in 3D. The first variable is the halo-total ratio, illustrated in Fig. 6.5a. The region outside of the Moliere radius, defined such that

90% of the cluster energy is contained within this radius, is considered the halo region. The hits in the halo are shown as green circles whereas any other hits are shown as grey circles. The halo-total ratio is then defined as

$$\text{Halo - Total Ratio} = \frac{\text{Charges in The Halo}}{\text{Total Charges}} \quad (6.1)$$

The second variable is called concentration, accounting for how concentrated the charge distribution is to the centre of the cluster. This is depicted in Fig. 6.5b, where each hit is assigned a colour showing how weighted it is with respect to its orthogonal distance to the cluster direction. The closer the hit to the centre, the more weighted it is. The concentration variable is defined as the total weighted charges divided by the total

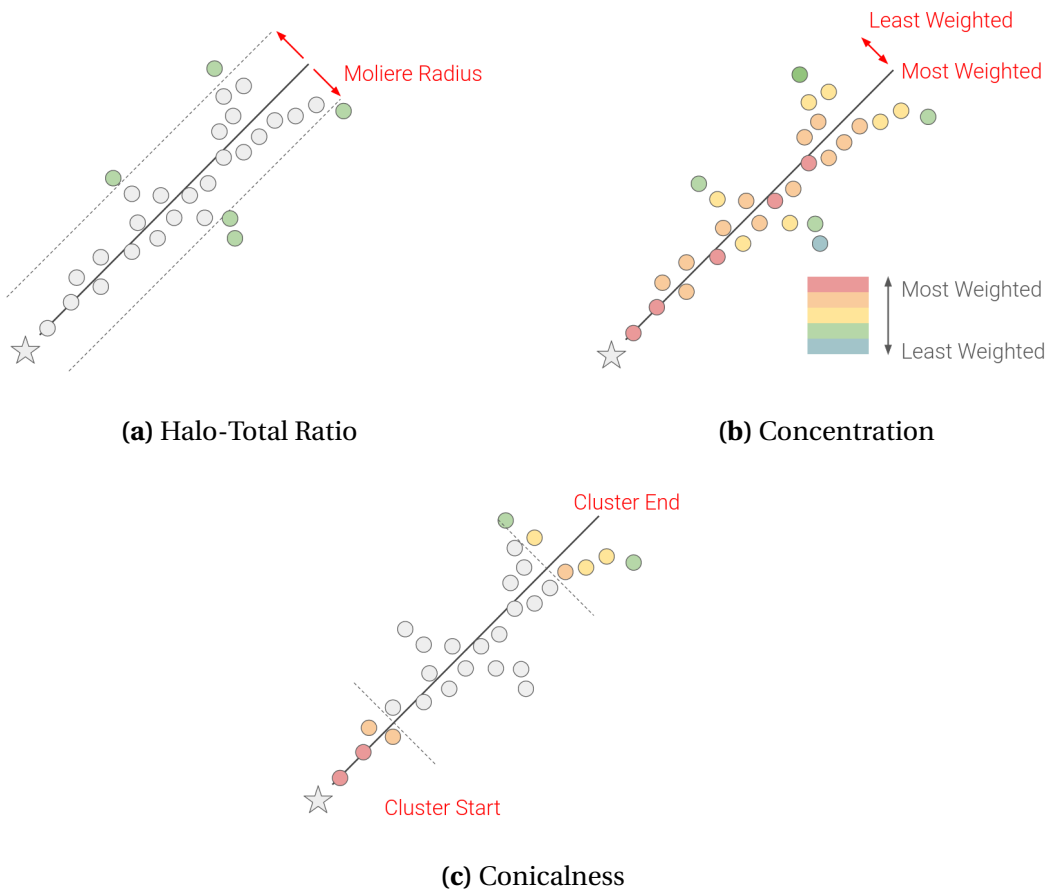


Fig. 6.5 Diagrams illustrating the variables describing how cone-like the charge distribution of a particle .

6.2 Time Projection Chamber Reconstruction

charge as following

$$\text{Concentration} = \frac{\sum \text{Charge} \times \text{Weight}}{\text{Total Charges}} \quad (6.2)$$

Finally, the conicalness variable examines the hit distribution at the end and the start of the cluster as depicted in Fig. 6.5c. It is defined as the ratio between the concentration at the end of the cluster compared to at the start of the cluster

$$\text{Conicalness} = \frac{\text{Concentration at The End}}{\text{Concentration at The Start}} \quad (6.3)$$

On top of the cone variables, another new variable was introduced to the track-shower separation BDT to describe the hierarchy of the particle within the reconstructed interaction or slice. For a given particle, the daughters originating from that particle are identified and their number of hits are counted. The distributions of the four new variables for a track-like and shower-like particle are shown in Fig. 6.6. The concentration and con-

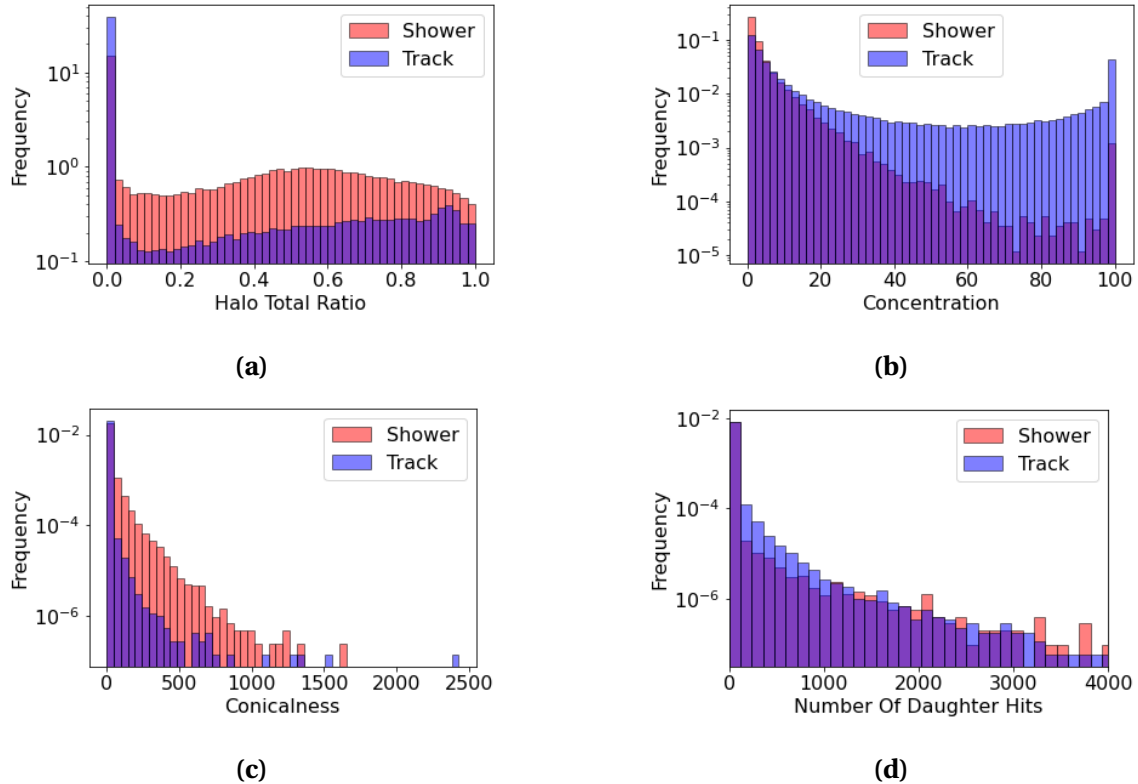


Fig. 6.6 Distributions of new BDT variables: (a) halo-total ratio, (b) concentration, (c) conicalness and (d) number of daughter hits.

icalness variables display the strongest separation power between tracks and showers compared to the halo-total ratio and the number of daughter hits variables.

Fig. 6.7 shows the score distribution of the BDT retrained with the four new variables. The left figure shows two distinct distributions in red and blue for showers and tracks respectively. This demonstrates a good separation power of the BDT, where particles with a score less than 0.5 closely resemble showers whilst particles with a score more than 0.5 are more track-like. The score distribution is broken down into different particle types as shown in the right figure. The distribution is expected given that electrons and photons leave electromagnetic shower activities inside the detector whilst charged particles like muons, pions and protons leave track-like signatures. The updated BDT resulted in $0.1 \sim 2.0\%$ improvement in correctly classifying particle type as shower-like or track-like. The track-shower separation score distribution will be used in downstream high level analysis tools, to be detailed in Sec. 6.4.1, as well as will be employed as a cut variable in the HNL selection, to be detailed in Chapter 9.

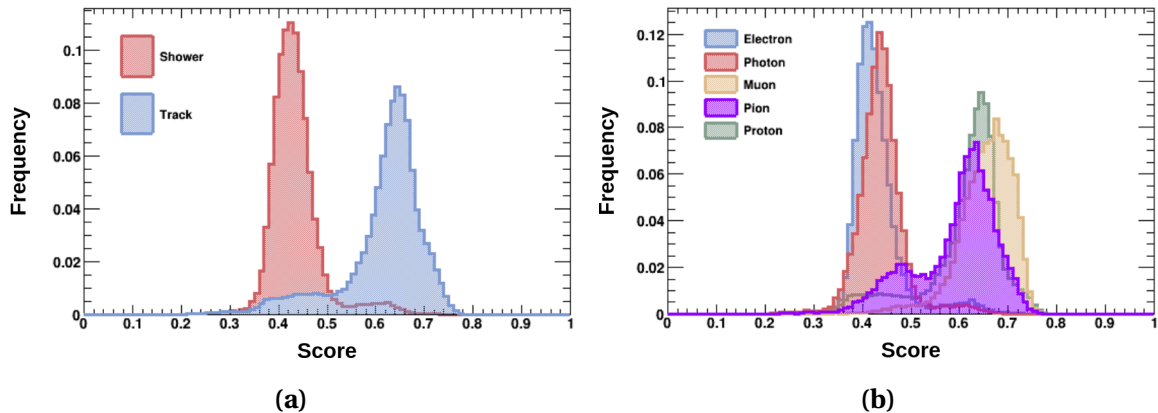


Fig. 6.7 Score distribution of the updated track-shower BDT, plotted for (a) track-like and shower-like particles and (b) different particle types.

6.3 Photon Detection System and Cosmic Ray Tagger Reconstruction

The reconstruction workflow of the two detection subsystems, PDS and CRT, are detailed in the following Sec. 6.3.1 and 6.3.2.

6.3.1 Photon Detection System Reconstruction

The reconstruction of optical detectors, PMTs and X-ARAPUCAs, share the same steps of waveform deconvolution, hit finding and light reconstruction. However, different algorithms and parameter settings are required for each optical detector type due to their different responses. More details on the PDS reconstruction at the SBND detector can be found in Ref. [68]. Here focuses on the reconstruction of PMT waveforms, which have an averaged Single Electron Response (SER) pulse peaking at ~ 25 ADC and a full width at half maximum of ~ 10 ns. The fast response of PMT plays a key role in the nanosecond timing resolution requirement for the HNL search.

The first step is the PMT waveform deconvolution, aiming mainly at noise removal. Fig. 6.8a depicts an example of a simulated PMT waveform before and after the deconvolution. The top figure shows the number of *true*, or MC, PhotoElectrons (PEs) seen by a PMT as a function of time in green. The middle figure shows the raw waveform resulting from the deposited PEs in blue, convolved with the PMT response and noise. The AC circuits of PMTs lead to over/undershoot features across the raw waveform with respect to the baseline. A 1D deconvolution and a high frequency Gaussian filter are applied subsequently. The deconvolved waveform is shown in orange in the bottom figure, demonstrating that bipolarity features are removed while maintaining peaks' magnitudes and positions.

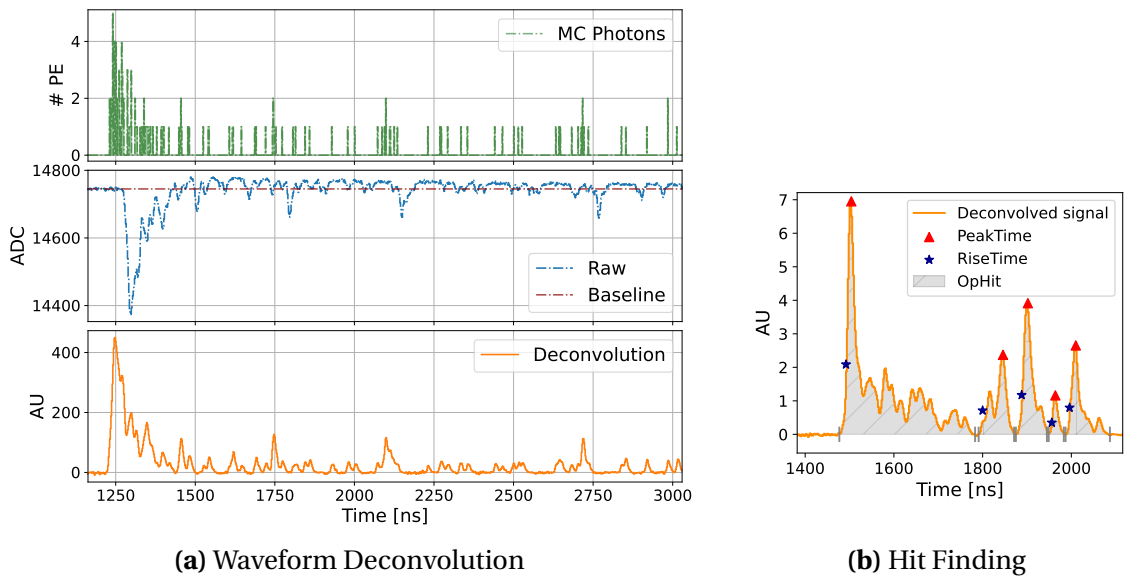


Fig. 6.8 Example demonstrating the waveform deconvolution and hit finding applied to a PMT waveform [68].

Hit finding is performed next on deconvolved PMT waveforms, beginning with a baseline subtraction. Optical hits are identified by finding pulses that go above a threshold of 1/4 the amplitude of the deconvolved SER and 3 standard deviations away from the baseline root mean square. Fig. 6.8b demonstrates a PMT waveform after baseline subtraction with 4 identified optical hits. Peak times, corresponding to the maximum of an optical hit, are denoted with red triangles. The first optical hit contains multiple peaks merged into a single optical hit due to multiple photons arriving very closely in time to the PMT. The rise time of an optical hit is defined as when the first peak goes above 15% of its amplitude, denoted with blue stars. It is an estimation of the arrival time of the first photon contributing to the optical hit. The integral of the optical hit is used to compute the number of PEs.

Next, the light reconstruction algorithm then clusters optical hits into an *optical flash*. The length of an optical flash is set as 8 μs to account for the total light produced in a neutrino interaction, from both prompt and slow components of scintillation photons. The clustering algorithm is based on the number of PEs of optical hits, timing distribution between hits and geometrical location of the PMTs. The number of PEs in an optical flash is the sum of PEs of optical hits clustered in that flash, representing the total light generated by an interaction.

The start time of the optical flash represents the start time of an interaction, t_0 , which is the key variable of the HNL search, and therefore requires great care in reconstruction. The flash start time is the average of the rise time of optical hits in a flash, only considering PMTs that contribute 50% of the prompt light in the 30 ns window of the largest PE pulse. Then, a correction is applied for the propagation of the photons from the scintillation position in the TPC to the PMTs.

The correction can be computed by exploiting the high density of PMTs as well as having coated and uncoated PMTs sensitive to direct VUV light and reflected visible light respectively. Fig. 6.9 shows the reconstructed light yield seen by TPB-coated and uncoated PMTs based on simulation, as a function of the photon mean drift distance, d_{drift} (x -axis). The error bars show the uncertainty due to the geometrical effects of the detector. Closer to the anode at $d_{drift} = 0$ cm, the light yield primarily comes from direct VUV photons, detected by coated PMTs as shown in purple. Closer to the cathode at $d_{drift} = 200$ cm, and hence the reflective foils, the contribution to the light yield from reflected visible photons increases, which are detected by uncoated PMTs as shown in red. For a given scintillation position, and therefore a drift position, the amount of direct and visible photons leads to a specific ratio of the two components seen by PMTs. This ratio is used to compute the

6.4 High Level Analysis Tools

correction for the drift propagation effect when reconstructing the flash time. The timing resolution of the flash time varies by ~ 2 ns across the entire drift distance, demonstrating the excellent capability of the PDS reconstruction at SBND [68].

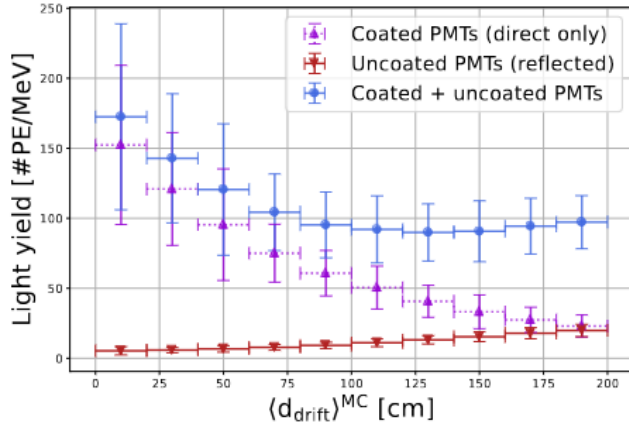


Fig. 6.9 Reconstructed light yield as a function of the mean drift distance [68].

6.3.2 Cosmic Ray Tagger Reconstruction

The reconstruction of the CRT subsystem is the simplest compared to the TPC and the PDS. As previously detailed, the output data of the CRT readouts are in a group of 32 ADC values, for a single ADC per SiPM. The reconstruction begins with a hit finding algorithm to identify which pair of SiPMs in the group goes above a threshold. The SiPM pair determines the lateral position of a cosmic muon hit within a CRT strip. A clustering algorithm groups hits from orthogonal CRT strips of the same wall within a 50 ns window to yield 3D space points. For each CRT space point, the timing and calorimetry information is calculated and corrected for the propagation effect from the hit position to the SiPM. CRT space points from multiple CRT walls are matched together to form a CRT track based on the goodness of timing agreement and prioritising three-point tracks over two-point tracks. The outputs of the CRT reconstruction are both CRT space points and CRT tracks.

6.4 High Level Analysis Tools

The reconstructed variables from each detection subsystem, slices from the TPC, flashes from the PDS, space points and tracks from the CRTs, can be used collectively by down-

stream algorithms to compute useful characteristics regarding the interaction. This section covers the main high level analysis tools used in the HNL search and their usage will be detailed in Chapter 9. Firstly, Sec. 6.4.1 provides the details on how variables from different detection subsystems can be matched to the same interaction. Presented in Sec. 6.4.2 are the cosmic rejection tool. Finally, Sec. 6.4.3 illustrates the method employed for particle identification.

6.4.1 Subsystem Matching

The reconstructed tracks using the TPC can be matched to a space point or tracks from the CRTs to provide additional information for cosmic rejection. An example is that a through-going cosmic ray produces a long track in the TPC as well as deposit energy in the nearest CRT walls where the track starts and ends. Another example is that tracks produced in the TPC deposit energy in the nearest CRT strips only when they enter or exit the detector, enabling the tagging of stopping cosmic muons or exiting neutrinos.

Two types of matching are performed: (1) matching a TPC track to CRT space points and (2) matching a TPC track to CRT tracks. The former method extrapolates the TPC track and matches with the nearest CRT space points by computing a Distance of Closest Approach (DCA), confining the matching to a single CRT wall. The latter method uses a compound score from the average DCA of a TPC track to many CRT tracks and the angle between them, enabling matching a TPC track to many CRT walls. Both methods use the timing information of the CRT objects for further constraints and no matching duplications are allowed.

The second subsystem matching of interest is matching an interaction reconstructed using TPC wires, a slice, to an interaction reconstructed using PMTs, a flash. This matching is vitally important since the flash time matched to a slice represents the start time of the interaction reconstructed in that slice. It is the key variable employed to separate the HNL signal from the SM neutrino background, which will be detailed in Chapter 9.

The matching of the TPC to the PDS is done with the OptOfinder module [116]. The matching is based on the estimation of charge yield in a slice seen by the wires to predict the light yield, and whether the predicted light yield is in good agreement with the measured light yield seen by PMTs. Firstly, the charge yield of a slice is converted to energy to light yield based on the topology of particles in the slice. The track score of the particles in the slice, assigned by the track-shower separation BDT detailed in Sec. 6.2.4, is used to indicate whether the particle is track-like or shower-like. If the particle is track-

6.4 High Level Analysis Tools

like, the calorimetry computation uses the ModBox recombination formalism with the charge-light anti-correlation. If the particle is shower-like, the calorimetry computation uses a charge-to-light conversion by multiplying a constant.

From the estimated light yield, a hypothesis of the number of PE seen by each PMT is constructed by re-running the semi-analytical light library. Finally, the hypothesis PE is compared to the measured PE for any given flash by a χ^2 computation. The flash that is best matched to a slice is the one with the lowest χ^2 . Only one-to-one match is allowed such that only a single optical flash is matched to a slice.

A useful variable from this matching process is the comparison between the hypothesis PE predicted from the measured charge, denoted as L_Q , and the measured PE seen by PMTs, denoted as L . The variable is defined as follows

$$\frac{L_Q - L}{L} \quad (6.4)$$

This fraction indicates the level of agreement between L_Q and L , and thus, the level of agreement of the interaction calorimetry using the measured charge or the measured light. If the fraction is positive, the predicted light from the measured charge is overpredicted compared to the measured light, otherwise, it is underestimated. This variable is particularly useful in the selection of HNL signals, which will be further elaborated in Chapter 9.

6.4.2 Cosmic Rejection

Cosmic Rejection Using a Multi-system Boosted decision tree Score (CRUMBS) uses all three detection subsystems of SBND for cosmic rejection [117]. CRUMBS is a binary classification BDT that outputs a score whether a reconstructed slice is cosmic-like or neutrino-like. Reconstruction variables from all three detection subsystems that are complementary to each other are input into CRUMBS, and therefore vastly reduce inefficiencies compared to using a single system. The TPC information includes variables describing a particle as both neutrino-like and cosmic-like, accounting for its charge distribution, position within the TPC and calorimetry. The PDS information is from the flash best matched to the slice of interest, particularly the number of PEs in the flash and the χ^2 from the matching agreement. Finally, the CRT information consists of both TPC-CRT matching algorithms, including the timing information of the CRT space points/tracks and the matching score. The score distribution of CRUMBS shows a significant separating power between neutrino-like signals and cosmic-like backgrounds.

6.4.3 Particle Identification

The main particle identification tool at SBND is called Razzled [118], which is a multi-classification BDT designed to identify particle type that would deposit energy inside SBND: e , γ , μ , π and p . The reconstruction variables input into Razzled are only TPC variables, mainly from the Pandora package. There are three categories of variables for training Razzled: (1) generic reconstruction variables, (2) track-like variables and (3) shower-like variables. The generic variables describe the particle multiplicity, topology, directionality and charge distribution. Track reconstruction variables include track lengths, calorimetry kinematics in the stopping region to identify Bragg peak, and multiple coulomb scattering for μ - π separation. Shower reconstruction variables include shower conversion gaps, opening angles and calorimetry aiming towards γ - e separation. A full description of the input variables and training can be found in Ref. [114]. This collection of variables allows Razzled to exploit the correlation between variables, thereby significantly improving the identification performance over traditional hand cuts. For each reconstructed particle, Razzled outputs a score for each particle type and assigns the highest particle type score to that particle.

6.5 Concluding Remarks

The reconstruction workflow of SBND is described, outlining the reconstruction process for each detection system, the TPC, the PDS and the CRT. The three detection subsystems together provide complementary information regarding the underlying reconstructed interaction and have been used collectively by different analysis tools for different purposes. Focusing on the HNL search, the background rejection and signal selection will be based on a combination of variables and tools employing all three subsystems to achieve a high signal-to-background ratio, as will be discussed in Chapter 9.

Particularly, the most important variable is the reconstructed interaction time, t_0 , which is subsequently used to compute the arrival time at the front face of SBND. These timing variables, having a resolution of ~ 2 ns, enable the reconstruction Gaussian-shaped neutrino beam bucket and therefore, are powerful discriminations to differentiate HNLs from SM neutrinos. To achieve such high timing resolution at the high level reconstruction, the low level readout electronics must have sufficient timing resolution to maintain a high quality data stream at a high sampling rate. The timing characterisation of the readout electronics will be discussed in Chapter 7 next.

Chapter 7

Timing Performance of the Data Acquisition System

Achieving a timing precision $\mathcal{O}(1\text{ ns})$ is a pivotal goal for the Data Acquisition (DAQ) at SBND as it is essential for high precision physics analysis. Most importantly, the Cosmic Ray Taggers (CRTs) and PhotoMultiplier Tubes (PMTs) are the two detection subsystems with sufficient timing resolution to resolve the buckets of the Booster Neutrino Beam. Their readout electronics must also have sufficient timing resolution to record the signals with a high level of precision and minimal smearing. It is therefore important to characterise the timing performance of the readout electronics to identify areas of improvement in preparation for the nanosecond goal.

The work undertaken to assess the timing performance of the DAQ electronics is outlined in this chapter. An overview of the timing system at SBND is first given in Section 7.1. The timing characterisation of the CRT and PMT readout electronics are detailed in Section 7.2 and 7.3 respectively. Finally, Sec. 7.4 provides some concluding remarks.

7.1 Timing Reference System of the Data Acquisition

The event building process of the DAQ relies entirely on fragment timestamps to construct a physics event, as was detailed in Sec. 4.2.7. The timestamp generated by each subsystem readout electronic must be generated with a high level of precision and synchronisation. At SBND, the strategy is to utilise the White Rabbit (WR) timing system. It is a collaborative project developed at the European Organisation for Nuclear Research (CERN) and is now a widely-used synchronisation solution in the scientific community [119]. The WR has the

capability to offer fully deterministic time transfer with sub-nanosecond accuracy over distances exceeding 80 km. The application of the WR timing system at SBND for time transferring and timestamping is detailed in Sec. 7.1.1 and Sec. 7.1.2 as follows.

7.1.1 Time and Frequency Transfer To Subsystems

Fig. 7.1 provides an overview of the WR timing system at SBND. Starting from the first column of the figure is the Grandmaster switch. It distributes time and frequency to all other slave WR switches within the WR network via optical links. The WR switch has dynamic calibration and thus, is a very reliable and robust delivery system. The system ensures that the Pulse Per Second (PPS), which is 1 Hz, from all slave WR switches are aligned to the Grandmaster's PPS with sub-nanosecond accuracy and tens of picoseconds precision. The Grandmaster switch is also connected to an atomic clock locked to a global navigation satellite system. As a result, the time and frequency distributed by the WR system are derived from the International Atomic Time (TAI) and the Coordinated Universal Time (UTC) format.

At SBND, there are two slave WR switches, as shown in the second column labelled *Servers Hosting Slave Switches*. Each slave switch server hosts a different module of Field programmable gate arrays Mezzanine Card (FMC). The first server contains 2 SVEC-FD modules, which are Fine Delay (FD) cards carried by Simple VME FMC Carrier (SVEC). The second server hosts a single SPEC-TDC module, a Time to Digital Converter (TDC) card carried by a Simple PCIe FMC Carrier (SPEC). The usage of SVEC-FD modules is discussed here, whilst the usage of the SPEC-TDC will be discussed in Sec. 7.1.2 next.

SVEC-FD modules are high precision pulse generators, with 10 ps resolution and timebase accuracy of 2.5 ppm when used within a WR network. They are used to generate

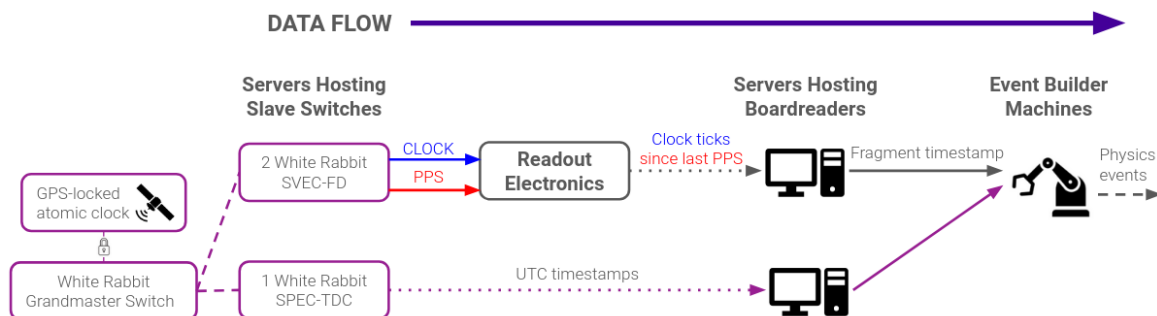


Fig. 7.1 Flow chart showing the distribution of the White Rabbit timing system.

7.1 Timing Reference System of the Data Acquisition

frequencies sent to readout electronics to ensure timing synchronisation across all subsystems of the DAQ. There are two types of frequencies: (1) clock as shown by the blue arrow and (2) PPS as shown by the red arrow in Fig. 7.1.

The clock signal provides a *metronome frequency* customised for each readout hardware's internal clocks. This signal behaves as the master clock that the internal clocks of readout electronics can latch onto, thereby maintaining their accuracy and stability over time. The PPS signal provides the *same reference frame* for all readout electronics in the DAQ. All internal clock counters of readout electronics reset upon the arrival of a PPS and thus share the same reference frame as the PPS. Details of the PPS and clock distribution can be found in Appendix C.

Raw data sent from the readout electronics to computer servers, as shown by the dotted grey arrow, contains timing information regarding the arrival time of the trigger at the readout. The timing information at this stage is only the number of clock ticks since last the PPS arrived, and therefore, does not contain sufficient information for event building across multiple subsystems.

To facilitate event building, raw data is packaged into *fragments*, previously detailed in Sec. 4.2.7. The fragment timestamp is in the UTC format, thereby containing timing information about the number of seconds since the Unix Epoch on the 1st of January 1970. This is the *universal* reference frame and allows for direct comparison of fragment timestamps from different subsystems during event building. The number of seconds is generated by the computer servers under the network time protocol with a precision level $\mathcal{O}(100 \text{ ms})$.

The nanosecond-level of precision of fragment timestamps are derived from the number of clock ticks since the last PPS, generated by internal clocks of each readout electronics. They are converted to the number of nanoseconds since the last whole second using the tick-to-time conversion. This level of precision of fragment timestamp necessitates the event building process, as well as, is stored for downstream reconstruction and analysis.

7.1.2 Precise Timestamping

Also shown in Fig. 7.1, another component of the WR timing system is the SPEC-TDC module. This module can timestamp signals with a precision of 700 ps, and output timestamps in the UTC format. The timestamps can be acquired by the DAQ and be built within a physics event, as shown by the dotted and solid purple arrows.

At SBND, SPEC-TDC is employed to timestamp the arrival time of important signals, recording additional timing information on top of the TPC, PDS and CRT data. This timing information can be leveraged for different physics applications. For instance, it can be used to characterise the timing resolution of the readout electronics. The recorded timestamps can be also used to derive the correction for hardware synchronisation or enable an alternative method to reconstruct the timing of a physics event.

Fig. 7.2 shows the five signals input to the SPEC-TDC. Firstly, two beam signals, shown in blue, provide the status of the BNB beam. The first one is the Booster Extraction Signal (BES), which is an early warning signalling when protons are extracted in the Booster cycles. The second one is the Resistor Wall Monitor (RWM), which measures the instantaneous beam current onto the BNB target. The RWM signal arrives at the SBND detector building almost simultaneously with the beam itself. Additionally, two trigger signals, shown in green, are recorded to monitor the DAQ synchronisation with respect to the triggers. The recorded trigger signals are the flash triggers and the event triggers, which were detailed in Sec. 4.2.5. Finally, clock reset signals for the CRT readout electronics are recorded in the last channel of the SPEC-TDC, as shown in pink.

Two applications of the SPEC-TDC to characterise the timing precision of the readout electronics were explored for the CRT readouts in Sec. 7.2 and the PMT readouts in Sec. 7.3. For the CRT readouts, an alternative timing reconstruction was also derived using the timing information recorded by the SPEC-TDC. For the PMT readouts, the SPEC-TDC timestamps helped validate the timing synchronisation across multiple digitisers.

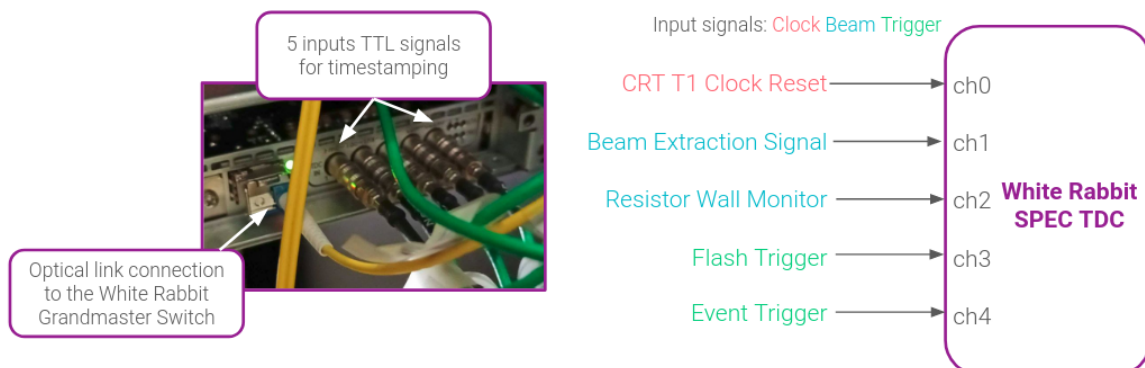


Fig. 7.2 Photograph of the SPEC-TDC module installed at SBND (left) and diagram showing the input signals into the module for timestamping (right).

7.2 Timing Performance of Front End Board Modules

This section provides a description of the characterisation of the timing performance of the CRT readout electronics, Front End Board (FEB) modules, in Sec. 7.2.1 and an alternative timing reconstruction in Sec. 7.2.2.

7.2.1 Evaluation of Internal Clock Resolution

The readout electronics of CRTs are FEB modules, which were detailed in Sec. 4.2.4. Here, the focus is on the precision of the internal clocks of FEB modules. Internal clocks of FEB modules are TDC units with a coarse counter of 4 ns per tick (250 MHz frequency). A high resolution time interpolation method is implemented within the TDC clock cycle to improve the counter to 1 ns per tick [120].

There are two internal clocks per FEB module. The first one is referred to as *T0 clock*, which is reset by the PPS signal therefore its *T0 timestamps* share the same PPS reference frame as all other DAQ readout electronics. The second internal clock is referred to as *T1 clock*, which is reset by a delayed BES signal of the frequency ~ 5 Hz. It produces *T1 timestamps*, referencing the BES signal coincident with the beam arrival time. In addition, FEB modules timestamp the arrival time of reset signals, whether a PPS or a BES and store the timestamps as *T0 or T1 clock reset events*. Each of these reset events is timestamped by both the T0 and T1 clocks, and therefore each has the corresponding T0 and T1 timestamps.

The work to characterise the internet clock was undertaken at Fermilab in 2022 during the commissioning of SBND. It was conducted using a temporary setup called *CRT Sharps*. The CRT Sharps were made up of two sets of CRT panels, where each set of panels was placed upstream and downstream of the SBND detector cryostat, centred on the BNB location. The downstream setup is shown in Fig. 7.3 where 4 CRT panels are arranged orthogonal to each other. Each panel was read out by a FEB module, totalling 8 FEB modules with 4 upstream and 4 downstream. The CRT Sharps was commissioned during the period at which the BNB beam was on. The triggering condition was to have signal coincidences between the upstream and downstream panels during the beam spill. This was to ensure that the CRT Sharps setup only recorded events produced by muons coming from beam neutrinos and therefore, functioned as a beam telescope. The analysis described below used a dataset recorded by the CRT Sharps during the summer and fall of 2022.

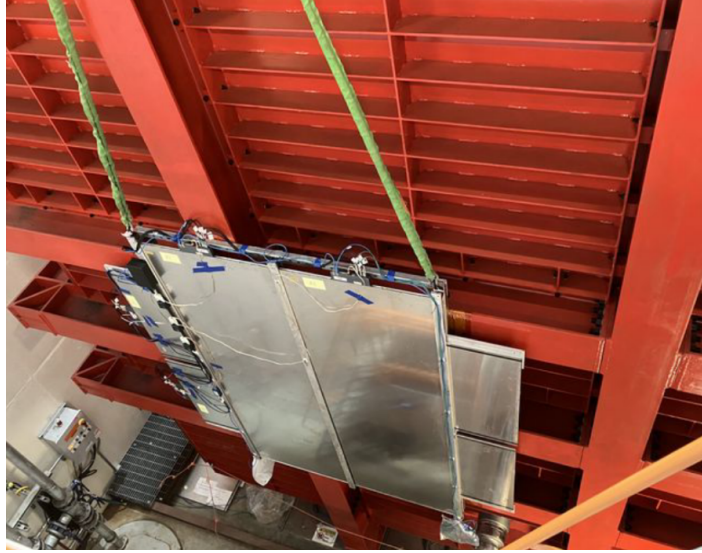


Fig. 7.3 Photograph showing the downstream panels of the CRT Sharps on the back wall of the SBND cryostat.

The T0 clock is characterised using the T0 timestamps of T0 clock reset events. To measure the clock variation, one can simply compare these timestamps with respect to a whole second. An example is shown in Fig. 7.4 for a single FEB module numbered 79. The left plot shows the timestamp variation with respect to the event number to check for clock stability over a period of time. The right plot is a 1D histogram to check for the spread of the distribution. The standard deviation (s.d.) of this distribution is a direct measurement of the T0 clock variation. It is 2.37 ns with a mean of -1.89 ns, indicating that the FEB module 79 consistently received the PPS signal every second to reset its T0 clock. This measurement was repeated for all 8 FEB modules of the CRT Sharps. The T0 clock resolution was found to be $\mathcal{O}(2 \text{ ns})$, consistent across all FEB modules.

The characterisation of the T1 clock is less trivial since its T1 timestamps do not share the same reference frame with any other readout electronics. The only direct comparison is via T0 timestamps, which contain the T0 clock resolution. The T0 timestamps of T1 clock resets were compared against the SPEC-TDC timestamps of the BES signal since they both measured the same signal and reference to the PPS. This comparison was motivated because the SPEC-TDC has higher precision than FEB internal clocks, 700 ps compared to $\sim 1 \text{ ns}$.

The left plot shows the variation with respect to the event number, indicating that the FEB module 79 regularly received BES signals to reset its T1 clock. The right plot shows the 1D histogram of the variation. The s.d. here is not a direct measurement of the T1

7.2 Timing Performance of Front End Board Modules

clock resolution, however, is expected to be lower than the T0 clock resolution since it is reset more frequently at ~ 5 Hz. The s.d. is smaller at 1.95 ns and the mean is closer to 0 at -0.443 ns. This measurement was carried out for all FEB modules and the same results were observed.

Moreover, the T1 clock reset events also provide another method to monitor the drift of the T0 clock. This can be done by plotting the variation of T0 timestamps of T1 clock reset events as a function of the T0 timestamps, equivalent to when it is generated within the clock cycle. An example is shown in Fig. 7.6 for the FEB module 79. Early in the clock cycle, when T0 timestamps are close to 0 ns, small variations within 2 ns can be seen.

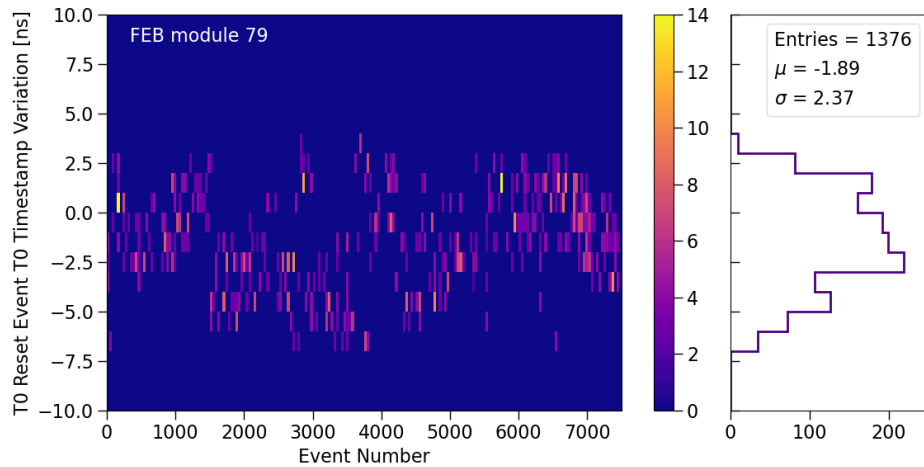


Fig. 7.4 Variation of T0 timestamps of T0 clock reset events with respect to a whole second.

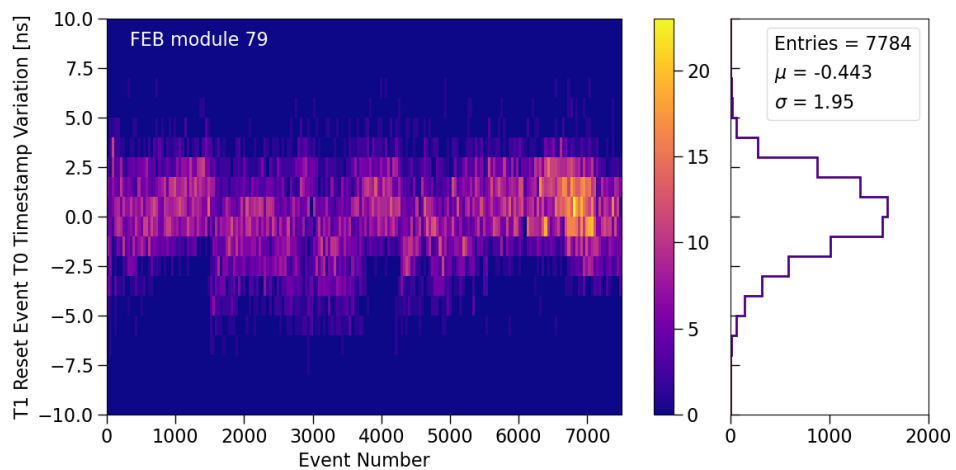


Fig. 7.5 Variation of T0 timestamps of T1 clock reset events with respect to the SPEC-TDC's recorded timestamp of the BES signal.

However, later in the clock cycle, when T0 timestamps are close to a full second, larger variations up to 7 ns occur. This illustrates that the precision of its T0 timestamp depends on at which point in the clock cycle it is in. It is also possible that the T0 clock counter can overflow and the resulting timestamps are meaningless. This clock drift behaviour is expected to be more prevalent with the T0 clocks than the T1 clocks due to lower reset frequency.

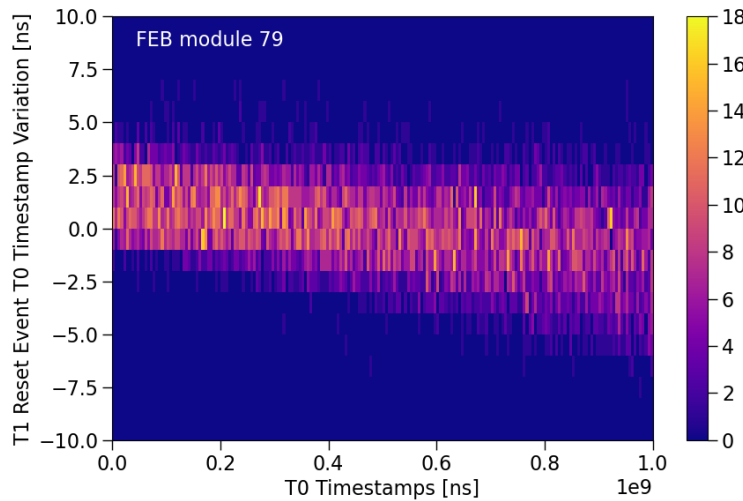


Fig. 7.6 Variation of T0 timestamps of T1 clock reset events as a function of the T0 timestamp.

These plots are useful diagnostic tools to characterise the timing of the FEB modules, including monitoring the magnitude and stability of the T0 and T1 clocks as well as the drift of the T0 clock. It is important to note that the T0 and T1 clocks of the FEB can potentially vary from run to run, and they are very sensitive to external noises. The plots have been reproduced by the CRT working group of SBND during the CRT installation periods and they will also be produced for online monitoring purposes in order to track the clock stability and resolution of the FEB modules.

7.2.2 Alternative Timing Reconstruction

In addition to the timing characterisation, the SPEC-TDC can also provide an alternative timing reconstruction method for events recorded by CRTs. The study here was performed using a data set recorded by the CRT Sharps of ~ 9000 beam events. The CRT 2D hit time was reconstructed from coincidental hits of 2 cross scintillator strips, and corrected for cable and propagation delay. The CRT hit time T0 was reconstructed using the T0 times-

7.2 Timing Performance of Front End Board Modules

tamp whilst the CRT hit time T1 was reconstructed using the T1 timestamp. Commonly, the timing reconstruction of CRT data only uses the CRT hit time T1 in reference to the beam. Here, the timing reconstruction using CRT hit time T0 instead is presented.

Firstly, the beam spill was reconstructed as shown in Fig. 7.7a and 7.7b using CRT hit time T1 and T0 respectively. The beam spill in Fig. 7.7a was plotted directly using CRT hit time T1 since it is a reference to the BES signal. The plot shows a beam excess to the cosmic background, corresponding to the BNB beam arriving $333 \mu\text{s}$ after the BES signal and lasting for $1.6 \mu\text{s}$. On the other hand, CRT hit time T0 is in the reference frame of the PPS and needs to be corrected to the beam arrival time to reconstruct the beam spill. The correction was done using BES signals recorded by the SPEC-TDC, of which the timestamps are also with respect to the PPS. The beam spill structure acquired from this method shows a good agreement as shown in Fig. 7.7b, where the same beam excess can be seen. It is important to note that the reconstruction of the beam spill only requires a resolution $\mathcal{O}(1 \mu\text{s})$, which is satisfied by both the T0 and T1 clock resolution $\mathcal{O}(2 \text{ ns})$.

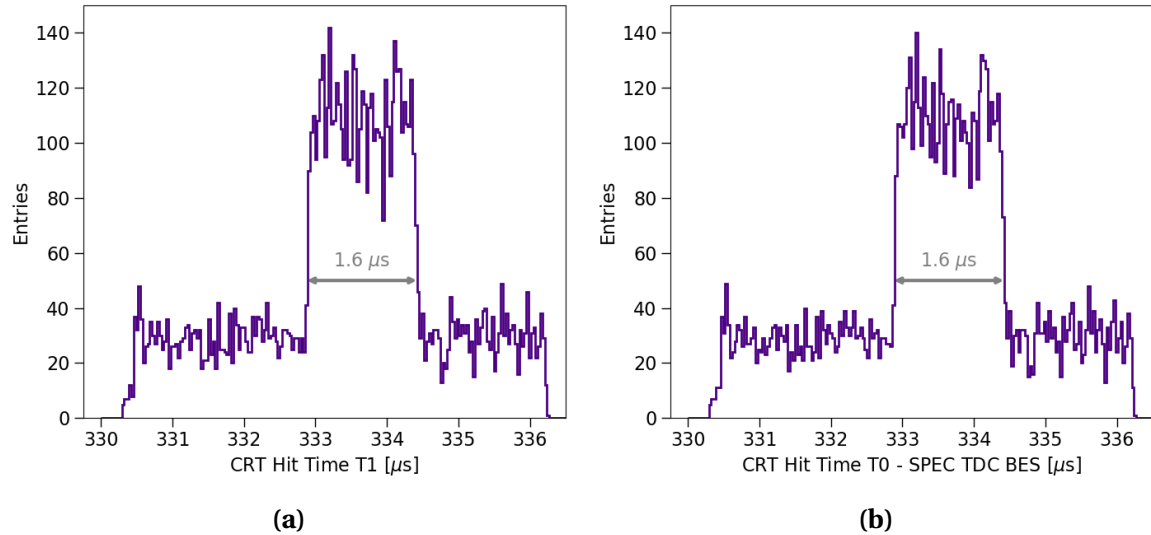


Fig. 7.7 Beam spill reconstructed using (a) CRT hit time T1 and (b) CRT hit time T0 combined with the SPEC-TDC timing information.

The next step was to reconstruct the substructure of the BNB, made up of 81 Gaussian buckets of width 1.308 ns and separated by 19 ns . Given the limited statistics of the sample to fully plot 81 buckets of a whole beam spill, the buckets were overlaid on top of each other by taking the modulus of 19 ns . The resulting beam buckets using CRT hit time T1 and CRT hit time T0 combined with the SPEC-TDC timestamps are shown in Fig. 7.8a and 7.8b respectively. Using the CRT hit time T1, the beam bucket was resolved even with the limited statistics, recovering a Gaussian width of 3.2 ns . However, from the CRT hit time

T0 distribution, the Gaussian shape is more smeared out with a larger width of 3.5 ns. This is due to the resolution of the T0 clock being shown to be $\mathcal{O}(2 \text{ ns})$, which is larger than the width of the beam bucket.

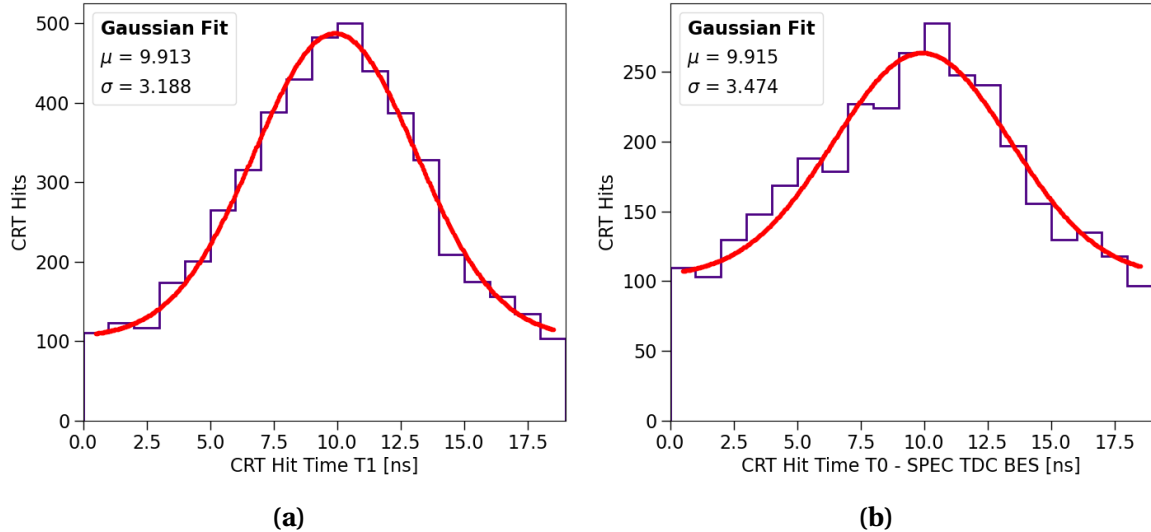


Fig. 7.8 Beam bucket reconstructed using (a) CRT hit time T1 and (b) CRT hit time T0 combined with the SPEC-TDC timing information.

Both the reconstruction of the beam spill and beam bucket demonstrate that the CRT hit time T0 can be utilised together with the SPEC-TDC. This alternative timing reconstruction shows promising early results and certainly has the potential for more improvements. Additionally, this showcases the versatile usages of the SPEC-TDC, where its recorded timestamps can be used in conjunction with other detection subsystems.

7.3 Timing Performance of CAENV1730 Digitisers

Following the timing characterisation of the CRT readout electronics, the next focus is on the PMT readout electronics, CAENV1730SB digitisers. Sec. 7.3.1 provides a description of the CAENV1730's internal clocks. Following that, an evaluation of the timing synchronisation across multiple digitisers is presented in Sec. 7.3.2 and a clock jittering correction method is presented in Sec. 7.3.3.

7.3.1 Internal Clock and Timestamp Structure

A description of the PMT readout electronics, CAENV1730SB digitisers, was provided in Sec. 4.2.4. The internal clock of interest is called REF-CLOCK in the clock domains of CAEN digitiser [91]. The REF-CLK is a clock chain responsible for a synchronous sampling and triggering rate, and thus the timing precision of the CAEN digitiser. The REF-CLK frequency serves as an input to a clock distribution device AD9510, generating three types of frequencies: (1) an ADC sampling clock, (2) a trigger clock and (3) an output clock for external use. The AD9510 device must be programmed for an input frequency to the REF-CLK connector so that all three clock frequencies are phase-locked-loop with the input.

Firstly, the ADC sampling clock has a frequency of 500 MHz. The PMT waveform is therefore sampled with a tick value of 2 ns/tick. Secondly, the trigger clock operates at 125 MHz and is responsible for handling the triggering and synchronisation logic. The trigger clock has a tick value of 8 ns/tick. However, since it is read every two clock cycles, it potentially has a fluctuation of up to 16 ns/tick. Finally, the last clock is a programmable frequency output via the CLK-OUT connector and can be propagated to another CAEN digitiser for synchronisation purposes.

At SBND, CAEN digitisers are configured to use an external clock fed to the REF-CLK with signals from the WR timing system described in Sec. 7.1.1. The clock signal is input to the CLK-IN connector, with frequency depending on the clock synchronisation scheme. This signal behaves as a *metronome frequency* for all three clocks described above. The PPS signal is input to the S-IN connector and is used by the trigger clock. It resets the counter of the trigger clock every second so that the timestamps output by CAEN digitisers share the same reference frame as other readout electronics.

Unlike the timestamp generated by FEB modules or the SPEC-TDC, where it is the number of clock ticks upon receiving a trigger, the timestamp produced by CAEN digitisers is structured differently. Fig. 7.9 illustrates the time structure of a waveform recorded by CAEN digitisers. Upon receiving a trigger at the TRG-IN connected, as shown in grey, there is a latency before the digitiser acting on the trigger, as shown in red. The waveform duration can be any portion pre or post-trigger as shown by the red and blue boxes. For every trigger, the CAEN trigger clock produces a timing object called a trigger time tag. However, the trigger time tag is not instantaneous upon the trigger arrival, it is instead the timestamp value of the last tick on the waveform, as shown in green. Therefore, careful timing reconstruction is needed when decoding the waveforms from CAEN digitisers.

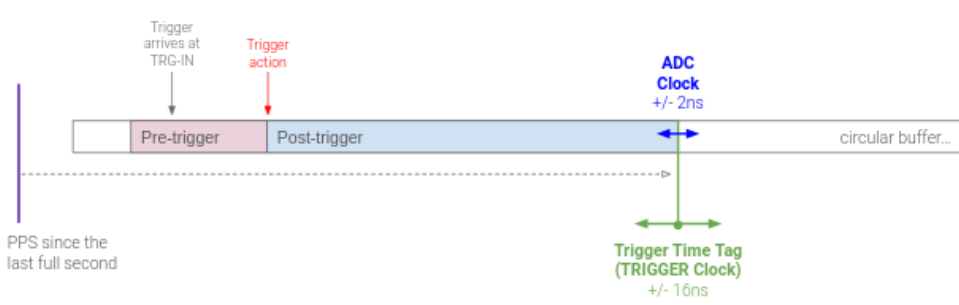


Fig. 7.9 Timing structure of a waveform digitised by CAEN digitisers.

7.3.2 Evaluation of Clock Synchronisation

Multiple CAEN digitisers can be synchronised to behave as if a single digitiser. It is crucially important to record PMT waveforms in synchronisation since they are the key ingredients for timing reconstruction with a resolution $\mathcal{O}(2 \text{ ns})$ as previously detailed in Sec 6.3.1. The synchronisation can be achieved through two different clock synchronisation schemes: (1) fan out and (b) daisy chain, as shown in Fig. 7.10.

In fan out mode, each digitiser is input with the clock signal set at 10 MHz clock. The 10 MHz was chosen at the time since it is the highest frequency produced by the SVEC-FD card. The clock signal is distributed to a fan out module, and then into the CLK-IN connector of each digitiser. The cable length of each clock signal is identical so that all clock signals arrive at CAEN digitisers at the same time.

In daisy chain mode, the first CAEN digitiser in the daisy chain receives the 10 MHz clock, referred to as the master clock. Its clock is then propagated to the next digitiser in the chain, referred to as the slave clock. The master clock can be precisely programmed with a delay $\mathcal{O}(300 \text{ ps})$ to account for cable lengths, ensuring that the master and slave



Fig. 7.10 Diagram illustrating two clock synchronisation schemes, (a) fan out and (b) daisy chain.

7.3 Timing Performance of CAENV1730 Digitisers

clocks are in phase with each other. The clock propagation continues from one digitiser to the next digitiser in the chain, until the last digitiser in the chain is in the same clock phase as the first one.

The timing characterisation study was carried out to determine which clock synchronisation scheme provides the best precision and stability. The setup consisted of 8 CAEN digitisers located in the same VME crate. Each digitiser received an identical trigger with the same cable length so every digitiser was triggered simultaneously. The trigger rate was set as 1 Hz for simplicity.

To evaluate the synchronisation of CAEN digitisers, their timestamps of triggered events were directly compared against the same timestamps recorded by the SPEC-TDC since both are referenced to the PPS signal. Similar to the approach with the CRT readout electronics, the SPEC-TDC offers a higher level of precision compared to the CAEN digitiser, 700 ps compared to \sim 1 ns. For an ideal synchronisation, the timestamps of every triggered event from every digitiser should be identical with respect to each other, and also with respect to the SPEC-TDC after cable correction.

Some results of synchronisation using the daisy chain are shown in Fig. 7.11, depicting the differences of timestamps CAEN digitisers from the SPEC-TDC as a function of the event number. Only 4 out of 8 CAEN digitisers are shown for run 7980 and run 8060, however, similar results were observed for the rest of the digitisers. Run 7980 in Fig. 7.11a demonstrates a perfect synchronisation across all 8 CAEN digitisers. Their differences with respect to the SPEC-TDC are constant at 0 across all the events and all the digitisers. This shows a very good and stable synchronisation. In contrast, run 8060 exhibited some interesting effects as shown in Fig. 7.11b. Firstly, board 5 shows a straddling effect, where the observed differences jitters between 0 and 8 ns. This behaviour could be due to the CAEN trigger clock of the CAEN digitiser being read every 2 clock cycles, introducing some fluctuations. Moreover, board 7, which received a clock signal from board 5 in the daisy chain, drifted by 8 ns. Following that, board 9, receiving clock from board 7, also drifted by 8 ns. This demonstrates that if one clock in the daisy chain drifts, subsequently clocks in the chain will also drift.

The same test was repeated for the fan out fan scheme. Some example results are shown in Fig. 7.12 for run 8178 and run 8196. Firstly, in both of these runs, board 5 shows the same straddling effect, causing timestamps to jitter by 8 ns. The second observation is that the timestamp differences vary randomly between digitisers and across different runs. For instance, the timestamp difference of board 9 is stable at -8 ns in run 8178 but stays at +8 ns in run 8196.

Timing Performance of the Data Acquisition System

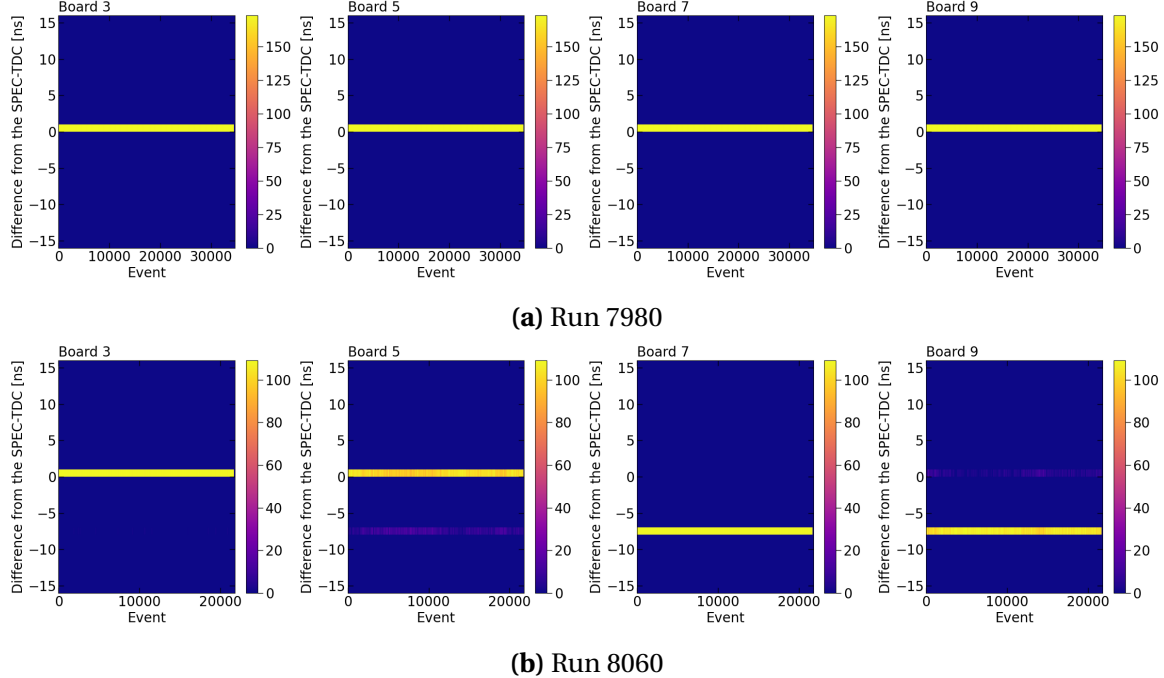


Fig. 7.11 Differences in trigger timestamps between CAEN digitisers and the SPEC-TDC with the CAEN digitisers using the daisy chain clock scheme.

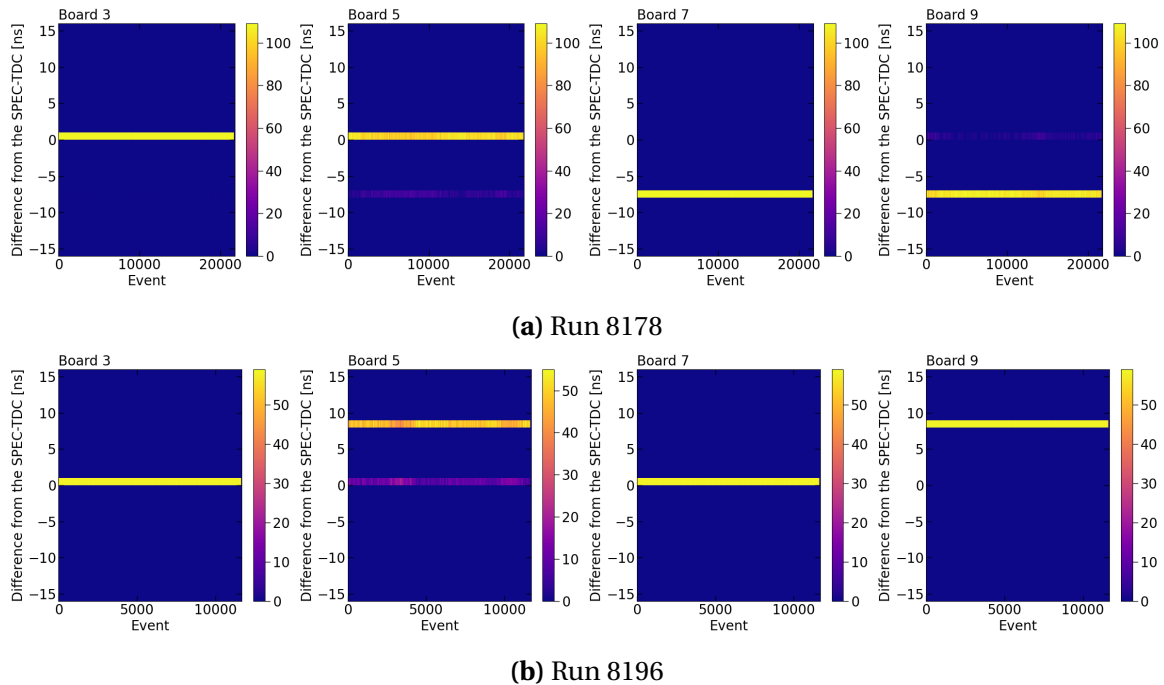


Fig. 7.12 Differences in trigger timestamps between CAEN digitisers and the SPEC-TDC with the CAEN digitisers using the fan out clock scheme.

7.3 Timing Performance of CAENV1730 Digitisers

This behaviour is due to the input frequency to the CLK-IN connector set at 10 MHz. As previously explained, the trigger clock is generated by the AD9510 chip, which must be in phase with the input frequency. However, the trigger clock operates at a frequency of 125 MHz, while the input frequency is at 10 MHz. Since these frequencies are not multiples of each other, they cannot be in phase. To generate an out-of-phase frequency, the AD9510 chip latches onto the first rising edge of the input frequency upon the digitiser initialisation. This results in a random phase offset at the beginning of every run, causing the timestamps to vary from run to run and from board to board.

Comparing the two clock schemes, the daisy chain mode offers better synchronisation across the 8 CAEN digitisers compared to the fan out mode. In the daisy chain scheme, only the first CAEN in the daisy chain receives the external 10 MHz clock. The master clock CAEN digitiser will have a random phase offset that is propagated down the daisy chain, resulting in synchronisation across all digitisers. However, the clock drift effect was observed during the testing the daisy chain scheme and therefore, a correction is necessary.

7.3.3 Clock Jittering Correction

To further characterise the timing of the CAEN digitiser, another study was carried out to verify if all 8 CAEN digitisers can digitise waveform in synchronisation with each other (\mathcal{O} (1 ns). The same setup was used as described in the previous section, with a new addition of digitising the waveform of the trigger signal in channel 15 of every CAEN digitiser. All the cable lengths were identical so that all trigger signals took the same amount to propagate to the digitisers. The daisy chain clock scheme was also calibrated so that the clock propagation from the master clock to the slave clock was delayed by a precise amount such that their clocks were exactly in phase. This was to ensure that trigger signals were simultaneously timestamped and digitised.

Examples of digitised waveforms of trigger signals are plotted in Fig. 7.13a for four digitisers, where the trigger signals can be seen as a single square wave per digitiser. To examine if trigger signals were digitised simultaneously, zooming into the rising edges of the trigger signals is plotted in Fig. 7.13b. Board 3, 5 and 9 are in synchronisation except for board 7. The rising edge of board 7 is at a different location compared to other boards, showing that its clock jittered. This behaviour although did not occur frequently, was unpredictable and could appear across different events, different runs and different boards. Therefore, a jittering correction was devised to account for clock jittering scenarios.

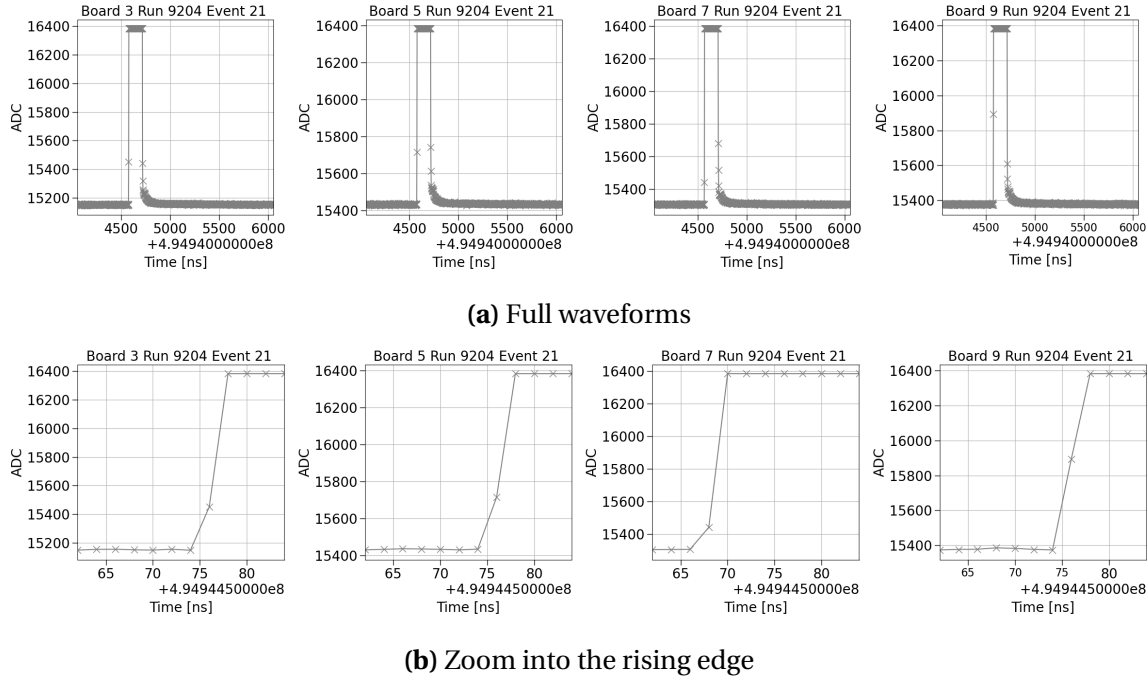


Fig. 7.13 Digitised waveforms trigger signals, including (a) full waveforms and (b) zoom into the rising edge.

The timestamp of the rising edge of trigger signals digitised by CAEN digitisers is then compared against the timestamp recorded by the SPEC-TDC of the same trigger signal. This comparison helps the understanding of the clock jittering behaviour of the CAEN digitiser. Three identified cases of jittering are illustrated in Fig. 7.14a. The trigger waveform is plotted in grey, the rising edge is marked with a red cross and the timestamp of the trigger recorded by the SPEC-TDC is plotted as the vertical green line.

In the far left plot, the timestamp of the rising edge and the SPEC-TDC agree with each and hence, the red cross and the green line align. The middle left plot shows the first case of clock jittering of one whole tick, equivalent to 2 ns. This is due to the ADC sampling clock jitters while the triggering clock remains stable, resulting in a different tick value of the rising edge. In the second case, the opposite situation arises such that the tick value of the rising edge is stable however the trigger clock jitters in the step of 8 ns. This is illustrated in the middle right plot, where the rising edge and the SPEC-TDC differ by exactly 8 ns. The last case is the combination of jittering from both clocks. This is shown in the far right plot, where the difference between the rising edge and the SPEC-TDC is equal to the sum of the trigger and ADC sampling clock tick, totalling at 10 ns.

7.3 Timing Performance of CAENV1730 Digitisers

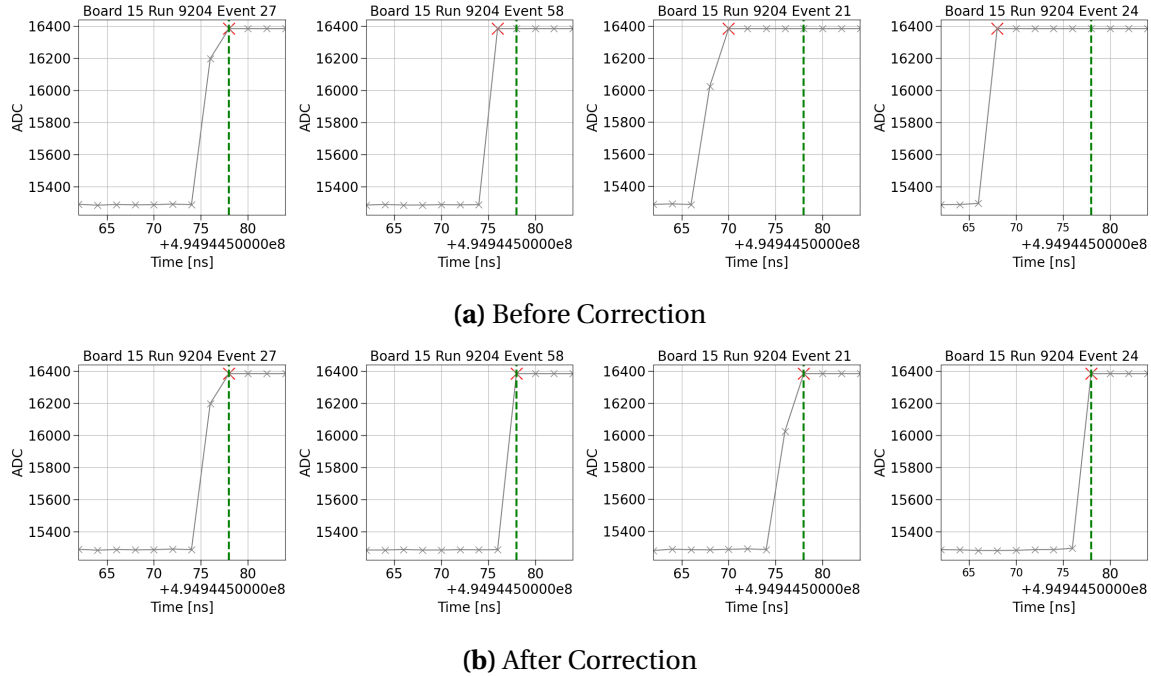


Fig. 7.14 Digitised waveforms of trigger signals zoom into the rising edge (a) before correction and (b) after correction.

This comparison exercise also demonstrated a possible clock jittering correction. By digitising the trigger signal synchronously on every digitiser, the recorded waveform of the trigger in combination with the SPEC-TDC provides all the necessary information to apply correction. One can simply derive the correction amount by performing the comparison as above. The digitised trigger waveforms after applying correction are illustrated in Fig. 7.14b.

This correction method was validated using multiple runs over one month. Each run duration varied from less than 1 hour up to 10 hours. Fig. 7.15a demonstrated the results conducted on a dataset of 30 runs, showing the 1D histogram of the difference between the timestamp of the rising edge as compared to the SPEC-TDC. The plots are area normalised to compare across different run durations. Before correction, some amount of jittering can be seen across different digitisers, events and runs, with peaks at 4 and 8 ns. The correction was first applied event by event, as shown in Fig. 7.15b. Then, the correction was applied run by run, as shown in Fig. 7.15c. The result is a perfect alignment between the CAEN digitisers and the SPEC-TDC, with their differences forming a single peak at 0 ns.

Timing Performance of the Data Acquisition System

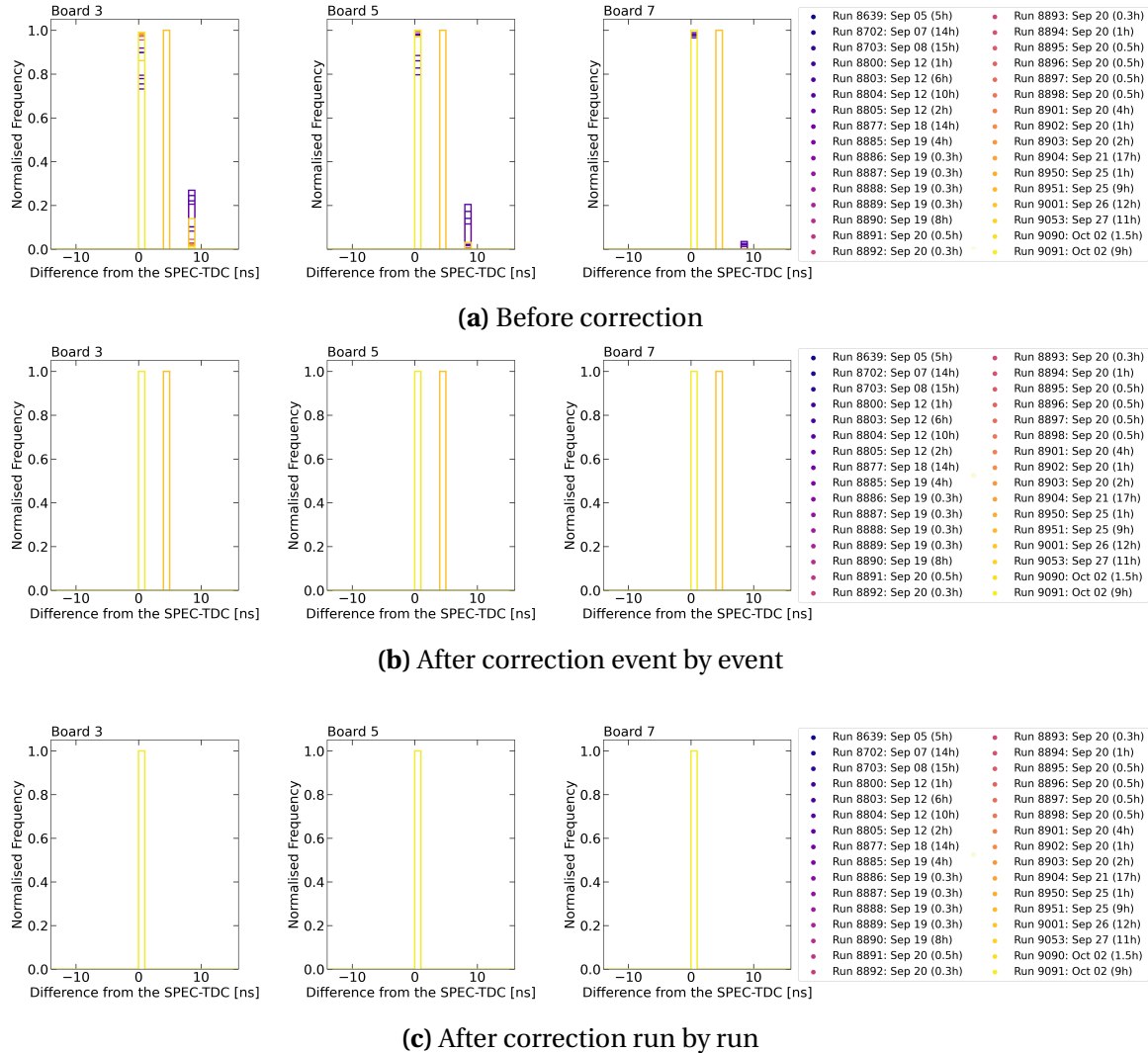


Fig. 7.15 Differences in trigger timestamps between CAEN digitisers and the SPEC-TDC at each correction step.

This clock jittering study presented here has resulted in a new hardware proposal at SBND. The proposal is to digitise the trigger signal in channel 15 of every CAEN digitiser as this will provide the necessary timing information for downstream jittering correction. Further adjustment to the proposal includes an additional CAEN digitiser specifically for digitising beam signals. This is vital timing information needed by downstream analysis to reconstruct the BNB substructure as demonstrated by the MicroBooNE collaboration [121].

At the time of writing, several changes have happened to the clock setup of CAEN digitisers. Firstly, further consultation with the CAEN manufacturer led to a new clock

7.4 Concluding Remarks

synchronisation scheme. A 6.25 MHz clock is now distributed in a fan out mode to every digitiser. Even though it is a lower frequency than 10 MHz, it is a multiple of both the trigger clock, 125 MHz, and the ADC sampling clock, 500 MHz. The same clock synchronisation study was performed and the digitised trigger waveforms show a good agreement to the SPEC-TDC within 1 ns. This configuration shows an improvement in clock synchronisation and stability than the two methods explored in Sec. 7.3.2. Secondly, digitised waveforms trigger signals, as shown in Fig. 7.13 and 7.14, were evidently saturated. Hardware attenuators were installed, followed by an adjustment of the waveform signal. This ensures to capture of the full shape of the trigger waveforms without damaging the digitisers.

7.4 Concluding Remarks

The timing system at SBND was outlined, detailing the signal distribution to ensure synchronisation across different DAQ subsystems. As part of the timing system, the SPEC-TDC module records extra timing information applicable for versatile usages. The SPEC-TDC has been demonstrated to characterise the timing of the CRT and PMT readout electronics as well as to explore alternative timing reconstruction to reconstruct the beam structure. Most importantly, it was used to examine the clock synchronisation of CAEN digitisers and helped devise a correction method to account for clock jittering. This is a crucial correction as PMT waveforms are the main signals to perform nanosecond timing reconstruction. In the following, the next Chapter 8 will focus on the calibration of the SBND detector, which is another essential step to pin down detector effects affecting physics measurement accuracy.

Chapter 8

Calibration of Time Projection Chambers

Calibrating the Time Projection Chamber (TPC) is a crucial step to study and correct for physics processes and detector effects impacting the deposited charges on wire planes. Key processes affecting the production, propagation and detection of ionisation electrons were detailed in Chapter 3, including recombination, diffusion, electron attenuation and Space Charge Effect (SCE). These effects have been well-studied by other LArTPC experiments like MicroBooNE [51, 122], ArgoNeuT [60], and ICARUS [64, 123]. Their results have demonstrated an improvement in the spatial, temporal, and energy resolution of charge signals after correcting for these effects, illustrating the importance of calibration to achieve high precision measurements.

Two Monte Carlo (MC) studies within the scope of charge calibration are presented in this chapter, focusing on electron attenuation and recombination. The first study of electron lifetime measurement is presented in Section 8.1. The second study is an assessment of the impacts of delta ray fluctuations on recombination, given in Section 8.2. Finally, Section 8.3 concludes the chapter with some remarks.

8.1 Electron Lifetime Measurement

Drifting electrons can be captured by electronegative impurities present in liquid argon, as previously described in Section 3.3.1. The reduction of the number of charges collected on a wire can be modelled as an exponential decay function following Eq. 3.6, where the electron lifetime τ indicates the argon purity level of the detector. A higher electron

lifetime corresponds to a higher purity and vice versa. The electron lifetime can be precisely measured and used to recover the original charge deposition on the wires.

At Short-Baseline Near Detector (SBND), there are several methods to measure the electron lifetime. Firstly, three purity monitors were installed, two inside the cryostat and one outside, which provide quick and real-time monitoring of the argon purity. Another method requires a dedicated extraction of electron lifetime using deposited charges as measured by the wires. This calibration procedure is often performed on a sample of cosmic muons that fully cross the drift distance of the TPC, known as *anode-to-cathode* cosmic tracks. Since they traverse the whole drift distance, they make a good sample to study the charge per unit length dQ/dx dependency on the drift distance. The Micro-BooNE experiment also employed the same anode-to-cathode-crossing cosmic tracks to study and correct for position- and time-dependent response of their TPCs[122].

The study aims to develop a procedure to measure electron lifetime and investigate detector effects that can introduce biases on the lifetime, such as diffusion and SCE. Within the scope of this study, anode-to-cathode cosmic tracks were simulated to perform the lifetime measurement. The procedure for electron lifetime measurement is outlined in Section 8.1.1, followed by Section 8.1.2 describing biases in lifetime measurement due to detector effects.

8.1.1 Electron Lifetime Extraction Procedure

The electron lifetime measurement requires information on the charge per unit length dQ/dx and the respective drift time t_{drift} of that charge cluster arrived at the wire. The charge reconstruction follows the workflow described in Section 6.2, whilst additional calculation is required to deduce the drift time. The drift time is defined as:

$$t_{drift} = \frac{x}{v_d}, \quad (8.1)$$

where x is the location the charge deposition in drift direction (x -axis) and v_d is the drift velocity. At SBND, the drift velocity is expected to be at 0.1563 cm/ μ s at an electric field of 0.5 kV/cm and temperature of 88.4 K. The drift time can be calculated using the time recorded by the TPC readout when a charge cluster arrives at a wire t_m which is defined as [124]:

$$t_m = t_0 - t_{trigger} + t_{drift}, \quad (8.2)$$

8.1 Electron Lifetime Measurement

where t_0 is the time when the particle enters the detector and $t_{trigger}$ is the time when the TPC readout is triggered. For a beam neutrino that triggers the TPC readout, the readout window is configured to align with when the beam arrives at the detector such that $t_{trigger} = t_0$, as illustrated in Fig. 4.8 in Section 4.2.7. On the other hand, a cosmic muon can occur anytime within the readout window and the time when it enters the detector t_0 is unknown.

A *cathode stitching* process was developed by the ProtoDUNE and Pandora collaboration to determine the t_0 of cosmic muons that cross the cathode [124]. This can be applied to any LArTPC experiments that have two TPCs sharing the same cathode. Fig. 8.1 depicts the *stitching* process. The reconstruction algorithm begins with an initial and incorrect assumption of $t_0 = 0$ [124], so that two cosmic track segments, shown by the red and blue lines, appear at the wrong positions in both drift volumes. The algorithm then shifts the drift coordinate in each TPC by an equal and opposite amount until the two segments are *stitched* at the cathode, shown by the black line, to recover the correct t_0 . This method has been implemented in the reconstruction workflow of SBND, and it was applied to reconstruct the sample of anode-to-cathode-crossing tracks in this study.

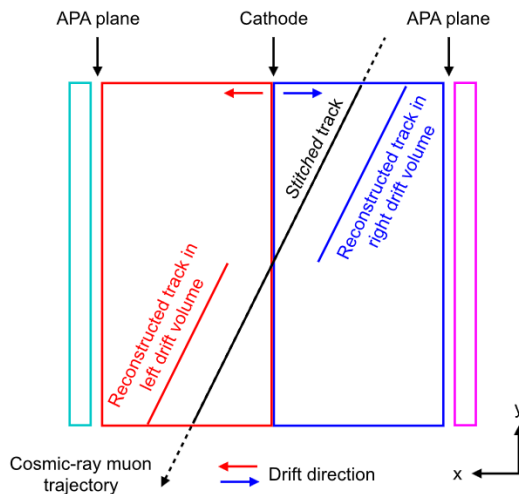


Fig. 8.1 Diagram depicting the cathode stitching process to determine the t_0 of cathode-crossing track [124].

The next step in the lifetime extraction procedure was to plot the charge per unit length dQ/dx in bins of the drift time t_{drift} . Fig. 8.2 shows an example dQ/dx profile in the drift time bin from 0.925 to 0.95 ms. A Landau-Gaussian convolution is fitted to the profile to extract the Most Probable Value (MPV) of dQ/dx [52]. This process was repeated for every drift time bin across the full drift distance of the TPC.

Fig. 8.3 shows the MPV dQ/dx as a function of drift time, for TPC 0 (east) and 1 (west) of SBND. Bins of drift time less than 0.25 ms and larger than 1.15 ms were excluded due to the close proximity to the anode and cathode respectively, which can introduce some boundary effects. The MPV dQ/dx distribution is fitted with Eq. 3.6 to determine the electron lifetime constant. The MC sample input to Fig. 8.3 was simulated with a lifetime of 10 ms and no detector effects enabled to validate the procedure. The lifetimes were determined to be 10.12 ± 0.24 and 10.40 ± 0.29 ms, for TPC 0 and 1 respectively, showing a good agreement between the result and the simulation.

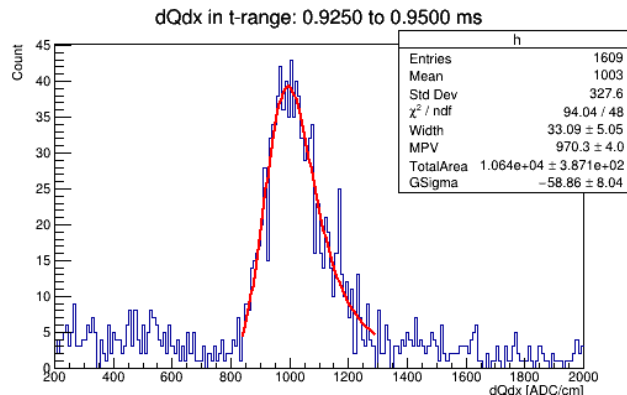


Fig. 8.2 Example of a dQ/dx profile in a drift time bin of 0.925–0.95 ms, fitted with a Landau-Gaussian convolution.

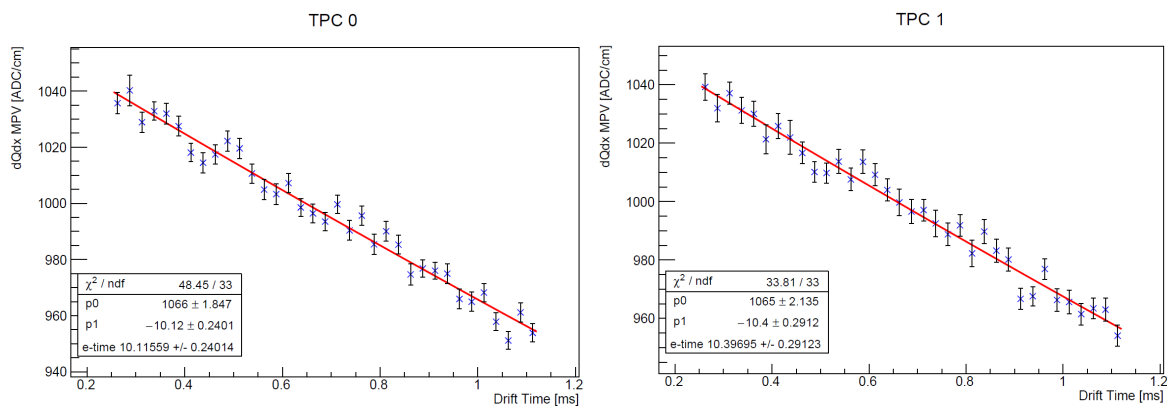


Fig. 8.3 MPV dQ/dx as a function of drift time, fitted with an exponential function.

8.1.2 Bias Study From Diffusion and Space Charge Effects

Some detector effects can introduce biases to the electron lifetime measurement, specifically those that can influence the propagation path of drifting electrons such as diffusion

8.1 Electron Lifetime Measurement

and SCE. Diffusion can smear both spatial and temporal resolution of the drifting electrons, and consequently the number of wires seen by the charge and the arrival time of charge measured by the wires. Meanwhile, SCE impacts both the amplitude of the measured charge as well as the temporal and spatial resolution due to electric field distortion. In view of this, a study was undertaken to understand how each effect introduces biases to the measurement of electron lifetime.

Three dedicated MC samples were simulated: (1) No SCE nor diffusion enabled, (2) only diffusion enabled and (3) only SCE enabled. In the diffusion-only MC sample, the longitudinal diffusion coefficient was set at $D_L = 4.0 \text{ cm}^2/\text{s}$, as measured by MicroBooNE [63], and the transverse diffusion coefficient was set at $D_T = 8.8 \text{ cm}^2/\text{s}$, as measured by ProtoDUNE [65] (See Section 3.3.1 Chapter 3). In the SCE-only MC sample, the simulation of electric field distortion follows the description in Ref. [67].

Biases in the lifetime compared to the simulated lifetime are shown in Fig. 8.4, for two simulated electron lifetimes at 3 ms (top) and 10 ms (bottom). When no detector effects are enabled in the simulation, the determined lifetimes are very similar to the simulated lifetimes, with negative biases well below the 2% level. When either diffusion or SCE was enabled in the simulation, positive biases in the lifetimes can be seen. Biases due to diffusion are at $\sim 2\%$ and $\sim 4\%$ for the simulated lifetimes of 3 ms and 10 ms respectively. On the other hand, biases due to SCE are higher at $\sim 5\%$ and $\sim 22\%$ at the 3 ms and 10 ms lifetime. The observed biases are also consistent across the two TPC volumes of SBND.

The first observation is that the magnitude of the biases due to SCE is much greater than due to diffusion at both simulated lifetimes. This is consistent with the observations from an electron lifetime measurement carried out by MicroBooNE [51]. The paper demonstrated that both SCE and the transverse component of diffusion cause biases in the lifetime, however, biases due to transverse diffusion are smaller in magnitude than SCE. The paper also pointed out that the longitudinal component of diffusion causes insignificant biases in the lifetime.

The second observation is that the longer the lifetime, the larger the biases as compared between the lifetimes at 3 ms and 10 ms. This is most likely due to the precision of this method worsening with increasing lifetimes. Larger lifetime leads to a more uniform dQ/dx distribution across the drift distance, and thus, fitting an exponential function can become less reliable.

Since the results of this study, an investigation at the ICARUS experiment demonstrated that transverse diffusion breaks down the Landau-Gaussian MPV approximation of the measured charge [64], which was employed in this study. This is due to transverse diffusion

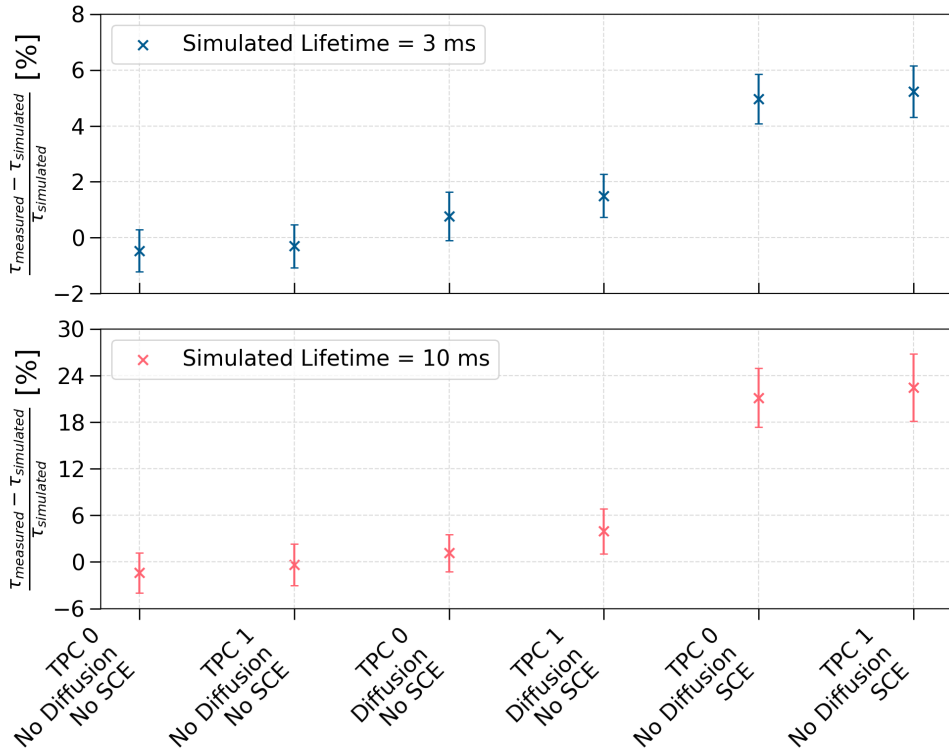


Fig. 8.4 Biases in electron lifetimes compared to the simulated values at 3 ms (top) and 10 ms (bottom).

smearing the charge cluster across multiple wires, resulting in a shift in the MPV value. The paper recommends using an averaged dQ/dx from a group of wires instead of dQ/dx from a single wire to mitigate the effect. The suggestion has now been implemented at SBND.

The study presented here demonstrates a method to measure electron lifetime using a sample of anode-to-cathode crossing cosmic tracks. These tracks have the advantage of spanning over a full drift distance and a reconstructable t_0 time tagging when the particle enters the detector. The electron lifetime measured by this method is the most affected by SCE, followed by diffusion, which is consistent with the results from MicroBooNE. This procedure has now been replicated in preparation for the calibration run of SBND at the time of writing. A trigger requiring coincidence in the east and west CRT wall was deployed to produce dedicated samples containing crossing cosmic muon tracks that can be used for electron lifetime measurement.

8.2 Delta Ray Fluctuations on Recombination Simulation

Recombination is a physics process that drives the charge and light yield as previously described in Section 3.2.3. SBND currently employs the Modified Box (ModBox) model for simulating recombination, with experimentally-derived parameters from ArgoNeuT [60]. The model approximates the recombination probability based on a cylindrical column surrounding a track-like charge deposition, effectively accounting for microphysics processes along the track. This approximation has proven to work well for the MeV to GeV-scale interactions, however, it breaks down at the keV-scale.

Delta rays are microphysics processes that can affect recombination, highlighted by NEST [125] and ArgoNeuT [60] collaborations. They are knock-out electrons with low energy but high energy loss per unit length dE/dx . As shown in Fig. 8.5, delta rays are short tracks produced along a longer primary track, in this case, a cosmic muon. Due to their high dE/dx , they are associated with a smaller recombination factor R (See Fig. 3.6 Section 3.2.3). A smaller R corresponds to a smaller probability of ionisation electrons surviving recombination. As a result, delta rays can lead to non-linear fluctuations in recombination that is not well-described by the ModBox model.

This study is motivated to asses the impacts of delta ray fluctuations on the simulation of recombination, and consequently, the charge to energy loss conversion of different particle types. An overview of the simulation framework of delta rays and recombination is given in Section 8.2.1. In following, Section 8.2.2 and 8.2.3 provides a description of the delta ray impacts on the recombination magnitude and smearing respectively. A summary of recombination studies carried out by the ICARUS collaboration is presented in Section 8.2.4.

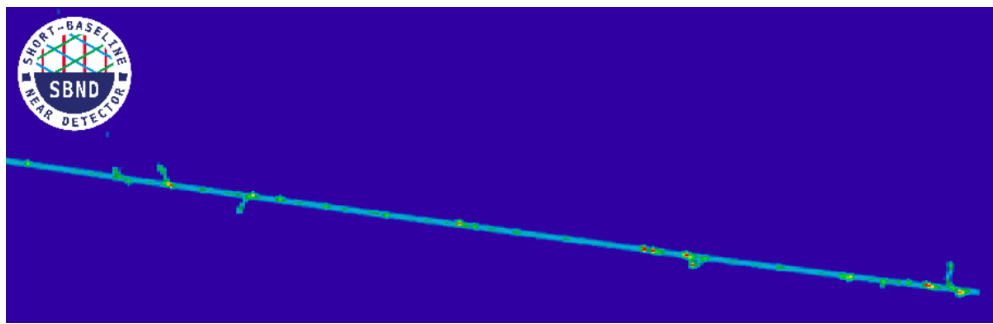


Fig. 8.5 Event display of a simulated cosmic muon track segment, with many delta rays produced along the primary track.

8.2.1 Simulation of Delta Rays and Recombination

Delta rays and recombination are simulated as part of the particle propagation simulation performed by the Geant4 toolkit [101], with details provided in Section 5.4.1. The simulation propagates the primary particle step by step and applies physics processes at each step of length dx . Particularly, this study focuses on the energy loss due to ionisation. It is simulated as two dependent processes: (1) a continuous energy loss dE of the primary particle along the step dx and (2) a discrete energy loss dE at the end of the step producing delta rays [101].

The continuous energy loss of the primary particle is simulated by Geant4 using complementary models depending on the particle Kinetic Energy (KE) [109]. For particles with KE > 2 MeV, the Bethe-Bloch formalism [52], detailed in Section 3.2.1, is used to compute the mean dE/dx . In the intermediate KE range range < 2 MeV, simulation models parameterised on data from Ref. [126] and Ref. [127] are implemented. In the low KE < 1 keV, Geant4 uses the free electron gas model since no data is available.

The discrete energy loss to produce delta rays is determined by a user-defined energy threshold. The energy threshold defines the lower limit of the KE of delta rays so that only delta rays with sufficient energy can be produced. This is to suppress the simulation of all low energy delta rays that would exhaust computation resources. This also means that the energy of the non-produced delta rays is transferred to the continuous energy loss of the primary particle. This is equivalent to setting the energy threshold as the upper limit for the primary particle so that its mean continuous energy loss is less than the threshold.

In Geant4 terminology, the energy threshold is also known as the secondary production threshold, where the minimum KE requirement for delta ray production is defined as the minimum distance the generated delta ray must be able to traverse in a given material. These thresholds will be referred to as *delta ray thresholds* in short from this point onwards in this study. Moreover, the maximum length dx that the particle can propagate per step is configured as 0.3 mm, one order of magnitude smaller than the wire pitch of 3 mm. This setup allows for a feasible computation of generating delta rays.

For each step dx , the number of electron-ion pairs is calculated by dividing the continuous energy loss dE by the ionisation work function of argon $W_{ion} = 23.6$ eV [128]. Then, the recombination factor R is applied to the number of electron-ion pairs according to the charge-light anti-correlation described by Eq. 3.2 and 3.3, to determine the final charge and light yield resulting from the step dx . Using the ModBox formalism, R is computed as

8.2 Delta Ray Fluctuations on Recombination Simulation

[60]:

$$R = \frac{\log(\alpha + (\beta \cdot dE/dx)/\epsilon)}{(\beta \cdot dE/dx)/\epsilon}, \quad (8.3)$$

where ϵ (kV/cm) is the electric field at the position of the step, dE/dx (MeV/cm) is the energy loss per unit length, and parameters $\alpha = 0.93 \pm 0.02$ and $\beta = 0.212 \pm 0.002$ (kV/cm)(g/cm²)/MeV were experimentally derived by ArgoNeuT [60]. Eq. 8.3 is plotted in Fig. 3.6 Section 3.2.3. It is important to note that R is dependent on the electric field and therefore can be influenced by local distortions of the field.

The simulation of delta rays and recombination described here gives rise to some concerns. The first concern is the assumption of a *universal* recombination factor R . The parameters α and β were measured by ArgoNeuT using a stopping proton sample, and wire planes with a pitch of 3 mm [60]. Nonetheless, they are applied to any type of ionising particles, which can influence the local ionisation density differently. Secondly, the delta ray thresholds remove low energy electrons in simulation. However, they are produced in reality and can affect recombination at a local scale.

The study was set up to address the individual concerns outlined above to better understand their impacts on recombination. Identical MC samples of muons and protons were simulated to investigate if recombination is particle-dependent. The particles were generated with a fixed energy of 1 GeV, uniform in positional and angular distributions. The Geant4 simulation was configured such that the particle can only deposit energy via ionisation. The *true* energy per unit length dE/dx was computed from the *true* number of electrons per unit length dQ/dx , where *true* indicates no detector simulations were applied. The computation follows the ModBox formalism for charge to energy loss conversion as [60]:

$$\frac{dE}{dx} = \frac{1}{\beta} \left[\exp\left(\beta W_{ion} \frac{dQ}{dx}\right) - \alpha \right], \quad (8.4)$$

where parameters are the same as Eq. 8.3. For each particle type, a range of delta ray thresholds were simulated. The largest value, and also the current value being used by SBND, was set at 700 μ m, equivalent to delta rays with a minimum KE of 273 keV. The smallest threshold was 1 μ m, enabling the simulation of delta rays with KE as low as 1 keV. This variation was chosen to study the impacts due to delta ray fluctuations.

8.2.2 Impacts of Delta Ray Fluctuations On Recombination Magnitude

Fig. 8.6 shows the simulated charge to energy loss conversion, dQ/dx to dE/dx , for protons at the delta ray threshold of 700 μ m and 1 μ m. The distribution was plotted for

the proton residual range from 1 cm to 90 cm to cover the full track length. The proton dE/dx ranges from 2 MeV/cm to 18 MeV/cm, allowing for the examination of delta ray fluctuation impacts at both low and high parts of the dE/dx spectrum. For the delta ray threshold of 700 μm shown in Fig. 8.6a, the distribution precisely follows the ModBox model with the ArgoNeuT parameters defined in Eq. 8.4. A good agreement is expected since the simulation of SBND is similar to that of ArgoNeuT [60].

However, for the delta ray threshold of 1 μm shown in Fig. 8.6b, deviations away from the ModBox model occur, such that the distribution shifts at both low and high parts of the dE/dx spectrum. Lowering the delta ray threshold leads to more energy loss carried by the delta rays instead of the primary proton, and thus, delta rays have a greater influence on recombination. At the low dE/dx spectrum of the proton, delta rays have higher dE/dx and a smaller recombination factor R than that of the proton. This results in the *effective recombination factor* being reduced, decreasing dQ/dx at the same value of dE/dx . The opposite effect is seen at the high dE/dx spectrum of the proton, where dQ/dx is higher than the ModBox model. This indicates that the effective recombination factor increases, that accounts for both the primary proton and delta rays.

The proton charge to energy loss conversion at the thresholds of 700, 10, 5, and 1 μm , equivalent to delta rays with a minimum KE of 272.58, 14.60, 2.58, 1.06, and 0.99 keV are shown in Fig. 8.7. To compare dQ/dx quantitatively at the same dE/dx bin, the mean dQ/dx was calculated per dE/dx bin as shown in Fig. 8.7a. The percentage difference of the mean dQ/dx relative to the ModBox model is depicted in Fig. 8.7b to quantify the magnitude of the differences.

Lowering the KE of delta rays results in two key trends. Firstly, the dE/dx position at which the proton charge to energy loss conversion shifts in upward/downward directions, increases with lower delta ray KE. This shift position can be seen in Fig. 8.7b. Secondly, the magnitude of the deviations depends on the delta ray threshold. At low $dE/dx < \sim 8$ MeV/cm, the effective recombination is reduced the most at the 1 μm threshold, as shown in yellow. At high $dE/dx > \sim 8$ MeV/cm, the effective recombination is the highest at the 5 μm threshold, as shown in green. This is evidence that delta ray fluctuations can greatly influence the proton charge to energy loss conversion. The more energy loss is carried away by very low KE delta rays, the more distorted the charge to energy scale becomes.

The charge to energy loss conversion for muons is plotted in Fig. 8.8, for the delta ray threshold at 700 μm and 1 μm . Fig. 8.8a and 8.8b contain the full muon residual range, covering the track length 1–400 cm. Two distinct distributions can be seen here, one linear from the Minimum Ionising Particle (MIP) region, and another one that follows the

8.2 Delta Ray Fluctuations on Recombination Simulation

ModBox model indicating the stopping region. The linear charge to energy loss conversion of MIP muons has been well-observed by LArTPC experiments, including MicroBooNE [122] and ICARUS [123].

To examine only the stopping region, a residual range requirement of less than 10 cm was applied, as shown in Fig. 8.8c and 8.8d. The effects of lowering the delta ray can be seen by comparing the two figures. The same behaviour as protons at the same low $dE/dx < \sim 8$ MeV/cm is observed, where low energetic delta rays result in a smaller effective recombination factor, reducing dQ/dx at the same value of dE/dx .

The mean dQ/dx of muons and its percentage difference relative to the ModBox model are also shown in Fig. 8.9, at various values of delta thresholds. Similar to protons, the magnitude of the effective recombination reduction increases with lower delta ray KE.

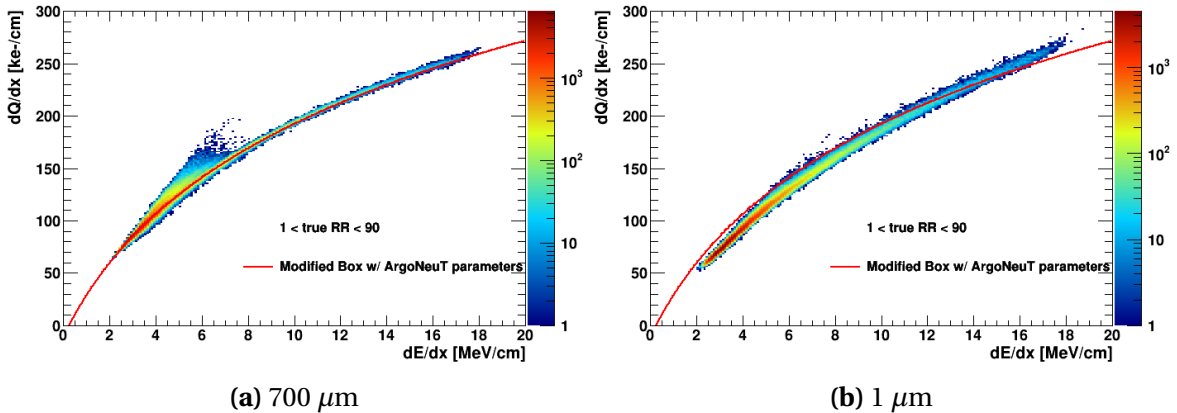


Fig. 8.6 dQ/dx as a function of dE/dx for a 1 GeV proton at the delta ray threshold of (a) 700 μm and (b) 1 μm .

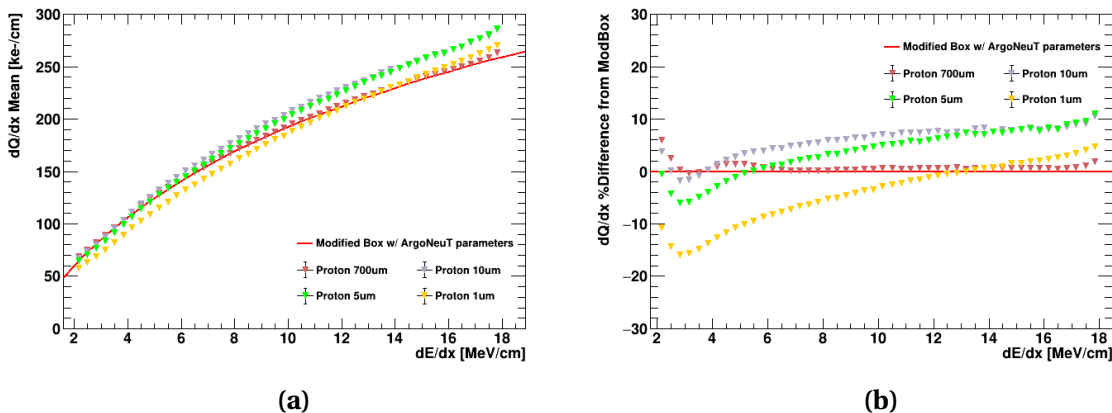


Fig. 8.7 (a) Mean dQ/dx and (b) its percentage difference relative to the ModBox model as a function of dE/dx for a 1 GeV proton.

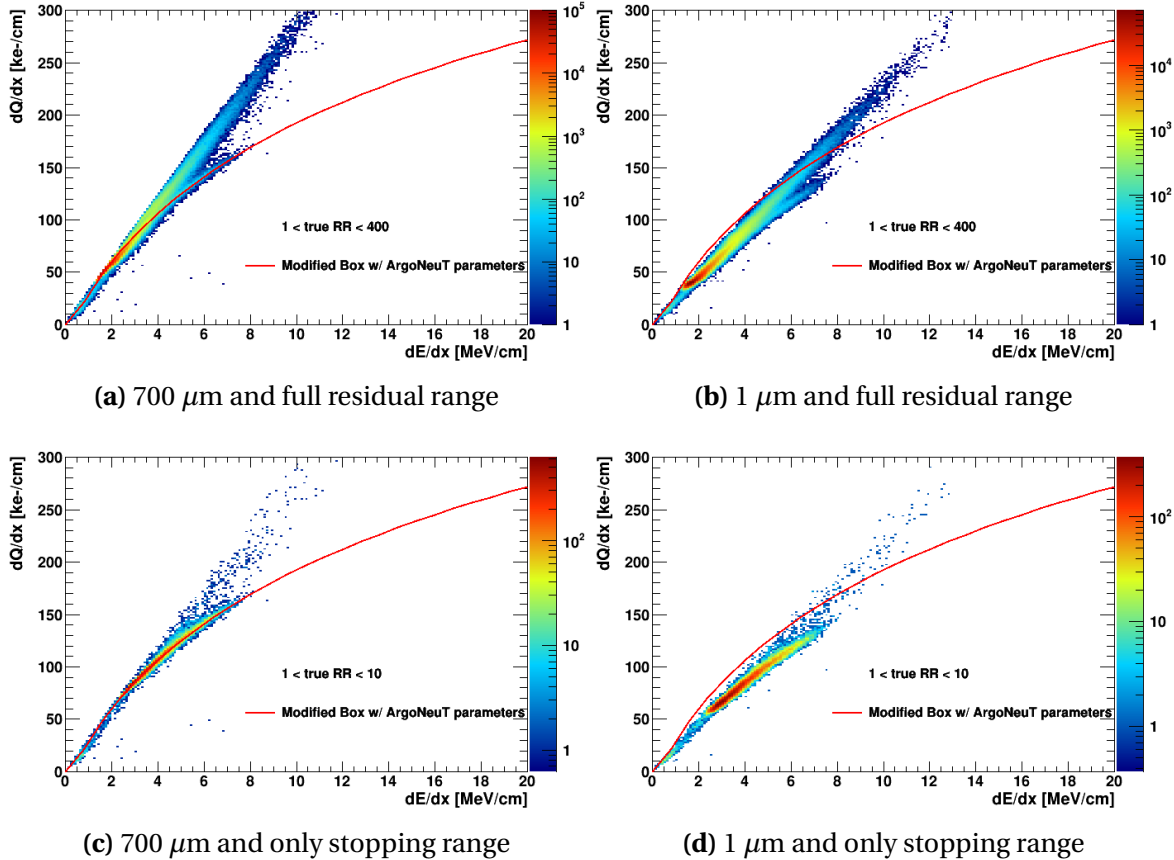


Fig. 8.8 dQ/dx as a function of dE/dx for a 1 GeV muon at the delta ray threshold of 700 μm (left) and 1 μm (right) and for the full residual range (top) and only the stopping range (bottom).

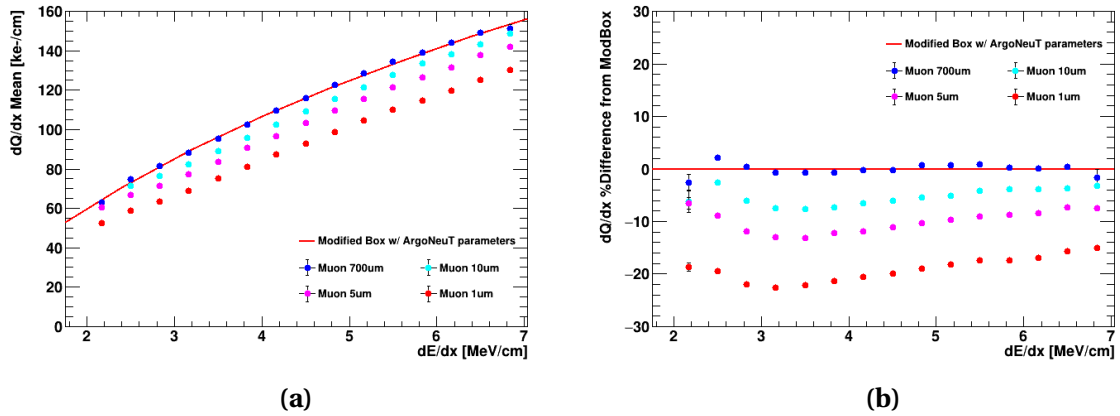


Fig. 8.9 (a) Mean dQ/dx and (b) its percentage difference relative to the ModBox model as a function of dE/dx for a 1 GeV muon.

8.2 Delta Ray Fluctuations on Recombination Simulation

The recombination factor is also the most affected at the threshold of $1 \mu\text{m}$, as shown in red. It is also important to note that the magnitude of the reduction is larger for muons compared to protons, which is likely due to the amount of delta rays produced by each particle type. For instance, at the same dE/dx of 3 MeV/cm and the threshold of $1 \mu\text{m}$, the percentage difference is at $\sim 24\%$ for muons and $\sim 16\%$ for protons.

The study here demonstrates that fluctuations of delta rays can affect recombination. Delta rays have a different dE/dx compared to the primary particle and therefore, can influence the effective recombination factor. At low $dE/dx < \sim 8 \text{ MeV/cm}$, this results in an overall reduction of recombination. Meanwhile, at high $dE/dx > \sim 8 \text{ MeV/cm}$, delta rays can increase the effective recombination factor. This leads to a distortion of the observed charge to energy loss conversion of a particle. The magnitude of recombination is more significant for muons than protons.

8.2.3 Impacts of Delta Ray Fluctuations On Recombination Smearing

Delta ray fluctuations affect not only the magnitude of the recombination factor but also its smearing, and consequently, the smearing of the charge to energy loss conversion. To disentangle how the Geant4 toolkit handles the smearing due to delta rays, an additional study was carried out in which the energy deposition of the primary particle was isolated from delta rays.

Fig. 8.10 shows the simulated dE/dx of the primary proton as a function of its residual range, compared against the Landau-Vavilov distribution [52]. Energy loss due to delta rays is included in the top two plots, Fig. 8.10a and Fig. 8.10b, for the delta thresholds of $700 \mu\text{m}$ and $1 \mu\text{m}$. Meanwhile, the bottom two plots, Fig. 8.10c and Fig. 8.10d, only include the energy loss of the primary proton and do not account for the energy loss of delta rays. The same set of plots for the case of muons are also shown in Fig. 8.11.

When delta rays are included in the energy loss, the dE/dx distribution agrees with the Landau-Vavilov distribution with some smearing in dE/dx across all residual range bins. The energy distributions are indistinguishable between the delta ray threshold of $700 \mu\text{m}$ and $1 \mu\text{m}$. This can be seen for both protons, comparing Fig. 8.10a and Fig. 8.10b, and muons, comparing Fig. 8.11a and 8.11b. The behaviour is expected since the total energy loss of the primary particle and the delta rays must stay the same regardless of the delta ray threshold. Moreover, comparing the protons and muons, including delta rays in the total energy loss introduces greater smearing in the dE/dx distribution for muons than protons.

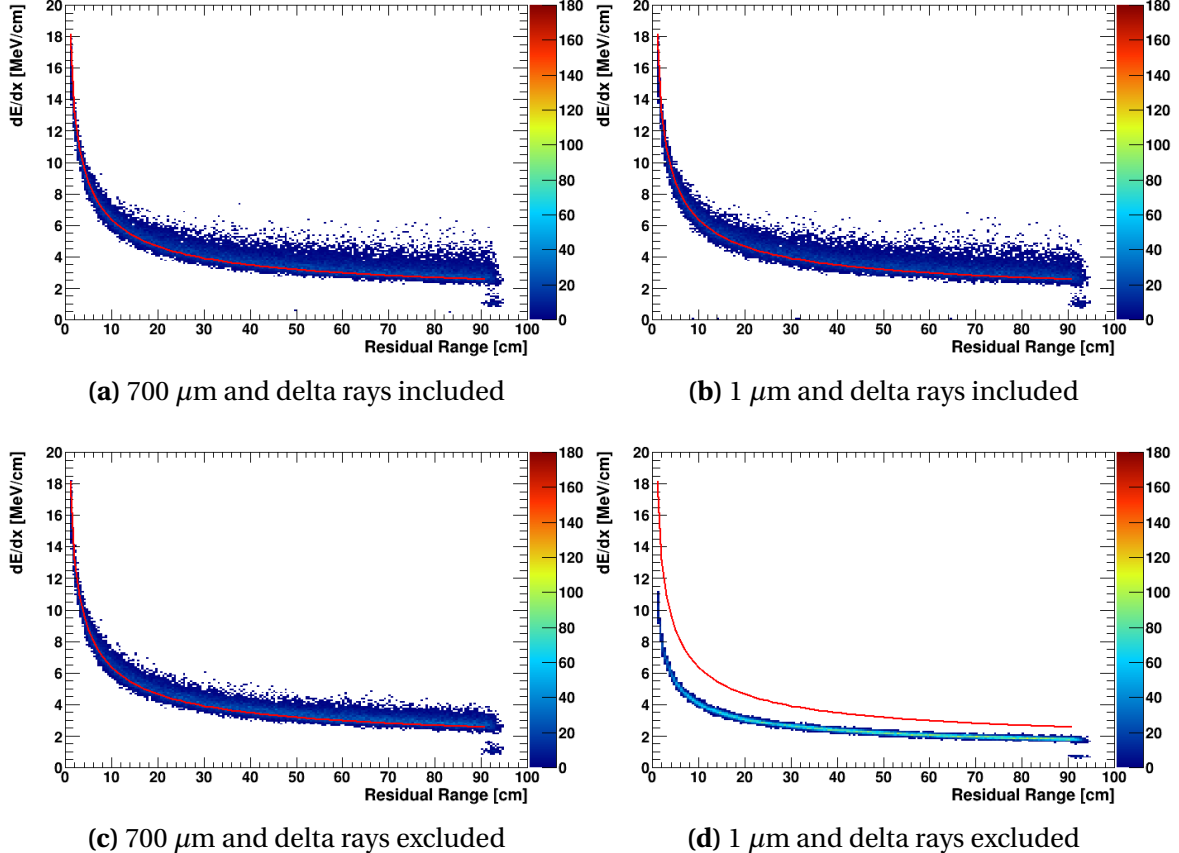


Fig. 8.10 dE/dx as a function of residual range for a 1 GeV proton at the delta ray threshold of 700 μm (left) and 1 μm (right), including (top) and excluding (bottom) the energy loss of delta rays.

When delta rays are excluded in the energy loss, some noticeable effects can be seen. At the threshold at 700 μm , the dE/dx distribution of only the primary particle but no delta rays still follows closely the Landau-Vavilov distribution, similarly to the dE/dx distribution containing both the primary particle and delta ray energy loss. This can be seen comparing Fig. 8.10a and Fig. 8.10c for protons, and comparing Fig. 8.11a and 8.11c for muons. However, less smearing in dE/dx is observed when delta rays are excluded in the energy loss, especially visible in Fig. 8.11c for muons. At this configuration, the majority of the energy loss is carried away by the primary particle, and Geant4 already accounts for delta ray fluctuations when sampling its mean energy loss [101]. Introducing energy loss by delta rays only adds some additional smearing to the total dE/dx distribution.

On the other hand, when the delta ray threshold is set to 1 μm and no delta rays are considered, the dE/dx distribution of only the primary particle becomes narrow without

8.2 Delta Ray Fluctuations on Recombination Simulation

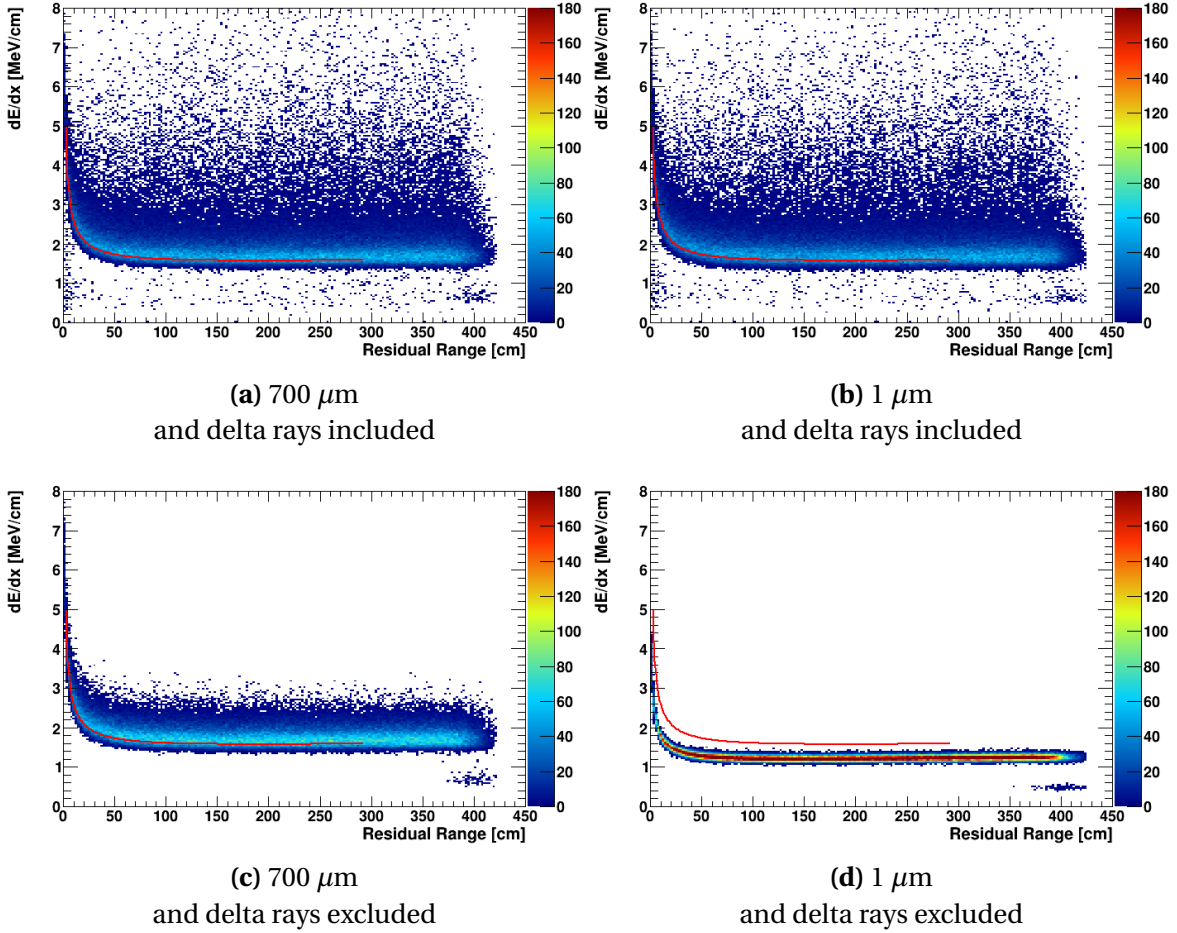


Fig. 8.11 dE/dx as a function of residual range for a 1 GeV muon at the delta ray threshold of 700 μm (left) and 1 μm (right), including (top) and excluding (bottom) the energy loss of delta rays.

any smearing and fails to follow the Landau-Vavilov distribution. This can be seen in Fig. 8.10d for protons and Fig. 8.11d for muons. Isolating only the energy deposition of the primary particle is equivalent to observing a *bare* proton or muon track without any delta rays produced along its path, which has not been experimentally measured before. In this case, the stopping power distribution of the primary particle is computed by Geant4 using interpolation instead of using data-based parametrisation [101]. This potentially leads to inaccuracy in simulating the energy loss due to ionisation.

This study here demonstrates another effect of delta ray fluctuations on recombination. Having a different dE/dx to the primary particle also means that delta rays can smear the observed charge to energy loss conversion. The amount of smearing vary differently between protons and muons, where including delta rays in the energy loss lead to more

smearing in the dE/dx distribution for muons than protons. Combining with the results from Section 8.2.2, this suggests a need for a particle-dependent recombination factor.

8.2.4 Recombination Studies From The ICARUS Experiment

A very similar study was carried out by the ICARUS collaboration in 2004 in Italy, to investigate delta ray fluctuations impacting recombination and also to compare against their experimental data [123]. The result is shown in Fig. 8.12, showing the recombination factor as a function of the delta ray threshold in MC. The dotted line is the expectation for a MIP muon with a KE of 250 MeV. The recombination factor increases with the threshold and peaks at ~ 0.7 , then decreases with higher thresholds. This result is similar to the observation of the study described above, where the effective recombination factor reduces at small values of delta ray thresholds.

The ICARUS collaboration proposed a few different approaches toward the simulation of recombination so that delta ray fluctuations can be more accurately simulated [123]. The first approach was to simulate *as microscopic as possible*, by simulating delta rays with KE $\mathcal{O}(1 \text{ eV})$ and range $\mathcal{O}(10 \text{ nm})$. However, they concluded that this approach was not feasible. Firstly, the effective recombination factor of a particle always contains effects due to delta rays, and secondly, computing resources are limited. Another proposal was an empirical approach, to choose the best delta ray threshold in simulation to reproduce

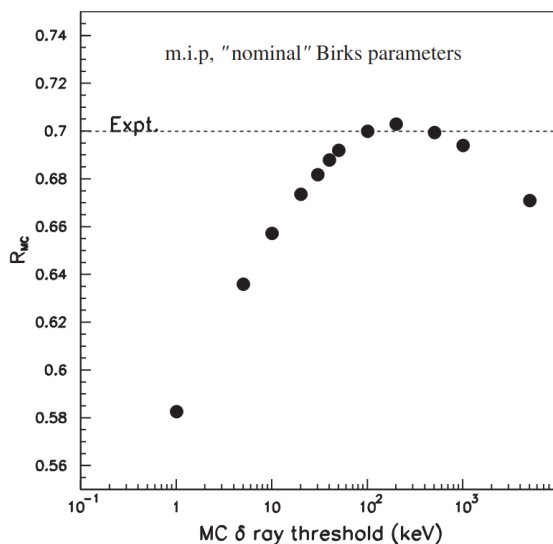


Fig. 8.12 Recombination factor as a function of the delta ray threshold [123].

8.3 Concluding Remarks

the data with a reasonable computing consumption. This number was found to be $3 \mu\text{m}$, equivalent to simulating delta rays having a KE as low as 10 keV.

Also recently from the ICARUS collaboration, now with the detector relocated to Fermilab, a study in 2024 of recombination showed a clear dependence of recombination on the angle of the particle track to the drift electric field [TODO]. A new ellipsoid modified box model of recombination was proposed and able to describe the data across all measured angles. This result has significantly improved the observed charge to energy loss conversion of a particle, which is critical for particle identification of an LArTPC.

These results from the ICARUS collaboration have collectively enhanced the understanding of recombination, as well as guided how to model recombination at SBND. In the scope of calibrating the SBND detector, it is highly recommended to follow a data-driven approach such that the simulation of delta rays and recombination should be tuned to best match the observed data, as done by earlier experiments like ICARUS and ArgoNeuT.

8.3 Concluding Remarks

Two studies within the scope of calibrating ionisation electron signals were presented. The first study described a procedure to measure electron lifetime using anode-to-cathode crossing cosmic muons and quantify biases in the acquired lifetime due to SCE and diffusion. The second study examined the simulation of delta rays and recombination, and how delta ray fluctuations can impact the effective recombination factor and consequently, the charge to energy loss conversion of a particle. These studies help understanding how different detector effects and physics processes can impact the charge depositions on wires, which can be pinned down and corrected for. This calibration process enables high precision measurements, which are essential for any physics analysis at SBND, including the search for HNLs. The following Chapter 9 focuses on the selection of HNLs, of which many reconstruction variables describing the calorimetry and topology of a particle relies on having an accurate charge information.

Chapter 9

Selection of Heavy Neutral Leptons

The selection of Heavy Neutral Lepton (HNL) signals from Standard Model (SM) neutrino and cosmic backgrounds using Monte Carlo (MC) is presented. MC samples were simulated using the framework detailed in Chapter 5 and reconstructed using the framework detailed in Chapter 6. This is the very first exploration of Short-Baseline Near Detector (SBND) physics capabilities to search for HNLs, and this selection provides the first benchmark for understanding the current reconstruction performance of HNL signals based on MC. The selection exploits the boosted topology and late arrival features of HNL signals using the reconstructed charge and light signals from the Time Projection Chamber (TPC) and Photon Detection System (PDS) combined. This set up the ground work that can be carried out on data once the detector is operational.

The following chapter covers details on the selection workflow to identify HNL signals from backgrounds. The foundation of the selection is given in Section 9.1, including a description of signals and backgrounds, the generated MC samples and relevant parameter and distributions to evaluate to selection. The first stage of the selection is to reject cosmic backgrounds as discussed in Section 9.2 and the second stage is to reject SM neutrino backgrounds as discussed in Section 9.3. Then, Section 9.4 contains details the last stage of the selection to identify HNL showers from shower-like backgrounds. The result of the selection procedure is summarised in Section 9.5. A discussion of possible improvements in sensitivity with better timing resolution is detailed in Section 9.6. Finally, some concluding remarks are provided Section 9.7.

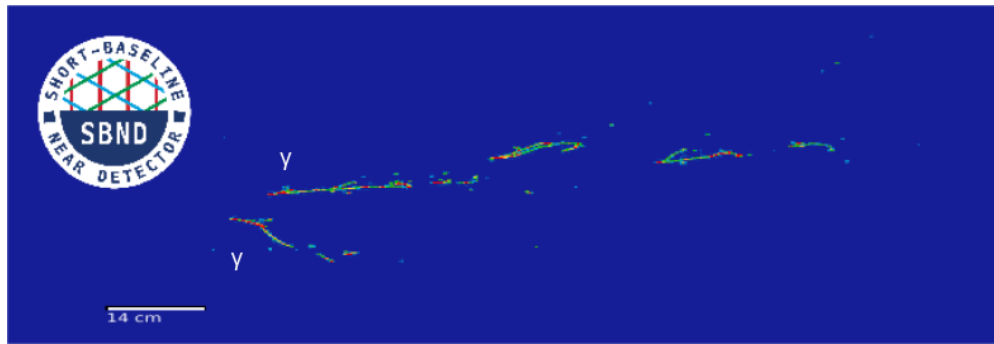
9.1 Selection Introduction

This section provides details of all the ground work before performing the selection. Definitions of signals and backgrounds are presented in Section 9.1.1. Descriptions of MC samples used in the selection are provided in Section 9.1.2. Parameters to evaluate the selection, including definitions of efficiency and the beam bucket distribution, are detailed in Sections 9.1.3 and 9.1.4 respectively.

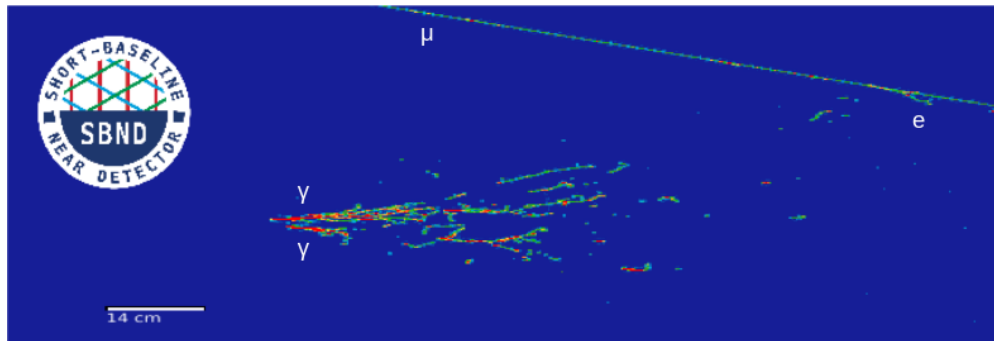
9.1.1 Signal and Background Definition

The selection begins with defining the signal topology, namely $\pi^0 \rightarrow \gamma\gamma$ showers resulting from HNLs decaying inside the Fiducial Volume (FV) of the SBND detector. FV is a smaller volume approximately 70% of the active volume, to be defined in the forthcoming Section 9.3.1. The di-photon showers of HNLs result in one or more showers without any hadronic activities at the vertex. Fig. 9.1a shows an event display of two separable photon showers, where each shower can be seen distinctively. In the case where only a single shower is reconstructed, two scenarios can happen. The first scenario is that only a single photon shower deposits energy inside the detector while the other one escapes. The second scenario is that the di-photon showers are very boosted and forward-going. Fig. 5.4 in Section 5.2 shows that the angle of π^0 to the beam direction is very small $< 20^\circ$ for HNLs in the mass range of 140–260 MeV. Thus, the resulting di-photon showers can overlap each other, in which case the opening angle between the two showers is too small to be reconstructed as two distinct showers. Fig. 9.1b shows an event display of very boosted di-photons showers, which are likely to be reconstructed as a single energetic shower.

Given this signal topology, the first-order background topology from SM neutrinos is Neutral Current interactions that produce π^0 (NC π^0). This interaction type also produces di-photon showers with little or no hadronic activities at the vertex. The second-order background topology is from Charged Current electron (anti-)neutrinos (CC ν_e) interactions. This interaction type typically produces one or multiple hadrons in addition to a single shower. However, in some scenarios, the hadrons are too low in energy to be reconstructed, resulting in a single shower topology after reconstruction. Fig. 9.2 shows an event display of the observable di-photon showers from NC π^0 interaction, which is indistinguishable from the di-photon showers from HNLs. The key distinction separating HNL showers from these SM neutrino showers is the boosted topology of HNL showers, where HNL di-photon showers have smaller opening angles and tend to travel preferably in the beam direction.



(a) Separable di-photon showers



(b) Overlapped di-photon showers

Fig. 9.1 Event displays showing two common topologies of simulated di-photon showers from HNLs.

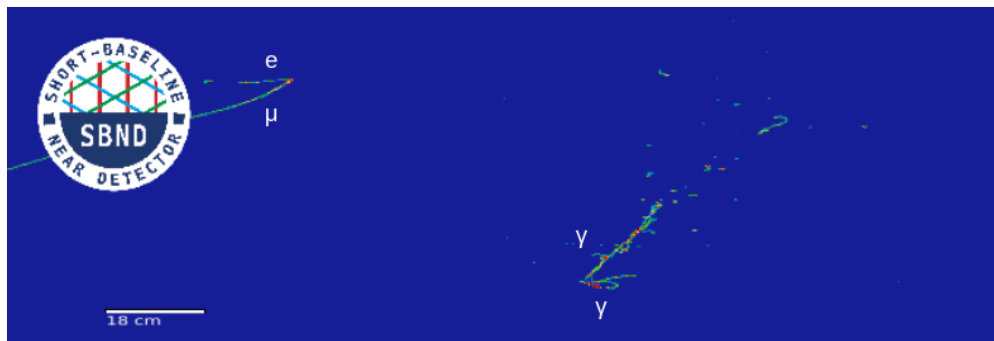


Fig. 9.2 Event display showing di-photon showers from a simulated NC π^0 interaction and a cosmic stopping muon.

SM neutrino interactions can occur outside the FV, but their products can have sufficient energy to propagate inside the FV. Interactions occurring outside the FV but inside the detector volume are referred to as Non-FV interactions. Interactions occurring completely outside the detector volume are referred to as dirt neutrino interactions. As previously discussed in Section 5.3.1, despite interacting outside of the FV, these interac-

tions can introduce non-negligible backgrounds, especially if their products also contain showers in the final states.

Finally, any background interactions that produce tracks are considered low-priority backgrounds since a track topology is easily distinguishable from a shower topology. From SM neutrinos, these interactions are from Charged Current muon (anti-)neutrinos (CC ν_μ) or any Neutral Current interactions that do not produce a neutral pion (Other NC). Fig. 9.3 shows an event display of a common observable from CC ν_μ interactions containing 1 muon and 1 proton in the final state. Similarly, cosmic muons typically leave very long tracks crossing the entire detector with features of delta rays or Michel electrons (See Sections 8.2 and 3.2.1). Fig. 9.1b (top right) and Fig. 9.3 (bottom left) both show a long cosmic track with some delta rays along the track. Fig. 9.2 (top left) shows a cosmic muon coming to a stop and decaying into a Michel electron.

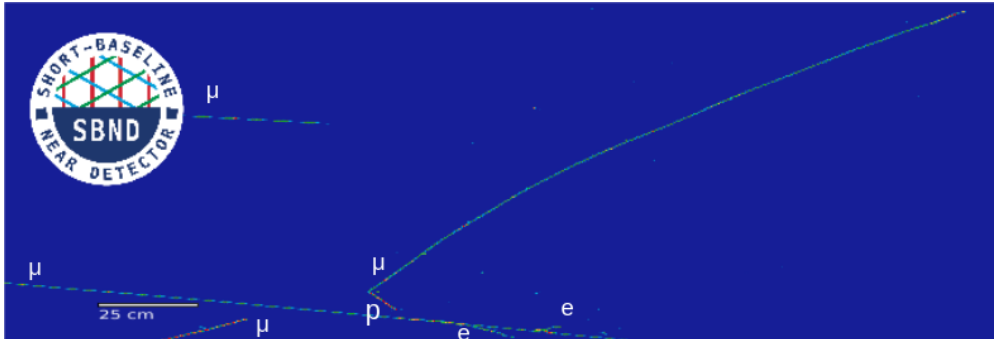


Fig. 9.3 Event display showing a muon and a proton track from a simulated CC ν_μ interaction together with a few cosmic muons.

9.1.2 Description of MC Samples

HNL signals were overlaid with cosmic muons occurring within the TPC readout window. Samples at the HNL mass of 140, 160, 180, 200, 220, 240 and 260 MeV were generated, totalling 7 samples with 60,000 events per sample. The number of events per sample can be re-weighted from the simulated coupling $|U_{\mu 4}|^2$ to another coupling $|U'_{\mu 4}|^2$ by applying a weight as follows:

$$w = \left(\frac{|U_{\mu 4}|^2}{|U'_{\mu 4}|^2} \right)^2. \quad (9.1)$$

Eq. 9.1 allows for the signal scaling required to perform the limits setting in Chapter 10.

Three samples of SM neutrinos were also generated. The first one is a core sample with all SM neutrino interactions occurring inside the detector volume as well as outside the

9.1 Selection Introduction

detector in the *Rockbox* volume, as discussed in Section 5.3.1. Two additional dedicated samples of enriched NC π^0 and CC ν_e backgrounds were also generated, to improve the limited statistics of these interactions in the core sample. The three samples were normalised to an exposure of 1×10^{21} Protons On Target (POT) to account for 3 years of data taking. This yields $\sim 331,000$ NC π^0 interactions and $\sim 33,000$ CC ν_e interactions which are the primary background. Other background from CC ν_μ and Other NC interactions make a total of ~ 5 million interactions. An additional ~ 2 million and ~ 3 million interactions from Non-FV and dirt interactions are also considered as backgrounds, although only a fraction of them deposit energy in the detector.

Finally, a cosmic-only sample was generated to account for in-time cosmics (See Section 5.3.2). This sample consists of events triggered by cosmic-only interactions. However, it is important to note that a dedicated trigger efficiency study will be carried out to better understand the rate of in-time cosmic events once SBND is operational. The cosmic-only sample was also normalised to the target POT, and combined with SM neutrino samples to form a single sample describing the background to the HNL signal.

The unit of the selection relies on *events*, where a single event corresponds to a single trigger (See Fig. 4.8 Section 4.2.7). After reconstruction, each event contains multiple *slices*, which are reconstruction units created by Pandora to describe interactions (See Section 6.2). A slice encapsulates all energy in the TPC from a single origin and consists of a hierarchy of particles starting from the interaction vertex, where each particle can resemble a track or a shower. The equivalent reconstruction unit to a slice from the PDS reconstruction is a *flash*, where a flash contains all the light produced from an interaction (See Section 6.3). The selection is performed on slices, where slices are accepted or rejected based on the series of cuts using the reconstructed information of the slice or by matching a slice to a flash.

9.1.3 Selection Efficiency Definition

For monitoring and quantifying the impacts of selection cuts, selection efficiencies are defined for signals and backgrounds respectively. The selection efficiency is defined as:

$$\text{Signal Efficiency} = \frac{\text{Number of selected signal slices with completeness } > 50\%}{\text{Number of signal slices reconstructed as neutrinos}}. \quad (9.2)$$

In the numerator, the requirement of $> 50\%$ completeness implies that at least 50% of the slice energy must be deposited by a HNL. This prevents double counting, such that only

well-reconstructed signal slices are considered. In the denominator, the requirement for slices to be reconstructed as neutrinos is embedded by the Pandora workflow. As stated in Section 6.2.3, Pandora performs a cosmic rejection very early in the reconstruction so that only neutrino-like slices are reconstructed. The Pandora cosmic rejection is also employed as the first cosmic cut detailed in Section 9.2.1. The denominator describes the starting number of signal slices and the numerator describes the selected signal slices. Thus, Eq. 9.2 describes the efficiency of signals remained after selection.

On the other hand, the background efficiency is defined as:

$$\text{Background Efficiency} = \frac{\text{Number of selected background slices}}{\text{Number of background slices reconstructed as neutrinos}}. \quad (9.3)$$

Here, the background slices encapsulates both SM neutrino and cosmic slices, that are reconstructed by Pandora as neutrino-like slices. The denominator describes the starting number of background slices and the numerator describes number of selected background slices. Eq. 9.3 therefore describe the efficiency of background slices being selected as signals.

The selection aims for a high background *rejection* without compromising the signal *efficiency*. This is equivalent to achieving a low background efficiency defined in Eq. 9.3 and a high signal efficiency defined in Eq. 9.2. Both of these efficiency numbers are discussed for each cut and included in the legends of the upcoming plots.

9.1.4 The Beam Bucket Distribution

The selection workflow was developed by exploiting distinct features of HNLs. One previously stated feature is the boosted topology of HNL showers as discussed in Section 9.1.1. Another feature is the late arrival of HNLs relative to SM neutrinos, as previously depicted in Fig. 5.7 in Section 5.2 showing the arrival time distribution of HNLs and SM neutrinos. The distribution of SM neutrinos resembles a Gaussian-shaped bucket as they travel nearly at the speed of light, whilst HNLs travel at a slower velocity and smear the Gaussian. It is referred to as the *beam bucket distribution* in this work. It is also the key distribution for setting the upper limits on the coupling $|U_{\mu 4}|^2$ of HNLs since it demonstrates the distinct shape difference between the signal and the background, which is required by the setting limits procedure to be discussed in Chapter 10.

To reconstruct the beam bucket distribution, the required information is the flash time matched to a slice that corresponds to the start time t_0 of the interaction, of which the

9.2 Cosmic Background Removal

timing reconstruction is detailed in Section 6.3.1. From the interaction time t_0 , the arrival time at the upstream wall of the detector was computed by shifting from the interaction vertex z -position to $z = 0$. The arrival time corresponds to 81 beam buckets in a single beam spill and thus, to overlay 81 buckets as a single one, a modulus equal to the spacing between buckets is applied. The spacing was measured to be 18.936 by the MicroBooNE experiment [121]. Discussion on different smearing contributors to the beam bucket reconstruction is given in Section 9.6.

The beam bucket distributions are shown throughout this chapter to demonstrate the impacts of the selection. In each plot, HNL signals are plotted as a solid red line while components of backgrounds are plotted as a stacked histogram. Backgrounds include NC π^0 shown in dark blue, Other NC shown in light blue, CC ν_μ shown in green, CC ν_e shown in light purple, dirt neutrinos shown in brown and cosmic muons shown in light grey. The number of slices for each component is also shown in the legend for records.

9.2 Cosmic Background Removal

Cosmic rejection is the first step of selection, targeting two cosmic components: (1) in-time cosmics occurring inside the beam spill and (2) out-of-time cosmics occurring outside the beam spill but inside the readout window (See Section 5.3.2). The cosmic removal by Pandora is the first cut, presented in Section 9.2.1. The beam spill cut is given in Section 9.2.2 and the last cut employing a Boosted Decision Tree (BDT) is provided in Section 9.2.3.

9.2.1 Pandora Unambiguous Cosmic Removal

Being a surface detector, SBND is exposed to a high rate of cosmic rays, expecting ~ 185 million reconstructed slices from cosmics for the POT exposure of 1×10^{21} . As a comparison, the expected rate of reconstructed slices from SM neutrino interactions is ~ 11 million slices. The first cosmic rejection step targets primarily at removing out-of-time cosmic muons. As described in Sections 6.2.3 and 9.1.3, Pandora performs an unambiguous cosmic removal early in the reconstruction chain and only neutrino-like slices are reconstructed. The selection thus begins with selecting only slices reconstructed as a neutrino. This rejects 90% of the ~ 185 million slices from cosmic, leaving behind only 19.5 million slices. Meanwhile, only 0.6% of the reconstructed slices from HNL signals are removed, with similar reductions across different SM neutrino interactions.

9.2.2 Beam Spill Cut

The second cut to remove cosmics is to consider the flash time of a slice, corresponding to the start time t_0 of an interaction. Only slices matched to a valid flash are selected, where the slice-to-flash matching relies on the level of agreement between reconstructed energy from charge and light (See Section 6.4.1). Moreover, the time of the matched flash is required to be within the beam spill window. In the simulation of MC samples, the beam spill window is configured to be between $[0.367, 1.967] \mu\text{s}$, with $t = 0 \mu\text{s}$ corresponding to the first POT of a beam spill. Moreover, an interaction can occur anywhere along the 500 cm z -length of the detector, equivalent to a smearing of 17 ns in timing. Thus, the beam spill acceptance window is widened to $[0.350, 1.984] \mu\text{s}$. The beam spill is illustrated in Fig. 9.4a, with the acceptance window shown as red lines.

The cut rejects 4 million cosmic slices while minimally reducing signal efficiency by 3%. Fig. 9.4b shows the beam bucket distribution after applying the cut, where two components of cosmic rays can be observed. There is a flat distribution coming from out-of-time cosmics and a very small Gaussian-shaped distribution coming from in-time cosmics.

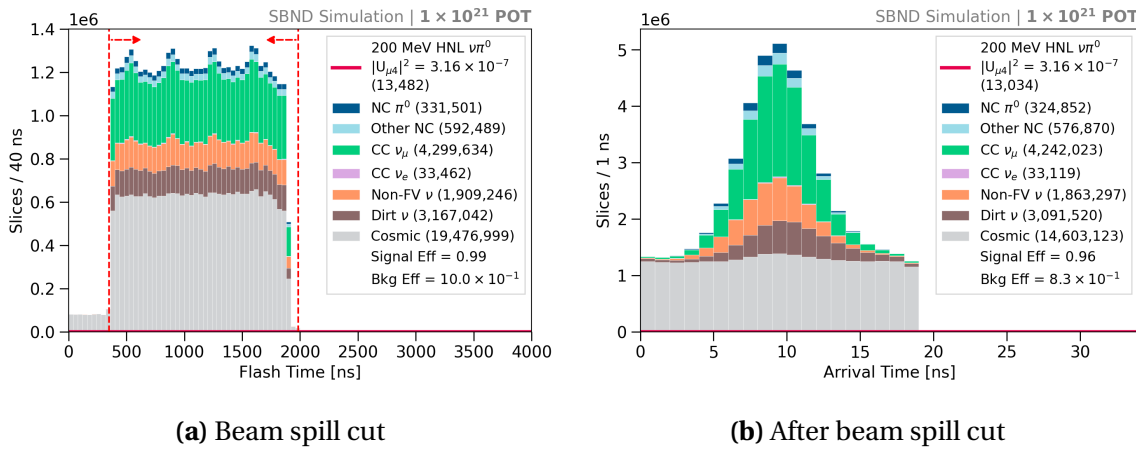


Fig. 9.4 Beam spill cut (left) and the beam bucket after the cut (right).

9.2.3 CRUMBS Cut

The third cut targets the out-of-time cosmic components by employing the CRUMBS score of a slice, which is scored by a BDT to distinguish between a neutrino-like slice and a cosmic-like slice (See Section 6.4.2). The score distribution of CRUMBS is plotted in Fig. 9.5a, showing a good separation between neutrino-like and cosmic-like. A cut is placed to

9.3 Neutrino Background Removal

reject any slices with CRUMBS scores less than 0, effectively removing 14 million of the remaining cosmic slices.

Comparing the beam bucket distribution before and after the CRUMBS cut, Fig. 9.4b and 9.5b, demonstrates that the majority of the removed cosmics are the out-of-time component. The remaining cosmic slices are the in-time component, concentrating at the centre of the beam bucket. This cut results in an effective background rejection as the background efficiency reduces more than half from 8.3×10^{-1} to 3.0×10^{-1} , whilst the signal efficiency only drops by 5%. By the end of the cosmic rejection, only $\sim 432,000$ of the starting 185 million cosmic slices remain, equivalent to a 99.9% removal of the cosmic background alone.

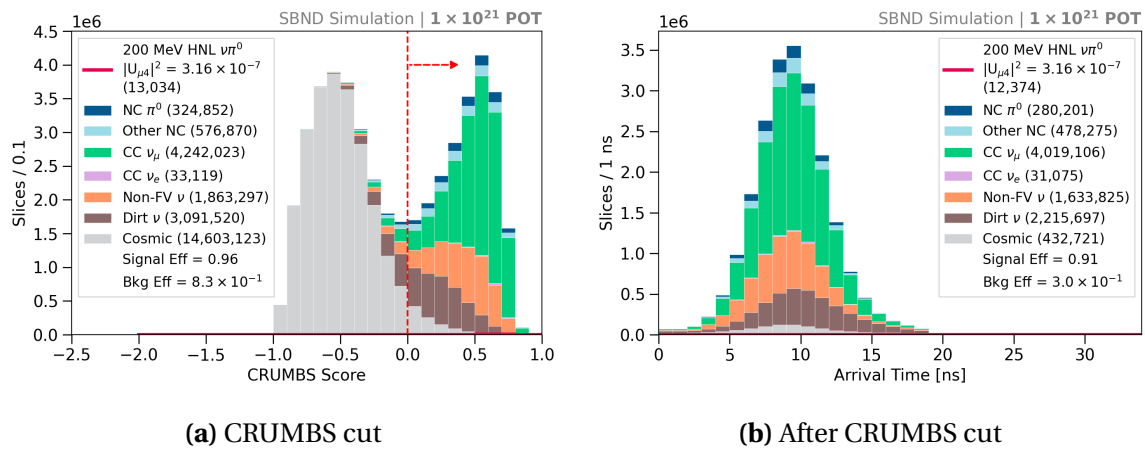


Fig. 9.5 CRUMBS cut (left) and the beam bucket after the cut (right).

9.3 Neutrino Background Removal

The next set made up of three cuts focusing on rejecting backgrounds of SM neutrinos. The cut on detector volume is presented Section 9.3.1. The cut on the reconstruction quality is detailed in Section 9.3.2. Finally, the cut targeting at removing track-like particles from SM neutrino interactions is provided in Section 9.3.3.

9.3.1 Fiducial Volume Cut

The cut on detector volume aims to remove backgrounds from Non-FV neutrinos and dirt neutrinos that interact outside of the FV but for which their products can deposit energy

inside the FV. The cut requires the reconstructed vertex of a slice to be inside the FV, which is approximately 70% of the entire active volume of the detector. The FV is defined as follows:

- x -position: $-180 < x < -5, 5 < x < 180$ cm,
- y -position: $-180 < y < 180$ cm,
- z -position: $10 < z < 450$ cm.

The boundary is set on the x -axis to reject vertices reconstructed close to the anode and cathode. Vertices close to the cathode means the charge clusters must traverse the full drift distance before reaching the anode for detection, therefore, are more susceptible to detector effects (See Section 3.3.1), resulting in poor reconstruction. Meanwhile, vertices close to the anode might also indicate particles entering from the side of the detector which are likely to be cosmic muons and Non-FV/dirt neutrino backgrounds. The boundary on the y -axis rejects interactions that might enter the detector from the top, such as cosmic muons, or bottom, such as Non-FV/dirt neutrinos. Finally, the boundary on the z -axis for $z > 10$ cm rejects entering particles and $z < 450$ cm requires enough downstream volume for a shower to grow. Overall, these cuts ensure the quality of reconstruction.

The distribution of vertices reconstructed inside and outside of the FV is shown in Fig. 9.6a and the result of the cut is demonstrated in Fig. 9.6b. Dirt neutrino slices reduce from ~ 2 million slices to only $\sim 306,000$ slices while Non-FV neutrino slices drop from ~ 1.6 million slices to only $\sim 99,000$ slices. The cut reduces both the background efficiency and signal efficiency by a third as it is consistent with rejecting 30% of the detector volume.

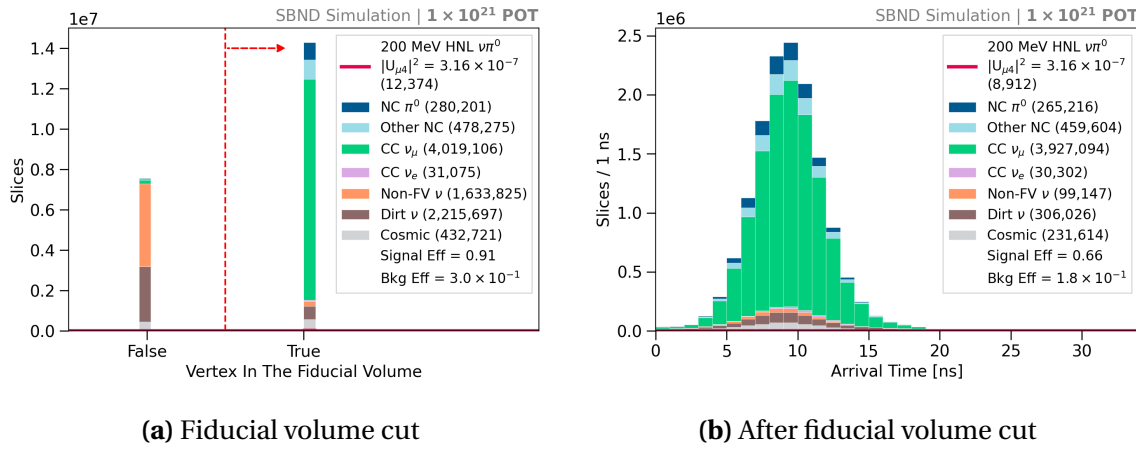


Fig. 9.6 Fiducial volume cut (left) and the beam bucket after the cut (right).

9.3 Neutrino Background Removal

9.3.2 Number of Hits Cut

This cut aims to select well-reconstructed slices by examining the number of hits of the primary particle in a slice that deposits the most energy. The number of hits is particularly important given that Pandora relies on hit information to reconstruct 3D information of particles in a slice (See Sections 6.2.2 and 6.2.3). The more hits associated with a particle, the more information is available for Pandora to reconstruct its topology and calorimetry. The number of hits requirement for the primary particle is ≥ 50 hits to provide sufficient information for a reliable Pandora reconstruction. Fig. 9.7a demonstrates the distribution of the number of hits of the primary particle in a slice. Only the first bin is rejected by this cut, demonstrating that only a small amount of slices containing primary particles with < 50 hits, which are likely to be poorly reconstructed. The beam bucket distribution after the cut is shown in Fig. 9.7b, where it can be seen that the cut reduces the signal and background efficiency by $< 1\%$.

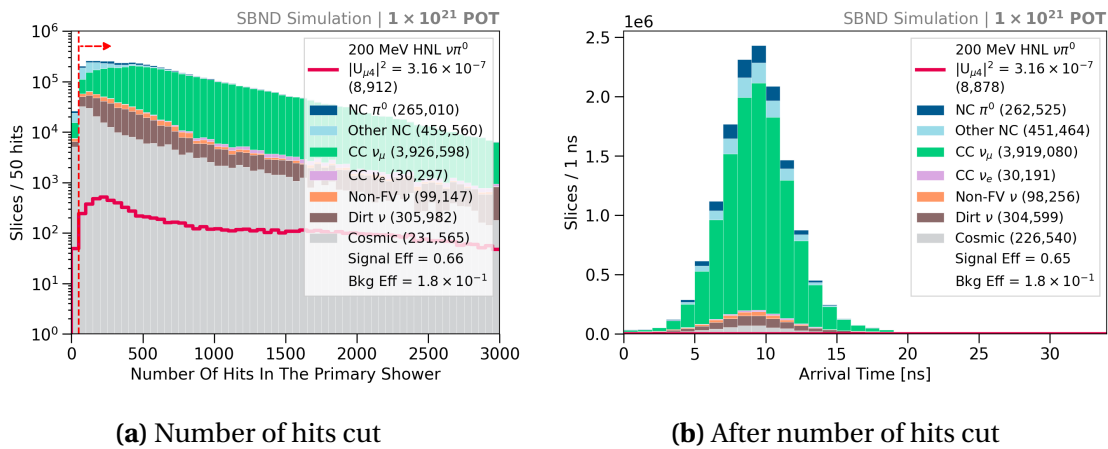


Fig. 9.7 Number of hits cut (left) and the beam bucket after the cut (right).

9.3.3 SM Neutrino Track Removal

The next sets of cuts focus on rejecting SM neutrino backgrounds that produce tracks originating from muons, protons and charged pions. The cut uses the score distribution from the Razzled BDT (See Section 6.4.3). There are two types of Razzled variables examined for this cut: (1) the number of p , μ , π in a slice as identified by Razzled and (2) the Razzled p , μ , π scores of all particles in a slice. The former cut relies on Razzled assigning a type to a particle based on its highest particle type score from the BDT. The latter cut is to further reject slices if they contain particles with a Razzled score higher than a chosen threshold.

Fig. 9.8a and 9.8b demonstrate the two cuts respectively for rejecting muon-like particles. Fig. 9.8a shows the requirement on the number of Razzled-identified muons is 0 while Fig. 9.8b shows that only slices containing particles with Razzled muon score < 0.04 are selected. The cuts are very aggressive without compromising signal efficiency due to the distinction between HNL signals and muon tracks. Comparison between the beam bucket distribution before and after the muon cut, Fig. 9.7b and Fig. 9.8c, can be made to evaluate the impacts of the cut. The muon cut effectively rejects 96% of the 4 million CC ν_μ slices, leaving only $\sim 161,000$ slices remaining. HNL slices are also affected by the cut such that the signal efficiency reduces from 65% to 51%.

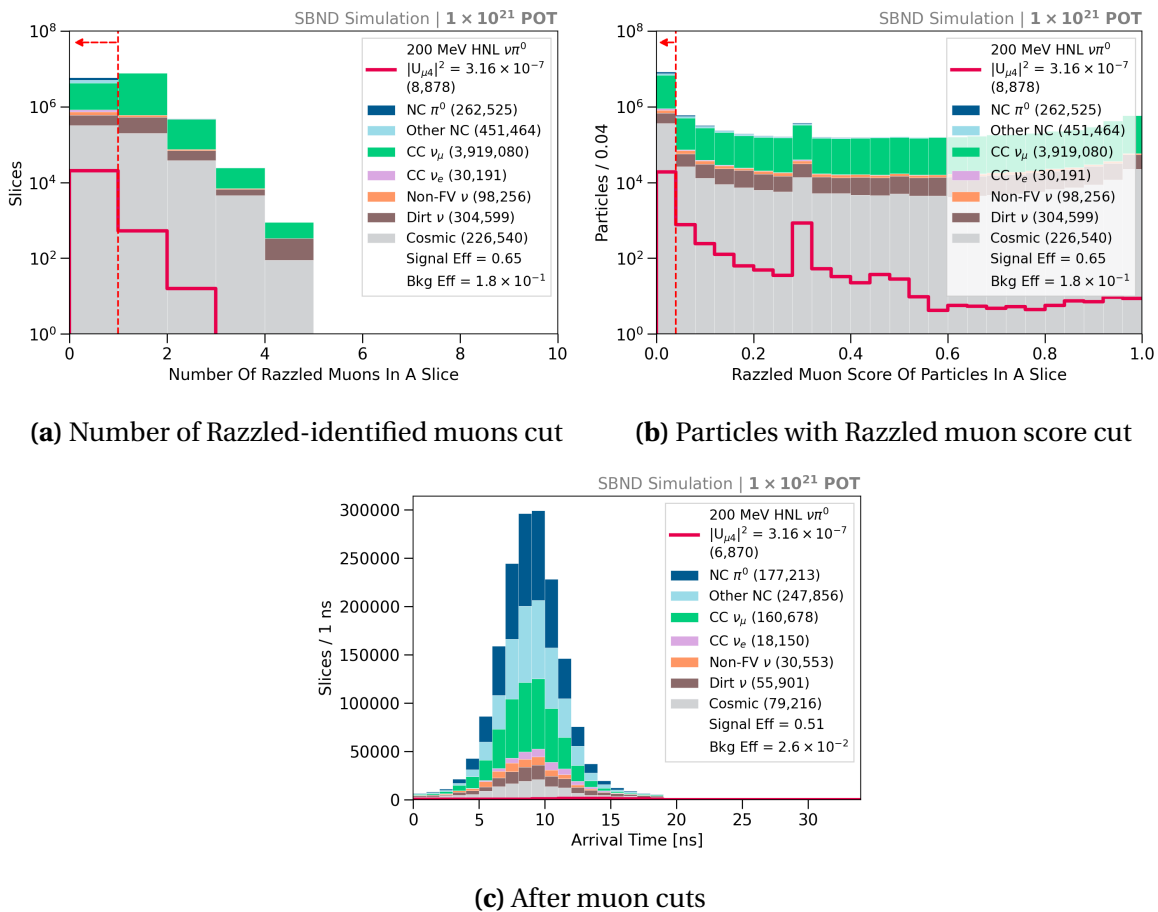


Fig. 9.8 Muon cuts (top) and the beam bucket after the cuts (bottom).

Similar cuts are then applied consecutively to reject protons and charged pions. As with the muon cuts, the cuts on the number of p , μ , π as identified by Razzled in a slice are very aggressive to require that the selected slices not contain any track-like particles. On the other hand, the cuts on the Razzled p , μ , π scores were optimised for each particle type to maximise the background rejection without costing the signal efficiency. Additional

9.3 Neutrino Background Removal

conditions are required on the reconstructed Kinetic Energy (KE) to be > 32.7 MeV for protons and < 32.1 MeV for charged pions to ensure particles are well-reconstructed. The energy requirements were found to identify protons and charged pions more effectively.

The cuts to reject protons are illustrated in Fig. 9.9a and 9.9b. The impacts of the proton cut can be seen in the beam bucket distribution in Fig. 9.9e, as any interactions producing protons are removed, significantly reducing SM neutrino backgrounds. The most impacted interaction modes are Other NC interactions reducing from $\sim 249,000$ to $\sim 17,000$ slices, CC ν_μ interactions reducing from $\sim 161,000$ to $\sim 46,000$ slices and NC π^0 interactions reducing from $\sim 177,000$ to $\sim 88,000$ slices.

The pion cuts are depicted in Fig. 9.9c and 9.9b. The result of the pion cut can be observed in the beam bucket distribution shown in Fig. 9.9f, where the cut further cleans up any SM neutrino slices that are not already rejected by the muon and proton cuts. CC ν_μ interactions are the most affected, decreasing from $\sim 46,000$ to $\sim 30,000$ slices. This is followed by a reduction of Other NC interactions from $\sim 17,000$ to $\sim 9,000$ slices.

To summarise, the cuts to reject muons, protons and charged pions are as follows:

1. Muon cuts:

- Number of Razzled-identified muons in a slice = 0,
- Slices containing only particles with Razzled muon score < 0.04 .

2. Proton cuts:

- Number of Razzled-identified protons with KE > 32.7 MeV in a slice = 0,
- Slices containing only particles with Razzled proton score < 0.96 .

3. Pion cuts:

- Number of Razzled-identified pions KE > 32.1 MeV in a slice = 0,
- Slices containing only particles with Razzled pion score < 0.82 .

The background efficiency at the end of the track removal significantly decreases by two orders of magnitudes from $\mathcal{O}(10^{-1})$ to $\mathcal{O}(10^{-3})$, demonstrating the effectiveness of these cuts. Meanwhile, the HNL signal efficiency only decreases by 65% to 46%.

Selection of Heavy Neutral Leptons

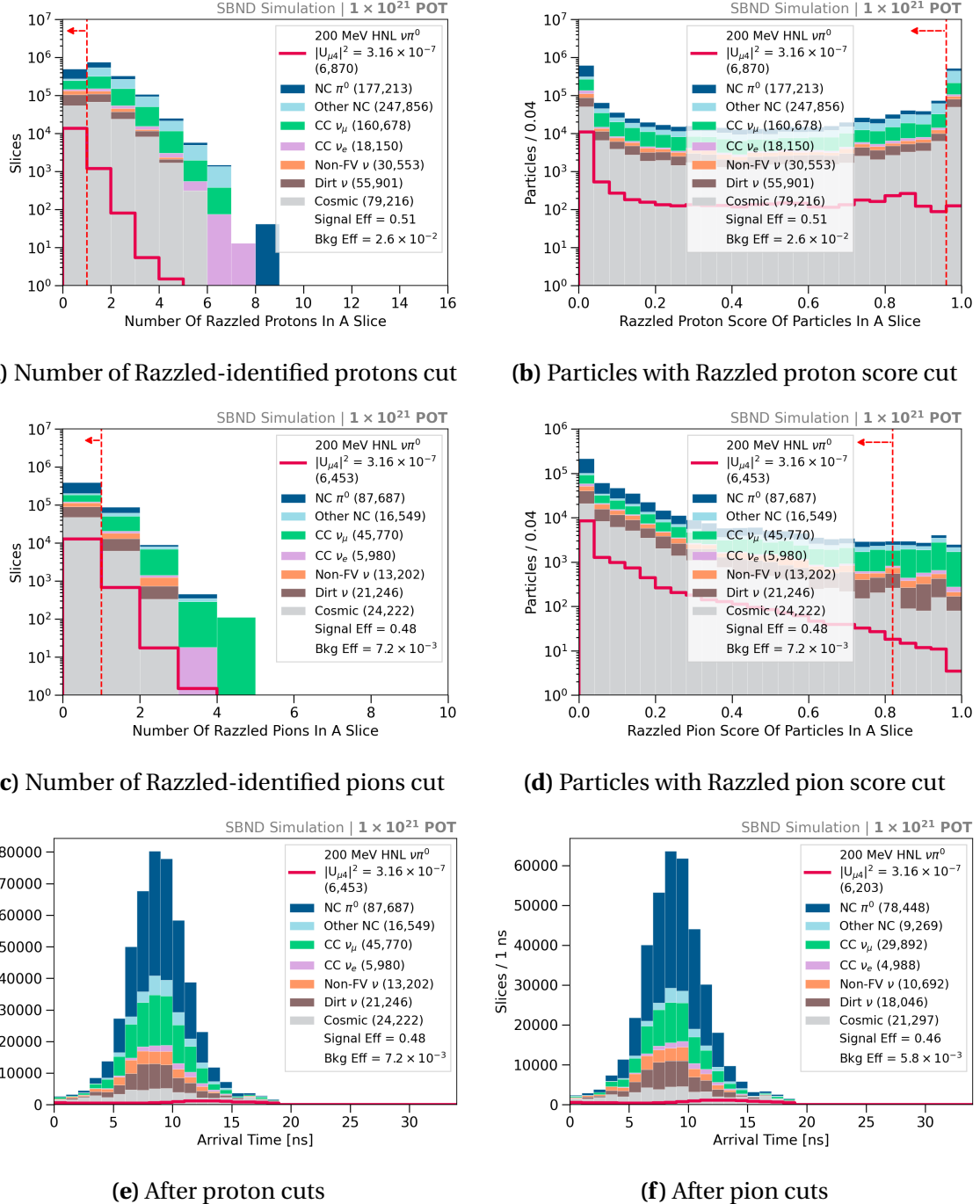


Fig. 9.9 Proton (top) and pion cuts (middle) and the beam buckets after the cuts (bottom).

9.4 HNL Shower Selection

After the track removal, the next five cuts targets at identifying HNL showers from shower-like backgrounds. The electron shower cut is provided in Section 9.4.1. The track score cut, to keep only very shower-like signals, is detailed in Section 9.4.2. In following, the calorimetry and theta cuts in Sections 9.4.3 and 9.4.4 exploit the boosted topology of HNL showers. Finally, since the π^0 invariant mass can be reconstructed, it is also used as a cut variable to be discussed in Section 9.4.5.

9.4.1 Electron Shower Removal

The first cut of this HNL shower selection aims at rejecting showers originating from electrons. The key differences between electron showers and photon showers are the shower conversion gap and the shower dE/dx . The conversion gap describes the gap between the interaction vertex and the start of the shower, where electron showers start immediately at the vertex but photon showers might propagate away from the vertex before showering. The dE/dx describes the charge distribution per unit length, such that the dE/dx of a photon shower is twice that of an electron shower since a photon shower is made up of a pair of electron-positron showers. Both these shower characteristics are provided during the training of the Razzled BDT for classifying photons and electrons.

The Razzled electron score is examined for the primary shower that deposits the most energy in a slice. The cut is demonstrated in Fig. 9.10, where only slices containing primary showers with a Razzled electron score < 0.96 . The rejected slices are clearly-identified

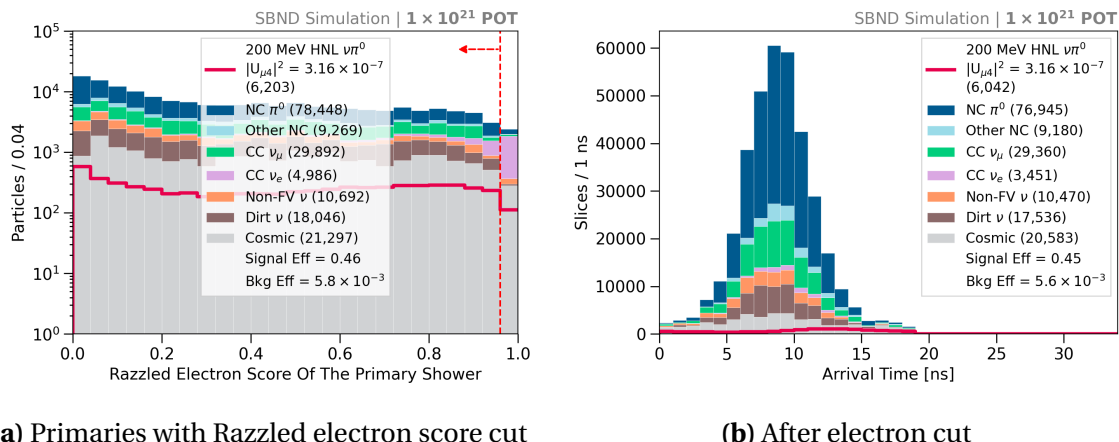


Fig. 9.10 Electron cut (top) and the beam bucket after the cut (bottom).

CC ν_e showers with high Razzled electron scores. This is a very soft cut compared to the previous track removal cuts since showers from CC ν_e interactions and showers from HNLs are very similar to each other. The cut rejects 31% of the remaining $\sim 5,000$ CC ν_e slices while minimally reduces HNL slices by only 3%.

9.4.2 Track Score Cut

To further reject backgrounds containing showers, careful considerations were taken into developing cuts by separating the shower topology into subsets. As previously stated, di-photon showers from HNLs can result in either a single shower topology or multiple shower topology. Thus, two cases can be considered when applying cuts: (1) slices containing only one shower and (2) slices containing two or more showers. The distribution of signal and background slices in the phase space of the cut variable vary differently between the two cases. This results in a different signal-to-background ratio across the distribution for each case. From this cut onwards, individual cut is examined per case to optimise the efficiency of background rejection and signal selection.

The second cut of the HNL shower selection employs the track-shower separation BDT, that outputs a track score to a particle indicating if it is track-like or shower-like (See Section 6.2.4). The track score is examined for the primary shower that deposits the most energy energy in a slice. Fig. 9.11 displays the track score distribution of primary particles for the two cases of slices containing 1 shower and 2+ showers. For both cases, the remaining primary particles are already shower-like since the track score concentrates in the region < 0.5 .

The cut sets the upper boundary of the track score at 0.5 for both cases, to reject any primary particles leaning towards track-like. On the other hand, the cut on the lower boundary of track score aims at trimming some shower-like backgrounds. The cut is optimised for each case depending on individual signal-to-background distribution. A more lenient cut is applied for the single shower case selecting the primary shower with a track score of ≥ 0.225 . The cut is tightened up for the multiple showers case for better background rejection, requiring the primary shower to have a track score of ≥ 0.25 . The resulting beam bucket distribution is depicted in Fig. 9.11c, showing a reduction of 3-16% across different SM neutrino interaction types. The signal selection efficiency only reduces from 45% to 43%.

9.4 HNL Shower Selection

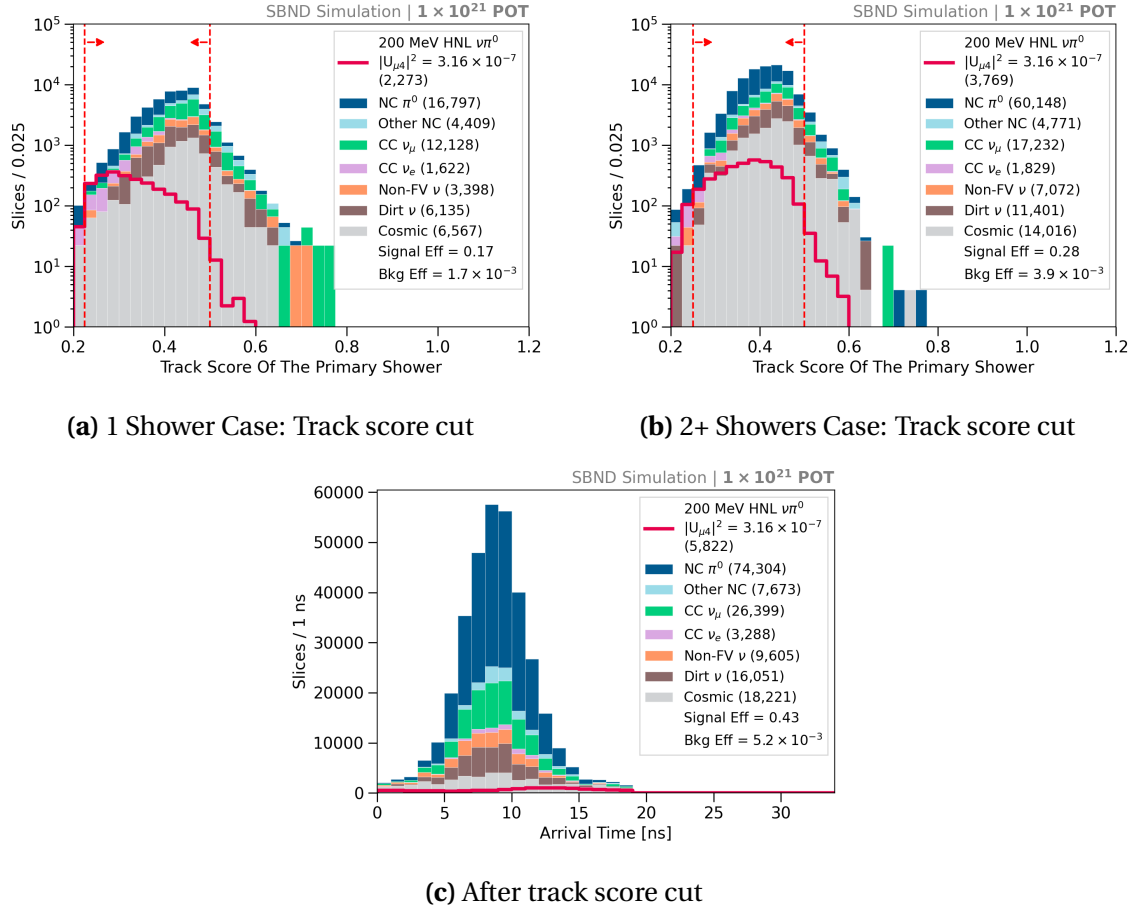


Fig. 9.11 Track score cut (top) and the beam bucket after the cut (bottom).

9.4.3 Calorimetry Cut

The third cut of the HNL shower selection targets the highly energetic aspect of HNL showers compared to SM neutrino showers. Outputs from the flash-to-slice matching process are examined, particularly the fraction variable defined in Eq. 6.4 in Section 6.4.1. For a matched flash, the fraction describes the level of agreement between L_Q and L , where L_Q is the number of PhotoElectrons (PEs) predicted from the reconstructed charge and L is the number of PEs measured by PMTs. A large disagreement indicates poor reconstruction, whether under or overestimation in light prediction or non-coincident cosmic backgrounds.

The fraction is useful to identify showers originated from HNLs due to their boosted topology. Very forward-going HNL showers are likely to overlap and clustered as a single shower merged from multiple showers by Pandora. The reconstructed energy from deposited charge of the merged HNL shower tends to be much higher than that for SM

neutrinos. The number of PEs predicted from the reconstructed charge L_Q is therefore also likely to be overestimated compared to the number of PEs measured by PMTs L .

The overestimation is demonstrated in Fig. 9.12, where it can be seen that HNL slices mainly concentrate in the region $\frac{(L_Q - L)}{L} \geq 0$. The calorimetry cut exploits this feature and is optimised for the single shower as well as the multiple shower case. For slices containing a single shower, the requirement on the fraction is between -0.1 and 0.4 to select well-predicted showers with the fraction centred around 0, as well as overestimated showers with the fraction > 0 . For slices containing multiple showers, the requirement on the fraction is restricted to between 0.04 and 0.3 to strictly select only overestimated showers, rejecting backgrounds more aggressively. The beam bucket distribution after the cut is shown in Fig. 9.12c, demonstrating the effectiveness of the cut as the background efficiency decreases by a whole order of magnitude from $\mathcal{O}(10^{-3})$ to $\mathcal{O}(10^{-4})$. Meanwhile, the signal selection efficiency only decreases from 43% to 35%.

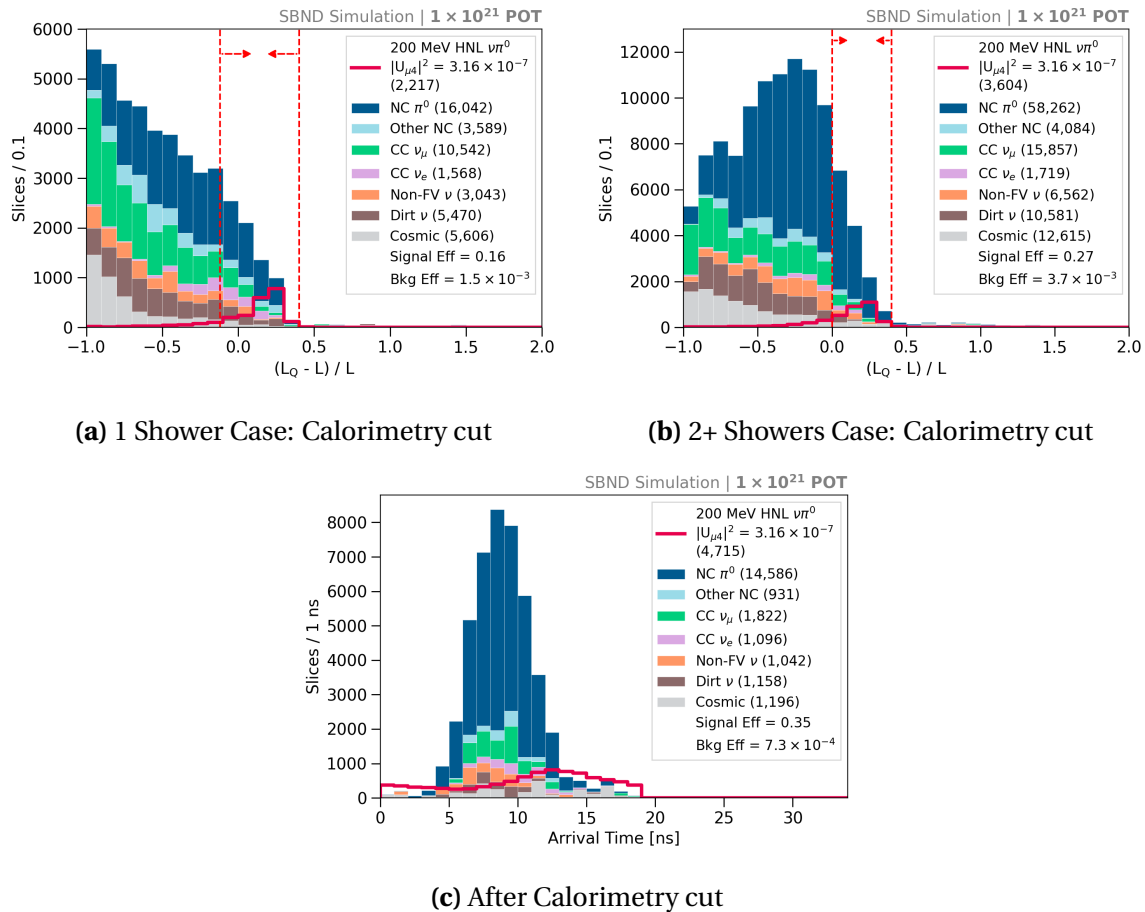


Fig. 9.12 Calorimetry cut (top) and the beam bucket after the cut (bottom).

9.4 HNL Shower Selection

9.4.4 Theta Angle Cut

The fourth cut exploits the topology of the forward-going HNL showers such that their angles with respect to the beam direction, referred to as *theta angles*, are small. Fig. 9.13a shows the angular distribution for slices containing a single shower. In this case, the signals are mainly highly energetic and boosted di-photon showers reconstructed as a single merged and beam-collimated shower. As a result, their theta angles concentrate in the region $< 25^\circ$. An aggressive selection of $< 25^\circ$ can be placed without compromising signal efficiency.

Fig. 9.13b shows the theta angle distribution for slices containing multiple showers. In this case, HNL showers are less boosted and more likely to result in separated showers. Their theta angles with respect to the beam are larger compared to the single shower case. To preserve signal selection efficiency, a widened selection of $< 30^\circ$ is applied.

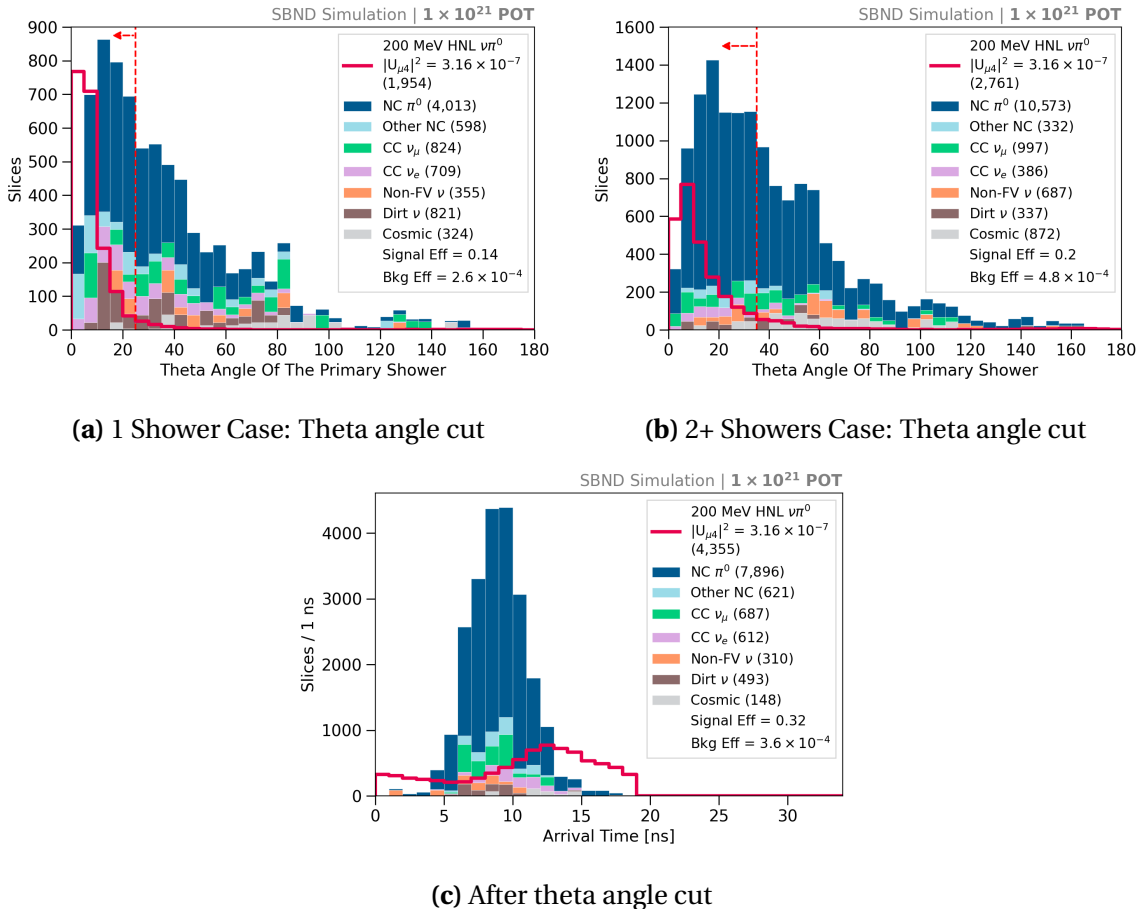


Fig. 9.13 Theta angle cut (top) and the beam bucket after the cut (bottom).

Fig. 9.13c shows the beam bucket distribution after applying the cut. The theta angle cut effectively rejects any shower-like backgrounds that are not beam-collimated, resulting in a reduction across all SM neutrino interaction types. This is a very impactful cut given that the background efficiency decreases by half from 7.3×10^{-4} to 3.6×10^{-4} . The signal efficiency of HNL slices only drops by 2%.

9.4.5 Invariant Mass Cut

The final cut of the HNL shower selection exploits the fact that di-photon showers originate from a π^0 decay, allowing for the reconstruction of π^0 invariant mass, m_{π^0} . For slices containing multiple showers, the invariant mass can be reconstructed using the reconstructed momenta of any two showers combination in the slice. For two massless photon showers with an opening angle α and a total energy E_1 and E_2 respectively, m_{π^0} is computed as:

$$m_{\pi^0} = \sqrt{2E_1 E_2 \times (1 - \cos\alpha)}. \quad (9.4)$$

For a given slice, the π^0 invariant mass was reconstructed for all combinations of two showers, and the best mass was considered for the cut. The cut is illustrated in Fig. 9.14, where the solid red line indicates the π^0 mass of 135 MeV. A cut is applied to select slices corresponding to a reconstructed invariant mass of 300 MeV or less. This rejects any slices with a poorly reconstructed π^0 mass, which could be due to backgrounds from SM neutrino interactions such as CC ν_μ , Other NC, Non-FV and dirt as well as energetic cosmic rays. However, poor shower reconstruction can also result in di-photon showers from π^0 getting mistakenly rejected by this cut, as it is evident that some NC π^0 interactions and HNL signals are affected. This cut reduces both signal and background slices by than 3%.

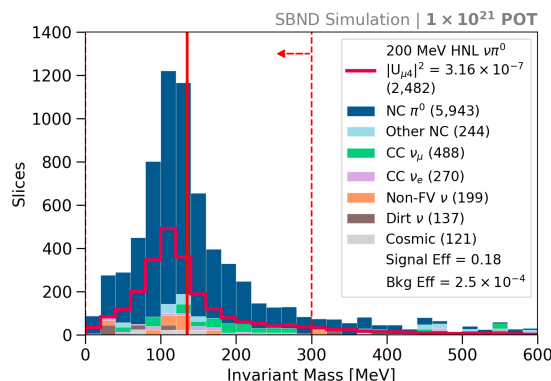


Fig. 9.14 π^0 invariant mass cut applied to the multiple showers case.

9.5 Selection Result

Fig. 9.15a shows the beam bucket distribution after the selection. The background efficiency is 3.3×10^{-4} , demonstrating the extreme background rejection achieved amounting to four orders of magnitude. Meanwhile, the signal selection efficiency is still well-preserved as 30%. The peak region of the bucket is dominated by NC π^0 interactions, which have proven to be tricky backgrounds to remove due to their similarity with HNL showers. A combination of CC ν_μ and Other NC interactions remain even though they were not originally considered to be a background. These interactions likely undergo deep inelastic scattering, producing shower-like products like π^0 or e^\pm . Some CC ν_e interactions persist as they can produce a single shower topology. In addition, some Non-FV and dirt neutrino interactions can still be seen, since their products can propagate to the FV and deposit energy. Finally, cosmic muons are almost fully rejected.

The multi-binned analysis for limits setting depends on the signal-to-background ratio per bin, of which signal-rich bins drive the limits. Fig. 9.15c zooms into the first and last 4 bins of the beam bucket distribution, which are the highest purity bins. These contribute towards sensitivity significantly more than bins located at the peak region. A *timing cut* can be applied to select only these bins, which would result in a background efficiency decreasing from $\mathcal{O}(10^{-4})$ to $\mathcal{O}(10^{-6})$ while still maintain a signal efficiency of 10%. However, the cut is not formally applied as part of the selection, but to highlight the importance of these edge bins due to their excellent signal-to-background ratio. The timing cut is discussed further in Chapter 10.

To better understand the sensitivity dependence on the signal-to-background ratio, two selections were developed. The selection presented up until this point is referred to as *the lenient cut*. An additional more aggressive cut, referred to as *the stringent cut*, was developed by tightening the two most impactful cuts on calorimetry and theta angle. The resulting beam bucket distribution for the stringent cut is shown in Fig. 9.15b and 9.15d for the entire distribution and only the edge bins. The key difference between these two cuts is that the lenient cut retains more signals however at a lower purity, whilst the stringent cut results in higher purity at the cost of signal efficiency. The two selections are summarised in Table 9.1.

Fig. 9.16 shows the signal and background rejection efficiency cut by cut. The signal efficiency, Eq. 9.2, is plotted using the left axis in pink and the background efficiency, Eq. 9.3, is plotted using the right axis in blue. It is important to note that the right axis is in the logarithm scale as the background rejection is very aggressive. The band of

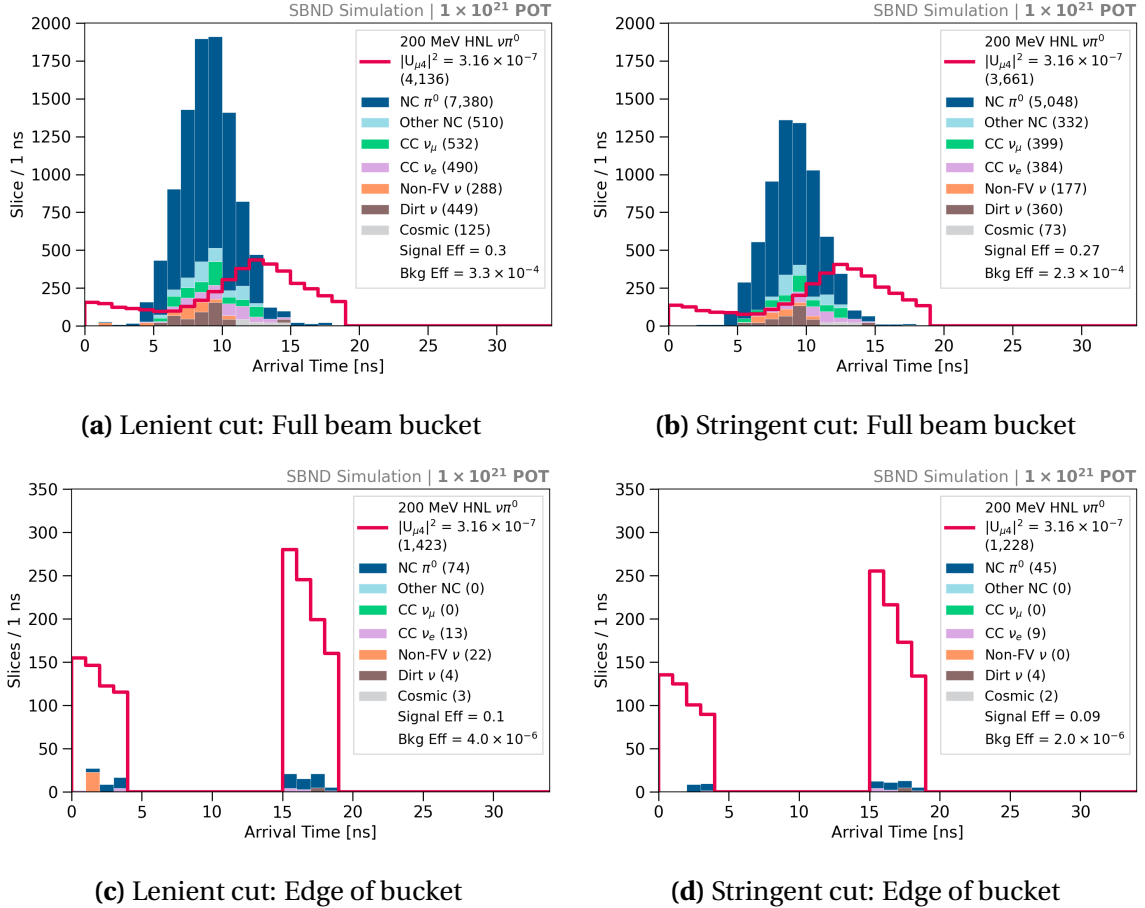


Fig. 9.15 The beam buckets after the lenient (left) and stringent cut (right).

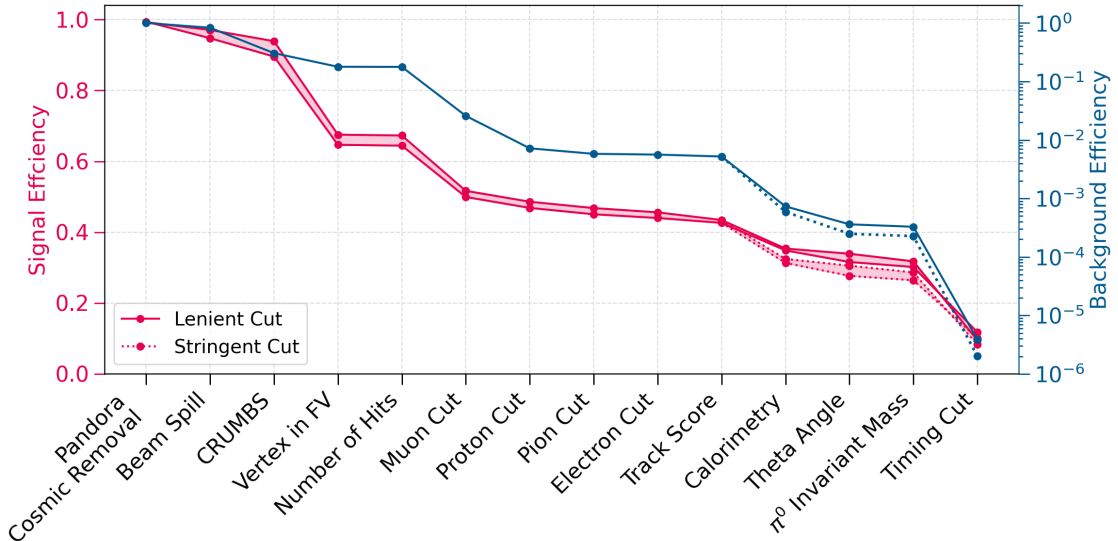


Fig. 9.16 Summary of signal (left axis) and background efficiencies (right axis).

9.6 Study of Timing Resolution Improvement

signal efficiency corresponds to the efficiency across the entire mass range of HNLs from 140 to 260 MeV, with efficiency increasing with masses. The selection differs from the calorimetry cut onwards, where the lenient cut is shown in solid line and the stringent cut is shown in dotted line. Overall, the most significant cuts are the muon/proton/pion cut for track removal, followed by the calorimetry and theta angle cut by exploiting the boosted topology of HNLs that significantly reject backgrounds without compromising signal efficiency.

9.6 Study of Timing Resolution Improvement

The timing cut described above demonstrates the importance of a high precision timing reconstruction in this analysis and thus, a study was carried out to understand the smearing contributors to the beam bucket distribution. Fig. 9.17 illustrates several factors that can smear the arrival time of a SM neutrino at SBND, and consequently smearing the Gaussian shape of the beam bucket. The intrinsic Gaussian width of the proton bucket from the Booster synchrotron is 1.308 ns, as shown by the brown arrow. This structure is then smeared out due to the Time of Flight (ToF) of secondary mesons, as shown by the blue arrow. Moreover, the ToF of the tertiary SM neutrinos from the production location to the detector further smears the Gaussian, as shown by the pink arrow. Once the neutrino arrives at the detector, two additional smearing factors need to be considered. The first one is its ToF inside the detector, as shown by the purple arrow. The second one is the ToF of the photon from the production to the detection location, assuming the photon production location is close to the interaction vertex, as shown by the green arrow.

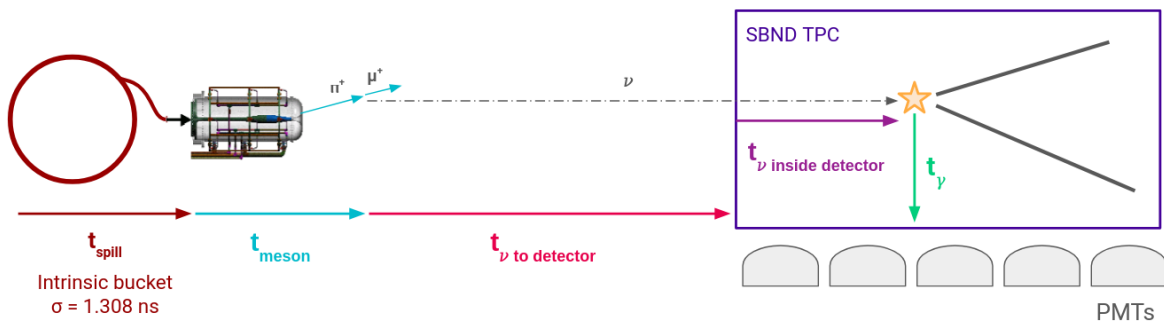


Fig. 9.17 Diagram showing smearing contributors to the beam bucket.

A beam bucket distribution was plotted using *true* variables to better understand the impacts of the smearing factors, where *true* indicates that no detector simulation and reconstruction were applied. The truth beam bucket of SM neutrinos that arrive at the

Table 9.1 Table summarising the lenient and stringent selection.

	Common Cut	
Cosmic Removal:		
Slice reconstructed by Pandora as a neutrino Flash time inside the beam spill CRUMBS score	True [0.367, 1.967] μ s ≥ 0	
SM Neutrino Removal:		
Reconstructed vertex inside the FV # of hits in the primary shower	True ≥ 50	
# of Razzled muons	0	
Razzled muon score of particles in a slice	< 0.04	
# of Razzled protons with KE > 32.7 MeV	0	
Razzled proton score of particles in a slice	< 0.96	
# of Razzled pions with KE > 31.2 MeV	0	
Razzled pion score of particles in a slice	< 0.82	
HNL Shower Selection:		
Razzled electron score of the primary shower	< 0.96	
Track score of the primary shower		
1 shower case	0.225 $<$ score $<$ 0.5	
2+ shower case	0.250 $<$ score $<$ 0.5	
(L _Q - L) / L fraction of a slice		
1 shower case	-0.12 $<$ frac $<$ 0.40	-0.10 $<$ frac $<$ 0.40
2+ showers case	0.00 $<$ frac $<$ 0.40	0.04 $<$ frac $<$ 0.30
Theta angle of the primary shower		
1 shower case	$\leq 25^\circ$	$\leq 20^\circ$
2+ showers case	$\leq 35^\circ$	$\leq 30^\circ$
Invariant mass of any 2 showers in a slice	≤ 300 MeV	
Timing Cut *(applied when setting limits):		
Arrival time within the beam bucket	0 ns \leq t \leq 4 ns and 15 ns \leq t \leq 19 ns	

9.6 Study of Timing Resolution Improvement

front face of SBND is shown in the left of Fig. 9.18. This distribution was computed using the true interaction time at the vertex, marked by the yellow star in Fig. 9.17, and then corrected for the SM neutrino ToF inside the detector, depicted by the purple arrow. In the truth phase space, it is evident that the combination of the ToF of mesons and of SM neutrinos to the detector smears the Gaussian width by a negligible amount from 1.308 ns to 1.37 ns.

The reconstructed beam bucket distribution of SM neutrinos is plotted in the right of Fig. 9.18. As detailed in Section 9.1.4, the beam bucket is reconstructed using the flash time that is matched to a slice (See Sections 6.3.1 and 6.4.1). The flash time was reconstructed using the prompt light occurring in the first 30 ns window such that the scintillation location is close to the interaction vertex. The flash time was also corrected for the photon propagation time from the production location to PMTs, depicted by the green arrow in Fig. 9.17. Then, the SM neutrino ToF inside the detector, as shown by the purple arrow, was corrected by applying a shift from the reconstructed vertex z -position to $z = 0$ at the detector's front face. As a result, the reconstruction depends on 3 variables: (1) the matching of flash-to-slice, (2) the flash time and (3) the slice vertex. Each of these variables has its own reconstruction uncertainty, thus, the reconstructed beam bucket is even more smeared.

Comparing the two beam bucket distributions in Fig. 9.18, the Gaussian mean is shifted by 1.82 ns from 7.44 to 9.26 ns. This includes a shift of 1.45 ns introduced by the light reconstruction [68]. The rest might be due to the slice vertex reconstruction and/or the slice-to-flash matching. Additionally, the Gaussian width is smeared from 1.37 ns to 2.26 ns. This width smearing is detrimental to the HNL search since it results in more SM neutrinos at the edge of the beam bucket, reducing the signal-to-background ratio in this region.

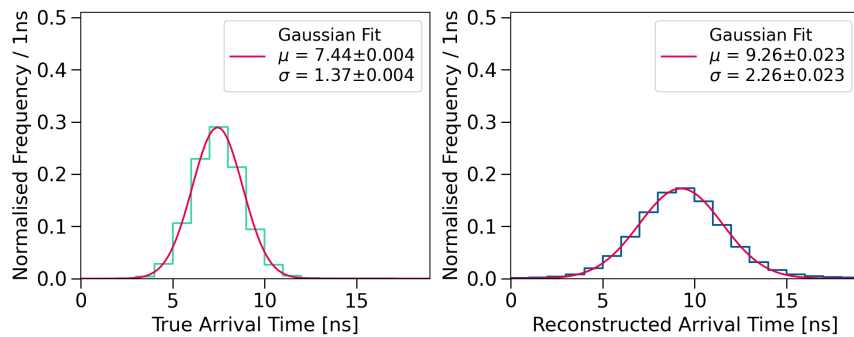


Fig. 9.18 The beam bucket of SM neutrinos using true (left) and reconstructed arrival times (right).

This motivates the assessment of sensitivity assuming a better timing reconstruction. The two assumptions of the beam bucket distribution reconstructed with an improved timing resolution are as follows:

1. A shifted Gaussian mean of 1.45 ns,
2. A smeared Gaussian width of 1.73 ns.

The first assumption is motivated by the impact of the light reconstruction in SBND reported by Ref. [68]. The second assumption is motivated by the MicroBooNE experiment reporting on their intrinsic timing resolution [121]. Although ambitious, it is an achievable goal for SBND to have a reconstructed timing resolution < 2 ns, given that SBND employs a similar detector technology to MicroBooNE. Moreover, Chapter 7 details the excellent timing performance of the SBND data acquisition and the preparation that already took place to achieve better timing resolution. Particularly, the SPEC-TDC device, as discussed in Section 7.1.2, records important timing information on the trigger and beam arrival that can only improve downstream reconstruction once incorporated.

For modelling the background using true variables under these assumptions, only SM neutrinos are considered and not cosmics for simplicity. The truth beam bucket distribution of SM neutrinos was smeared with the two assumptions, referred to as *smeared truth*. Fig. 9.19 shows the truth, smeared truth and the reconstructed distribution after selection, all normalised to the same area for direct comparison. The left figure shows the truth distribution without any smearing applied with a width of 1.37 ns. The middle figure shows the smeared truth distribution with the assumed width of 1.73 ns. The right figure shows the reconstructed distribution after applying the lenient selection with a width of 1.99 ns. It is important to note the difference between the reconstructed beam bucket before and after selection such that the distribution after selection has a less shifted Gaussian mean and a smaller Gaussian width. This is due to cuts having non-uniform effects on the distribution. It was observed in this work that different topologies, for instance tracks and showers, have different timing reconstruction resolutions.

For modelling the signal, the same smearing assumptions are applied to the true arrival time distribution of HNLs. Unlike the background modelling approach of normalising the same area, an efficiency of 30% was applied to the HNL distribution to account for the combined effects of reconstruction and selection. Fig. 9.20 shows the beam bucket distribution of SM neutrinos and HNLs across the phase space of truth, smeared truth and reconstruction after selection for comparison. The smeared truth distribution shows a higher signal-to-background ratio particularly for the bins at the edge of the bucket

9.7 Concluding Remarks

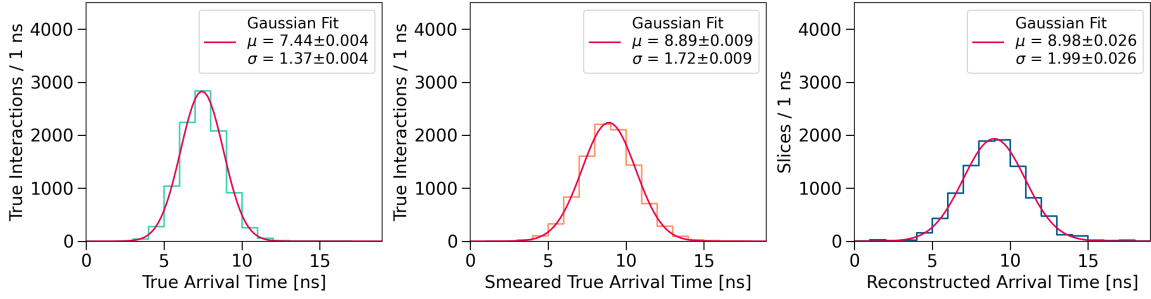


Fig. 9.19 The beam bucket of SM neutrinos using true (left), smeared true (middle) and reconstructed arrival time after the lenient selection (right).

compared to the reconstructed distribution. This smeared truth distribution is also used for determining the sensitivity alongside the reconstructed distributions, as this is to assess the impacts of timing resolution improvement.

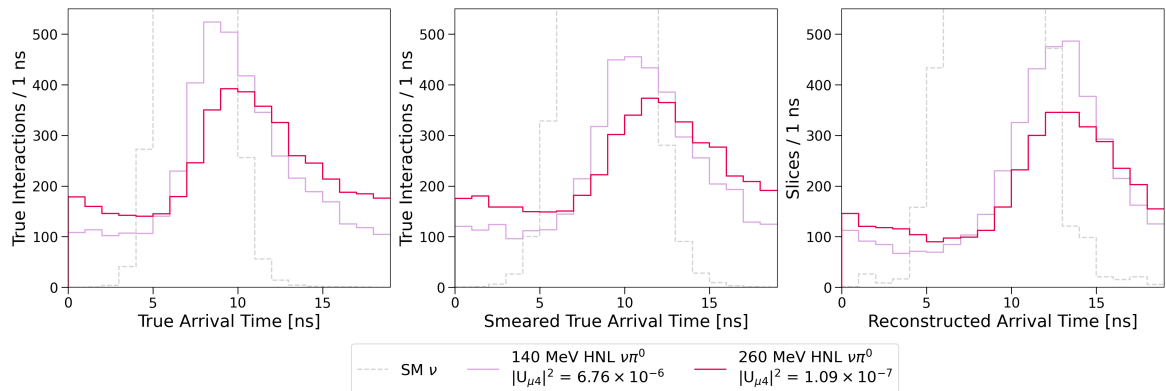


Fig. 9.20 The beam bucket of SM neutrinos and HNLs using true (left), smeared true (middle) and reconstructed arrival time after the lenient selection (right).

9.7 Concluding Remarks

The selection of HNLs using MC samples is provided in this chapter, as a procedure to identify HNL signals from SM neutrino and cosmic backgrounds. Two selection procedures on reconstructed variables are presented, the lenient and stringent cut, with the stringent rejecting backgrounds more aggressively than the lenient. Both exploit the highly energetic and forward-going features of HNL showers to achieve an excellent background rejection without compromising signal efficiency.

The resulting background efficiency is in the order of $\mathcal{O}(10^{-4})$ while the signal selection efficiency still maintains at 30%. When considering only bins at the edge of the beam bucket distribution, or the so-called *timing cut*, the background efficiency decreases significantly by two orders of magnitude to $\mathcal{O}(10^{-6})$. Meanwhile, the signal efficiency only decreases from 30% to 10%. This demonstrates that these edge bins contain an exceptional signal-to-background ratio, which is the main factor driving the sensitivity.

Furthermore, a study was motivated to explore the impact on sensitivity if the timing reconstruction is achieved. The study resulted in a beam bucket distribution acquired by smearing true variables, assuming it is reconstructed with an improved timing resolution. All three beam bucket distributions, from both the lenient and stringent cut on reconstructed variables and from the smeared true variables, are used for studying the sensitivity to HNLs in Chapter 10 next.

Chapter 10

Sensitivity Predictions for Heavy Neutral Leptons at SBND

After the selection performed on Monte Carlo (MC) samples, the analysis continues with assessing and propagating uncertainties. This is a critical step which includes an evaluation of statistical fluctuations due to the size of the MC samples as well as uncertainties due to the simulated physics models of the Booster Neutrino Beam (BNB) flux, Standard Model (SM) neutrinos and the Short-Baseline Near Detector (SBND). Following this, the sensitivity of SBND to Heavy Neutral Leptons (HNLs) is determined by setting an upper limits on the coupling $|U_{\mu 4}|^2$ of HNLs, under the assumption of no detected signals to allow for direct comparison with existing limits. The limits setting is performed using the likelihood-based hypothesis testing for exclusion limits [8]. The beam bucket distribution with fully propagated uncertainties is the input of the limits setting, which exploits the exceptionally high signal-to-background ratio of bins at the edge of the distribution, as discussed in Chapter 9, to achieve competitive sensitivity.

The following chapter provides details of the analysis steps employing the three beam bucket distributions after the selection, including two acquired from the lenient and stringent selection performed on reconstructed variables and a third acquired by smearing true variables. Section 10.1 outlines the assessment of statistical as well as systematic uncertainties. Following that, Section 10.2 delves into the limits setting procedure. The results of the upper limits on the coupling $|U_{\mu 4}|^2$ of HNLs are presented in Section 10.3. Finally, Section 10.4 concludes the chapter with some remarks.

10.1 Uncertainty Assessment

Since many physics measurements to be made by SBND will heavily rely on comparing data and MC samples, it is vitally important to understand the input physics models used to simulate the MC sample. As previously discussed in Chapter 4 describing the detector and Chapter 5 detailing the simulation framework, many different theoretical as well as data-driven models are used to predict the incoming flux from the BNB and the SM neutrino interaction cross sections. Each model has its own uncertainty and needs to be propagated to the final physics result.

The assessment of statistical and systematic uncertainties is presented in this section. Section 10.1.1 details the reweighting method to assess uncertainties of BNB flux and SM neutrino predictions. Following this, the error propagation is given in Section 10.1.2. Finally, Section 10.1.3 and 10.1.4 provide a description of uncertainty sources for the HNL signal and SM neutrino and cosmic backgrounds respectively.

10.1.1 The Reweighting Method

The impact of systematic uncertainties on a physics measurement can be assessed by simulating and reconstructing a number of different samples, referred to as *universes*, each with a physics parameter tweaked within its uncertainty range. The physics measurement is then performed in each universe in the same manner as done on the Central Value (CV) sample that does not have any parameters tweaked. The variation of the results across universes compared to the CV sample describes the uncertainty that the tweaked parameter has on the measurement. However, fully simulating and reconstructing a large MC sample for multiple systematic parameters can be computationally intensive, the *reweighting* technique is used instead by producing a weight associated with the tweaked parameter per universe. The weight can be applied to smear the physics result by an amount as expected by the tweaked parameter. Or vice versa, the smeared physics result can be unweighted to recover the original result without any uncertainties from the tweaked parameter [129].

The reweighting technique begins with transforming a physics parameter x to x' as:

$$x' = x \cdot f(x), \quad (10.1)$$

where $f(x)$ describes some transformation functions as a function of x . If $f(x) = 1$, then x' is equal to the unweighted x . A common form of the transformation function is a Gaussian

10.1 Uncertainty Assessment

function, where the physics parameter x is thrown to x' by randomly sampling from a unit Gaussian with its mean and width set as 1. Another common formalism is the Delta function, where x' can take only the value of 0 or 1.

Then, from the probability $P(x)$ describing an outcome of physics measurements parameterised by the parameter x , the weight w can be computed as:

$$w = \frac{P(x')}{P(x)}. \quad (10.2)$$

The weight w describes whether the probability $P(x')$ is more or less likely to occur given the transformed parameter x' compared to the CV parameter x . The distribution of w therefore describes the Probability Density Function (PDF) of the parameter x . A universe associated with a weight w represents an outcome sampled from the PDF. Moreover, the weight example shown in Eq. 10.2 is associated with a single physics parameter x that is non-correlated to any other parameters. A weight associated with multiple correlated parameters can also be computed in the same manner.

The reweighting framework provides a quick way to compute PDFs, allowing for the assessment of the impact of systematic uncertainties without the computational expense of simulating and reconstructing the sample multiple times. A series of universes is first simulated and weights for every interaction, whether SM neutrino or HNL, and are then calculated from the PDFs for each universe. The variation of the physics results across universes is used to quantify the uncertainties of the weighted parameters on the physics measurement, of which the error propagation is given in Section 10.1.2 next.

In some cases, reweighting is not applicable such as evaluating uncertainties due to detector effects. For example, recombination, as detailed in Section 8.2, influences not only the charge and light yield but also the non-uniformity of charge deposition on wires [60, 123]. Consequently, it is non-trivial to quantify analytically the downstream impacts due to the variation in recombination parameters on the charge reconstruction by Pandora or any high level analysis tools using the reconstructed charge information. A full simulation and reconstruction of a single universe using the varied recombination parameter is needed to fully assess the impact on the physics measurement. This method is commonly used for assessing detector systematic uncertainties.

10.1.2 Error Propagation Formulation

The impact of uncertainties can be evaluated by constructing the covariance matrix V of a series of observations n . The matrix describes the average deviation of the value in bins i and j from the CV away from the universe k , totalling U universes. The matrix is computed as follows:

$$V_{ij} = \frac{1}{U} \sum_k^U (n_i^n - n_i^{CV})(n_j^n - n_j^{CV}). \quad (10.3)$$

The diagonal term of the covariance matrix represents the variance in a given bin and the error σ can be derived as:

$$V_{ii} = \sigma_i^2. \quad (10.4)$$

Since there are multiple sources of error, the total covariance matrix is computed by summing the covariance matrix from each error source together, effectively adding the errors in quadrature as follows:

$$V_{ij}^{Total} = \sum_{Sources} V_{ij}^{Source} = V_{ij}^{Stat} + V_{ij}^{Flux} + V_{ij}^{Cross Section} + \dots \quad (10.5)$$

The total error is then computed from the total covariance matrix V_{ij} using Eq. 10.4. Additionally, the fractional matrix describing the relative error in each bin is computed as:

$$V_{ij}^{Frac} = \frac{V_{ij}}{n_i^{CV} n_j^{CV}}, \quad (10.6)$$

which allows for easy and direct comparison across bins of signal and background samples.

10.1.3 Signal Uncertainty Sources

For the HNL signal, there are four primary sources of uncertainties that will affect physics measurements made by SBND: (1) statistical, (2) cosmic mistagging, (3) flux and (4) detector. The statistical uncertainty is evaluated using the number of signal slices selected after the selection presented in Chapter 9, of which the following plots show the distribution after the lenient selection. Meanwhile, the cosmic mistagging uncertainty is evaluated using the number of cosmic muon slices occurring in the same readout window of HNLs that remain after selection. The impact of the uncertainties due to flux modelling can be measured using the reweighting method. The detector systematic however is not reweightable and requires a fully simulated and reconstructed MC sample for assessing

10.1 Uncertainty Assessment

uncertainties due to the detector as previously explained in Section 10.1.1. At the time of writing, the SBND detector is not yet operational, and it is undetermined which detector parameters are impactful on physics measurements. Thus, detector systematics are not included in the limits setting presented here but should be included in future iterations of this analysis.

The statistical uncertainty describes the statistical fluctuation of the MC sample. It is computed using the number of HNL signal slices remaining after the selection binned to the beam bucket distribution. The statistical uncertainty of each bin is defined as follows

$$\sigma_{\text{statistics}} = \sqrt{\text{Number of entries in the bin}} \quad (10.7)$$

The uncertainty is computed before the normalisation to the Proton On Target (POT) exposure of 3 years of data taking. After the normalisation, the resulting statistical uncertainty is plotted in Fig. 10.1a, showing the uncertainty is minimal across the entire distribution. The fractional statistical uncertainty, as depicted by the blue line in the bottom figure of Fig. 10.2, shows that it is well-constrained under < 6%.

The cosmic mistagging uncertainty accounts for the selected slices that are cosmic muons occurring in the same readout window as HNLs. In some cases, highly energetic cosmic muons can overlap with showers from HNLs, resulting in a pile-up of charge clusters at the same location in the detector. These charges arriving at the same wires and at the same time can mislead the clustering process of Pandora during reconstruction, such that a reconstructed shower object might contain more charges from cosmic muons than HNLs. This reconstruction failure results in several cosmic slices remaining after the selection, and therefore, is considered as the cosmic mistagging uncertainty. The cosmic mistagging uncertainty is plotted in Fig. 10.1b, however, the uncertainty is so small that it is not visible in the plot. The uncertainty can be seen in the fractional format in the bottom figure of Fig. 10.1 in the gray line, demonstrating it is almost negligible at < 1%.

The flux systematic was assessed using the reweighting method. The flux prediction and the reweighting framework for assessing the uncertainties were both developed by the MiniBooNE experiment and furthered by the MicroBooNE experiment [3]. The framework has now been implemented for SBND, called SBN Event Weight [130] and intended for a consistent reweighting method across the experiments in the SBN program, including SBND, ICARUS and MicroBooNE. The flux systematic uncertainties are as follows

- **Proton Delivery:** The proton intensity on the target of the BNB is measured using two steroids, which have an uncertainty of 2% attributed to calibration.

- **Production:** The flux prediction for the number of secondary mesons produced in the BNB target has an uncertainty associated with each particle type (See Section 4.3). The main meson parent of HNLs is K^+ , of which the production is extrapolated from the global data of K^+ using the Feynman Scaling to the relevant BNB energy range and further constrained by the SciBooNE’s direct measurement of K^+ from the BNB.
- **Hadronic Interactions:** Hadrons produced in the target may interact with the beryllium target elastically or inelastically, affecting the kinematics of secondary mesons and consequently, tertiary daughter particles like HNLs and SM neutrinos. The cross section uncertainties of $p/n + Be$ and $\pi^\pm + Be$ are propagated through the flux prediction.
- **Horn Magnetic Field:** The magnetic field of the horn impacts the focusing of charged particles produced in the target. Uncertainties associated with the horn magnetic field including the current pulsed through the horn and the skin current induced on the surface of the target are computed.

Fig. 10.1c shows the combined uncertainty of all the flux systematics listed here for HNLs, where the uncertainty is consistent across every bin. The flux fractional uncertainty is plotted in the green line in the bottom figure of Fig. 10.2 that it is well-constrained < 8%.

Finally, the top figure of Fig. 10.2 shows the total uncertainty combining the statistical, cosmic mistagging and flux uncertainties combined. It can be seen that the uncertainty is evenly distributed across the beam bucket distribution with minimal biases in any bins. The total fractional uncertainty is shown in the purple line in the bottom figure of Fig. 10.2, demonstrating that it is well-constrained < 10% across the full distribution.

10.1.4 Background Uncertainty Sources

For the background of SM neutrinos and cosmic muons, there are four primary sources of uncertainties: (1) statistical, (2) flux, (3) SM neutrino cross section and (4) detector. The uncertainties due to statistics and flux are computed in the same manner as the uncertainty treatment of the HNL signal. The detector systematic uncertainty is also currently not included but should be included in future work. A new addition is the neutrino cross section uncertainty, of which the impact due to the cross section modelling is measured using the reweighting method.

10.1 Uncertainty Assessment

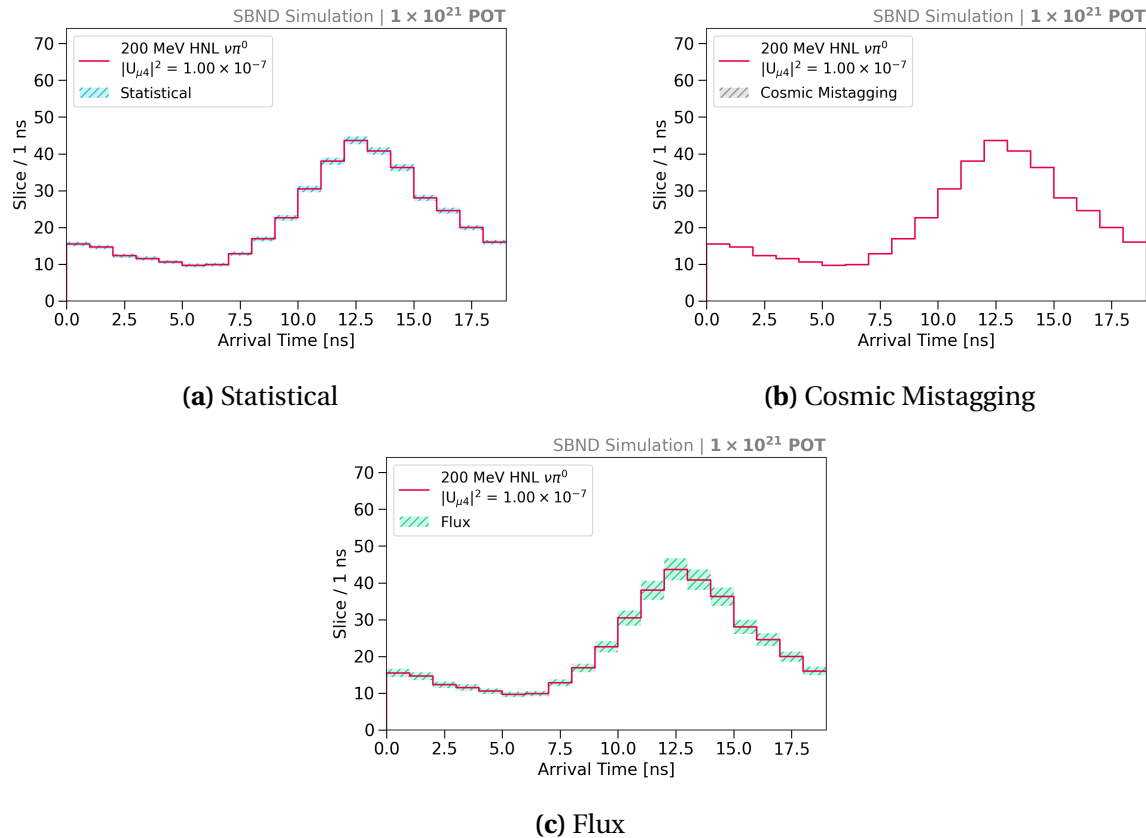


Fig. 10.1 Uncertainties of HNLs, including (a) statistical, (b) cosmic mistagging and (c) flux.

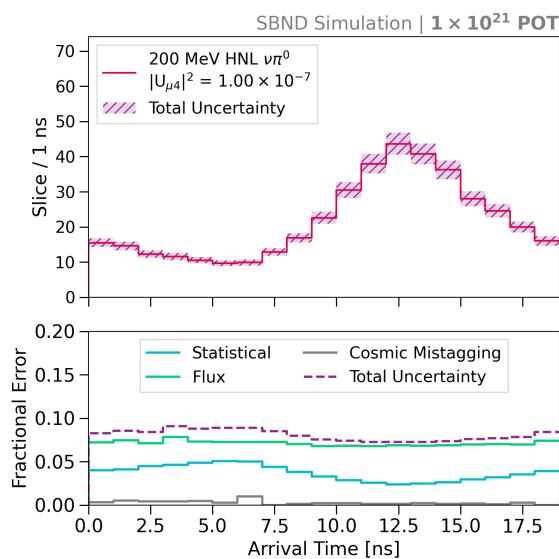


Fig. 10.2 Total uncertainty (top) and fractional uncertainties (bottom) of HNLs.

The statistical uncertainty of the background was assessed using the number of SM neutrino and cosmic muon slices after the selection and computed using Eq. 10.7. Fig. 10.3a shows the statistical uncertainty of the background. It is evident that the background statistics are abundant for bins at the centre of the beam bucket however, limited for bins at the edge. Therefore, the statistical uncertainty is better constrained for bins at the centre, while bins at the edge have a higher statistical fluctuation. This is visually evident in the statistical fractional uncertainty plotted in the blue line in the bottom figure of Fig. 10.4. For bins at the centre of the beam bucket, the statistical fractional uncertainty is constrained at < 20%. For bins at the edge of the beam bucket distribution, particularly the first and last 4 bins, where the statistical fractional uncertainty reaches as high as 100%.

The flux systematic of the background was measured using the reweighting method similar to HNLs. One key difference in the flux systematics between the signal and the background is the uncertainties due to the secondary meson production in the BNB. Unlike HNLs coming from only K^+ , SM neutrinos can result from π^\pm , K^\pm and K_L^0 . Particularly, the Sanford-Wang parametrisation for modelling the π^+ production introduces biases for NC π^0 interactions [114], which is the main background contributor. The resulting flux uncertainty of the background is plotted in Fig. 10.3b and the flux fractional uncertainty is plotted in the green line in the bottom figure of Fig. 10.4. The flux fractional uncertainty is very well-constrained < 20% and consistent across the entire beam bucket distribution.

The SM neutrino cross section uncertainty was assessed using the SBN Event Weight, with systematic variable inputs from the GENIE generator. There are two types of weights for SM neutrino interaction cross section: (1) weights associated with a group of correlated physics parameters and (2) weights associated with a single non-correlated physics parameter. The SM neutrino systematics for a group of physics parameters are as follows

- **Charged Current Quasi-Elastic Scattering (CC-QE):** Coefficients of the Z expansion of the axial form factor for CC-QE interactions are varied.
- **Deep Inelastic Scattering (DIS):** Parameters and correction factors of the Bodek-Yang model, which is used for modelling DIS cross sections, are varied.
- **Neutral Current Elastic Scattering (NC-EL):** The axial mass and the strange axial vector of the dipole form factor of NC-EL interactions are varied.
- **Neutral Current Resonant Scattering (NC-RES):** The axial mass and the strange axial vector of the dipole form factor of NC-RES interactions are varied.

10.1 Uncertainty Assessment

- **Charged Current Resonant Scattering (CC-RES):** The axial mass and the strange axial vector of the dipole form factor of CC-RES interactions are varied.
- **Hadron Transport Interactions:** The mean free path, inelastic scattering, absorption, and pion production cross section are varied for both pions and nucleons.

The SM neutrino systematics for a single non-correlated physic parameter are as follows

- **Charged Current Quasi-Elastic Scattering (CC-QE):** The shape of vector form factor, the random phase approximation and the strength of the Coulomb corrections of CC-QE interactions are varied.
- **Meson Exchange Current Interactions (MEC):** The decay angle and the normalisation factor of CC-MEC and NC-MEC are varied.
- **Coherent Scattering (COH):** Normalisation factors of NC-COH and CC-COH cross section interactions are varied.
- **NonRES Backgrounds:** Non-resonant backgrounds are varied for CC and NC, ν and $\bar{\nu}$, neutron and proton, 1π and 2π for a total of 16 systematic parameters.
- **Angular Distribution:** The angular distribution of γ and π are varied.
- **Branching Fraction:** The branching fraction scale factor for resonant decays with either a single γ or π are varied.

Fig. 10.3c shows the combined uncertainty of all the SM neutrino interaction cross section systematics. Compared to statistical and flux uncertainties, the magnitude of the cross section uncertainty is significantly larger. This is due to the primary background after selection being NC π^0 , of which the cross section is not well-measured. Uncertainties associated with NC-COH and NC-RES scattering are the main contributors to this channel. Moreover, a small fraction of CC ν_e interactions remains after selection and the cross section is also not well-measured. For this channel, uncertainties associated with CC-QE scattering systematics contribute the most. Finally, uncertainties for modelling hadron transport interactions and NonRES backgrounds of NC 1π interactions are significant contributors to the cross section uncertainty.

The cross section fractional uncertainty is plotted in the orange line in the bottom figure of Fig. 10.4. For bins at the centre of the beam bucket distribution, it is the lowest in the entire distribution at < 50%. It increases towards the bins at the edge of the beam bucket, reaching almost 100% for very low statistics bins.

The total fractional uncertainty combining the statistical, flux and cross section uncertainty, is plotted in the purple line in Fig. 10.4. For bins at the edge of the bucket, which are the bins driving the sensitivity limits, the total uncertainty is particularly high at > 100% due to the combined contribution from all three uncertainty sources.

10.2 Limits Setting Procedure

The sensitivity of SBND to HNLs is determined as the upper limits on the coupling $|U_{\mu 4}|^2$ of HNLs. The upper limits are set under the assumption of no detected signals so that the results can be directly compared against existing limits in the mass range 140-260 MeV, as previously summarised in Fig. 2.5 in Section 2.4. The limits setting procedure employs the likelihood-based hypothesis test [8], of which likelihood functions are constructed using the beam bucket distribution of signals and backgrounds. The end-to-end procedure was performed using the pyhf package [7, 131].

This section begins with the definition of hypotheses for exclusion limits in Section 10.2.1 and the construction of the test statistic for each hypothesis in Section 10.2.2. Then, the CL_s method to determine p -values of test statistics is described in Section 10.2.3 and two approaches of computing test statistics are presented in Section 10.2.4. Finally, an overview of the limits setting done under the hood of the pyhf package is given in Section 10.2.5

10.2.1 Hypothesis Definition

The setting limit procedure employs the frequentist approach by performing hypothesis testing to quantify the level of agreement between the observed data and a given hypothesis H . To exclude a signal region, the test hypothesis H_b is defined as describing only known processes, or a background-only model. Meanwhile, the null hypothesis H_{s+b} is defined as the model including both background and signal processes.

A given hypothesis H is constructed to represent the expectation value for an observable distribution, which is chosen to be the beam bucket distribution. For a series of observations n , the expectation value of the i th bin can be constructed as

$$E[n_i] = \mu s_i + b_i \quad (10.8)$$

10.2 Limits Setting Procedure

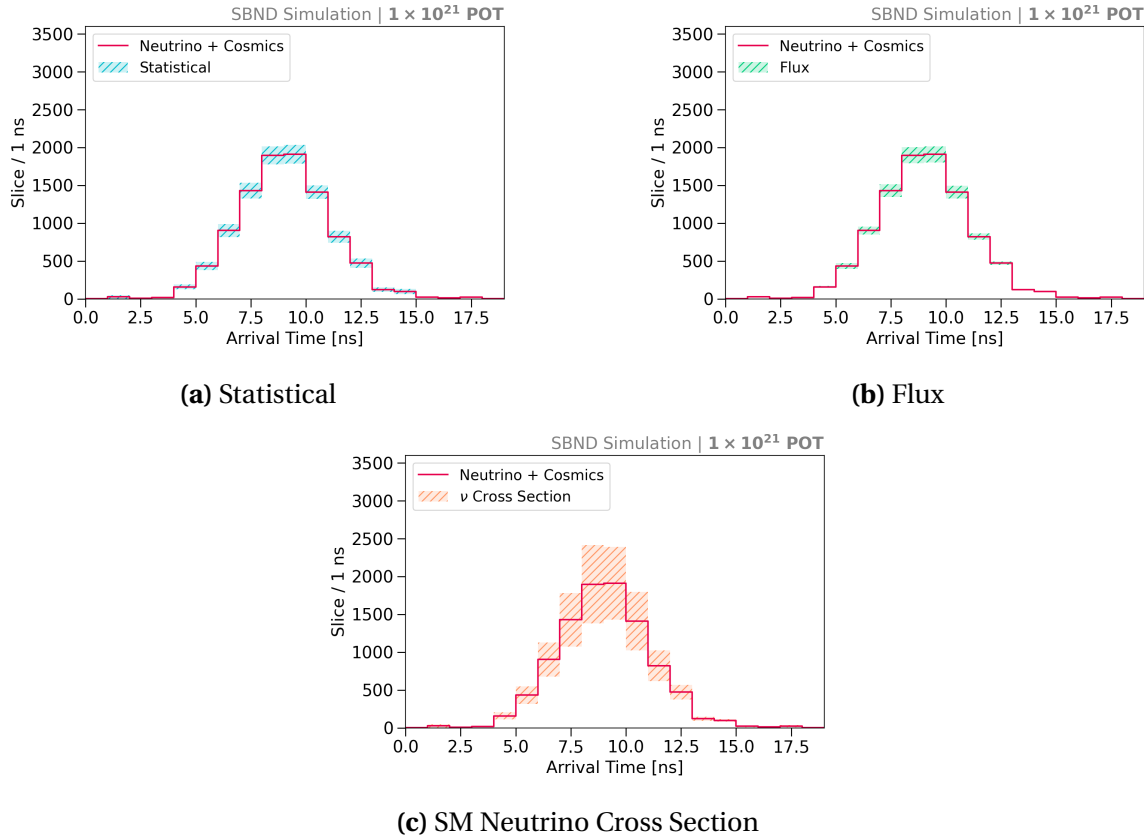


Fig. 10.3 Uncertainties of SM neutrino and cosmic backgrounds, including (a) statistical, (b) flux and (c) SM neutrino cross section.

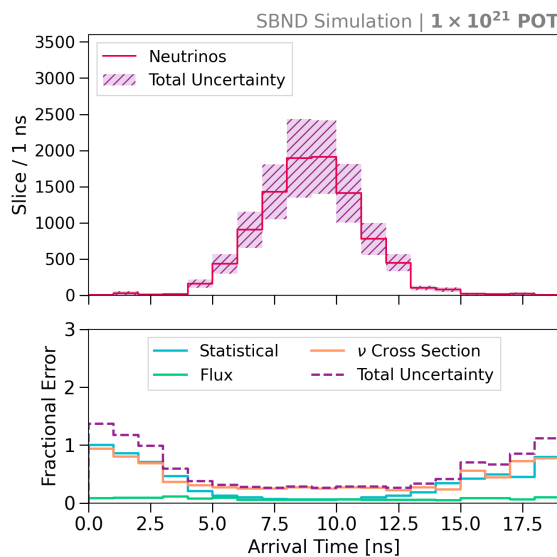


Fig. 10.4 Total uncertainty (top) and fractional uncertainties (bottom) of SM neutrino and cosmic backgrounds.

where s_i and b_i are the number of entries from the signal and background distributions for bin i . The *parameter of interest* μ determines the strength of the signal process, where $\mu = 0$ corresponds to the background-only H_b hypothesis and $\mu = 1$ corresponds to the nominal signal H_{s+b} hypothesis. It is an unconstrained parameter and is written separately from other parameters in the hypothesis. In the HNL search, varying the μ parameter is equivalent to varying the coupling $|U_{\mu 4}|^2$. Other parameters in the hypothesis characterising the shape of the distributions are grouped as *nuisance parameters*, denoted as θ . Then, the null and test hypotheses can be formally written as

$$\text{Null hypothesis: } H_{s+b} = H(\mu = 1, \theta) \quad (10.9)$$

$$\text{Test hypothesis: } H_b = H(\mu = 0, \theta) \quad (10.10)$$

10.2.2 Likelihood-based Test Statistic

To exclude the null hypothesis H_{s+b} at some confidence levels, a test statistic is performed for a hypothesised μ against H_{s+b} and H_b . To construct a test statistic for a multi-binned histogram, likelihood-based functions are chosen. The likelihood function is the product of Poisson probabilities of all bins in the histogram [8]

$$L(\mu, \theta) = \prod_{i=1}^N \frac{(\mu s_i + b_i)^{n_i}}{n_i!} e^{-(\mu s_i + b_i)} \prod_{\theta \in \Theta} c_\theta(a_\theta | \theta) \quad (10.11)$$

The first product describes the likelihood of the histogram n with bin index i , which is constructed using the beam bucket distribution of HNLs as signals and SM neutrinos with cosmics as backgrounds. The second product is a constraint term $c_\theta(a_\theta | \theta)$ with measurement a_θ constraining the nuisance parameter θ . Each uncertainty source of signals and backgrounds, as discussed in Section 10.1, corresponds to a constraint term.

For a hypothesised value of μ , the profile likelihood ratio can be constructed from the likelihood function as [8]

$$\lambda(\mu) = \frac{L(\mu, \hat{\hat{\theta}}(\mu))}{L(\hat{\mu}, \hat{\theta})} \quad (10.12)$$

The numerator is the *conditional* maximised likelihood for the hypothesised value μ and $\hat{\hat{\theta}}(\mu)$ is a function of μ . The denominator is the *unconditional* maximised likelihood, where $\hat{\mu}$ and $\hat{\theta} = \hat{\hat{\theta}}(\hat{\mu})$ are the best fit parameters to the observed data.

A modification in the likelihood ratio is required for cases where the signal process only increases the mean event rate, such that $\mu \geq 0$. If the observed data results in the best

10.2 Limits Setting Procedure

fit $\hat{\mu} < 0$, then the best level of agreement between the data and the prediction is forced to occur at $\hat{\mu} = 0$. This is equivalent to the late arrival of HNLs relative to the SM neutrino beam bucket, which can only increase the event rate for bins at the edge of the beam bucket. The profile likelihood ratio is then modified as [8]

$$\tilde{\lambda}(\mu) = \begin{cases} \frac{L(\mu, \hat{\theta}(\mu))}{L(0, \hat{\theta}(0))} & \hat{\mu} < 0 \\ \frac{L(\mu, \hat{\theta}(\mu))}{L(\hat{\mu}, \hat{\theta})} & \hat{\mu} \geq 0 \end{cases} \quad (10.13)$$

where $\hat{\theta}(0)$ is a function of $\mu = 0$.

From the modified profile likelihood ratio, the test statistic for setting upper limits is [8]

$$\tilde{q}_\mu = \begin{cases} -2 \ln \tilde{\lambda}(\mu) & \hat{\mu} \leq \mu \\ 0 & \hat{\mu} > \mu \end{cases} = \begin{cases} -2 \ln \frac{L(\mu, \hat{\theta}(\mu))}{L(0, \hat{\theta}(0))} & \hat{\mu} < 0 \\ -2 \ln \frac{L(\mu, \hat{\theta}(\mu))}{L(\hat{\mu}, \hat{\theta})} & 0 \leq \hat{\mu} \leq \mu, \\ 0 & \hat{\mu} > \mu \end{cases} \quad (10.14)$$

In the region $\hat{\mu} > \mu$, equivalent to an upward fluctuation in the data compared to the prediction, the test statistic \tilde{q}_μ is set to 0. For setting an upper limit, this fluctuation does not represent less incompatibility and therefore is not taken into the rejection region of the test. A larger value of \tilde{q}_μ corresponds to an increasing disagreement between the data and the prediction for the hypothesised μ .

The distribution $f(\tilde{q}_\mu | \mu')$ of a test statistic \tilde{q}_μ can be interpreted as a PDF. The subscript of \tilde{q} refers to the value of μ being tested in the numerator of the likelihood ratio in Eq. 10.12. The second argument μ' refers to the value of μ being assumed in the denominator of Eq. 10.12. For setting an upper limit with hypotheses testing, the PDF of interest is \tilde{q}_μ under the assumption of a different strength parameter $\mu' \neq \mu$. Therefore, the corresponding PDFs for a test signal strength μ , under the assumption of the null hypothesis H_{s+b} and the test hypothesis H_b , are respectively as

$$f(\tilde{q}_\mu | s + b) = f(\tilde{q}_\mu | \mu' = 1) \quad (10.15)$$

$$f(\tilde{q}_\mu | b) = f(\tilde{q}_\mu | \mu' = 0) \quad (10.16)$$

10.2.3 The CL_s Method

To quantify the level of significance of a test statistic, a p -value is computed as an integration of the PDF $f(\tilde{q}_\mu | \mu')$ on either side of $\hat{q} = \tilde{q}_\mu(\mu = \hat{\mu})$ where \hat{q} is the test statistic value

for the observed data. Typically, one might only consider the p -value resulting from the null hypothesis H_{s+b} , denoted as p_{s+b} , to exclude the null hypothesis. This represents the probability of finding data more background-like under the assumption that the signal is true, also known as the probability of getting the type I error in hypothesis testing.

However, this approach does not factor in the probability of finding data under the assumption of the background-only hypothesis. In scenarios where the test statistic is not sensitive to the prediction models, the PDFs of the H_{s+b} and H_b hypotheses would greatly overlap each other. One might make the mistake of interpreting having observed data highly contaminated with background-like events as a statement on the nominal signal hypothesis [10]. Therefore, a penalty for poor background modelling is necessary to account for how sensitive the test statistic is to the prediction model.

The CL_s method is a modified frequentist method to compute a modified p -value. This statistical method was developed specifically by particle physics experiments for the purpose of discovery as well as exclusion. This is a conservative approximation of the confidence level to account for poor background modelling and/or statistical fluctuations. Using the CL_s method, the p -values for the hypotheses H_{s+b} and H_b are defined as follows [8–10]

$$p_{s+b} = \int_{\hat{q}}^{\infty} f(\tilde{q}_\mu | s + b) d\tilde{q}_\mu \quad (10.17)$$

$$p_b = \int_{-\infty}^{\hat{q}} f(\tilde{q}_\mu | b) d\tilde{q}_\mu \quad (10.18)$$

p_{s+b} represents the probability of finding data more background-like under the assumption of the signal+background hypothesis H_{s+b} . p_b represents the probability of finding data more signal-like under the assumption of the background-only hypothesis H_b .

The modified p -value is then computed from the p -value for each hypothesis as [8–10]

$$CL_s = \frac{CL_{s+b}}{CL_b} = \frac{p_{s+b}}{1 - p_b} \quad (10.19)$$

Since $(1 - p_b)$ only varies between 0 and 1, the resulting CL_s is always greater or equal to p_{s+b} . Thus, the CL_s is more conservative in quantifying the Confidence Level (C.L.) of hypothesis testing. The threshold was chosen to be 0.1, such that $CL_s < (1 - 0.9)$, equivalent to setting an upper limit with a C.L. of 90%. This level was motivated in order to compare against existing experiment results.

10.2.4 Computing Test Statistic Distributions

One way to obtain the PDF of \tilde{q}_μ for a given hypothesis is by throwing toys (or pseudo-experiments) sampled from the observables n , with constrained nuisance parameters θ . Each toy result represents a potential outcome of \tilde{q}_μ and thus, the toy distribution represent the test statistic \tilde{q}_μ distribution. For a study using MC samples without having the observed data to determine \hat{q} , one can consider the distribution under the assumption of the background-only hypothesis H_b . In this case, $\hat{q} = \hat{q}_{expected}$ represents the *expectation* given the model prediction and is taken as the median of the H_b test statistic distribution, equivalent to assuming the observed data is the same as the background-only prediction.

Fig. 10.5 shows an example PDF of \tilde{q}_μ for a test signal strength μ acquired from 4000 toys thrown. The \tilde{q}_μ PDF under the assumption of H_{s+b} and H_b is shown in green and yellow respectively. The value $\hat{q}_{expected}$ is plotted as the dashed red line. The area under the curve $f(\tilde{q}_\mu|s+b)$ to the right of $\hat{q}_{expected}$ gives the median p_{s+b} and the area under the curve $f(\tilde{q}_\mu|b)$ to the left gives the median p_b . The CL_s value is then calculated to give the expected limit on the signal strength μ . To identify which μ value results in CL_s < 0.1, a range of μ is considered until the desired value CL_s is achieved. The test signal strength μ plotted here gives exactly CL_s < 0.1.

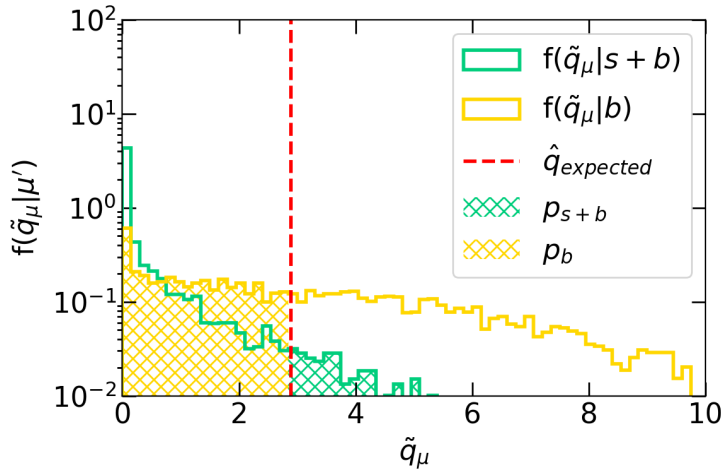


Fig. 10.5 Example of \tilde{q}_μ distributions using the toy throwing approach.

An alternative method to calculate the test statistic \tilde{q}_μ and its PDF is by asymptotic approximation. This approach assumes that $\hat{\mu}$ follows a Gaussian distribution around a mean of μ' with a standard deviation of σ . Via the pyhf package, PDFs are computed using the HistFactory module according to the formulae provided by Ref. [8]. Similar to

the toy throwing approach for an MC study, $\hat{q}_{expected}$ is also taken as the median of the background-only H_b test statistic distribution. To determine $CL_s < 0.1$, pyhf scans over a range of μ and the best value is calculated using interpolation.

Fig. 10.6 shows an example PDF of \tilde{q}_μ computed using the asymptotic approximation. The expected $\hat{q}_{expected}$ is plotted as the dashed red line. The median p -values under the H_{s+b} and H_b hypotheses are plotted as shaded green and yellow areas respectively. The test signal strength μ shown here gives $CL_s < 0.1$. Standard deviations of the CL_s can also be computed by substituting μ' with $\mu' \pm N\sigma$, where $N\sigma$ is the number of standard deviations away from the mean μ' . A validation was also carried out to compare the signal strength μ resulting from the toy throwing and asymptotic approximation. Both approaches returned μ values within 5% of each other, showing a good agreement.

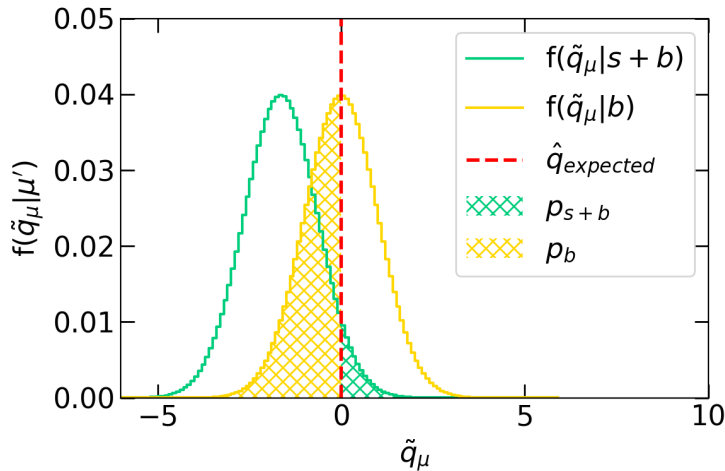


Fig. 10.6 Example of \tilde{q}_μ distributions using the asymptotic approximation.

10.2.5 Setting The Upper Limits

The setting limit procedure is performed fully using the pyhf package, with the steps described in the previous section. The beam bucket distribution is input into the pyhf package to infer the upper limit at C.L. of 90%. The histograms input to the background-only H_b and the signal+background H_{s+b} hypothesis are as following

- H_b : The SM neutrinos and cosmic beam bucket distribution.
- H_{s+b} : The HNL beam bucket distribution on top of the background distribution.

10.2 Limits Setting Procedure

These histograms are the ingredients for the first product in Eq. 10.11. Since the likelihood functions are products of individual bins of the histograms, one can reduce the computing time by considering only high signal-to-noise bins that contribute the most to the sensitivity. As previously stated as the timing cut, the relevant high signal-to-noise bins are the first and last 4 bins of the beam bucket distribution, which lead to the same result as demonstrated later in Section 10.3 (See Section 9.5).

Three beam bucket distributions were used in the limits setting. Appendix D and E contain the beam bucket distributions for signals and backgrounds after the lenient and stringent cut respectively, with all uncertainties propagated. Additionally, appendix F contains the smeared truth distributions under the assumption of timing reconstruction improvement as discussed in Section 9.6.

The uncertainties of the beam bucket distribution discussed in Section 10.1 are the constraints on the nuisance parameters $c_\theta(a_\theta|\theta)$ in the second product Eq. 10.11. Different types of constraints can take different statistical shapes, which are called *modifiers* in the pyhf package [7, 131]. Table 10.1 summarises the uncertainties and their corresponding modifiers of the signal and background distribution.

For the signal distribution, the assumption is that the signal rate is relatively low and expected to follow a Poisson distribution. Similarly, the cosmic mistagging rate falls under the same assumption since it is proportional to the signal rate. Thus, the modifier for both statistical and cosmic mistagging uncertainties of the signal distribution follows a Poisson shape, treating each bin uncorrelated. The flux uncertainty of the signal distribution uses a Gaussian-shaped modifier instead, to enable correlation bin-wise.

For the background distribution, the treatment of statistical uncertainty employs a modified version of the Beeston-Barlow method [132] to account for statistical fluctuations due to finite statistics. The modifier in this case follows a Gaussian shape for bins with high statistics and falls back to a Poisson shape for bins with low statistics while treating each bin uncorrelated. Moreover, the flux and SM neutrino cross section uncertainty also use a Gaussian-shaped modifier, however, with correlation bin-by-bin.

For a single mass point, pyhf performs a scanning of signal strength μ until the desired value giving the 90% CL is determined. To infer from the signal strength μ to the coupling $|U_{\mu 4}|^2$, the proportionality of the number of signals N_{HNL} to the coupling is employed. The signal rate observed at the detector is proportional to the coupling at the HNL production as well as the coupling at the HNL decay, and thus, $N_{HNL} \propto |U_{\mu 4}|^4$. The upper limit of the coupling is then $\sqrt{\mu}$ multiplied by the input coupling $|U_{\mu 4}|^2$. This process is repeated across all the mass points.

Table 10.1 Table summarising modifiers used to constrain uncertainties.

	Uncertainty	Modifier	Sample Correlation	Bin Correlation
Signal	Statistical	Poisson	False	False
	Cosmic mis-tagging	Poisson	False	False
	Flux	Gaussian	False	True
Background	Statistical	Gaussian	False	False
	Flux	Gaussian	False	True
	SM Neutrino Cross Section	Gaussian	False	True

10.3 Results

Results acquired from three different beam bucket distributions are presented in this section. The first two distributions were acquired by using fully reconstructed MC samples mimicking data, of which one was applied with a lenient selection as shown in Fig. 10.7a and the other one was applied with a stringent selection as shown in Fig. 10.7b. The third distribution is the smeared truth as shown in Fig. 10.7c, which was constructed by smearing *true* variables without any detection simulation and reconstruction applied. The smeared truth distribution was motivated under the assumption of a better timing reconstruction resolving the beam bucket with a resolution of 1.73 ns. Unlike, the reconstructed distributions with full uncertainties propagated, the smeared truth distribution does not contain any uncertainties for simplicity. Moreover, the first and last 4 bins of every distribution are also shown to demonstrate the significantly high signal-to-background ratio of these bins.

10.3.1 Comparison Across Different Beam Bucket Distributions

The upper limits on the coupling of Majorana HNLs at 90% C.L. are presented in Fig. 10.8, comparing results from fitting the beam bucket distribution with the lenient and stringent distribution. The expected limit is plotted as the solid black line. The deviation band at 1 and 2σ away from the expectation, also known as the *Brazil* band, is plotted in shaded green and yellow respectively. The lenient distribution results in limits excluding the coupling $|U_{\mu 4}|^2$ from 9.18×10^{-7} to 1.35×10^{-8} across the mass range from 140 to 260

10.3 Results

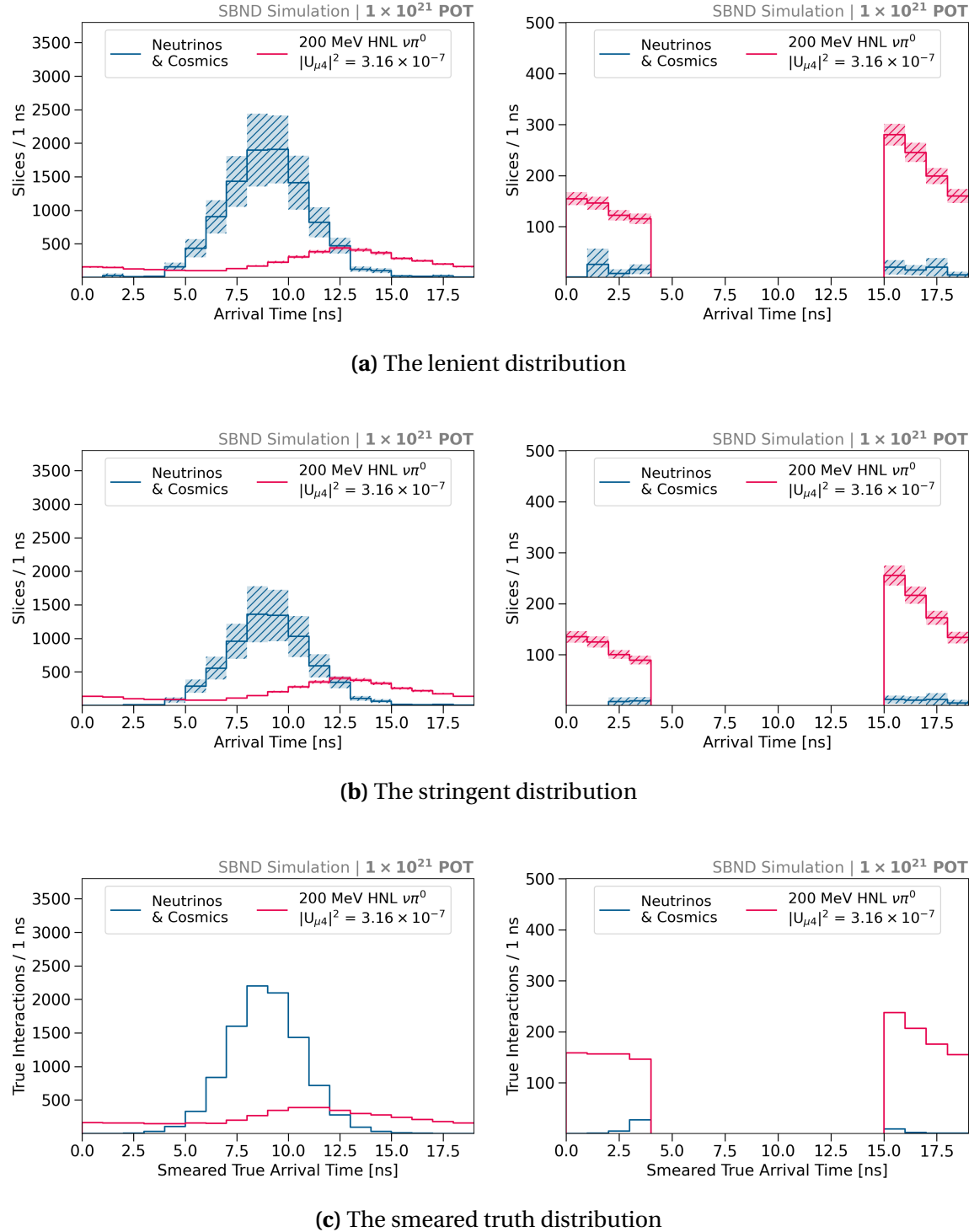


Fig. 10.7 Beam bucket distributions used for the limits setting, including (a) the lenient, (b) the stringent and (c) the smeared truth distribution.

MeV. The stringent cut results in more competitive limits, pushing the exclusion region of the coupling further down from 5.37×10^{-7} to 7.65×10^{-9} at the same mass range. This is due to the stringent distribution having a better signal-to-background ratio for bins at the edge of the beam bucket. This is evident when comparing between Fig. 10.7a and 10.7b, where the signal rate is very similar across the two distributions but the background rate is much lower in the stringent than the lenient distribution. Particularly, the first two bins of the stringent distribution are background-free, thus, driving the limit significantly.

However, the magnitude of the Brazil band of the stringent result is larger than the lenient result, indicating that the stringent result has larger uncertainties. This is likely due to the limited statistics of the background MC samples after the stringent selection. As can be observed from bins at the edge of the beam bucket distribution shown in Fig. 10.7b, the lack of background statistics might be insufficient to describe the underlying distribution, which can lead to large statistical fluctuations. Although the stringent distribution leads to a more competitive result, a future iteration of this selection is recommended to perform on larger statistics MC samples so that the statistical uncertainty can be better constrained.

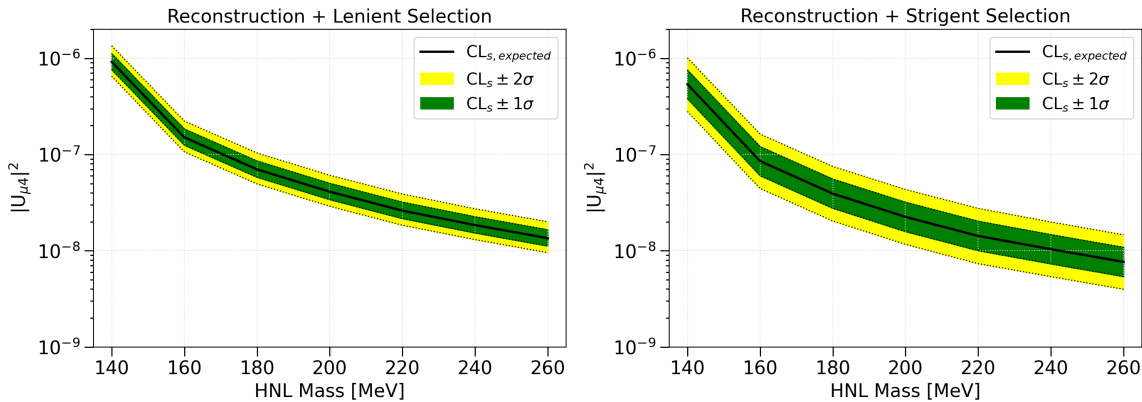


Fig. 10.8 Expected upper limits and the Brazil bands on the coupling $|U_{\mu 4}|^2$ for Majorana HNLs, for the lenient (left) and stringent distribution (right).

Fig. 10.9 shows the comparison between limits setting using the entire histogram and only the first and last 4 bins, which were previously referred to as the timing cut in Chapter 9. The upper limits are the same for both cases. The result demonstrates that the first and last 4 bins are the highest signal-to-background ratio bins, and therefore are the main contributor to the limits. This provides a useful insight for future iterations of this analysis indicating the region on the beam bucket distribution should be focused on when performing the selection. A recommendation is to focus on optimising the signal-to-background only in the edge region. Another recommendation is to develop

10.3 Results

different selections for different regions of the bucket, capitalising on their different signal-to-background ratios.

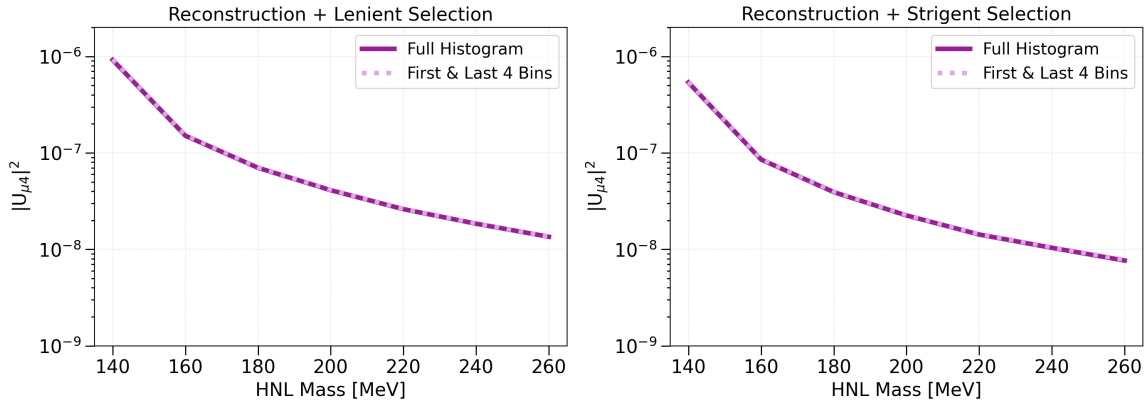


Fig. 10.9 Comparison between limits setting using the entire histogram and only the edge bins of the lenient (left) and stringent distribution (right).

Finally, Fig. 10.10 shows the upper limits from all three beam bucket distributions. The result from the smeared truth distribution, as shown by the green line, is significantly more competitive than the results using reconstructed distributions, as shown by the red and blue lines. The upper limits of the smeared truth distribution range from 1.81×10^{-7} to 2.46×10^{-9} across the mass range of 140 - 260 MeV. As detailed in Section 9.6, the smeared truth distribution was produced under the assumption of a better timing reconstruction to explore its impact on sensitivity. The background beam bucket distribution of the smeared truth follows a Gaussian with a sigma of 1.73 ns as compared to 1.99 ns of the reconstructed distribution after the lenient or stringent cut. The impact of the timing resolution improvement is evident in Fig. 10.7c, particularly for bins at the edge region. It can be seen that the background rate is lower while the signal rate is significantly higher in the smeared truth distribution than the reconstructed distribution. The resulting signal-to-background ratio is therefore higher for the edge bins, driving the sensitivity limits more aggressively.

This presents a positive outlook as an area for improvement for SBND to achieve more competitive results in the search for HNLs. Particularly, this can be done with a more sophisticated timing reconstruction that can resolve the beam bucket with higher resolution < 2 ns. The expected upper limits at 90% C.L. and the Brazil bands acquired from the three beam bucket distributions are summarised below in Table 10.2.

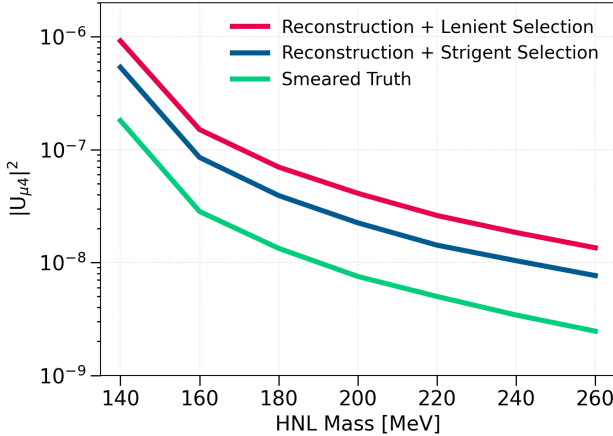


Fig. 10.10 Comparison between limits resulting from the lenient and stringent reconstructed distributions and the smeared truth distribution.

10.3.2 Comparison With Other Experiments

Fig. 10.11 shows the expected upper limits of SBND on the coupling $|U_{\mu 4}|^2$ of Majorana HNLs, comparing against existing experimental results as previously discussed in Section 2.4. All limits presented here are at 90% C.L.

For the limits acquired from the lenient and stringent distributions, as shown by the solid red and blue line respectively, they are comparable to existing limits. The lenient limit is almost the same as the limit achieved by the MicroBooNE experiment, as shown by the solid light blue line. On the other hand, the stringent limit is slightly more competitive than MicroBooNe, excluding a new region of the coupling in the mass range < 200 MeV. However, in the mass range > 200 MeV, the phase space is already excluded by the E949 and NA62 experiments, as shown by the dashed pink and orange lines. These two limits feature the first benchmark of SBND in this phase space of HNLs, given the current detector and reconstruction capabilities.

The limits acquired from the smeared truth distribution, as shown by the green line, is the most competitive out of the three results presented here. The result is projected to exclude a new region beyond the existing limits from the MicroBooNE, E949 and NA62 experiments. This demonstrates the potential of the physics capability of SBND, under the assumption of an exposure of 1×10^{21} POT and an exceptional timing reconstruction with a resolution of 1.73 ns. The POT exposure presented here is equivalent to 3 years of physics data taking, which allows for a lot of time and opportunities to work on improving the timing reconstruction of SBND to achieve the target resolution from the time of writing.

10.4 Concluding Remarks

Table 10.2 Table summarising expected upper limits results.

	Mass [MeV]	Expected Limit	+1 σ	-1 σ	+2 σ	-2 σ
Lenient	140	9.18×10^{-7}	1.12×10^{-6}	7.62×10^{-7}	1.35×10^{-6}	6.51×10^{-7}
	160	1.51×10^{-7}	1.84×10^{-7}	1.25×10^{-7}	2.22×10^{-7}	1.07×10^{-7}
	180	7.00×10^{-8}	8.57×10^{-8}	5.80×10^{-8}	1.04×10^{-7}	4.95×10^{-8}
	200	4.10×10^{-8}	5.02×10^{-8}	3.40×10^{-8}	6.08×10^{-8}	2.90×10^{-8}
	220	2.61×10^{-8}	3.20×10^{-8}	2.16×10^{-8}	3.88×10^{-8}	1.84×10^{-8}
	240	1.84×10^{-8}	2.26×10^{-8}	1.53×10^{-8}	2.73×10^{-8}	1.30×10^{-8}
	260	1.35×10^{-8}	1.65×10^{-8}	1.12×10^{-8}	2.00×10^{-8}	9.55×10^{-9}
Stringent	140	5.37×10^{-7}	7.56×10^{-7}	3.80×10^{-7}	1.01×10^{-6}	2.80×10^{-7}
	160	8.53×10^{-8}	1.21×10^{-7}	6.02×10^{-8}	1.63×10^{-7}	4.43×10^{-8}
	180	3.92×10^{-8}	5.56×10^{-8}	2.76×10^{-8}	7.50×10^{-8}	2.04×10^{-8}
	200	2.25×10^{-8}	3.20×10^{-8}	1.58×10^{-8}	4.32×10^{-8}	1.17×10^{-8}
	220	1.42×10^{-8}	2.03×10^{-8}	1.00×10^{-8}	2.75×10^{-8}	7.34×10^{-9}
	240	1.04×10^{-8}	1.47×10^{-8}	7.31×10^{-9}	1.99×10^{-8}	5.39×10^{-9}
	260	7.65×10^{-9}	1.09×10^{-8}	5.39×10^{-9}	1.46×10^{-8}	3.98×10^{-9}
Smeared Truth	140	1.81×10^{-7}	2.45×10^{-7}	1.35×10^{-7}	3.21×10^{-7}	1.05×10^{-7}
	160	2.83×10^{-8}	3.84×10^{-8}	2.11×10^{-8}	5.05×10^{-8}	1.63×10^{-8}
	180	1.33×10^{-8}	1.81×10^{-8}	9.94×10^{-9}	2.38×10^{-8}	7.70×10^{-9}
	200	7.52×10^{-9}	1.02×10^{-8}	5.62×10^{-9}	1.34×10^{-8}	4.38×10^{-9}
	220	5.00×10^{-9}	6.78×10^{-9}	3.73×10^{-9}	8.90×10^{-9}	2.90×10^{-9}
	240	3.42×10^{-9}	4.65×10^{-9}	2.55×10^{-9}	6.10×10^{-9}	1.99×10^{-9}
	260	2.46×10^{-9}	3.34×10^{-9}	1.84×10^{-9}	4.39×10^{-9}	1.44×10^{-9}

10.4 Concluding Remarks

Three upper limits on the coupling $|U_{\mu 4}|^2$ of Majorana HNLs are presented in this chapter to demonstrate the range of the physics capability of SBND. The limits from the lenient and stringent beam bucket distribution demonstrate the current performance of SBND, which is currently comparable to existing experimental limits. The limits from the smeared truth distribution are the most competitive that can exclude a new region not yet explored by other experiments. This limit also demonstrates the potential that SBND can achieve if the timing reconstruction is improved with a better timing resolution. Although ambitious, this goal is within reach in the next couple of years given the ongoing work towards a nanosecond timing resolution at SBND, one of which was presented in Chapter 7 and many more to be expected in the near future.

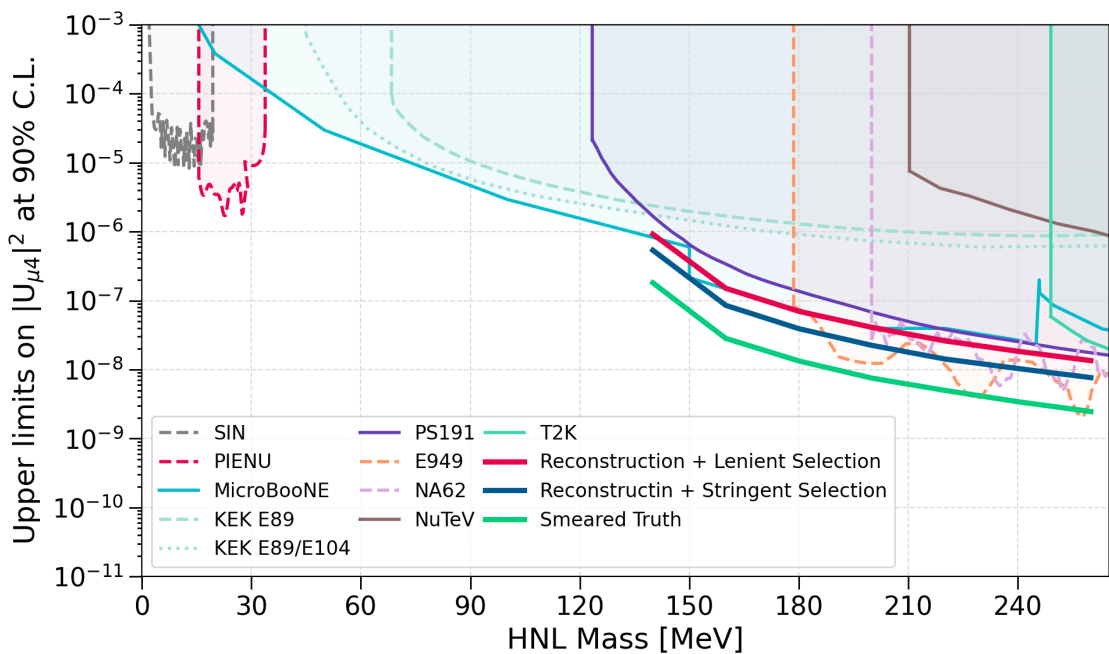


Fig. 10.11 Upper limits on the coupling $|U_{\mu 4}|^2$ at the 90% confidence level for Majorana HNLs in the mass range of $0 < m_N < 265$ MeV, comparing SBND MC results against existing experimental results.

Chapter 11

Conclusions

This thesis presents the first assessment of the physics capabilities of the Short-Baseline Near Detector (SBND) to search for Heavy Neutral Leptons (HNLs) in the mass range of 140-260 MeV. This right-handed heavy neutrino state is motivated to provide a mass mechanism for the left-handed SM neutrinos. HNLs are hypothesised to be produced from the Booster Neutrino Beam (BNB) from meson decays and subsequently decay into SM observables inside SBND. Due to having mass, the two exploitable features of HNLs are their boosted topologies and late arrival compared to SM neutrinos. Particularly, the late arrival of HNLs can be observed as an excess in the tails of the Gaussian-shaped neutrino beam bucket. The beam bucket can be reconstructed with a resolution $\mathcal{O}(2\text{ ns})$ using light signals from the PhotoMultiplier Tubes (PMTs), part of the Photon Detection System (PDS) of SBND.

Towards this goal of achieving nanosecond resolution of SBND, developments in the scope of the timing performance of the Data AcQuisition (DAQ) were performed. An overview of the White Rabbit timing system was given, including the description of the SPEC-TDC as a precise timestamping device with a resolution of 700 ps to record important signals, including beams and triggers. This additional timing information enables many high precision physics analyses. For instance, the SPEC-TDC was used to perform the timing characterisation of the readout electronics of the Cosmic Ray Taggers (CRTs), of which their clock resolutions were determined to be $\mathcal{O}(2\text{ ns})$. Moreover, the SPEC-TDC was used to assess the timing synchronisation of the readout electronics of the PDS. This resulted in a clock scheme proposal and a correction method to synchronise multiple digitisers. It is a vitally important results since PMT signals are the key ingredients for timing reconstruction.

Two selection workflows were additionally developed to identify di-photon showers resulting from HNLs while rejecting backgrounds from SM neutrinos and cosmic muons. One selection is more lenient while the other is more stringent in rejecting backgrounds more aggressively. Both selections result in a background efficiency $\mathcal{O}(10^{-4})$ while still maintaining the signal efficiency at $\sim 30\%$. If only bins at the edge of beam bucket distribution are considered, equivalent to the so-called *timing cut*, the background efficiency decreases by two orders of magnitude to $\mathcal{O}(10^{-6})$ while the signal efficiency only reduces to 10%. The timing cut demonstrates the importance of the edge bins having an exceptionally high signal-to-background ratio, which is the driving factor for a competitive sensitivity. This motivates an assessment of sensitivity assuming an improvement in timing reconstruction. An additional beam bucket distribution was acquired by smearing true variables with an assumption of a smaller Gaussian width.

Finally, building upon the selection previously discussed, setting upper limits on the coupling $|U_{\mu 4}|^2$ of HNLs at a confidence level of 90% was performed on three sets of beam bucket distributions after selection on MC samples: (1) lenient, (2) stringent and (3) smeared truth. It was found that the stringent beam bucket distribution results in a more competitive limit than the lenient distribution due to having background-free bins, however, the stringent limit suffers large statistical fluctuations. These two limits were found to exclude the phase space already explored by the MicroBooNE, NA62 and E949 experiments. However, they are the first benchmark of the current physics capability of SBND in the search for HNLs. Moreover, it was demonstrated that the edge bins of the beam bucket distribution are the key bins that drive the upper limits. The smeared truth beam bucket distribution led to the most competitive limits out of the three, surpassing existing results from other experiments.

The first iteration of this analysis provides some guidelines applicable to future work. Firstly, detector systematics should be included in error propagation, with parameters that are impactful to physics measurement identified when SBND is operational. Secondly, due to the aggressive background rejection, the analysis should be performed on larger background MC samples, $\mathcal{O}(10^6)$ events compared to the presented $\mathcal{O}(10^5)$ events, to avoid statistical fluctuations. Finally, the results of the smeared truth distribution motivate the need for a resolution improvement when reconstructing the beam bucket distribution. The preparation work towards the nanosecond resolution has already begun with the DAQ readout electronics and the implementation of the SPEC-TDC for high precision timestamping. A more sophisticated timing reconstruction can be developed incorporating the extra timing information of beam and trigger signals. This improvement will not

only benefit the HNL analysis but any other analysis that exploits the Gaussian tails of the beam bucket to either look for a new signal or to reject cosmic backgrounds.

References

- [1] P. A. Machado et al., “The Short-Baseline Neutrino Program at Fermilab”, Annual Review of Nuclear and Particle Science **69**, 363–387 (2019).
- [2] R. Acciarri et al. (SBND), “Construction of precision wire readout planes for the Short-Baseline Near Detector (SBND)”, JINST **15**, P06033 (2020).
- [3] A. A. Aguilar-Arevalo et al. (MiniBooNE Collaboration), “Neutrino flux prediction at miniboone”, Phys. Rev. D **79**, 072002 (2009).
- [4] G. Cheng et al. (SciBooNE Collaboration), “Measurement of K^+ production cross section by 8 GeV protons using high-energy neutrino interactions in the SciBooNE detector”, Phys. Rev. D **84**, 012009 (2011).
- [5] C. Adams et al., “Ionization electron signal processing in single phase LArTPCs. Part I. Algorithm Description and quantitative evaluation with MicroBooNE simulation”, Journal of Instrumentation **13**, P07006 (2018).
- [6] J. S. Marshall et al., “The Pandora Software Development Kit for Pattern Recognition”, Eur. Phys. J. C **75**, 439 (2015).
- [7] L. Heinrich et al., *pyhf: v0.7.6*, version 0.7.6, <https://github.com/scikit-hep/pyhf/releases/tag/v0.7.6>.
- [8] G. Cowan et al., “Asymptotic formulae for likelihood-based tests of new physics”, Eur. Phys. J. C **71**, [Erratum: Eur.Phys.J.C 73, 2501 (2013)], 1554 (2011).
- [9] T. Junk, “Confidence level computation for combining searches with small statistics”, Nucl. Instrum. Meth. A **434**, 435–443 (1999).
- [10] A. L. Read, “Presentation of search results: The CL_s technique”, J. Phys. G **28**, edited by M. R. Whalley et al., 2693–2704 (2002).
- [11] M. Thomson, *Modern particle physics* (Cambridge University Press, New York, 2013).
- [12] E. Majorana, “Teoria simmetrica dell’elettrone e del positrone”, Nuovo Cim. **14**, 171–184 (1937).
- [13] C. Giunti et al., *Fundamentals of Neutrino Physics and Astrophysics* (Oxford University Press, Incorporated, 2007).
- [14] S. F. King, “Neutrino mass models”, Rept. Prog. Phys. **67**, 107–158 (2004).
- [15] P. Ballett et al., “MeV-scale sterile neutrino decays at the Fermilab Short-Baseline Neutrino program”, JHEP **04**, 102 (2017).
- [16] A. Aguilar et al. (LSND Collaboration), “Evidence for neutrino oscillations from the observation of $\bar{\nu}_e$ appearance in a $\bar{\nu}_\mu$ beam”, Phys. Rev. D **64**, 112007 (2001).

- [17] A. A. Aguilar-Arevalo et al. (MiniBooNE Collaboration), “Significant Excess of Electronlike Events in the MiniBooNE Short-Baseline Neutrino Experiment”, Phys. Rev. Lett. **121**, 221801 (2018).
- [18] M. A. Acero et al., “White Paper on Light Sterile Neutrino Searches and Related Phenomenology”, (2022).
- [19] J. M. Berryman et al., “Searches for Decays of New Particles in the DUNE Multi-Purpose Near Detector”, JHEP **02**, 174 (2020).
- [20] A. Atre et al., “The Search for Heavy Majorana Neutrinos”, JHEP **05**, 030 (2009).
- [21] P. Coloma et al., “GeV-scale neutrinos: interactions with mesons and DUNE sensitivity”, Eur. Phys. J. C **81**, 78 (2021).
- [22] P. A. Zyla et al. (Particle Data Group), “Review of Particle Physics”, PTEP **2020**, 083C01 (2020).
- [23] P. Ballett et al., “Heavy Neutral Leptons from low-scale seesaws at the DUNE Near Detector”, JHEP **03**, 111 (2020).
- [24] O. Goodwin, “Search for Higgs Portal Scalars and Heavy Neutral Leptons Decaying in the MicroBooNE Detector”, PhD thesis (The University of Manchester, 2022).
- [25] R. Abela et al., “Search for an Admixture of Heavy Neutrino in Pion Decay”, Phys. Lett. B **105**, [Erratum: Phys.Lett.B 106, 513 (1981)], 263–266 (1981).
- [26] R. C. Minehart et al., “Search for Admixtures of Massive Neutrinos in the Decay $\pi^+ \rightarrow \mu^+ + \bar{\nu}$ ”, Phys. Rev. Lett. **52**, 804–807 (1984).
- [27] M. Daum et al., “Search for admixtures of massive neutrinos in the decay $\pi^+ \rightarrow \mu^+ + \nu$ ”, Phys. Rev. D **36**, 2624–2632 (1987).
- [28] A. Aguilar-Arevalo et al. (PIENU), “Search for heavy neutrinos in $\pi \rightarrow \mu\nu$ decay”, Phys. Lett. B **798**, 134980 (2019).
- [29] Y. Asano et al., “Search for a Heavy Neutrino Emitted in $K^+ \rightarrow \mu^+$ Neutrino Decay”, Phys. Lett. B **104**, 84–88 (1981).
- [30] R. S. Hayano et al., “Heavy-Neutrino Search Using $K_{\mu 2}$ Decay”, Phys. Rev. Lett. **49**, 1305–1309 (1982).
- [31] T. Yamazaki et al., “Search for Heavy Neutrinos in Kaon Decay”, in Proc. of the 22nd International Conference on High Energy Physics, Vol. 840719, edited by A. Meyer et al. (1984), p. 262.
- [32] A. V. Artamonov et al. (E949), “Search for heavy neutrinos in $K^+ \rightarrow \mu^+ \nu_H$ decays”, Phys. Rev. D **91**, [Erratum: Phys.Rev.D 91, 059903 (2015)], 052001 (2015).
- [33] E. Cortina Gil et al. (NA62), “Search for heavy neutral lepton production in K^+ decays”, Phys. Lett. B **778**, 137–145 (2018).
- [34] E. Cortina Gil et al. (NA62), “Search for K^+ decays to a muon and invisible particles”, Phys. Lett. B **816**, 136259 (2021).
- [35] G. Bernardi et al., “Search for neutrino decay”, Physics Letters B **166**, 479–483 (1986).
- [36] G. Bernardi et al., “Further limits on heavy neutrino couplings”, Physics Letters B **203**, 332–334 (1988).

References

- [37] C. A. Argüelles et al., “Heavy neutral leptons below the kaon mass at hodoscopic neutrino detectors”, Phys. Rev. D **105**, 095006 (2022).
- [38] A. Vaitaitis et al. (NuTeV, E815), “Search for neutral heavy leptons in a high-energy neutrino beam”, Phys. Rev. Lett. **83**, 4943–4946 (1999).
- [39] K. Abe et al. (T2K), “Search for heavy neutrinos with the T2K near detector ND280”, Phys. Rev. D **100**, 052006 (2019).
- [40] P. Abratenko et al. (MicroBooNE), “Search for Heavy Neutral Leptons Decaying into Muon-Pion Pairs in the MicroBooNE Detector”, Phys. Rev. D **101**, 052001 (2020).
- [41] P. Abratenko et al. (MicroBooNE), “Search for long-lived heavy neutral leptons and Higgs portal scalars decaying in the MicroBooNE detector”, Phys. Rev. D **106**, 092006 (2022).
- [42] P. Abratenko et al. (MicroBooNE), “Search for heavy neutral leptons in electron-positron and neutral-pion final states with the MicroBooNE detector”, (2023).
- [43] C. Rubbia, “The Liquid Argon Time Projection Chamber: A New Concept for Neutrino Detectors”, (1977).
- [44] J. N. Marx et al., “The Time Projection Chamber”, Phys. Today **31N10**, 46–53 (1978).
- [45] D. R. Nygren, “Origin and development of the TPC idea”, Nuclear Instruments and Methods in Physics Research Section A: Accelerators, Spectrometers, Detectors and Associated Equipment **907**, Advances in Instrumentation and Experimental Methods (Special Issue in Honour of Kai Siegbahn), 22–30 (2018).
- [46] W. Willis et al., “Liquid-argon ionization chambers as total-absorption detectors”, Nuclear Instruments and Methods **120**, 221–236 (1974).
- [47] R. Acciarri et al., “Design and construction of the MicroBooNE detector”, Journal of Instrumentation **12**, P02017 (2017).
- [48] S. Amerio et al. (ICARUS), “Design, construction and tests of the ICARUS T600 detector”, Nucl. Instrum. Meth. A **527**, 329–410 (2004).
- [49] B. Abi et al. (DUNE), “Deep Underground Neutrino Experiment (DUNE), Far Detector Technical Design Report, Volume IV: Far Detector Single-phase Technology”, JINST **15**, T08010 (2020).
- [50] R. S. Jones, “Muon-neutrino disappearance with multiple liquid argon time projection chambers in the Fermilab Booster neutrino beam”, PhD thesis (The University of Liverpool, 2021).
- [51] R. Acciarri et al. (MicroBooNE,), “A Measurement of the Attenuation of Drifting Electrons in the MicroBooNE LArTPC”, 10.2172/1573054 (2017).
- [52] D. E. Groom et al., “Passage of particles through matter”, The European Physical Journal C - Particles and Fields **15**, 163–173 (2000).
- [53] C. Anderson et al., “The ArgoNeuT detector in the NuMI low-energy beam line at Fermilab”, Journal of Instrumentation **7**, P10019 (2012).
- [54] C. Adams et al. (MicroBooNE), “Reconstruction and measurement of $\mathcal{O}(100)$ MeV energy electromagnetic activity from $\pi_0 \rightarrow \gamma\gamma$ decays in the MicroBooNE LArTPC”, Journal of Instrumentation **15**, P02007 (2020).

- [55] R. Acciarri et al. (MicroBooNE), “Michel Electron Reconstruction Using Cosmic-Ray Data from the MicroBooNE LArTPC”, JINST **12**, P09014 (2017).
- [56] W. Foreman et al. (LArIAT Collaboration), “Calorimetry for low-energy electrons using charge and light in liquid argon”, Phys. Rev. D **101**, 012010 (2020).
- [57] A. Hitachi et al., “Effect of ionization density on the time dependence of luminescence from liquid argon and xenon”, Phys. Rev. B **27**, 5279–5285 (1983).
- [58] T. Doke et al., “Estimation of absolute photon yields in liquid argon and xenon for relativistic (1 MeV) electrons”, Nucl. Instrum. Meth. A **291**, 617–620 (1990).
- [59] T. Doke et al., “Absolute Scintillation Yields in Liquid Argon and Xenon for Various Particles”, Jap. J. Appl. Phys. **41**, 1538–1545 (2002).
- [60] R. Acciarri et al., “A study of electron recombination using highly ionizing particles in the ArgoNeuT Liquid Argon TPC”, Journal of Instrumentation **8**, P08005 (2013).
- [61] S. Kubota et al., “Dynamical behavior of free electrons in the recombination process in liquid argon, krypton, and xenon”, Phys. Rev. B **20**, 3486–3496 (1979).
- [62] Y. Li et al., “Measurement of longitudinal electron diffusion in liquid argon”, Nuclear Instruments and Methods in Physics Research Section A: Accelerators, Spectrometers, Detectors and Associated Equipment **816**, 160–170 (2016).
- [63] P. Abratenko et al. (MicroBooNE), “Measurement of the longitudinal diffusion of ionization electrons in the MicroBooNE detector”, Journal of Instrumentation **16**, P09025 (2021).
- [64] G. Putnam et al., “Effect of diffusion on the peak value of energy loss observed in a LArTPC”, JINST **17**, P10044 (2022).
- [65] B. Abi et al., “First results on ProtoDUNE-SP liquid argon time projection chamber performance from a beam test at the CERN Neutrino Platform”, Journal of Instrumentation **15**, P12004 (2020).
- [66] M. Antonello et al., “Study of space charge in the ICARUS T600 detector”, Journal of Instrumentation **15**, P07001 (2020).
- [67] M. Mooney, “The MicroBooNE Experiment and the Impact of Space Charge Effects”, in Meeting of the APS Division of Particles and Fields (Nov. 2015).
- [68] P. Abratenko et al. (SBND), “Scintillation Light in SBND: Simulation, Reconstruction, and Expected Performance of the Photon Detection System”, (2024).
- [69] E. Grace et al., “Index of refraction, Rayleigh scattering length, and Sellmeier coefficients in solid and liquid argon and xenon”, Nucl. Instrum. Meth. A **867**, 204–208 (2017).
- [70] M. Babicz et al., “A measurement of the group velocity of scintillation light in liquid argon”, JINST **15**, P09009 (2020).
- [71] B. J. P. Jones et al., “A Measurement of the Absorption of Liquid Argon Scintillation Light by Dissolved Nitrogen at the Part-Per-Million Level”, JINST **8**, [Erratum: JINST 8, E09001 (2013)], P07011 (2013).
- [72] B. J. P. Jones et al., “The Effects of Dissolved Methane upon Liquid Argon Scintillation Light”, JINST **8**, P12015 (2013).

References

- [73] J. Calvo et al. (ArDM), “Measurement of the attenuation length of argon scintillation light in the ArDM LAr TPC”, *Astropart. Phys.* **97**, 186–196 (2018).
- [74] P. J. Green, “Light and Dark in Liquid argon time Projection Chamber Neutrino Detectors”, PhD thesis (The University of Manchester, 2022).
- [75] R. Acciarri et al., “Demonstration and Comparison of Operation of Photomultiplier Tubes at Liquid Argon Temperature”, *JINST* **7**, P01016 (2012).
- [76] A. Gola et al., “Nuv-sensitive silicon photomultiplier technologies developed at fondazione bruno kessler”, *Sensors* **19**, 10.3390/s19020308 (2019).
- [77] E. Segreto et al., “First liquid argon test of the x-arapuca”, *Journal of Instrumentation* **15**, C05045 (2020).
- [78] E. Segreto, “Evidence of delayed light emission of TetraPhenyl Butadiene excited by liquid Argon scintillation light”, *Phys. Rev. C* **91**, 035503 (2015).
- [79] G. Mention et al., “Reactor antineutrino anomaly”, *Phys. Rev. D* **83**, 073006 (2011).
- [80] P. Huber, “Determination of antineutrino spectra from nuclear reactors”, *Phys. Rev. C* **84**, 024617 (2011).
- [81] W. Hampel et al., “GALLEX solar neutrino observations: results for GALLEX IV”, *Physics Letters B* **447**, 127–133 (1999).
- [82] J. N. Abdurashitov et al., “The SAGE and LNGS experiment: Measurement of solar neutrinos at LNGS using gallium from SAGE”, *Astropart. Phys.* **25**, 349–354 (2006).
- [83] L. Alvarez-Ruso et al., “NuSTEC White Paper: Status and challenges of neutrino–nucleus scattering”, *Progress in Particle and Nuclear Physics* **100**, 1–68 (2018).
- [84] V. De Romeri et al., “DUNE-PRISM sensitivity to light dark matter”, *Phys. Rev. D* **100**, 095010 (2019).
- [85] E. Bertuzzo et al., “Neutrino masses and mixings dynamically generated by a light dark sector”, *Physics Letters B* **791**, 210–214 (2019).
- [86] E. Bertuzzo et al., “Dark Neutrino Portal to Explain MiniBooNE Excess”, *Phys. Rev. Lett.* **121**, 241801 (2018).
- [87] R. Acciarri et al. (MicroBooNE, SBND, ICARUS), “A Proposal for a Three Detector Short-Baseline Neutrino Oscillation Program in the Fermilab Booster Neutrino Beam”, (2015).
- [88] R. Acciarri et al., “Construction of precision wire readout planes for the Short-Baseline Near Detector (SBND)”, *Journal of Instrumentation* **15**, P06033 (2020).
- [89] *HAMAMATSU Datasheet - R5912*, Accessed: 25-02-2023, https://www.hamamatsu.com/resources/pdf/etd/LARGE_AREA_PMT TPMH1376E.pdf.
- [90] S. Gao (SBND), “Low Noise Cold Electronics System for SBND LAr TPC”, in Meeting of the Division of Particles and Fields of the American Physical Society (Oct. 2019).
- [91] *730 Digitizer Family 16/8 Ch. 14-bit 500 MS/s Digitizer*, Accessed: 25-02-2023, <https://www.caen.it/products/v1730/>.
- [92] *740 Digitizer Family 64/32 Ch. 12-bit 62.5 MS/s Digitizer*, Accessed: 25-02-2023, <https://www.caen.it/products/vx1740/>.
- [93] I. Kreslor (SBND Collaboration), *SBND CRT Technical Note*, tech. rep. (2016).

-
- [94] M. Stancari, “Capabilities of the SBND Trigger System”, in CPAD Workshop 2022 (2022).
 - [95] K. Biery et al., “Flexible and Scalable Data-Acquisition Using the artdaq Toolkit”, (2018).
 - [96] A. A. Aguilar-Arevalo et al. (MiniBooNE Collaboration), “Neutrino flux prediction at MiniBooNE”, Phys. Rev. D **79**, 072002 (2009).
 - [97] M. Backfish, *Measuring the Bunch Length of the Booster Neutrino Beamline Beam*, tech. rep. (Fermilab, Nov. 2015).
 - [98] M. Backfish, *MiniBooNE Resistive Wall Current Monitor*, tech. rep. (Fermilab, Nov. 2015).
 - [99] D. W. Schmitz, “A Measurement of Hadron Production Cross Sections for the Simulation of Accelerator Neutrino Beams and a Search for ν_μ to ν_e Sscillations in the δm^2 about equals $1 - eV^2$ Region”, PhD thesis (Columbia U., 2008).
 - [100] E. L. Snider et al., “LArSoft: Toolkit for Simulation, Reconstruction and Analysis of Liquid Argon TPC Neutrino Detectors”, J. Phys. Conf. Ser. **898**, edited by R. Mount et al., 042057 (2017).
 - [101] S. Agostinelli et al., “Geant4—a simulation toolkit”, Nuclear Instruments and Methods in Physics Research Section A: Accelerators, Spectrometers, Detectors and Associated Equipment **506**, 250–303 (2003).
 - [102] B. Patt et al., “Higgs-field portal into hidden sectors”, (2006).
 - [103] S. Weinberg, “A new light boson?”, Phys. Rev. Lett. **40**, 223–226 (1978).
 - [104] S. D. Porzio, “Searches for Heavy Neutral Lepton Decays in the MicroBooNE Detector”, PhD thesis (The University of Manchester, 2019).
 - [105] L. Alvarez-Ruso et al. (GENIE), “Recent highlights from GENIE v3”, Eur. Phys. J. ST **230**, 4449–4467 (2021).
 - [106] D. Heck et al., *CORSIKA: a Monte Carlo code to simulate extensive air showers*. (1998).
 - [107] J. Tena-Vidal et al. (GENIE Collaboration), “Neutrino-nucleus CC0 π cross-section tuning in GENIE v3”, Phys. Rev. D **106**, 112001 (2022).
 - [108] GENIE, “Liquid Argon Experiment tune”, Visited 06/05/2024.
 - [109] S. Giani et al., “GEANT4 simulation of energy losses of ions”, (1999).
 - [110] D. Garcia-Gamez et al., “Predicting Transport Effects of Scintillation Light Signals in Large-Scale Liquid Argon Detectors”, Eur. Phys. J. C **81**, 349 (2021).
 - [111] H. Yu et al., “Augmented signal processing in liquid argon time projection chambers with a deep neural network”, Journal of Instrumentation **16**, P01036 (2021).
 - [112] L. Tung, “Signal Processing in SBND with WireCell”, in APS April Meeting 2024 (2024).
 - [113] LArSoft, “GausHitFinder module”, (Visited 03/04/2024).
 - [114] E. Tyley, “Reconstructing and Selecting Electron Neutrino and Anti-Neutrino Interactions on Argon in the Short-Baseline Near Detector”, PhD thesis (The University of Sheffield, 2023).

References

- [115] M. Haigh, “MVAAlg module”, (Visited 21/05/2024).
- [116] L. Tung et al., “OptOFinder module”, (Visited 22/05/2024).
- [117] H. Lay, “CRUMBS module”, (Visited 22/05/2024).
- [118] H. Lay et al., “Razzled module”, (Visited 22/05/2024).
- [119] J. Serrano et al., “The White Rabbit Project”, in Proceedings of the 12th International Conference on Accelerator and Large Experimental Physics Control Systems, Vol. 1 (2009), p. 93.
- [120] A. Aloisio et al., “FPGA implementation of a high-resolution time-to-digital converter”, in 2007 IEEE Nuclear Science Symposium Conference Record, Vol. 1 (2007), p. 504.
- [121] P. Abratenko et al. (MicroBooNE Collaboration), “First demonstration of $\mathcal{O}(1 \text{ ns})$ timing resolution in the MicroBooNE liquid argon time projection chamber”, Phys. Rev. D **108**, 052010 (2023).
- [122] C. Adams et al. (MicroBooNE), “Calibration of the charge and energy loss per unit length of the MicroBooNE liquid argon time projection chamber using muons and protons”, JINST **15**, P03022 (2020).
- [123] S. Amoruso et al., “Study of electron recombination in liquid argon with the ICARUS TPC”, Nuclear Instruments and Methods in Physics Research Section A: Accelerators, Spectrometers, Detectors and Associated Equipment **523**, 275–286 (2004).
- [124] A. A. Abud et al. (DUNE Collaboration), “Reconstruction of interactions in the ProtoDUNE-SP detector with Pandora”, The European Physical Journal C **83**, 618 (2023).
- [125] M. Szydagis et al., “A Review of Basic Energy Reconstruction Techniques in Liquid Xenon and Argon Detectors for Dark Matter and Neutrino Physics Using NEST”, Instruments **5**, 13 (2021).
- [126] H. H. Andersen et al., *Hydrogen Stopping powers and ranges in all elements* (Pergamon Press, United States, 1977).
- [127] “ICRU Report 49, Stopping Power and Ranges for Protons and Alpha Particles”, Journal of the ICRU **os-25** (1993).
- [128] M. Miyajima et al., “Average energy expended per ion pair in liquid argon”, Phys. Rev. A **9**, 1438–1443 (1974).
- [129] G. Cowan, *Statistical data analysis*, Oxford science publications (Clarendon Press, 1998).
- [130] K. Duffy et al., “SBN Event Weighting module”, (Visited 26/06/2024).
- [131] L. Heinrich et al., “Pyhf: pure-python implementation of histfactory statistical models”, Journal of Open Source Software **6**, 2823 (2021).
- [132] R. J. Barlow et al., “Fitting using finite Monte Carlo samples”, Comput. Phys. Commun. **77**, 219–228 (1993).
- [133] G. V. Stenico, “SBND Trigger System: Status and MTC/A Configuration”, Physical Sciences Forum **8** (2023).

Appendix A

Hardware Triggering At SBND

The hardware triggering at SBND was previously discussed in Chapter 4 Sec. 4.2.5. Here a detailed description of the trigger signal distribution is provided. Fig. A.1 depicts the flow chart of signal inputs and outputs to and from the PTB, shown as the pink box, across different subsystems. The PTB receives the beam signal from the beam subsystem, shown as the green box. The beam signal denoted as *early warning* informs the PTB about the status of the BNB beam, indicating whether the beam has arrived at the detector hall. Also shown by the green box is the White Rabbit timing subsystem that distributes the Pulse Per Second (PPS) and 10 MHz clock signals to the PTB and other subsystems to maintain synchronisation. The White Rabbit timing, as part of the triggering and DAQ, was be discussed in detail in Chapter 7.

From the detection subsystems, the input signals to the PTB are from PMTs and CRTs. The PMTs provide information regarding the energy deposited inside the detector and whether its magnitude and location are consistent with a neutrino-induced event. The readouts of the PMTs are CAENV1730SB digitizers, shown as the light blue boxes. Each digitizer sends a *majority trigger* directly to the PTB if its channels cross a threshold. In addition, the number of channels above a threshold from the digitizers, denoted as *board sums*, are directed to the Master Trigger Card Analog (MTC/A), shown as the red box. The MTC/A performs a simple logic gate calculation to determine the number of PMT pairs above a threshold, denoted as *threshold crossing*, informing the PMT signal intensity and location. This signal from the MTC/A is input directly to the PTB. On the other hand, signals from the CRTs for triggering are much simpler. Coincident hits from any CRT walls, shown by the purple box, form *CRT triggers*, which are input straight to the PTB.

Once a trigger is formed, the PTB sends the trigger signals to subsequent readout subsystems to acquire the event, shown as the pink arrows leaving the PTB in Fig. A.1. An event contains two types of trigger signals: a single Event Trigger (ETRIG) and multiple Flash Triggers (FTRIGs). The ETRIG is issued to the TPC readout, shown as the orange box labelled Nevis Trigger Board (Nevis TB) to acquire waveforms from the wire planes. The FTRIGs are issued to the readouts of the PDS, shown as the light and dark blue boxes, to capture waveforms from the optical detectors.

An additional usage of the PTB is that it can output clock signals for some of the readout electronics. For the Nevis Trigger Board (TB) of the TPC readouts, it sends a PPS signal that is locked to the PPS signal that it receives from the White Rabbit timing system. This is depicted as the light pink arrow leaving the PTB to the Nevis TB. Moreover, the PTB sends a T1 Reset to CRT readouts shown as the pink arrows leaving the PTB to CRT, of which the CRT T1 clock was detailed in Sec. 7.2. The T1 Reset signal here is locked to the early warning signal from the beam system with some added delay so that it occurs some time *before* when the beam spill begins. Originally, the T1 Reset signal to the CRT readouts was the BES signal from the beam system, which occurred *right* when a beam spill begins. Resetting the T1 clock enforces some dead time on CRT readouts. Therefore, the T1 Reset signal was switched from the beam system to the PTB to have dead time outside of the beam spill window.

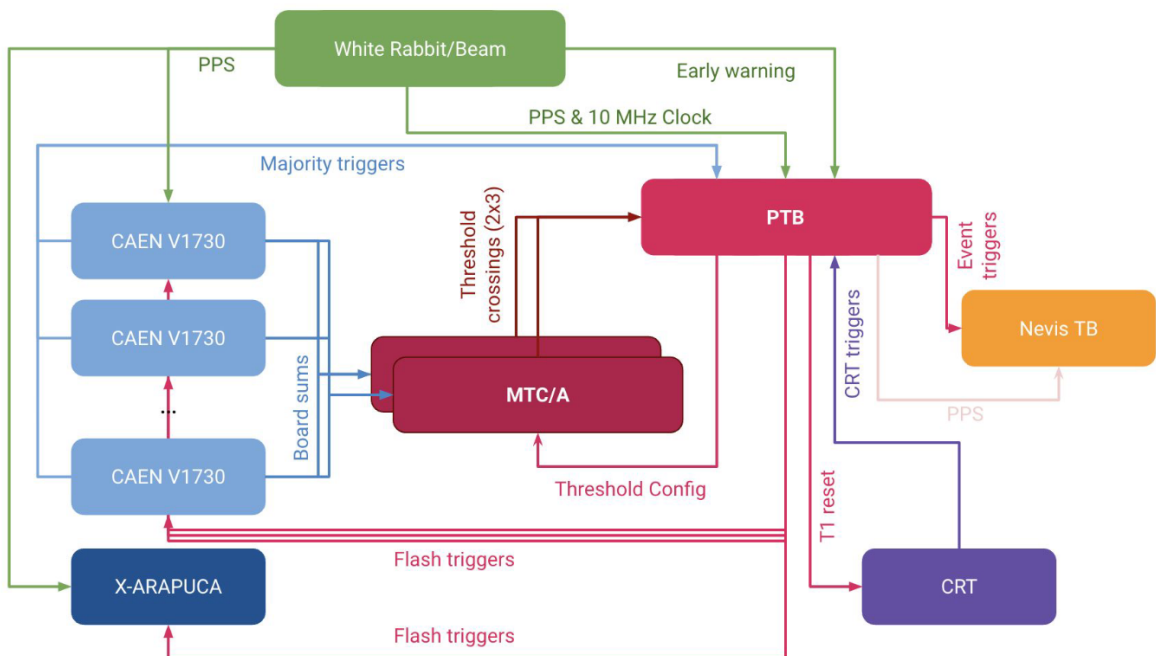


Fig. A.1 Flow chart showing the signal flow of the hardware triggering [133].

Appendix B

Data Streaming At SBND

The data streaming as the final step of the Data Acquisition (DAQ) at SBND was previously summarised in Chapter 4 Sec. 4.2.6. Details of the data streaming process is detailed here. After the event builder machines complete building a physics event, the resulting event can be filtered and sent to various storage locations for different analysis purposes, commonly referred to as data streaming. The artdaq Toolkit provides options to incorporate customisable filtering steps in real time. This allows the event builders to apply complex software metrics based on the fragment contents of an event. Once an event successfully passes through the filter, the event builders send it to a location defined by the filter for storage. However, if an event fails to pass the filters, it will be discarded during data taking.

The artdaq Toolkit also includes a built-in process for streaming data between event builder machines and online monitoring platforms. While operating in real time, fragments from boardreaders and physics events can be transmitted to these platforms for various monitoring purposes. SBND currently employs two online platforms: (1) Grafana and (2) Minargon.

Grafana provides real time monitoring of the health status of DAQ processes. A section of the Grafana website is displayed in Fig. B.1 for the boardreaders of PMTs. In the top left panel, the run number and a dial indicating the trigger rate issued by the PTB at 5.60 Hz are shown. The right panels display 9 dials, corresponding to 9 CAEN digitizers, showing the PMT fragment rates sent by the digitizers to the event builders, which is in good agreement with the trigger rate. The bottom left graph illustrates the PMT fragment rates as a function of time. The bottom middle and right graphs depict the rates of empty and missing PMT fragments as a function of time, which remain flat at zero, indicating a healthy DAQ state.

On the other hand, Minargon provides monitoring of the quality of data acquired by the DAQ. This online monitoring process applies simple reconstruction and event display to quantitatively verify the physics characteristics of an event. An example metric is displayed in Fig. B.2, which shows the root mean square of a PMT waveform baseline as a histogram in the left plot and as a function of time in the right plot. This metric helps monitor the baseline equalisation and stability over time.



Fig. B.1 Web page showing a section of Grafana for monitoring the health of PMT DAQ.

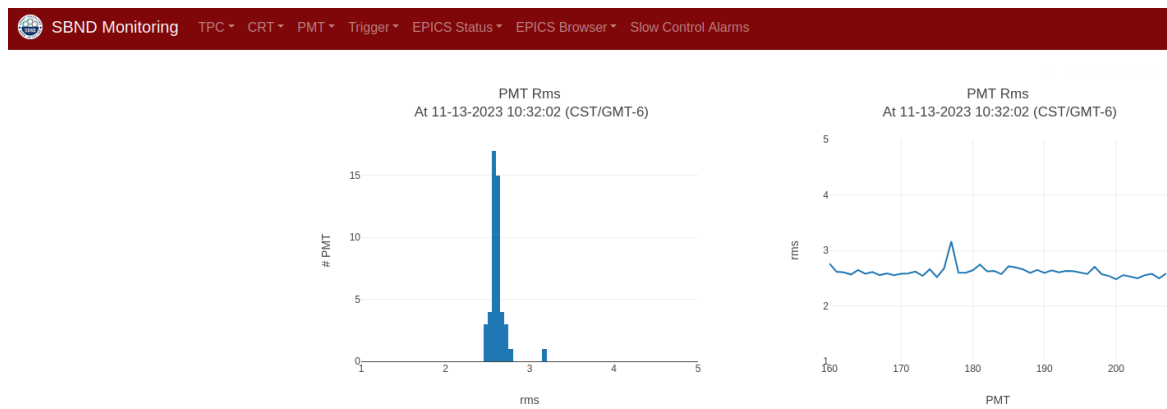


Fig. B.2 Web page showing a section of Minargon for monitoring the root mean square of a PMT waveform baseline.

Appendix C

Timing Distribution At SBND

The White Rabbit (WR) timing system at SBND was previously detailed in Chapter 7 Sec. 7.1.1. The signal distribution from the WR system is detailed here. Fig. C.1 illustrates the clock distribution across the DAQ components. Starting from the SVEC-FD module, two clock frequencies are generated: (1) 10 MHz and (2) 6.25 MHz, shown by the green and blue arrows respectively. The 10 MHz clock signal is directed through an LVDS fan out, and input to the Penn Trigger Board, as shown by the green box. The 6.25 MHz clock signal is directed through a LVDS fan out, and distributed in a fan out mode to all CAEN digitisers, as shown by the blue box. Moreover, the PTB also propagates the Beam Early Signal (BES) from the Multi-Function Timing Unit (MFTU), as shown by the solid orange arrow and box. The BES signal is delayed by the PTB, and directed to a CRT T1 fan out module to make multiple copies, which are all input to the FEB modules, as shown by the

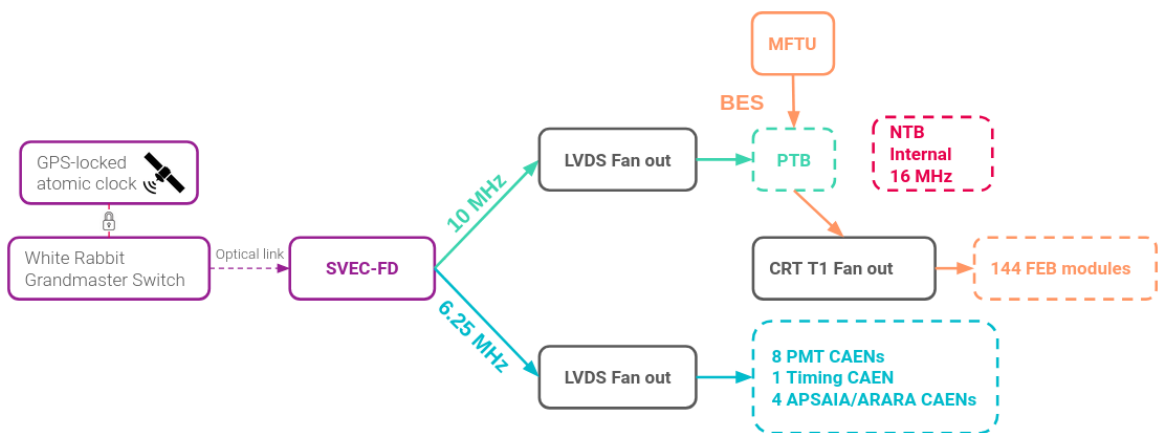


Fig. C.1 Clock signal distribution from the White Rabbit timing system to the DAQ subsystems.

dashed orange box. The Nevis Trigger Board (NTB), as shown by the red box, is the only readout component that does not receive an external clock. It instead uses an internal clock of 16 MHz.

Fig. C.2 shows the distribution of the Pulse Per Second (PPS) signal. The PPS is first generated by the SVEC-FD and input to fan out modules to make multiple copies. The copies are distributed to the PTB, CAEN digitisers and FEB modules. The NTB is a special case, where it receives the PPS from the PTB, where the TTL PPS signal is shifted to a NIM signal.

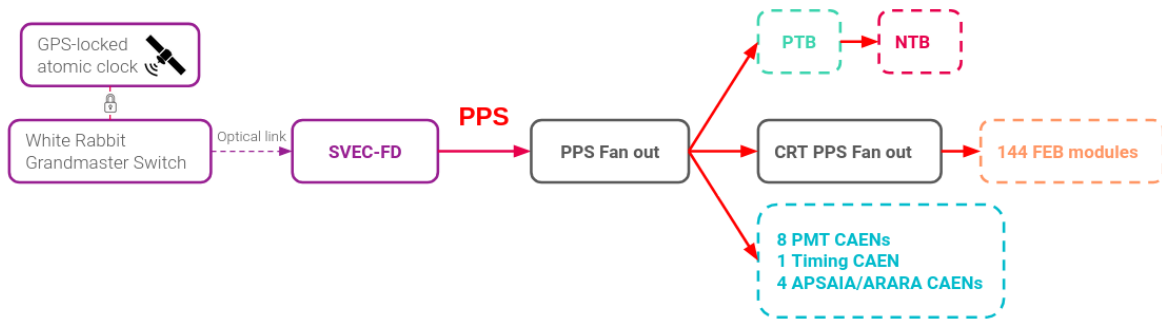


Fig. C.2 PPS signal distribution from the White Rabbit timing system to the DAQ subsystems.

Appendix D

Lenient Beam Bucket Distribution

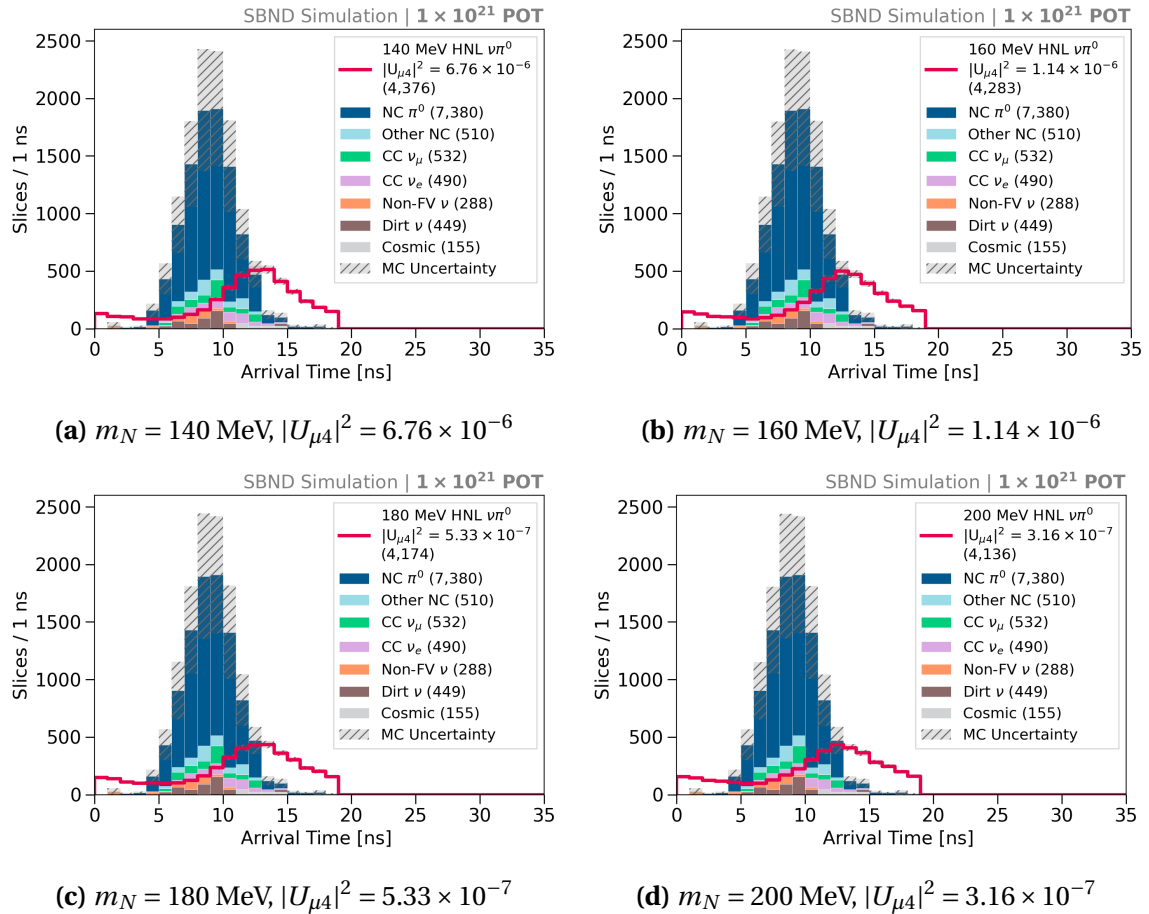


Fig. D.1 Beam bucket distributions after the lenient selection.

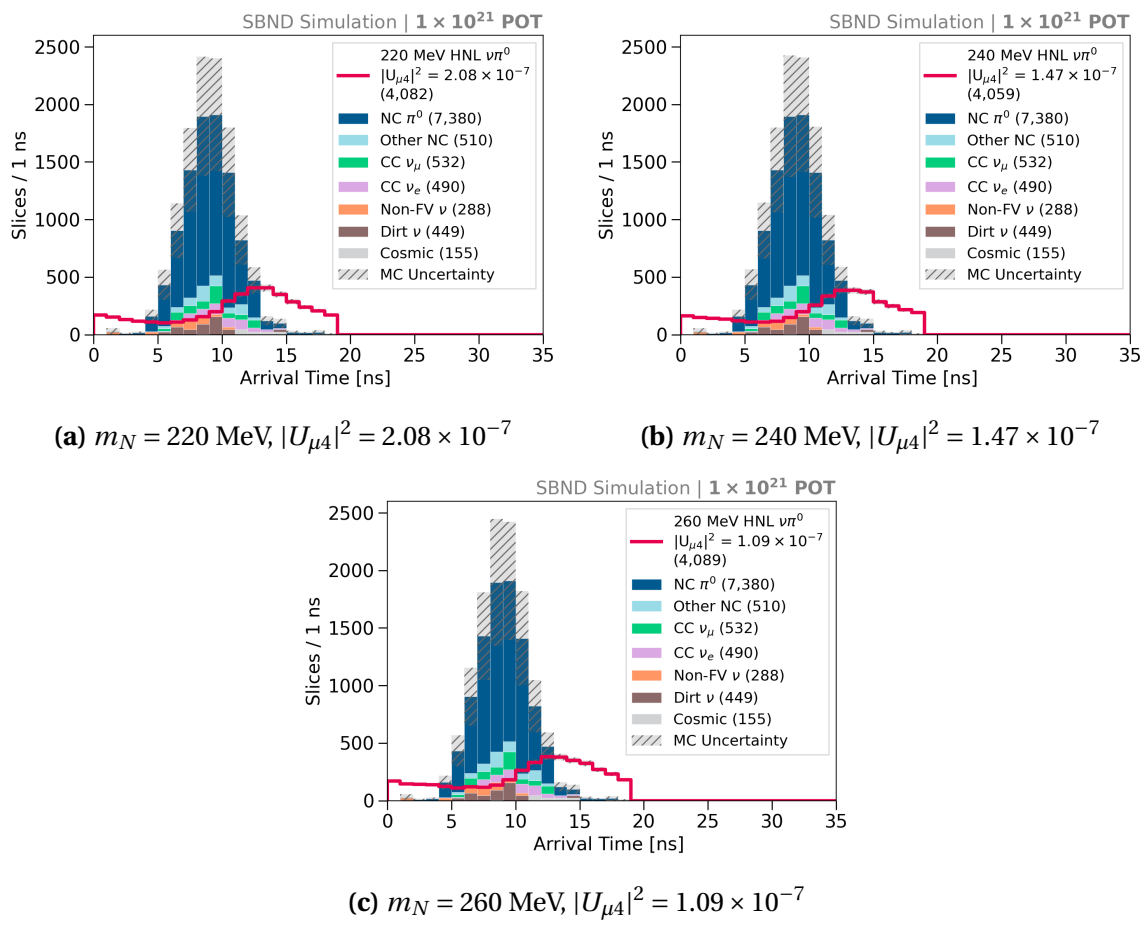


Fig. D.2 Beam bucket distributions after the lenient selection.

Appendix E

Stringent Beam Bucket Distribution

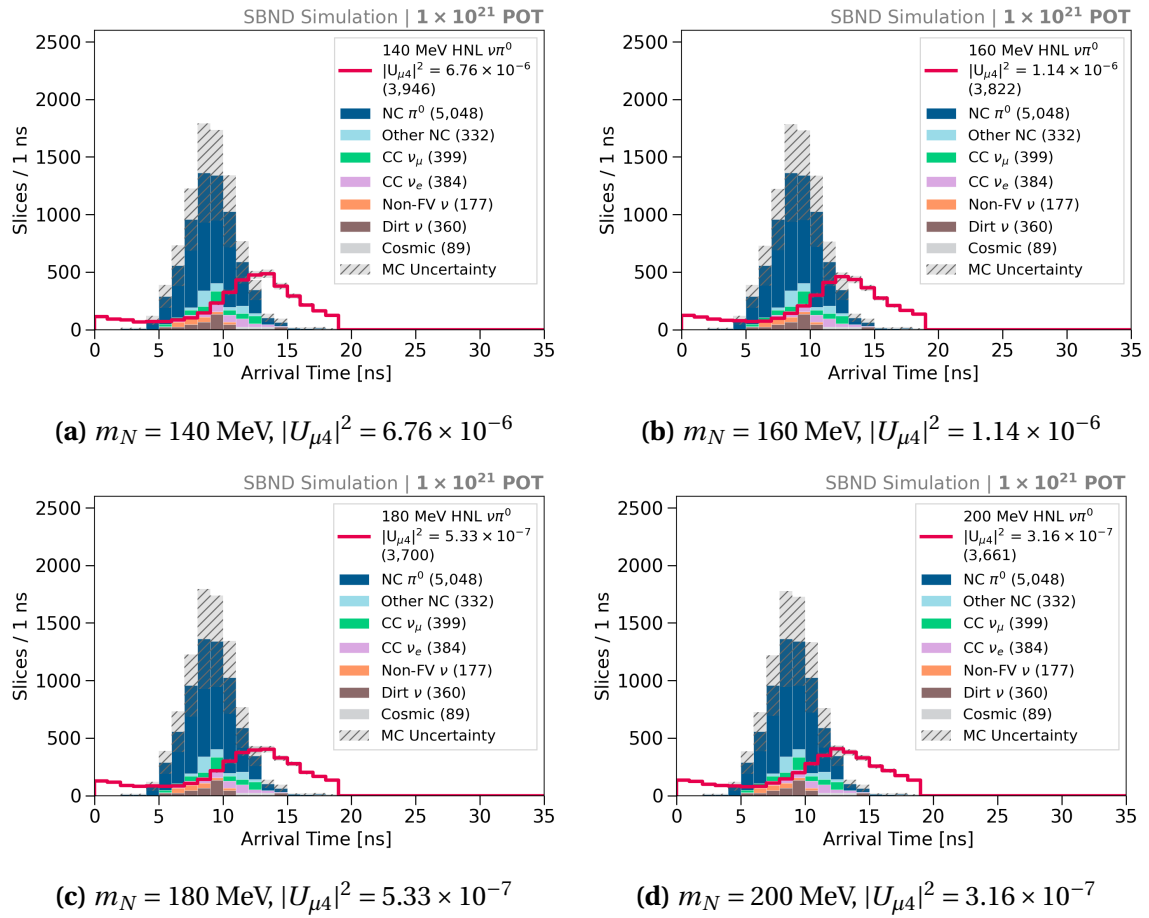


Fig. E.1 Beam bucket distributions after the stringent selection.

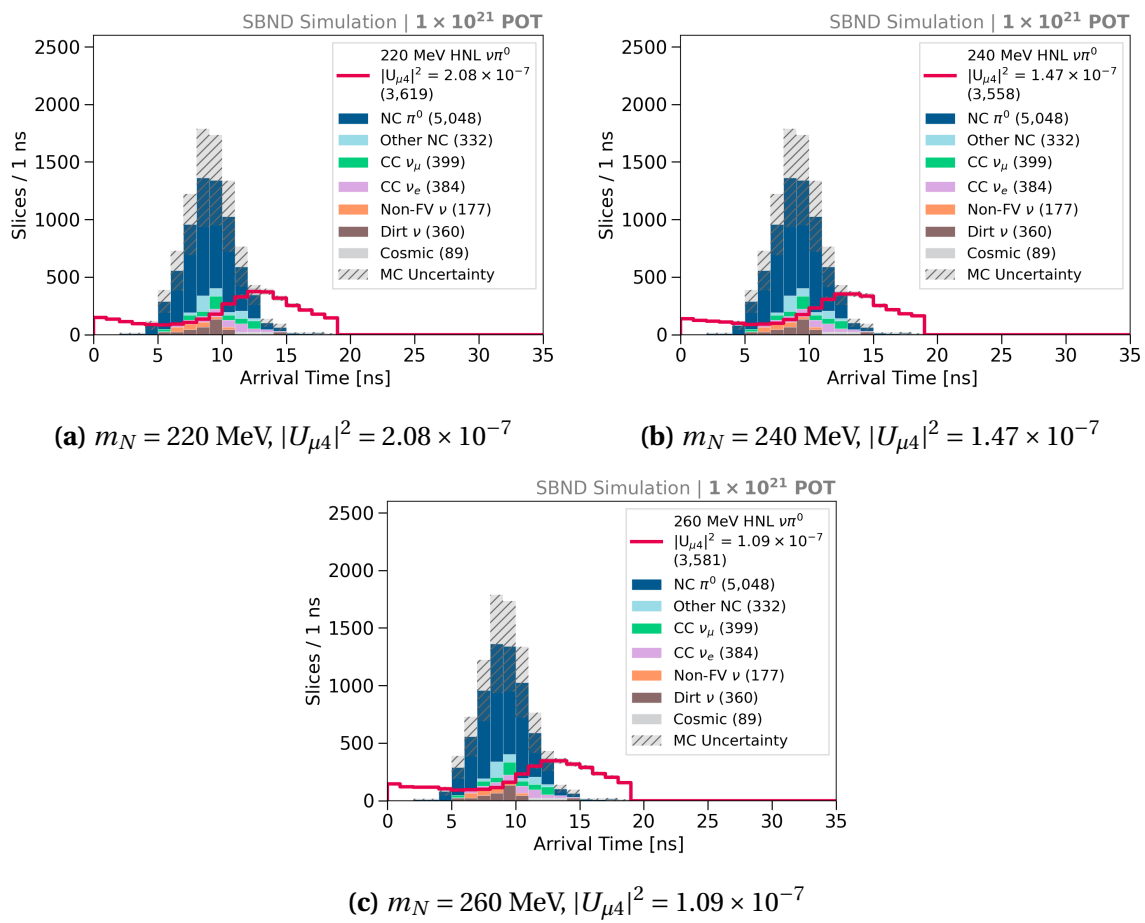


Fig. E.2 Beam bucket distributions after the stringent selection.

Appendix F

Smeared Truth Beam Bucket Distribution

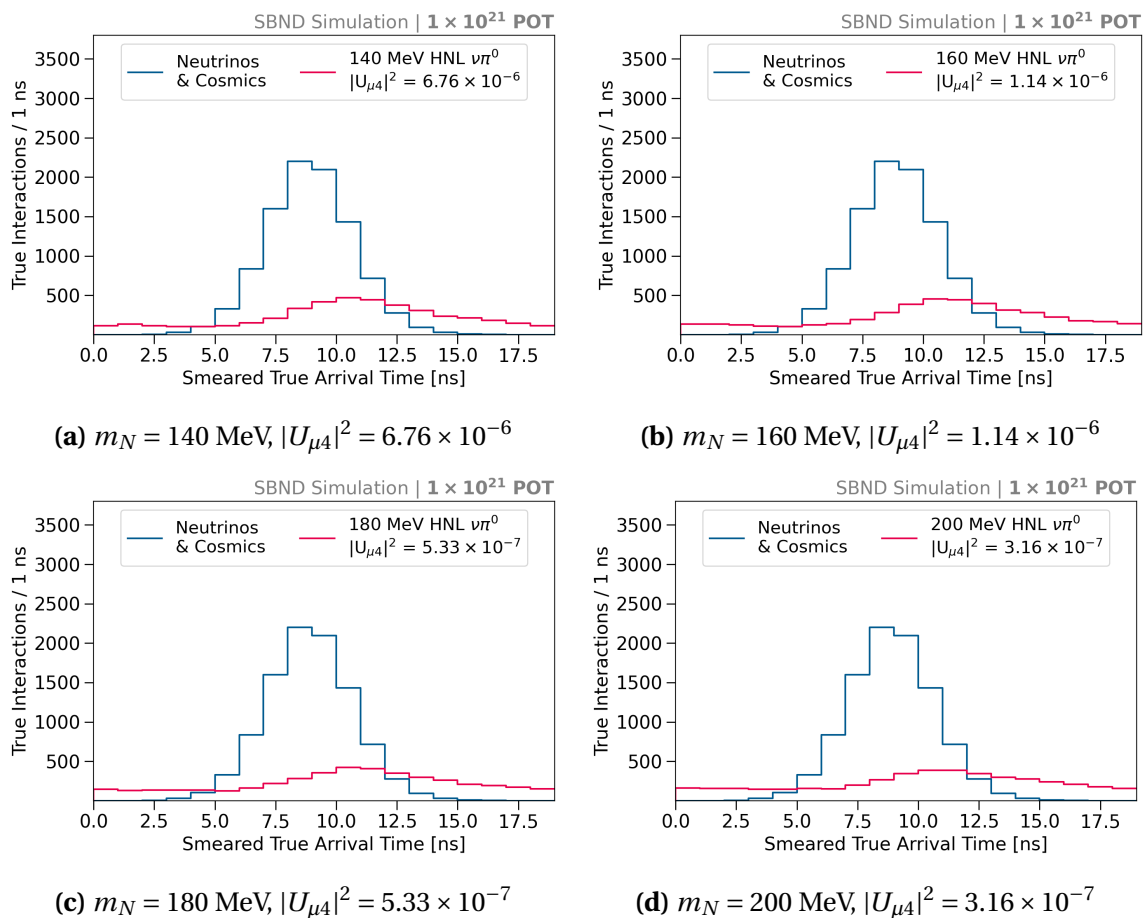


Fig. F.1 Beam bucket distributions from smearing true arrival times.

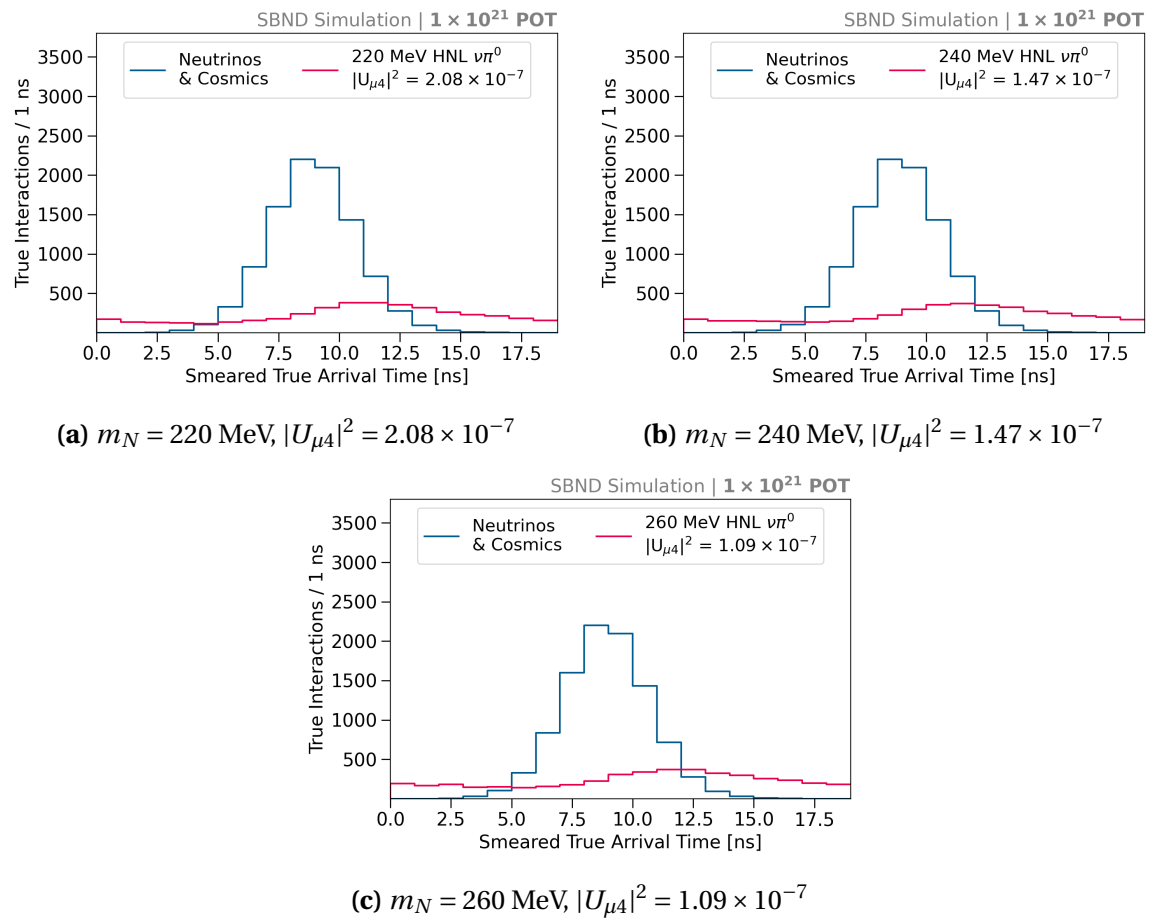


Fig. F.2 Beam bucket distributions from smearing true arrival times.